

# **Dissolution Behaviour of Beryl**

vorgelegt von

MSc. Geology

Raji Kurumathoor Parameshwaran

geb. in Taliparamba, Kerala, India

von der Fakultät VI- Planen Bauen Umwelt

der Technischen Universität Berlin

zur Erlangung der akademischen Grades

Doktor der Naturwissenschaften

- Dr. rer. Nat. -

Genehmigte Dissertation

Promotionausschluss:

Vorsitzender: Prof. Dr. Tomás Fernandez-Steeger

Gutachter: Prof. Dr. Gerhard Franz

Gutachter: Prof. Dr. Monika Koch-Müller

Gutachter: Dr. Vladimir Khomenko

Tag der wissenschaftlichen Aussprache: 11 November 2016

Berlin 2016

# Acknowledgements

## Dedicated to my Parents

I would like to express my sincere gratitude to my supervisor Prof. Gerhard Franz for his incessant support of my Ph.D study, for his persistent motivation and the immense knowledge he kindly shared during my studies. His supervision helped me at all times of my research and writing of this thesis.

Besides my advisor, I would like to thank Dr. Vladimir Khomenkho who gave me valuable suggestions in discussion and Prof. Gottschalk for his assistance in getting training in XRD. My sincere thanks to Prof. Monika Koch Müller, Dr. Caterina Tomasseo, Dr. Christian Agthe, Dr. Susanne Herting Agthe, Dr. Ulrike Kramm, Dr. Massimo Tallarido, Dr. Denis, Dr. Frederic Lucassen and Mr. Ferry Schipersky.

I would like to convey my gratitude to Mrs. Krista Zecha, Mrs. Krista Kotré, Mr. Jörg Nissen, Mr. Galbert and Ms. Cordelia for the technical assistance they had extended to me. I also acknowledge the efforts made by my fellow labmates Dr. David Evuk, Ms. Dina Schulz, Dr. Philip Gleissner and to all the members of Mineralogy and the Petrology department of the Technical University.

I would like to express my heartfelt gratitude to Mrs. Sujatha Singh, the then Ambassador of India to Germany for the timely help offered by her. I utilise this opportunity to express my sincere gratitude towards Mrs. Savita Mudgal, spouse of High Commissioner of India to Mauritius, who gave her precious time not only in proof reading but also giving me moral support throughout my stay in Mauritius.

Last but not least, I would like to thank my husband Ashok as well as my daughters Naina and Anjani who are my inspiration throughout my studies who kept faith in my abilities and boundlessly motivated me until this very moment. I am also grateful to my brother Hari, sister Rema and my friends for their moral support. Perhaps without them, my studies could not have been possible.

## Abstract

Beryl, a cyclosilicate, with an ideal chemical composition  $\text{Be}_3\text{Al}_2\text{Si}_6\text{O}_{18}$ , is the most important accessory Be mineral and an ore of the strategic element Be. It is mainly found in pegmatites, in some highly evolved granites and in some metamorphic rocks. In many cases, the beryl forming process extends over a wide range of P-T-X conditions. This process represents the major range of pegmatitic formation. Freely grown hydrothermal pegmatitic beryl crystals often show characteristic etch pits, which are indicators of dissolution. The objective of the present work is to study the dissolution behaviour of beryl, the most common Be-mineral and one of the most attractive and widely used precious gemstones, through the topography of its surface etch pits. The study was carried out in three stages. In the first stage, twenty one specimens of beryl crystals from different exemplary locations were investigated by comparing geology and petrogenesis of their source rocks, characterising the samples in terms of crystal chemistry by electron microprobe, infrared spectroscopy (pellet and single crystal method), X-ray powder diffraction (Rietveld), Raman spectroscopy and NIR spectroscopy. The results allowed differentiating alkali rich beryls from poor ones. In the second stage, surface topography was characterised by scanning electron microscope and image analysis. The emphasis was given to etch pit shape distribution analysis as the etch pits are not only the measures of dissolution but are also diagnostic tools to determine symmetry, identify crystal defects and in provenance separation. A direct linear relationship is established between the value of surface texture and surface area of the etch pits and the extent of dissolution. Surface texture and surface area are found to be maximum in P-type etch pits and minimum in F-type etch pits. However, values of fractal dimension and micro-hardness are inversely related to the above-mentioned values and are found to be minimum in P-type etch pits and maximum in F-type etch pits. Chemical analysis has shown a similar composition of fluid and solid inclusions and the materials deposited inside the etch pits. In the third stage, etch pits were created experimentally at 600°C, two kilobars and variable fluid composition: NaCl, KCl, NaOH and HCl solutions of different concentrations. The results were compared with the natural processes by characterising the surface topography of hydrothermally treated natural beryls by qualitative analysis of the materials deposited on the surface. These treated samples were powdered and further analyzed to study the effect of substitution of cations on dissolution by infrared spectroscopy and found that the dissolution starts by leaching of cations from the channel followed by the removal of cations from the Al-octahedron. This study indicates that the morphology of etch pits differ on samples from different localities and the factors that control dissolution of beryl are crystal structure (orientation; the maximum dissolution is along c-axis), crystal defects (inclusions and dislocations), substitution of cations, symmetry of the faces and solvents.

## Zusammenfassung

Beryll, ein Ringsilikat mit der chemischen Zusammensetzung  $\text{Be}_3\text{Al}_2\text{Si}_6\text{O}_{18}$  ist das wichtigste akzessorische Be-Mineral und Rohstoff für das strategische Element Be. Es kommt in erster Linie in Pegmatiten vor, in hoch-differenzierten Graniten und in einigen Metamorphiten. In vielen Fällen erstreckt sich der beryllbildende Prozess über einen weiten Bereich von P-T-Bedingungen. Dieser Prozess repräsentiert den weiten Bereich der Pegmatitbildung. Frei gewachsene hydrothermale pegmatitische Beryllkristalle zeigen oft typische Ätzfiguren, die Auflösung anzeigen. Das Ziel der Arbeit ist die Untersuchung des Auflösungsverhaltens von Beryll, das häufigste Be-Mineral und einer der am häufigsten verwendeten wertvollen Edelsteine, über die Topographie der Oberflächenätzfiguren. Die Studie wurde in drei Schritten durchgeführt. Im ersten Schritt wurden 21 Beryllkristalle von verschiedenen exemplarischen Lokalisationen ausgesucht, im Vergleich ihrer Geologie und Petrogenese der Wirtsgesteine, Charakterisierung der Kristallchemie durch Elektronenstrahlmikrosonde, Infrarotspektroskopie (an Press-tabletten und Einkristallen), Röntgenpulverdiffraktometrie (Rietveld), Ramanspektroskopie und NIR-Spektroskopie. Die Ergebnisse lassen Alkali-reiche von -armen unterscheiden. Im zweiten Schritt wurde die Oberflächentopographie mit dem Rasterelektronenmikroskop und Bildverarbeitung untersucht. Hauptaugenmerk lag auf der Analyse der Formverteilungsanalyse der Ätzfiguren, da die Ätzfiguren nicht nur ein Maß für die Auflösung sind, sondern auch diagnostisch sind für Symmetrie, für Kristallbaufehler und in der Provenienzanalyse. Es konnte eine direkte Abhängigkeit gefunden werden zwischen dem Wert der Oberflächentextur, der Oberfläche der Ätzfiguren und dem Betrag der Auflösung. Oberflächentextur und -fläche sind maximal bei P-Typ Ätzfiguren, minimal bei F-Typ Figuren. Im dritten Stadium wurden experimentell Ätzfiguren erzeugt, bei 600 °C, 2 kbar und variable Fluidzusammensetzung: NaCl, KCl, NaOH und HCl Lösungen variabler Konzentration. Die Ergebnisse wurden mit den natürlichen Prozessen verglichen über die Charakterisierung der Oberflächentopographie der hydrothermalbehandelten natürlichen Beryll durch qualitative Analyse der Ablagerungen auf deren Oberflächen. Die behandelten Proben wurden pulverisiert und mit IR analysiert, um den Effekt der Kationensubstitution auf den Lösungsprozess zu charakterisieren. Die Auflösung beginnt mit den Kanalonen, gefolgt von den Kationen im Al-Oktaeder. Die Arbeit zeigt, dass die Morphologie der Ätzfiguren von unterschiedlichen Lokalisationen unterschiedlich ist, ebenso wie die Faktoren, die die Auflösung von Beryll kontrollieren, nämlich Kristallstruktur (Orientierung; die Hauptauflösung geschieht entlang der c-Achse), Kristallbaufehler (Einschlüsse und Versetzung), Substitution der Kationen, Symmetrie der Flächen und die Lösung.

# Table of Contents

Acknowledgements .....	1
Abstract .....	2
Zusammenfassung .....	3
List of figures .....	6
List of Tables .....	9
1. Introduction .....	10
1.1 Aims and applications of current research .....	10
1.2 Objectives.....	11
1.3 Beryl formation.....	12
1.4 Uses of beryl.....	13
1.5 Crystal structure of beryl.....	13
1.6 Chemical composition of beryl.....	14
1.7 Physical properties.....	16
1.8 Previous studies on surface etch pits of beryl.....	17
1.9 Motivation for the current research.....	18
2. Methods.....	20
2.1 Sample material and geological occurrence .....	20
2.1.1 Minas Gerais, Brazil.....	21
2.1.2 Shigar valley, Higher Himalayan Crystalline zone .....	21
2.1.3 Lumäki pegmatites, Finland.....	22
2.1.4 Xueobaoding mountain, Sichuan Province, China .....	23
2.2 Characterisation of beryls .....	24
2.2.1 Investigation of morphology of crystals .....	24
2.2.2 Investigations of thin sections with polarizing microscope.....	24
2.2.3 Chemical analysis by electron microprobe EPMA.....	24
2.2.4 Refractive indices determination.....	25
2.2.5 X-ray powder diffraction .....	25
2.2.6 Vibrational spectroscopy.....	25
2.3. Characterisation of surface topography .....	26
2.3.1. Scanning Electron Microscopy (SEM).....	26
2.3.2 Atomic Force Microscopy (AFM).....	26
2.4 Hydrothermal experiments .....	27
3. Results.....	28

3.1 Morphology .....	28
3.2. Studies of inclusions under polarizing microscope and electron microprobe .....	30
3.3 EMP analysis .....	34
3.4 Refractive indices determination .....	39
3.5 XRD analysis .....	40
3.6 IR spectroscopic studies .....	45
3.7 Raman spectroscopic studies .....	54
3.8 NIR Spectroscopic Studies .....	57
3.9 Scanning Electron Microscopic investigations .....	59
3.9.1. General description of SEM images .....	59
3.9.2 SEM image analysis .....	71
3.10 Hydrothermal experiments .....	80
4. Discussion .....	96
4.1 Morphology .....	96
4.2 RI determination .....	96
4.3 EMPA .....	98
4.4 X-ray diffraction analysis .....	99
4.5 Inclusions .....	100
4.6 Vibrational spectroscopy .....	101
4.6.1 IR spectroscopy .....	101
4.6.2 Raman spectroscopy .....	106
4.6.3 NIR spectroscopy .....	108
4.7 Scanning Electron Microscopy .....	110
4.7.1 Results of the current study .....	110
4.7.2 Literature review on formation of etch pits .....	119
4.7.3 Literature review about the morphology of etch pits on beryl .....	119
4.8 Hydrothermal Experiments .....	121
4.8.1 SEM studies .....	121
4.8.2 IR spectroscopic studies of hydrothermally treated beryl .....	123
5. Summary and Conclusion .....	125
6. References .....	128
7. Appendix .....	141

## List of figures

Fig. 1.1 Minerals in the system $\text{BeO-Al}_2\text{O}_3\text{-SiO}_2\text{-H}_2\text{O}$ projected from $\text{H}_2\text{O}$ .....	10
Fig. 1.2 Diagram for applications of etch pit studies .....	11
Fig. 1.3 Pressure-temperature projection of phase relationships in the $\text{BeO-Al}_2\text{O}_3\text{-SiO}_2\text{-H}_2\text{O}$ (BASH) system. Barton, 2002.....	12
Fig. 1.4 Ball-and-stick model of beryl crystal structure .....	14
Fig. 1.5 General structure of beryl channel. Modified after Wood and Nassau, 1967 .....	15
Fig. 1.6 Beryl crystal's drawing with etch pits on different faces.....	18
Fig. 2.1 Representative samples from different localities .....	20
Fig. 3.1 Crystal drawings of the samples: (a) PAD-4 (b) PAD-5 (c) PAD-6 from Dassu mines, Himalayas .....	29
Fig. 3.2.1 Photograph of sample BA-1 cut parallel to the base under stereoscope.....	31
Fig. 3.2.2 Photomicrographs of thin sections .....	32
Fig. 3.2.3 Photomicrographs of thin sections .....	32
Fig. 3.2.4 BSE images and SE images from polished thin sections .....	33
Fig. 3.2.5 SE and BSE images of thin sections .....	33
Fig. 3.2.6 BSE images of thin sections.....	34
Fig. 3.3.1 BSE images of thin sections.....	34
Fig. 3.3.2 Plot of Si (apfu) vs Al (apfu).....	37
Fig. 3.3.3 Plot of Si (apfu) vs Na+Cs (apfu) .....	37
Fig. 3.3.4 Plot of Al (apfu) vs Na+Cs (apfu).....	38
Fig. 3.3.5 Plot of Al (apfu) vs Fe (apfu).....	38
Fig. 3.3.6 Plot of Si (apfu) vs Fe (apfu) .....	39
Fig. 3.3.7 Plot of Na+Cs (apfu) vs Fe (apfu) .....	39
Fig. 3.4.1 Plot of refractive indices ( $\omega$ ) vs Na+Cs (apfu) .....	40
Fig. 3.5.1 Plot of inter atomic distances vs. Na(apfu). .....	42
Fig. 3.5.2 Plot of samples vs. c/a ratio .....	43
Fig. 3.5.3 Plot of Al (apfu) vs. a-parameter .....	43
Fig. 3.5.4 Plot of a-parameter vs. Fe (apfu).....	44
Fig. 3.5.5 Plot of c- parameter vs. Na+Cs (apfu).....	44
Fig. 3.5.6 Plot of c-parameter vs. Si (apfu).....	45
Fig. 3.5.7 Plot of c-parameter vs. a-parameter .....	45
Fig. 3.6.1 Infrared spectrum of BA-1 in the frequency region from $400\text{cm}^{-1}$ to $1400\text{cm}^{-1}$ .....	46
Fig. 3.6.2 Infrared spectrum of BAA-1 in the frequency region from $400\text{ cm}^{-1}$ to $1400\text{ cm}^{-1}$ .....	46
Fig. 3.6.3 Infrared spectrum of CA-1 in the frequency region from $400\text{ cm}^{-1}$ to $1400\text{ cm}^{-1}$ .....	47
Fig.3.6.4 Infrared spectrum of BAA-2 in the frequency region from $400\text{ cm}^{-1}$ to $1400\text{ cm}^{-1}$ .....	47
Fig. 3.6.5 Plot of IR band position around $1200\text{ cm}^{-1}$ vs. Si (apfu).....	49
Fig. 3.6.6 Plot of IR band position around $1200\text{ cm}^{-1}$ vs. Al (apfu) .....	49
Fig. 3.6.7 Plot of IR band position around $1200\text{ cm}^{-1}$ vs. Na+Cs (apfu) .....	50
Fig. 3.6.8 Plot of IR band position around $810\text{ cm}^{-1}$ vs. Al (apfu).....	50

Fig. 3.6.9 Plot of IR band positions around $810\text{ cm}^{-1}$ vs. Na+Cs (apfu).....	51
Fig. 3.6.10 Polarised IR spectra of PA-2 single crystal from $1000\text{ cm}^{-1}$ to $7000\text{ cm}^{-1}$ .....	52
Fig. 3.6.11 Polarised IR spectra of PAD-1 single crystal from $1000\text{ cm}^{-1}$ to $7000\text{ cm}^{-1}$ .....	52
Fig. 3.6.12 Polarised IR spectra of PAY-3 single crystal from $1000\text{ cm}^{-1}$ to $7000\text{ cm}^{-1}$ .....	53
Fig. 3.6.13 IR spectra of BA-1 single crystal under unpolarised light from $1000\text{ cm}^{-1}$ to $4000\text{ cm}^{-1}$ .....	53
Fig. 3.7.1 Raman spectrum of alkali rich beryl BAA-1 (E c).....	54
Fig. 3.7.2 Raman spectrum of FH-3 (E c). .....	55
Fig. 3.7.3 Raman spectrum of PA-2 (E $\perp$ c).....	55
Fig. 3.7.4 Raman spectrum of PAD-8 (E $\perp$ c).....	56
Fig. 3.7.5 Raman spectra of BA-1, PA-2 and PAD-8 in the range from $3500\text{--}3700\text{ cm}^{-1}$ .....	56
Fig. 3.8.1 NIR spectrum of BAA-1 from $1000\text{ nm}$ to $2200\text{ nm}$ .....	57
Fig. 3.8.2 NIR spectrum of BAA-2 in the range from $1000\text{ nm}$ to $2200\text{ nm}$ .....	58
Fig. 3.8.3 NIR spectrum of CA-1 from $1000\text{ nm}$ to $2200\text{ nm}$ .....	58
Fig. 3.8.4 NIR spectrum of PAD-1 (Transmission method) under E $\perp$ c orientation .....	59
Fig. 3.9.1 SEM image of hexagonal etch pits with pointed base on $\{0001\}$ of PA-2 .....	60
Fig. 3.9.2 SEM image of basal pinacoid $\{0001\}$ of BA-1 .....	60
Fig. 3.9.3 SEM images of hollow cores on the basal pinacoid $\{0001\}$ of BA-1 .....	61
Fig. 3.9.4 SEM image of basal pinacoid $\{0001\}$ of BAA-1 .....	61
Fig. 3.9.5 Growth spirals (white arrow) and triangular shaped hollow cores on the base $\{0001\}$ of BA-1.....	62
Fig. 3.9.6 Overview of prism face $\{10\bar{1}0\}$ of BA-1.....	63
Fig. 3.9.7 Enlarged view of different kinds of etch pits on BA-1 .....	63
Fig. 3.9.8 SEM image of prism face of FH-3 .....	64
Fig. 3.9.9 SEM image of P-type etch pit with straight edges in BA-1.....	64
Fig. 3.9.10 SEM images of prism face of PA-2 .....	65
Fig. 3.9.11 Stepped Canoe shaped etch pit on the prism face of PAD-10 .....	65
Fig. 3.9.12 Prism face of PAY-1 .....	66
Fig. 3.9.13 Etch pits on the prism face of CA-1 .....	66
Fig. 3.9.14 SEM images of first and second order prism faces in BA-1.....	67
Fig. 3.9.15 Images of piece of BA-1 crystal from the inner side of the hollow core.....	68
Fig. 3.9.16 Canoe shaped structures oriented perpendicular to c-axis on the inner prism face of hollow beryl (BA-1b). .....	68
Fig. 3.9.17 Transition from basal pinacoid $\{0001\}$ , pyramid of second order $\{11\bar{2}2\}$ and pyramid of first order $\{10\bar{1}1\}$ in BA-1.....	69
Fig. 3.9.18 SEM images of pyramid of first and second order faces of BA-1 .....	70
Fig. 3.9.19 Pyramidal face of PAD-9 .....	70
Fig. 3.9.20 SE images of sample BAA-2 from Minas Gerais, Brazil.....	71
Fig. 3.9.21 SEM images of different etch pits on $\{10\bar{1}0\}$ of BA-1 which are used to determine shape distribution, surface texture, fractal dimension and eccentricity by image analysis .....	72
Fig. 3.9.22 Geometrical reconstruction of P-type etch pit on prism face of BA-1 .....	73
Fig. 3.9.23 Geometrical reconstruction of P-type etch pit in FH-3.....	73
Fig. 3.9.24 Plots of shape factors of different kinds of etch pits.....	74
Fig. 3.9.25 Plots of values of fractal dimension and surface texture of etch pits shown in Fig. 3.9.21 75	

Fig. 3.9.26 Plot of Vickers hardness vs values of surface texture (Ra) in different etch pits .....	76
Fig. 3.9.27 Plots of values of surface texture in different directions of etch pits .....	77
Fig. 3.9.28 Profile of texture along the length of different types of etch pits. ....	78
Fig. 3.9.29 Etch pits analysed to find out surface texture, fractal dimension and surface area .....	79
Fig. 3.9.30 Plots showing relationship between fractal dimension, surface area and surface texture in P-type etch pits of different samples .....	80
Fig. 3.10.1 SEM images of PAD- 8 hydrothermally treated in 1N NaCl solution .....	82
Fig. 3.10.2 SEM images of PAD-8 treated in NaCl solution.....	83
Fig. 3.10.3 SEM image of quench products with EDS spectra of PAD-8 treated in NaCl solution .....	84
Fig. 3.10.4 SEM images of crystals on the surface of PAD-8 treated in NaCl solution .....	85
Fig. 3.10.5 Images of surface of NaCl-treated PAD-8 after cleaning .....	85
Fig. 3.10.6 SEM image of KCl treated PAD-8.....	86
Fig. 3.10.7 SEM images of quench products in KCl treated PAD-8.....	87
Fig.3.10.8 SEM images of strongly dissolved surface of KCl treated PAD-8 .....	87
Fig. 3.10.9 SEM image of the surface of KCl treated PAD-8 after cleaning .....	88
Fig. 3.10.10 SEM images of prism face $\{10\bar{1}0\}$ of NaOH treated BA-1 .....	89
Fig. 3.10.11 SEM images of BA-1 treated in NaOH solution .....	89
Fig. 3.10.12 SEM image of NaOH treated BA-1.....	90
Fig. 3.10.13 SEM image of clusters of reprecipitated beryl on BA-1 treated in NaOH solution .....	90
Fig.3.10.14 SEM image of HCl-treated BA-1 .....	91
Fig. 3.10.15 SEM images of quench products in HCl treated BA-1.....	92
Fig. 3.10.16 SEM images of quench products on the surface of BA-1 treated in HCl solution .....	93
Fig. 3.10.17 IR spectrum of untreated BA-1 from $400\text{ cm}^{-1}$ to $4000\text{ cm}^{-1}$ wavenumber .....	94
Fig. 3.10.18 IR spectrum of NaOH treated BA-1 from $400\text{ cm}^{-1}$ to $4000\text{ cm}^{-1}$ wavenumber .....	94
Fig. 3.10.19 IR spectrum of HCl treated BA-1 from $400\text{ cm}^{-1}$ to $4000\text{ cm}^{-1}$ wavenumber .....	94
Fig. 4.1 Vibrations of type I and type II $\text{H}_2\text{O}$ molecules in the channel of beryl.....	104
Fig. 4.2. Geometrical reconstruction of P-type etch pits on the prism face $\{10\bar{1}0\}$ of the samples from different localities.....	112
Fig. 4.3 Schematic representation of formation of different kinds of etch pits after Motzer and Reichling, 2010. ....	115
Fig. 4.4 Schematic diagram showing different stages of formation of etch pits .....	118

## List of Tables

Table 1 Presenting samples, characteristics, methods and the locality .....	29
Table 2 Oxides (wt%) in different samples .....	35
Table 3 Number of cations based on 18 oxygen atoms .....	36
Table 4 Refractive indices, $\Delta n$ and Na+Cs (apfu) per 18 oxygen atoms of samples from three different locations.....	40
Table 5 Lattice parameters, c/a ratio and volume of unit cell .....	41
Table 6 Inter-atomic distances calculated by Rietveld method, coordination number and ionic radius of the cations in beryl samples .....	42
Table 7 IR spectra band positions of samples in wave numbers ( $\text{cm}^{-1}$ ).....	48
Table 8 Shape factors of different types of etch pits .....	74
Table 9 Fractal dimension and surface texture on different kinds of etch pits' surface .....	74
Table 10 Vickers Hardness and surface texture at different kinds of etch pits .....	75
Table 11 Surface texture Ra ( $\mu\text{m}$ ) in different directions of the etch pit .....	76
Table 12 Surface texture, fractal dimension and surface area of P-type etch pits in different samples .....	79
Table 13 Run conditions and results for the hydrothermal experiments (at 600°C, 2 kbars) .....	81
Table 14 Position of IR bands before treatment and after treatment in HCl and NaOH solutions .....	95
Table 15 IR vibration band assignment for beryl by different authors .....	103
Table 16 IR studies of beryl samples in the water region by different authors.....	106
Table 17 Band positions in the Raman spectra of samples, their assignments by different authors, orientation and their intensities .....	107
Table 18 Band positions in NIR spectra of the samples and assignment to various vibrations.....	109
Table 19 Etch pits on different faces of representative samples from different locations .....	111

## 1. Introduction

**1.1 Aims and applications of current research:** The kinetics of silicate mineral dissolution controls the geochemistry of earth system. Hence, the dissolution behaviour of minerals (especially silicates) has received considerable interest from weathering studies to high P-T processes. The dissolution of minerals and their re-precipitation or precipitation of new minerals plays an important role in the rheological behaviour of earth's crust (Heald, 1956; Schwarz and Stockhert, 1996). These processes have significance in oil recovery, formation of commercially important mineral deposits and the behaviour of metallic and radioactive contaminants in the subsurface. The formation of etch pits is prominent in most of the mineral dissolution process (Berner and Schott, 1982).

Beryl is the most persistent mineral among 8 beryllium containing minerals of 18 minerals belonging to the  $\text{BeO-Al}_2\text{O}_3\text{-SiO}_2\text{-H}_2\text{O}$  (BASH) system (Barton, 1986) and its stability field ranges from 300 °C to 1200 °C and up to very high pressure (Franz and Morteani, 2002). Therefore, it is assumed that beryl represents the conditions covering the major range of pegmatitic formation.

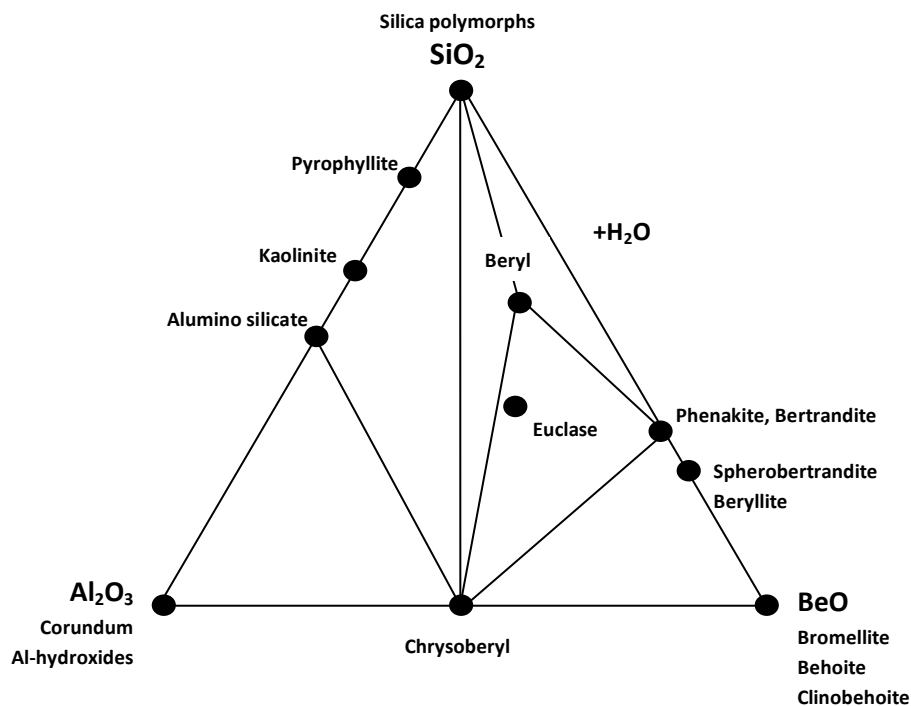


Fig. 1.1 Minerals in the system  $\text{BeO-Al}_2\text{O}_3\text{-SiO}_2\text{-H}_2\text{O}$  projected from  $\text{H}_2\text{O}$ . From Franz and Morteani, 2002.

Increased industrial importance of beryl has led to many studies in recent years. As beryl incorporates significant and variable amounts of different elements in the channel in order to compensate the charge deficiency caused due to complex cationic substitution, many

questions relating to the stability are still unanswered. Since congruent and incongruent dissolution are the stages for any mineral to become unstable, study of dissolution becomes very important in stability modelling.

Surface micro structures of crystals can provide useful information in deciding growth or post growth (dissolution) history that a crystal experienced. The studies of these micro structures have many applications in different fields, for example in determining crystal symmetry. Before X-rays were discovered, etching technique was used to determine the symmetry. The etch pits are the perfect indicators of dissolution behaviour of minerals. Freely grown beryl crystals from pegmatitic-hydrothermal environments often show characteristic etch pits. Not only the formation of etch pits has a major significance in some substances but also etching technique is used to investigate defects in technologically very important materials (Lin, 1994; Dam et al., 1996; Akatsuka et al., 2000; Yonenaga et al., 2001). Dislocation induced etch pits have a major role in the control of surface morphology in electronic and optical devices (Zhou et al., 2002; Wheeler et al., 2003).

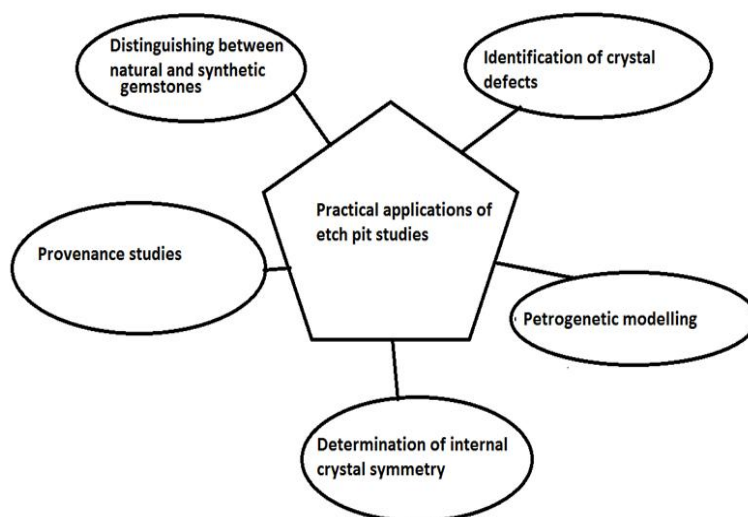


Fig. 1.2 Diagram for applications of etch pit studies. They vary from purely scientific to practical ones. Current study is focussed on applications of etch pits in identifying crystal defects, determining crystal symmetry and separation of provenances.

Morphology of etch pits possibly mirrors the provenance because etch pits depend on internal (crystal chemistry, symmetry and defects) and external factors (P-T-X-conditions of dissolution). They are likely different and characteristic for different deposits. Hence, the study of etch pit morphology could be a good tool in provenance separation and detecting crystal defects which are very important in gem industry. We can summarise the applications of etch pit studies through the above diagram (Fig. 1.2) which covers a major part of the current work.

**1.2 Objectives:** The objective is to study the dissolution behaviour of beryl through surface etch pits. It is achieved in 3 main stages: (1) Characterising beryl samples from



**1.4 Uses of beryl:** Beryl can be obtained in three forms: (1) as precious gemstone; (2) in powdered form for ceramic and porcelain industry and (3) to extract metallic beryllium. Pure beryl contains about 14% BeO or 5% Be. Beryl's hardness lies between 7 and 8 on Moh's scale of hardness and it is important to gem industry and collectors. Varieties of beryl like aquamarine, emerald, heliodor, morganite and goshenite are widely used as precious and semi-precious gem stones. Beryl increases the transverse strength, impact strength, heat resistance and dielectric strength in porcelains and hence powdered beryl can be used as a constituent in high tension insulator porcelains (Twells, 1922). Beryl is the most important ore of the strategic element beryllium. Beryllium is a good neutron moderator material because of its very low absorption cross section with respect to thermal neutrons (Everest, 1973; Greenwood and Earnshaw, 1997; Emsley, 2001). It has wide application in nuclear reactors and finds far reaching applications in alloys with copper, aluminium and other metals due to its refractory properties and resistance to corrosion (Grew, 2002).

**1.5 Crystal structure of beryl:** The crystal structure of beryl was first determined by Bragg and West, 1927 and later refined by Below and Matveeva, 1951; Gibbs et. al., 1968 and Morosin, 1972. Since silicon-oxygen tetrahedra are more or less uniformly distributed in the structure, Beus, 1960 had given a suggestion that it could also be classified as tectosilicate. The structure of beryl and tourmaline are almost similar being cyclo silicates except the way the apices of tetrahedra are oriented. In beryl, apices are pointed up and down alternatively giving a mirror plane of symmetry where as in tourmaline, the apices of silicate tetrahedra are pointed towards the same direction (hemimorphic). The salient feature of beryl crystal structure is the formation of  $\text{Si}_6\text{O}_{18}$  rings by linking six  $\text{SiO}_4$  tetrahedra and stacking of these rings on top of each other in perfect alignment along the c-axis, creating channels that run parallel to the c-axis. This crystal structure has great significance in its physical and chemical properties as well as crystal habit. These Si-O rings are linked laterally and vertically to adjacent rings by Be tetrahedra, thus forming four membered Be-Si rings parallel to c axis. The Al is situated between the six membered rings in a distorted octahedron, sharing oxygen with both Si and Be. Beryl belongs to hexagonal system: holosymmetric and dihexagonal-bipyramidal with space group  $P6/mcc$  in the Hermann-Mauguin notation and  $D_{6h}^2$  in the Schoenflies notation.

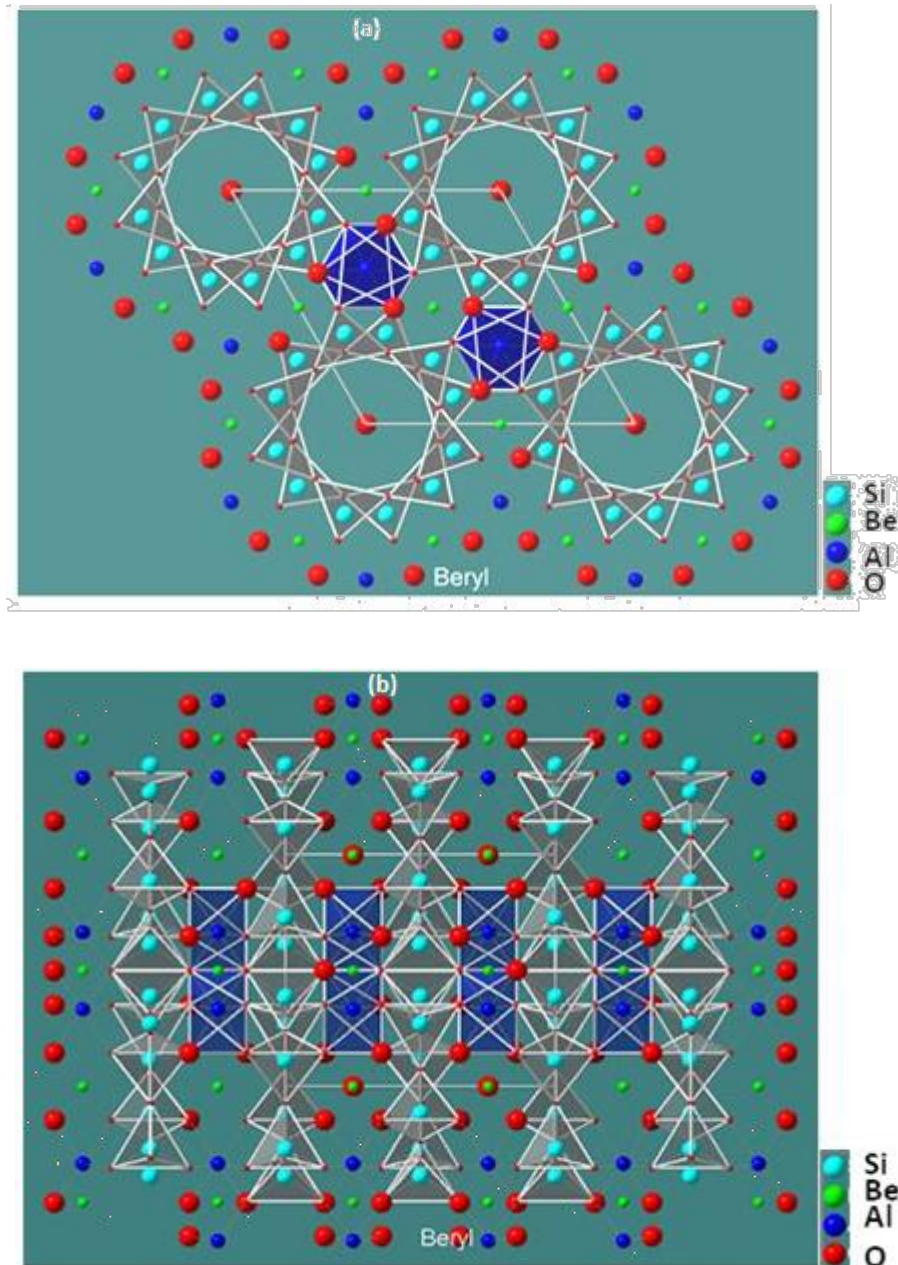


Fig. 1.4 Ball-and-stick model of beryl crystal structure. (a) With c-axis perpendicular to (0001). (b) With c-axis parallel to  $10\bar{1}0$  (made by program crystal maker). In Fig. 1.4a, the hexagonal unit cell is outlined.

**1.6 Chemical composition of beryl:** The ideal chemical formula of beryl is  $\text{Be}_3\text{Al}_2\text{Si}_6\text{O}_{18}$ . Analysis of natural beryls seldom confirms the ideal formula due to complex cationic substitutions. The most common replacements are the substitutions of  $\text{Si}^{4+}$  by  $\text{Al}^{3+}$  in tetrahedral sites,  $\text{Al}^{3+}$  by divalent, trivalent ions ( $\text{Mg}^{2+}$ ,  $\text{Mn}^{2+}$ ,  $\text{Fe}^{2+}$ ,  $\text{Fe}^{3+}$ ,  $\text{Cr}^{3+}$ ,  $\text{V}^{3+}$ ) and also  $\text{Ti}^{4+}$  in octahedral sites (De Almeida Sampaio Filho and Sighinolfi, 1973; Aurisicchio et al., 1994; Khaibullin et al., 2003). Substitution of  $\text{Li}^{+1}$  in Be tetrahedra is followed by charge balancing of  $\text{Na}^{+1}$  in the channel (Belov, 1958; Hawthorne and Černý, 1977). Alkalis (mainly

Na and Cs for charge balance) must be accommodated in the vacant channels because they are too large to be substituted in tetrahedral or octahedral coordination within the structure (Gibbs et al., 1968; Wood and Nassau, 1968; Aurisicchio et al., 1988). Andersson, 2006 has shown through electron paramagnetic resonance (EPR) measurements that  $\text{Li}^+$  impurities are located at two different positions in beryl, one in the crystal lattice and the other in the channel. The substitution causes distortion in beryl structure as well as variation in the bond lengths and angles (Aurisicchio et al., 1994).

The effective diameter of the channels varies from 2.8 Å to 5.1 Å. Therefore, it is large enough to accommodate big ions or molecules such as alkalis, earth alkalis,  $\text{OH}^-$ ,  $\text{H}_2\text{O}$ ,  $\text{F}^-$ , He,  $\text{CO}_2$ ,  $\text{CH}_4$ , N and  $\text{NO}_3^-$ . Mashkovtsev et al., 2004 have also proposed that  $\text{NH}_4^+$  can be trapped in beryl channel during hydrothermal synthesis with the addition of  $\text{NH}_4\text{Cl}$  to the solution, as determined by EPR and IR studies. Infrared spectroscopy was used by Leung et al., 1986 to differentiate synthetic from natural beryls by the presence of additional bands in the region  $2600\text{ cm}^{-1}$  to  $3300\text{ cm}^{-1}$  in synthetic ones depending on the medium from which they were grown. In synthetic beryls the presence of chlorine was detected by Hänni, 1982; Stockton, 1984 and Kane and Liddicoat, 1985.

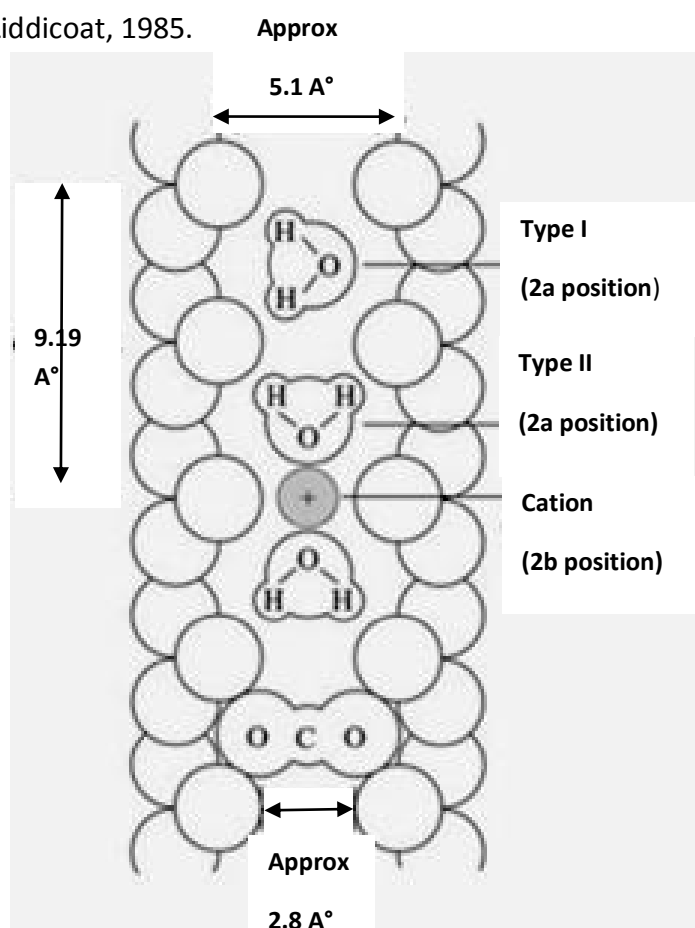


Fig. 1.5 General structure of beryl channel. Modified after Wood and Nassau, 1967. The cation in this figure is assumed to be a relatively smaller cation such as  $\text{Na}^+$ .

The incorporation of H<sub>2</sub>O namely in the form of type I and type II water molecules into the beryl channel has been confirmed by many authors (Wickersheim and Buchanan, 1959, 1965; Wood and Nassau 1967, 1968; Hawthorne and Černý, 1977; Aines and Rossman, 1984; Schmetzer, 1989; Hagemann et al., 1990; Schmetzer and Kiefert, 1990; Charoy et al., 1996; Mathew et al., 1997 and Kolesov and Geiger, 2000). The H-H vector of the H<sub>2</sub>O molecule is oriented parallel to the c-axis in type I and perpendicular in type II. The type II orientation is mainly due to its proximity to a cation. When there is no channel cation, the H<sub>2</sub>O molecule orients itself in type I configuration. The presence of a cation near the H<sub>2</sub>O molecule causes electrostatic attraction between the molecule's oxygen atom and the cation changes the orientation to type II. CO<sub>2</sub> molecule is oriented with its longer axis perpendicular to c-axis.

Beryl's colour is a function of transition metal content (Fe, Mn, V and Cr), oxidation state and also position in the crystal structure. Mn<sup>3+</sup>, Cr<sup>3+</sup> and V<sup>4+</sup> substituting in Al-octahedra give rise to pink and green colour and the gem varieties are known as morganite and emerald respectively. Fe<sup>+3</sup> in the Al-octahedra imparts golden yellow colour and the resultant beryl is heliodor. The presence of Fe<sup>2+</sup> in Al-octahedra does not produce any colour (Vianna et al., 2002) whereas Fe<sup>+2</sup> in channels gives beryl a pale blue colour which is aquamarine. It has been found that on irradiation, colourless beryl turns to either pale brown (Mukherjee, 1951 cited in Mathew et al., 2000) or blue (Maxixe and Maxixe type beryls; Nassau et al., 1976) or yellow orange (Sinkankas, 1981 and Read, 1985). Maxixe beryls were defined by Nassau et al., 1976 as deep blue beryls formed by natural radiation, in which the colouring agent was NO<sub>3</sub><sup>-</sup>. Mathew et al., 1998 have studied the change in colour of beryls from Orissa (India) upon irradiation and heat treatment and found that (1) on irradiation, colourless beryls transform to green or greenish yellow colour (2) subsequent heating to 300°C turn them to yellow (3) on gradual and controlled heating to 400°C, the colour changes to sky blue and (4) finally on heating to 500°C they become colourless. Gem traders sell heat-treated beryls by changing them to attractive sky-blue aquamarines.

**1.7 Physical properties:** Beryl is one of the most durable of all minerals. Beryl crystal structure and the strength of its bonds help the mineral to be practically unchanged in the deposits despite its prolonged exposure to chemical attack and physical weathering. Fizeau, 1866 observed a contraction along its c-axis and an expansion perpendicular to it with an increase in temperature. Voigt, 1887 found the coefficient of elasticity of beryl differ according to the crystallographic direction. For directions of 0°, 45° and 90° to the c-axis, the coefficients were 21,650, 17,960 and 23,120 kg/mm<sup>2</sup> respectively. The modulus of torsion parallel and perpendicular to the c-axis were 6,666 and 8,830 kg/mm<sup>2</sup> respectively. Birch, 1950 determined elastic constants on beryl and found modulus of elasticity as 21.8 x 10<sup>11</sup> in the direction parallel to c- axis and 21.9 x 10<sup>11</sup> in the direction at right angles to it. Newnham and Yoon, 1973 presented a simple mechanical model to rationalize observed compressional stiffnesses in beryl and other silicates on the basis of structural geometry.

They observed that the least compressible directions generally conform to directions of linked Si tetrahedra. Hazen et al., 1986 found that beryl compressibility is nearly isotropic, with the c-axis approximately 20% more compressible than a-axes, and a corresponding small decrease in  $c/a$  with increasing pressure. Linear compressibilities perpendicular and parallel to the c axis are  $\beta_{\perp} = 1.72 \pm 0.04 \times 10^{-4}$  kbar and  $\beta_{//} = 2.10 \pm 0.09 \times 10^{-4}$  kbar.

The conduction of heat is not uniform in the crystal, the conductivity being higher along c-axis than a-axes (Jannettaz, 1873). According to modern studies, the value of thermal conductivity is found to be 0.0131 cal/cm °C sec parallel to c-axis and 0.104 cal/cm °C sec parallel to a-axis (Chemical rubber company, 1966). The average value of conductivity of beryl from Minas Gerais, Brazil is determined as 0.00953 cal/cm °C sec by Chemical rubber company (1966).

Beryl is a non-conductor of electricity. Its dielectric constant was found by Curie, 1889 to be 6.24 parallel to c-axis and 7.58 in the direction perpendicular to that. Dielectric constant of powdered beryl at 20°C was determined by Rosenholtz and Smith, 1936 as 5.73. Modern experimental values are found to be 6.08 parallel and 7.02 perpendicular to c-axis and which are quite close to the values determined by Curie, 1889.

Density of ideal beryl was calculated as 2.661 g/cm<sup>3</sup> by Bragg and West, 1926. Bose, 1936 measured specific gravity and found that it ranges from 2.660-2.877, with the lowest for aquamarine and yellow beryl, moderate to high for emerald and the highest to pink beryl (morganite). There is a progressive increase in specific gravity with alkali content (Deer et al., 1962) from 2.66 for alkali poor beryl to about 2.77 for beryl containing 28 mol% of alkalis. It has been found that beryls from muscovite rich pegmatites are lower in specific gravity than those obtained from lithium-bearing bodies.

**1.8 Previous studies on surface etch pits of beryl:** Etch pits on beryl are a long-known feature. After the realization of their significance in the studies of internal symmetry, they have been the object of wide-spread studies. Wilk, 1887; Penfield and Sperry, 1888 and Petersson, 1891 have studied etch figures on natural beryl samples and concluded that their morphology correspond to the symmetry of the crystal faces. Traube, 1895 was the first one to create etch pits artificially by using molten potassium hydroxide and ammonium bifluoride. Kohlmann, 1907 investigated etch figures on natural specimens from Brazil. Honess, 1917 produced etch figures on beryls by immersing them in molten alkali and acidic solvents. Zedlitz, 1941 studied etch figures on gem quality aquamarines from Minas Gerais, Brazil. Feklichev, 1963 analyzed the morphology of dissolution figures on faces of natural beryl crystals. He found that beryl from different fields can be characterised by a different set of simple dissolution forms by producing etch figures artificially. All the above studies were carried out at atmospheric pressure and fused solids were used as etchants. Medina et al., 1983 were the first to use SEM to investigate natural etch pits on beryl.

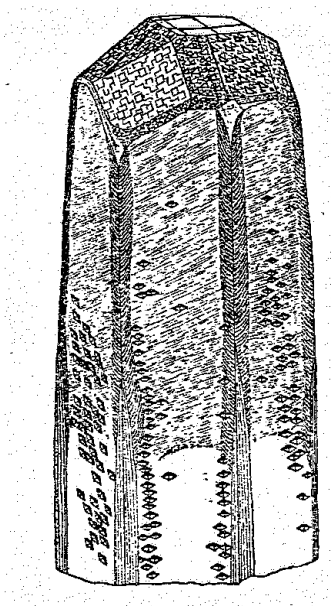


Fig. 1.6 Beryl crystal's drawing with etch pits on different faces (Goldschmidt, 1913).

**1.9 Motivation for the current research:** Even though the etch pits on beryl crystals have long been observed, they were mainly used to determine crystal symmetry and to correlate with structure. Their applications in different fields have not been comprehended and were in very primitive stage. The only study through the advanced technology SEM images on beryl available to us was carried out by Medina et al., 1983 where etch pits were correlated with the crystal structure. Deciphering the dissolution history of beryl by characterising surface topography using SEM is not yet delineated. Here, the characterisation of surface topography is done through shape distribution analysis of etch pits, surface texture analysis, micro hardness analysis and fractal analysis which would give an insight not only into crystal defects but also crystal chemistry, structure, symmetry, provenance and hence the dissolution behaviour of beryl.

The number and types of defects have an immense impact on physical properties of a crystal which largely determine the value of a gemstone. Etch pits are reflections of crystal defects in turn qualifying them to be useful in gem industry. Etch pits found on very few natural geological materials or gemstones are used to identify crystal defects; such as quartz and gypsum (Joshi et al., 1978 and Raju, 1980). In the field of metallurgy, attention has been paid to the etch pits and dislocation point. The current study is an attempt to explain the effects of crystal defects on surface micro structures of beryl. This research can be applied to other gemstones or minerals showing characteristic etch pits grown in pegmatitic-hydrothermal environment.

The present work also aims to fill the gap in the experimental studies on dissolution of beryl and creation of etch pits under hydrothermal conditions at high temperature and pressure (600°C and 2 kbar pressure) with variable fluid compositions (alkali, neutral and acidic

medium). Moreover, role of incorporated cations in the channel and substituted cations in the structure on the dissolution of beryl is not reported so far.

## 2. Methods

### 2.1 Sample material and geological occurrence:

Twenty one natural beryl crystals from different sources namely Shigar valley, Yuno village and Dassu mines from western parts of Higher Himalayan Crystalline zone; Minas Gerais from Brazil; Xueobaoding mountain, Sichuan province from China (all from museum collections, Technical University, Berlin) and Lumäki from Finland (courtesy of Dr. Seppo I. Lahti, Helsinki) were used for the purpose of studying surface etch pits and hence its dissolution behaviour.

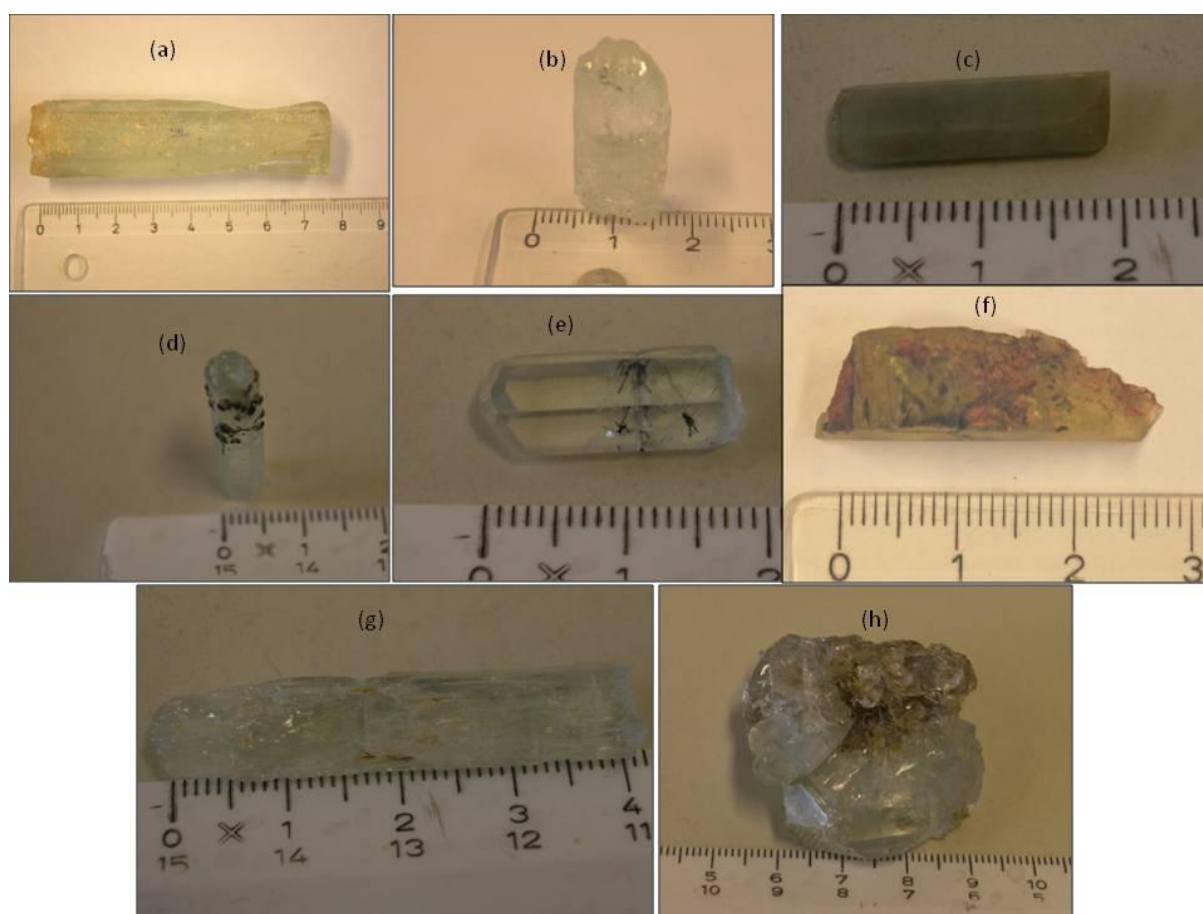


Fig. 2.1 Representative samples from different localities. Scale bar in cm. (a) Light greenish beryl BA-1, with well-developed faces from Minas Gerais, Brazil. (b) Light bluish beryl PA-2 from Shigar valley, Himalayas. (c) Translucent, prismatic and green coloured beryl from Dassu mines, Himalayas. (d) Prismatic, columnar slightly bluish beryl with well-developed faces from Yuno village, Himalayas. (e) Colourless and transparent goshenite with well-developed faces with inclusions of rutile needles from Yuno village, Himalayas. (f) Highly corroded golden yellowish green beryl from Lumäki pegmatites, Finland. (g) Slightly bluish, prismatic and highly corroded aquamarine from Dassu mines, Himalayas. (h) Tabular shaped, slightly bluish and transparent beryl associated with muscovite from Sichuan province, China.

**2.1.1 Minas Gerais, Brazil:** The world's most important gemstone-producing pegmatites are located in the north-eastern parts of the state of Minas Gerais, Brazil. Rough terrain, difficult access and deep chemical weathering slowed down detailed studies of the regional geology of Minas Gerais. The rocks in the region have been intensely weathered, most to a depth of 30 meters or more. A thick lateritic soil horizon covers the underlying rocks of Minas Gerais (Proctor, 1984).

The detailed mapping of Pecora and associates (1950a) revealed a Precambrian basement complex, the Complexo Fundamental. Dominant rock types of this unit are biotite schist interlayered with amphibolite schists and quartzites, banded and granitoid gneisses and biotite-garnet schists.

The Complexo Fundamental is unconformably overlain by a series of Precambrian meta-sediments named as Minas series. The Minas series consists mostly of sericitic phyllite. These rocks were later intruded by granitic batholiths that metamorphosed, domed and fractured the meta-sediments to provide channels for pegmatitic fluids that accompanied the magmas of subsequent intrusive activity.

The Minas series is overlain by the folded and faulted Itacolomy series of predominantly phyllites and quartzites of late Precambrian age. The Itacolomy series has also been intruded by pegmatites, suggesting that pegmatite-related magmatic activity continued for some time following the deposition of this unit. The conglomerates, phyllites and sandstones of the overlying early Palaeozoic lavas and Silurian Baubue series do not contain pegmatites (Proctor, 1984).

The gem-bearing pegmatites have been dated as approximately 490 Ma (Dirac and Ebert, 1967). Thousands of gem-bearing pegmatites are known in Minas Gerais. But the most important and best known among them are Cruzeiro, Golconda, Virgem da Lapa, and Itatiaia pegmatites (Proctor, 1984).

**2.1.2 Shigar valley, Higher Himalayan Crystalline zone:** The western areas of Higher Himalayan Crystalline zone have always been a place of attraction for the gem industry of the world because of the high quality gemstones and mineral specimens. Most of the gemstone-bearing pegmatites are well exposed due to the resistance to erosion making leucocratic wall-like projection with smooth and rugged slopes. Middlemiss and Parshad, 1918 reported aquamarine for the first time in pegmatites from Pakistan. Later Kazmi et. al., 1985 and O`Donoghue, 1990 carried out preliminary work on some pegmatitic bodies of Shigar valley.

The gem-bearing pegmatites in the Indo-Pakistan and Asian plates are mostly young with cooling ages less than 10 million years and are undeformed. Generally they form swarms of parallel to sub-parallel, locally anastomosing discordant dykes and lenses of nearly concordant sills. They attain a thickness of up to several meters (Laurs et al., 1998).

Pegmatites of northern areas of Pakistan occur within amphibolite to granulite facies schists and gneisses. The amphibolites in the region extend from Hunza River in the NW to the Shigar river near Dasso in the south-east (Laurs et al., 1998). Besides multiphase metamorphism and deformation, igneous intrusions of both pre and post collisions are exposed in the valley. The last phase of post-collision igneous intrusion is present in the form of leucogranites and gem bearing pegmatites.

The pegmatites of the Shigar valley are classified into the gem-bearing pegmatites and gem barren pegmatites. The gem-bearing pegmatites are generally zoned, having 3 or 4 zones. Symmetrical zoning is a common feature, while some of the dykes show asymmetrical zoning. On the basis of presence or absence of the relative proportion of accessory mineral phases, these pegmatites are further classified into (Agheem et al., 2011):

- 1) Muscovite-schorl pegmatites
- 2) Biotite-garnet-muscovite pegmatites
- 3) Muscovite-biotite garnet pegmatites

Gemstones of pegmatitic origin are mostly found at the core margin zone or in the intermediate zone of the zoned pegmatites in cavities. The cavities occur as large chambers, round or ovoid in shape and are tightly packed with gem crystals and sometimes surrounded by light pink or white clay material, which suggests that these miarolitic pegmatites experienced a late alteration stage. The larger the cavity, the larger will be the crystal (London, 1986). The geochemical data of the pegmatites show that they are mostly per-aluminous and granitic in character. These gem-bearing cavities are mined for aquamarine, tourmaline, topaz, quartz, fluorite, apatite, axinite, zoisite etc. Pocket mineral assemblages from Shigar valley pegmatites are mostly albite, orthoclase and muscovite. Albite is mostly associated with certain gemstones like aquamarine, topaz, schorl, fluorite and garnet. The plagioclase in the pegmatites is also of albite composition (Agheem et al., 2011). The complete absence of biotite and the higher percentage of muscovite in the gemstone bearing class of pegmatites can be used as indicators of gem exploration (Agheem et al., 2011).

**2.1.3 Lumäki pegmatites, Finland:** Southern Finland has numerous complex pegmatites in Precambrian rocks. However, gem minerals have only been found occasionally. Beryl was found in elongated pockets that were lined with quartz crystals. The outcrop represented the core of a small pegmatitic dyke which intruded into coarse-grained rapakivi granite. Rapakivi granites are predominantly coarse-grained porphyritic rocks with large ovoids of K-feldspar mantled by plagioclase (Wiborgite type).

Wiborgite is the most abundant rock type of the area (Simonen, 1987). It is coarse-grained porphyritic granite with ovoids of orthoclase mantled by plagioclase. The minerals of the

rock are K-feldspar, plagioclase and quartz. Hornblende and biotite are typical mafic minerals. The Lumäki pegmatite is situated in the northern corner of the large Wiborg rapakivi granite complex, which consists of several granites as well as minor anorthosite intrusions (some of which contain the local labradorite often called spectrolite). This complex covers an area about 100x180 km that extends from south-eastern Finland nearly to Karelia, Russia. Rapakivi is the youngest granite in the Precambrian of Finland. The ages of rapakivi granites in the region vary between 1650 and 1700 Ma (Vaasjoki, 1977); the pegmatites are found to be younger than rapakivi granite.

Geologic mapping of the Pre-Quaternary rocks of the map sheets area of rapakivi massif in SE Finland by Simonen, 1987 showed that the pegmatite is a poorly exposed dyke about 20 m wide in granite. A massive quartz core, about 10 m wide, makes up the central part of the dyke. It is surrounded by three feldspar-mica-quartz pegmatite zones corresponding to intermediate, wall and border.

The main minerals in the pegmatite, in addition to quartz, are reddish brown microcline, albite, biotite and muscovite. The intermediate zone contains a number of rare minerals. Very large crystals of common beryl, topaz (not of gem quality) and monazite are characteristics in the intermediate zone (Lathi and Kinnunen, 1993).

Pockets are abundant in the core and intermediate zones of the dyke extending from several centimeters to several tenths of a meter, may contain crystals of quartz, albite, microcline orthoclase and gem beryl and localized occurrence of betrandite, goethite and fluorite are common. The bottom of a pocket is usually covered by a layer of red-brown clay minerals and crystal fragments loosened from the walls suggesting miarolitic origin for these pegmatites.

Two generations of beryl can be identified in the pegmatite: The older common beryl (not gem quality) and the younger gem beryl. The common beryl is yellow, often strongly altered by hydrothermal solutions and usually stained and impregnated brown by iron compounds. The crystals of common beryl which normally range from 5 to 15 cm in diameter, have well-developed first order prisms and occasionally basal pinacoids (Pitkänen, 1991). Common beryl occurs in the intermediate zone of the pegmatite while gem beryl is found in pockets either associated with common beryl or embedded in microcrystalline reddish quartz (jasper). The gem beryl ranges from pale yellow to greenish yellow to yellowish green. Approximately 10 to 15 % of the total would be considered aquamarine with various shades of blue. Blue aquamarine can also be produced by heating pale green or yellow green beryl from this locality (Ehnröoth and Tuovinen, 1989; Lathi and Kinnunen, 1993).

**2.1.4 Xuebaoding mountain, Sichuan Province, China:** The sample (CA-1) with slightly bluish and transparent beryl associated with muscovite comes from Sichuan Province, China, 4500 m above sea level in the muscovite rich beryl-scheelite-cassiterite ore deposits (Liu Yan et al., 2007). Xuebaoding Mountain is situated in the northwestern parts of

Sichuan and is a part of transitional belt between the Sichuan basin and Tibetan plateau. It is famous for producing scheelite, cassiterite and beryls. A tungsten-cassiterite-mica-beryl Xuebaoding deposit is mainly formed by hydrothermal processes. Beryl found in this province is generally transparent, colourless and short hexagonal crystals. The typically tabular habit is very uncommon for light blue or colourless beryl. Until late 1990s, the beryl at this region was only mined for Be extraction. The deposit is located in the Ziboshan dome zone which is in the core of the overturned synclines in the Motianling complex tectonic belt. Four alkali granite bodies are present in the core of the Ziboshan dome and they intruded the Triassic lower Zagunao series. The lower Zagunao series is composed of epimetamorphic phyllites and marbles (Liu Yan et al., 2007).

The open joints in the coarse grained gray marble are well developed to provide ample space for the transport of the mineralizing fluid. The marble is up to 22 m thick and is the main ore-bearing layer. There are more than 40 ore-bearing veins with a large variation in thickness with length of 40-100 m and width of 0.5-1.5 m (Liu Yan et al., 2007). Most of these ore-bearing veins developed ribbon structures and several different types of ribbons can be found from the wall-rock outward: (1) A muscovitization-fluoritization marble zone with a thickness of 1 to 10 cm containing small amounts of scheelite, fluorite and beryl; (2) a fluorite-quartz zone rich in scheelite, fluorite, beryl and ore minerals and (3) a quartz zone: beryl, scheelite, cassiterite and sulphides are the main ore minerals and all these minerals often occur as assemblages.

## **2.2 Characterisation of beryls**

**2.2.1 Investigation of morphology of crystals:** The faces of the samples were studied through macroscopic investigation and crystal drawings.

**2.2.2 Investigations of thin sections with polarizing microscope:** Thin sections were prepared cutting the samples parallel to c-axis except two which were cut perpendicular to c-axis with the thickness ranging from 700  $\mu\text{m}$  to 900  $\mu\text{m}$ . They were then examined by a polarizing microscope to study inclusions.

**2.2.3 Chemical analysis by electron microprobe EPMA:** For the characterisation of beryls, polished carbon-coated thin sections of samples were analysed with CAMECA Electron Microprobe at ZELMI, Technical University, Berlin. Operating conditions were set to a beam current of 18.63 nA and accelerating voltage of 15.1 kV. The following standards were used: Albite (Na), olivine (Mg), andalusite (Si), wollastonite (Ca) and pure elements Mn, Fe, Rb and Cs. Since the amount of Mn, Rb, K and Ca were found to be below detection limit in first three samples, hence not measured in remaining samples. The Be value was set at 5 wt% for the correction procedure which was carried out by the CAMECA software according to Pouchou and Pichoir, 1984. The crystals were routinely checked with back scattered electron images (BSE) to detect possible zoning or inclusions. The analytical results

obtained by EPMA were recalculated from wt% of oxides to atoms per formula unit on the basis of 18 oxygen atoms.

**2.2.4 Refractive indices determination:** Refractive Indices were measured with the help of Gem LED Refractometer (System Eickhorst). Methylene iodide with sulphur was used as RI liquid of refractive index 1.79.

**2.2.5 X-ray powder diffraction:** Unit cell parameters and other structural parameters were refined with the help of GSAS (Larsen and Von Dreele, 2004) software package for Rietveld refinements. Powder X-ray diffraction patterns were obtained from aliquots of the investigated samples by crushing in a single-crystal corundum mortar by using Bruker D2-Phaser diffractometer at Mineralogy Department, Technical University (Cu K $\alpha$  radiation, wavelength 1.545056 Å). The reflections were measured between 5° and 80° 2 Theta with an interval of 0.01° at 30 kV and 10mA.

## **2.2.6 Vibrational spectroscopy:**

### **2.2.6.1. IR spectroscopy:**

**Pellet method:** The IR spectra of powdered beryl samples were recorded at room temperature with Fourier-transform infrared (FTIR) microspectrometer (Bruker) equipped with DTGS detector at Mineralogy Department, Technical University, Berlin. Approximately 3 mg of powdered samples were mixed with 300 mg of KBr and made into pellets with pellet pressing machine. The signal was collected over 200 scans for samples and back ground. The spectra were obtained in the frequency region 400 cm<sup>-1</sup> to 4000 cm<sup>-1</sup> with light source of Globar and KBr beam splitter in transmission mode. The spectral resolution and aperture size were set at 2 cm<sup>-1</sup> and 7 mm respectively. In order to find out the precision, two-three pellets were made from one sample.

**Single crystal method:** The IR spectra were obtained from doubly polished oriented plates of 100-120  $\mu\text{m}$  thickness with an aperture diameter of 100  $\mu\text{m}$  under microscope in order to detect the presence of H<sub>2</sub>O and CO<sub>2</sub> molecules in the channel in polarised and in ordinary light. Crystals were oriented parallel and normal to c-axis. The signal was collected over 128 scans with a resolution of 4 cm<sup>-1</sup>. Aperture size was set as 6mm and the mirror velocity was kept at 20.0 kHz in both methods. Additional investigation was done on one of the samples from Dassu mines with attenuated total reflection (ATR) and reflection method at Leibniz Institute Für Analytische Wissenschaften, Berlin.

**2.2.6.2 Raman spectroscopy:** Polished thin sections were analysed in polarised light with a Dilor Lab Ram Raman spectrometer which was operated with a 632 nm HeNe laser at Naturkunde Museum, Berlin. The laser light was focused with an Olympus microscope and x100 magnification to the sample. Spot size is about 2  $\mu\text{m}$ . The reflected light was directed through an edge filter and the Raman scatter split with a 1800 grating and analysed by a peltier cooled CCD detector.

**2.2.6.3. NIR spectroscopy:** Doubly polished single crystals of samples were used to obtain NIR spectra with Perkin Elmer's Lambda-950 spectrometer in polarised light at room temperature at Helmholtz-Zentrum Berlin für Materialien und Energie from 1000 nm to 2600 nm. Tungsten lamp, dispersive spectrometer, monochromator and InGaAs detectors were used. The spectra were taken in transmission and reflection mode at a slit width of 2 nm.

## 2.3. Characterisation of surface topography

**2.3.1. Scanning Electron Microscopy (SEM):** All the characterised samples were coated with platinum/gold/carbon and were analysed by scanning electron microscope by Hitachi S-3700 and Hitachi S-4000 model at ZELMI, Technical University, Berlin. Energy dispersive spectra were obtained all over the crystal surface especially in and around the etch pits with an accelerating voltage of 20 kV and a beam current of 500 pA to detect changes in composition and the products deposited on the surface during the dissolution. SEM images have been analysed by different image analysis softwares in order to:

- 1) analyse shape distribution (Shape factors: roundness, elongation, form factor, compactness and convexity) of etch pits and to classify them;
- 2) measurement of lengths of diameters of etch pits to find out the eccentricity and classification of etch pits;
- 3) surface texture analysis around etch pits and profile extraction;
- 4) determination of fractal dimension around etch pits and comparison with texture values;
- 5) micro-hardness (Vickers) analysis on different kinds of etch pits;
- 6) determination of surface area of deep etch pits in representative samples and comparison with surface texture and fractal dimension;
- 7) semi quantitative chemical analysis of the deposited particles in and around the etch pits.

Characterisation of surface topography is done with Gwyddion image analysis software by Czech Metrology Institute and SPIP image analysis software by Image Metrology.

Microhardness analysis (Vickers) and shape measurements of different etch pits were performed with SPIP software.

**2.3.2 Atomic Force Microscopy (AFM):** As the crystal surfaces were highly etched, it was difficult to get images of rough sample surfaces, which would have enabled us to get information on depths of etch pits. To get an understanding about defects, two polished samples were scanned in atmosphere with Veeco Atomic Force Microscope in contact mode at Brandenburg Technical University, Cottbus. Scanning tip used was MPP-31123-10. The phosphorous-doped cantilever had a length of 515-535 $\mu$ m, width of 30-40 $\mu$ m and thickness

of 3.5-4-5  $\mu\text{m}$ . Back side was coated with 50 $\pm$  10 nm Al. Slope of the topography was kept as -0.017. The force was increased from 355 Pn (N) to 395 Pn (N) at different stages. The images were later analysed by image analysis softwares. However, the information was not very useful in the current study.

## 2.4 Hydrothermal experiments

**Sample preparation:** Pieces of 3 unpolished and 1 polished beryl samples were cut parallel to c-axis. To create etch pits, the samples were immersed in HCl and set to boil for 20 minutes. Gold capsules of 3 cm length and 3 mm diameter were also cleaned in HCl along with the samples. The cleaned samples and capsules were dried in an oven at 110°C after washing them with distilled water. The capsule was weighed after welding one of the sides. Gold scrap was put into the capsule around the crystal to stabilize the capsule and avoid the breakage of the sample. The sample in the capsule along with the solution of definite concentration was weighed again. After getting the weight of solution and the sample, the capsule was welded from the other end. The sealed capsule was kept in the oven for an hour and was weighed again to check for possible leakage.

**Experimental conditions:** The capsules were then placed in externally heated cold-seal vessels, pressurized by water to 200 MPa, and heated under controlled pressure to 600 °C. The automatic temperature control keeps temperature constant within  $\pm 10$  °C at hydrothermal laboratories at Technische Universität Berlin. Checks of the pressure during the experiment were within the reading-precision of  $\pm 10.0$  MPa. The vessels were quenched in an air stream to room temperature within 5 min, while maintaining the pressure. 1N NaCl, 2N KCl, 0.5N HCl and 0.5N NaOH solutions were used as fluids. The samples were weighed again before further investigations. The hydrothermally treated samples were investigated with SEM and IR as described above. The fluids were not analysed after the run.

### 3. Results

**3.1 Morphology:** Most of the samples used in this study are euhedral and are characterised by well-developed faces. The results are summarised in Table 1, which also shows the methods of investigation of all materials. The samples from Minas Gerais, Brazil, BA-1, BAA-1 and BAA-2 are bluish to greenish. BA-1 is a yellowish green, transparent and euhedral. The first and second order prism faces  $\{10\bar{1}0\}$  and  $\{11\bar{2}0\}$  are well preserved. The upper pinacoid (0001) is well developed with macroscopically visible spiral (growth) features; the lower pinacoid is corroded. Hexagonal dipyrramids  $\{10\bar{1}1, 10\bar{1}2, \text{ and } 11\bar{2}2\}$  are clearly visible. Etch pits on the prism faces are macroscopically visible and fractured surfaces are brilliant. The faces of BAA-1 and BAA-2 are difficult to distinguish as they were highly corroded. These anhedral crystals have a tabular nature rather than the more common prismatic form. BAA-1 is light blue in colour and translucent. BAA-2 is colourless with yellowish green tinge and is surrounded by a rim of transparent phenakite.

The samples from Higher Himalayan Crystalline zone are mainly from Yuno village, Dassu mines and Shigar valley, Skardu district. Most of the samples are characterised by long, columnar and prismatic habit. The sample suite from Yuno village (PAY suite) is colourless and transparent with well developed faces. PAY-1 has only  $\{10\bar{1}0\}$  and  $\{0001\}$ . The samples from Dassu mines (PAD suite) are more corroded than those from Yuno. Some preserved faces found in PAD suite are  $\{10\bar{1}0\}$ ,  $\{10\bar{1}2\}$ ,  $\{11\bar{2}2\}$  and  $\{0001\}$  (Fig. 3.1a,b,c). PAD-5 has an additional face  $\{21\bar{3}0\}$  as in Fig. 3.1b.

The sample from Finland (FH-3) comes from Lumäki, Southeast Finland and is a cut piece (2.5 cm x 1 cm in size) of a large yellowish green crystal. It is highly corroded with step-like features on the prism faces which are the only developed faces. First and second order prisms cannot be distinguished.

The sample from China (CA-1) is transparent and slightly bluish in colour which is marked by its tabular habit with well-developed prism faces, pyramids, domes and basal pinacoids. Its tabular nature makes it unique among beryls which are normally of prismatic habit. It is found to be closely associated and intergrown with muscovite.

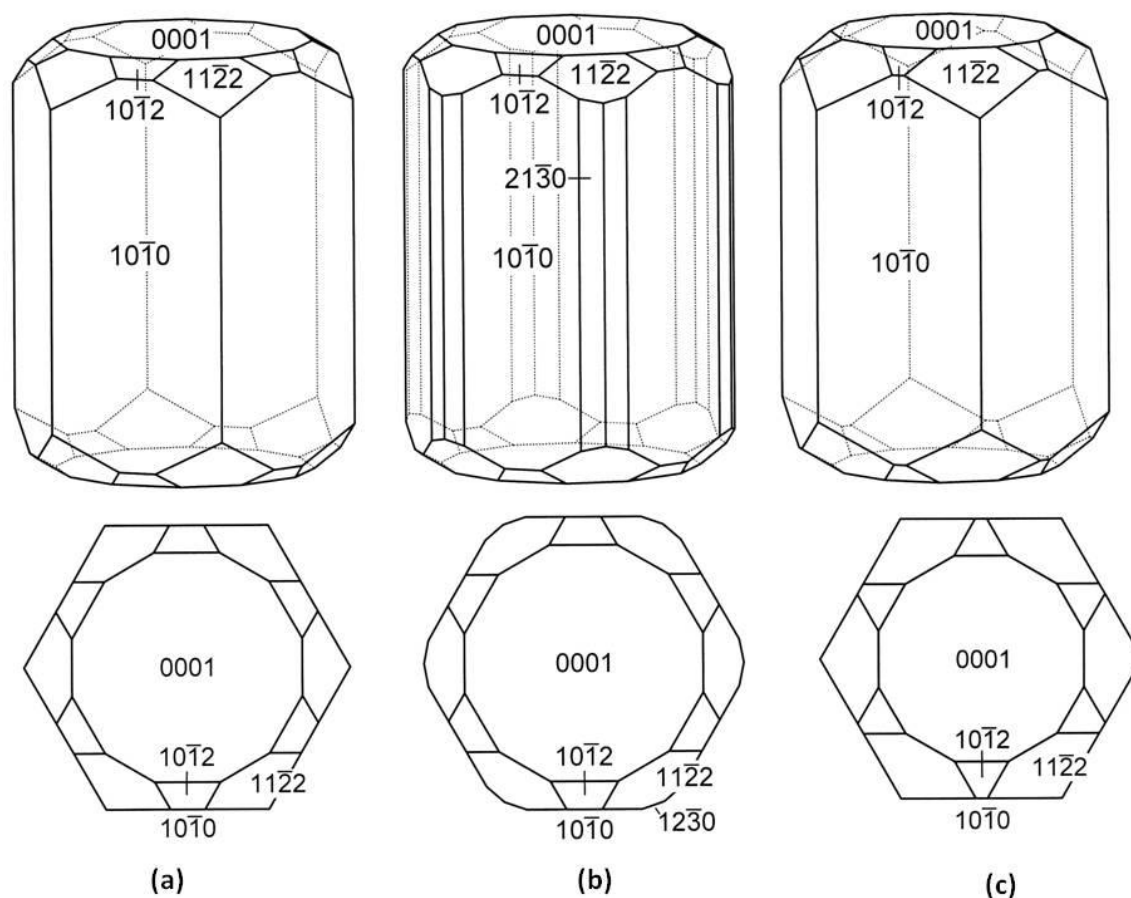


Fig. 3.1 Crystal drawings of the samples: (a) PAD-4 (b) PAD-5 (c) PAD-6 from Dassu mines, Himalayas. Upper images are prismatic sections and lower ones are basal sections.

Table 1 Presenting samples, characteristics, methods and the locality

Sample	Characteristics	Methods	Locality
BA-1	7cmx1.5cm in size, prismatic, yellowish greenish in colour, all faces are preserved 10 $\bar{1}0$ , 11 $\bar{2}0$ , 0001, 10 $\bar{1}1$ , 10 $\bar{1}2$ , and 11 $\bar{2}2$ , etch pits are visible with naked eye	EMPA, RI, XRD, IR (powder & single crystal under polarised light), Raman, SEM and AFM	Minas Gerais, Brazil
BAA-1	Tabular and anhedral, light blue, dissolved strongly, faces are not recognisable	EMPA, XRD, IR (powder), Raman, NIR and SEM	Minas Gerais, Brazil
BAA-2	Tabular and anhedral, yellowish green, dissolved strongly, faces are not recognisable	EMPA, XRD, IR (powder), Raman, NIR and SEM	Minas Gerais, Brazil
PAD-1	4cmx0.06cm in size, prismatic, transparent, light bluish to colourless, 0001 and 10 $\bar{1}0$ are developed but corroded, prismatic faces terminate in {0001}	EMPA, XRD, IR (powder & single crystal under polarised light), Raman, NIR and SEM	Dassu Mines, Higher Himalayan Crystalline zone
PAD-3	3.2cmx1cm in size, transparent, colourless, corroded, difficult to recognise faces	EMPA, XRD, IR (powder & single crystal), Raman, NIR and SEM	Dassu Mines, Higher Himalayan Crystalline zone
PAD-4	2cmx1cm in size, transparent, colourless, well developed first order prism faces 10 $\bar{1}0$ terminating in 10 $\bar{1}2$ and 11 $\bar{2}2$ , one of the basal pinacoids is well developed	EMPA, XRD, IR (powder & single crystal), Raman, NIR and SEM	Dassu Mines, Higher Himalayan Crystalline zone
PAD-5	1.4cmx1.2cm in size, transparent, colourless 10 $\bar{1}0$ , 21 $\bar{3}0$ , 0001, 10 $\bar{1}2$ and 11 $\bar{2}2$ are developed.	EMPA, XRD, IR (powder & single crystal), Raman, NIR and SEM	Dassu Mines, Higher Himalayan

			Crystalline zone
<b>PAD-6</b>	1cmx0.09cm in size, transparent, colourless, $10\bar{1}0$ , 0001, $10\bar{1}2$ and $11\bar{2}0$ are developed	EMPA, XRD, IR (powder& single crystal), Raman, NIR and SEM	Dassu Mines, Higher Himalayan Crystalline zone
<b>PAD-7</b>	1cmx1cm in size, $10\bar{1}0$ and $11\bar{2}0$ are present, base is highly corroded	EMPA, XRD, IR (powder& single crystal), Raman, NIR and SEM	Dassu Mines, Higher Himalayan Crystalline zone
<b>PAD-8</b>	2cmx0.4cm in size, light green, translucent, long and columnar, 6 prism faces of first order $10\bar{1}0$ terminate in basal pinacoids	EMPA, IR (powder& single crystal), Raman, NIR and SEM	Dassu Mines, Higher Himalayan Crystalline zone
<b>PAD-9</b>	0.7cmx0.7cm in size, transparent and colourless, well developed prism faces, $10\bar{1}2$ and $11\bar{2}2$ are present	EMPA, XRD, IR (powder& single crystal), Raman, NIR and SEM	Dassu Mines, Higher Himalayan Crystalline zone
<b>PAD-10</b>	1cmx0.4cm in size, transparent, colourless, prismatic faces at the bottom terminate in basal pinacoid, at the top they terminate in pyramids	EMPA, XRD, IR (powder& single crystal), Raman, NIR and SEM	Dassu Mines, Higher Himalayan Crystalline zone
<b>PAY-1</b>	1cmx1cm in size, transparent, colourless, prismatic faces $10\bar{1}0$ terminate in 0001 base	EMPA, XRD, IR (powder& single crystal), Raman, NIR and SEM	Yuno-village, Higher Himalayan Crystalline zone
<b>PAY-2</b>	3cmx1cm in size, transparent, colourless, well developed prismatic faces $10\bar{1}0$ , base 0001	EMPA, XRD, IR (powder& single crystal), Raman, NIR and SEM	Yuno-village, Higher Himalayan Crystalline zone
<b>PAY-3</b>	Transparent, colourless, characterised by prism of first and second order with pyramids of first and second order $10\bar{1}1$ and $11\bar{2}2$	EMPA, XRD, IR (powder& single crystal), Raman, NIR and SEM	Yuno-village, Higher Himalayan Crystalline zone
<b>PAY-4</b>	1.6cmx0.5cm in size, transparent, colourless, well developed prismatic faces, pyramids of first, second and third order with basal pinacoid	EMPA, XRD, IR (powder& single crystal), Raman, NIR and SEM	Yuno-village, Higher Himalayan Crystalline zone
<b>PAY-5</b>	1.1cmx0.5cm in size, transparent, colourless, prismatic faces terminate in first order pyramids, one of the basal pinacoids is present	EMPA, XRD, IR (powder& single crystal), Raman, NIR and SEM	Yuno-village, Higher Himalayan Crystalline zone
<b>PAY-6</b>	3cmx0.3cm in size, transparent, slight bluish, columnar, well developed prismatic faces $10\bar{1}0$ , basal pinacoids 0001 are developed	EMPA, XRD, IR (powder& single crystal), Raman, NIR and SEM	Yuno-village, Higher Himalayan Crystalline zone
<b>PA-2</b>	3cmx0.3cm in size, transparent, prismatic, well developed prisms of first order, basal pinacoids	EMPA, XRD, RI, IR (powder& single crystal), Raman, NIR and SEM	Skardu district, Shigar valley, Higher Himalayan Crystalline zone
<b>CA-1</b>	Tabular, transparent, slightly bluish, associated with muscovite, 0001, $10\bar{1}0$ , $11\bar{2}1$ , $31\bar{4}3$ (small faces of dihexagonal bipyramid)	EMPA, XRD, IR (powder), NIR, SEM.	Sichuan Province, China
<b>FH-3</b>	Golden yellowish mixed with green colour with $10\bar{1}0$ face, all other faces are subjected to dissolution	EMPA, RI, XRD, IR (powder), Raman, SEM and Mössbauer	Lumäki pegmatites, Finland

### 3.2. Studies of inclusions under polarizing microscope and electron microprobe:

The study of inclusions was preliminarily carried out by a polarizing microscope. All the samples have a number of fluid inclusions and some solid inclusions. Some of the solid inclusions are identified by EMPA. Stereoscopic investigation of the sample BA-1 shows the presence of small round to elongated empty cavities or hollow cores parallel to c-axis giving the sample a porous appearance (See arrow in Fig. 3.2.1). The fluid

inclusions in BA-1 are found to be more concentrated along the edges of these cavities rather than in other parts of the crystal. Rows of inclusions are found to be terminating at these cavities giving a feather-like impression (Fig. 3.2.2a). Small red arrows in Fig. 3.2.2b indicate irregular to perfectly polygonal (majority are hexagonal) shaped cavities or hollow cores in BA-1. Semi qualitative analysis of fluid inclusion in BA-1 crystal indicated the presence of Cl and K in higher amounts and Ca and S in lesser amounts. In FH-3, rows of solid and fluid inclusions are aligned in bands parallel to each other (Fig. 3.2.2c). Fig. 3.2.2d shows triangular (red arrow), disseminated and irregularly shaped two-phase fluid inclusions (black arrow) in PA-2. In Fig. 3.2.3a of PAY-1, arrow points to rectangular shaped two-phase inclusions oriented perpendicular to c-axis. Needle-like inclusions and fluid inclusions are aligned parallel to each other. Irregularly shaped inclusions are also visible. Fig. 3.2.3b shows the association of CA-1 with muscovite mica. BSE image of PAD-4 shows secondary fluid inclusions form a wavy pattern along a fracture which is enriched in Ca and S with traces of Fe (Fig. 3.2.4a). In BSE image of PAD-5, a bright contrast zone rich in Ca (Fig. 3.2.4b) is visible. SE image of PAD-6 shows inclusions arranged in the form of a crescent moon (Fig. 3.2.4c). PAD-8 has elongated fluid inclusions running parallel to c-axis enriched in Ca (Fig. 3.2.4d). In Fig. 3.2.5a of SE image of BAA-2, the arrow indicates a zone with irregular distribution of Si and Al and the bright area on both sides shows pure beryl composition. BSE image of FH-3 shows fluid inclusions enriched in Ca and S (Fig. 3.2.5b). Zircon and muscovite mica are the solid inclusions identified in PAY-6 and PAY-5 respectively (Fig. 3.2.6a, b).

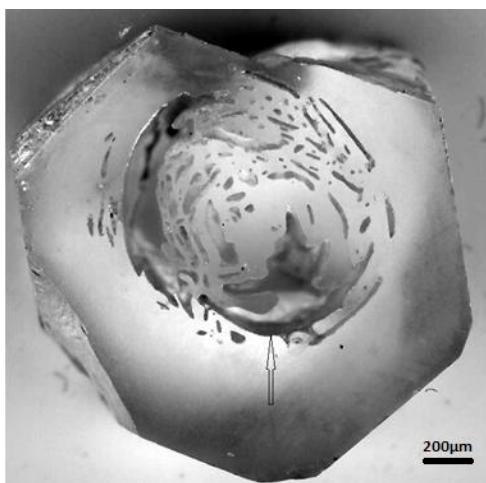


Fig. 3.2.1 Photograph of sample BA-1 cut parallel to the base under stereoscope.

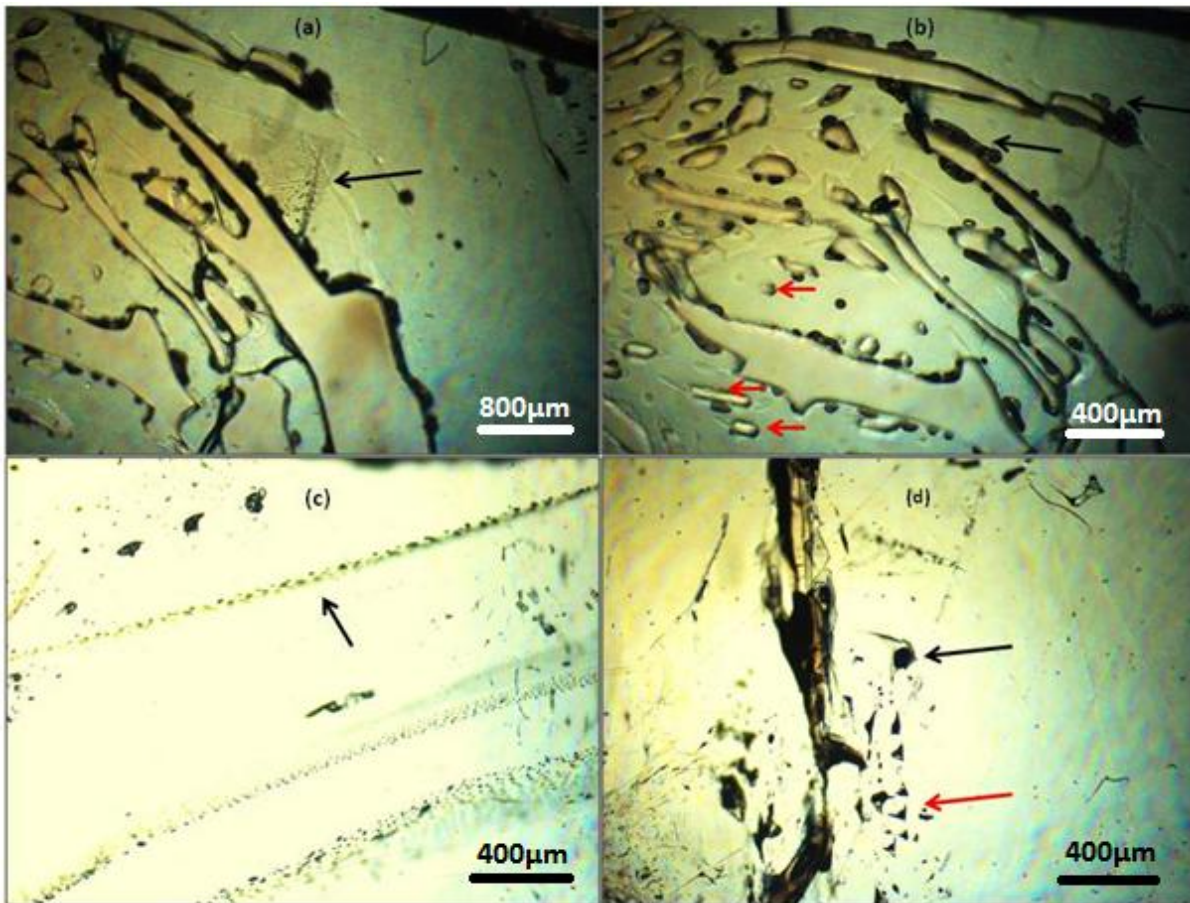


Fig. 3.2.2 Photomicrographs of thin sections: (a) & (b) of BA-1 cut parallel to {0001}. (c) FH-3 (d) PA-2

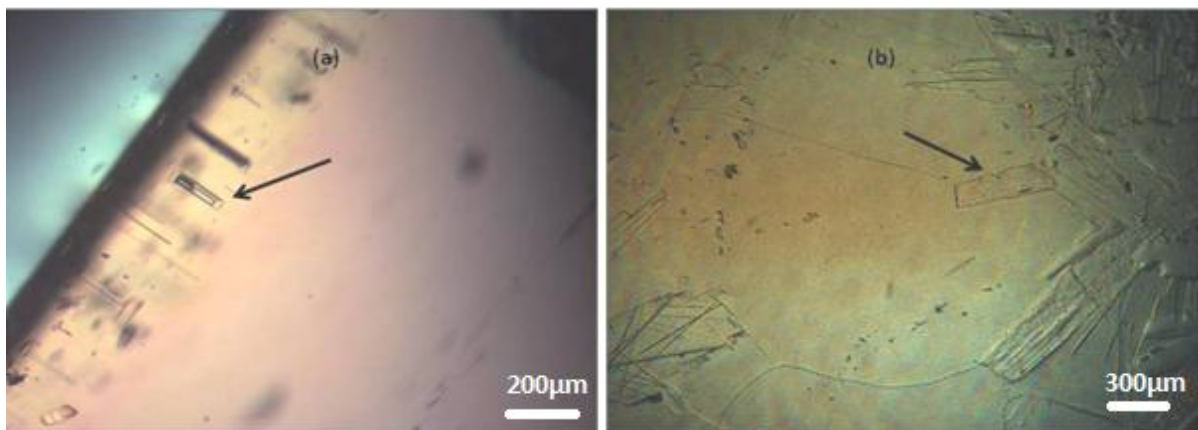


Fig. 3.2.3 Photomicrographs of thin sections. (a) Fluid inclusions in PAY-1. (b) CA-1 in association with muscovite.

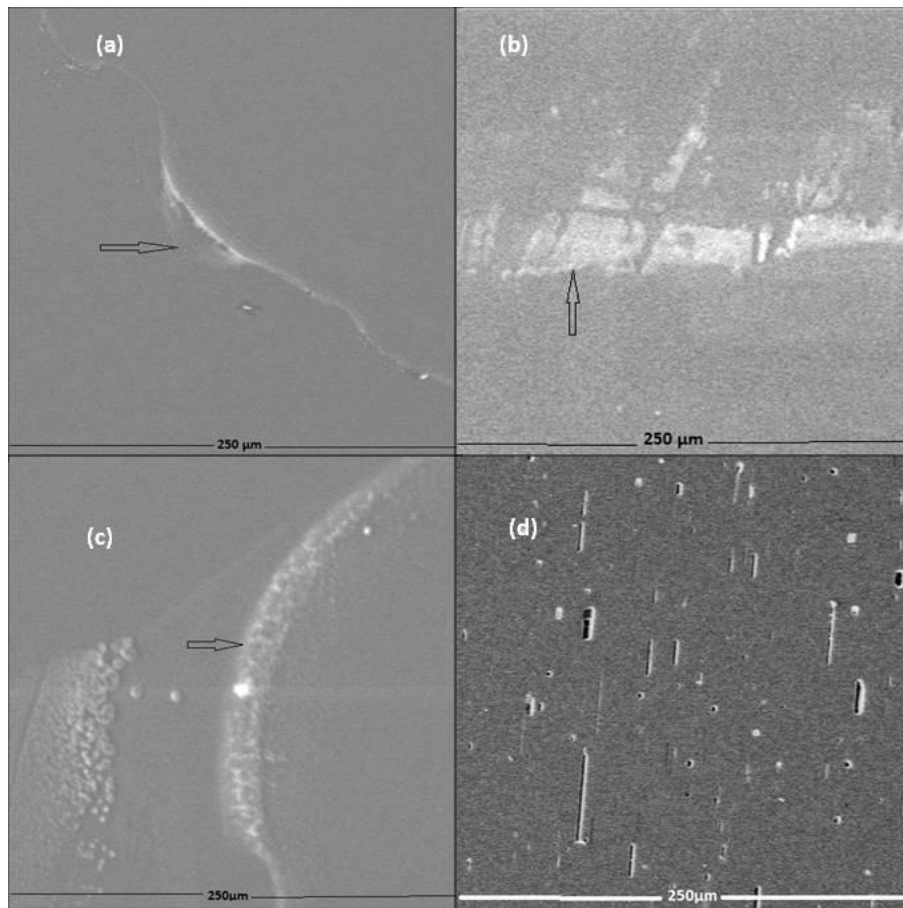


Fig. 3.2.4 BSE images and SE images from polished thin sections. (a) BSE image of PAD-4 (b) BSE image of PAD-5 (c) SE image of PAD-6 (d) BSE image of PAD-8.

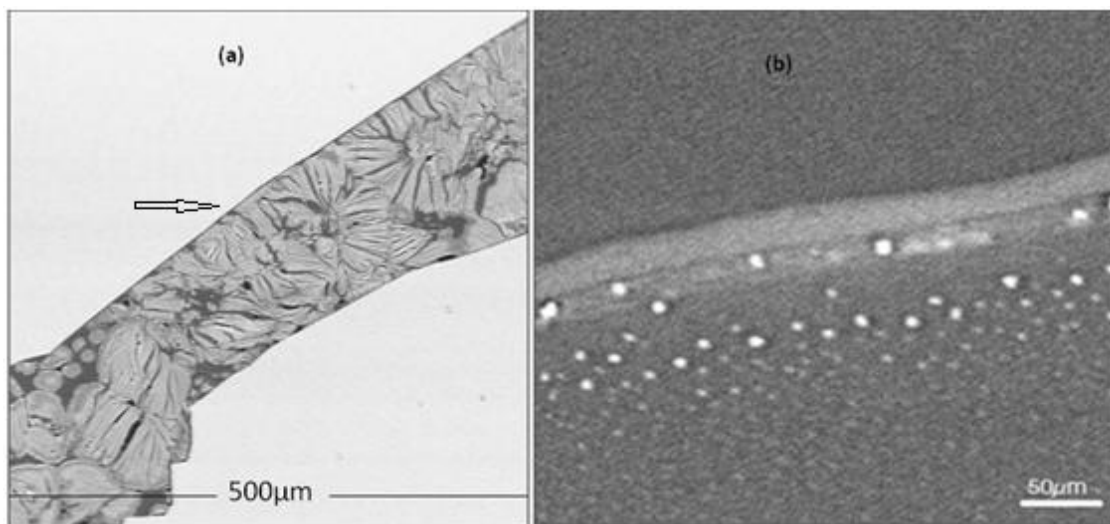


Fig. 3.2.5 SE and BSE images of thin sections. (a) SE image of BAA-2 (b) BSE image of FH-3.

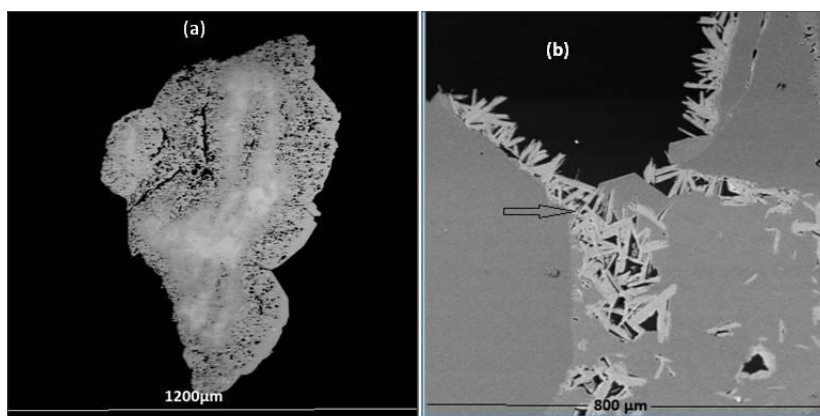


Fig. 3.2.6 BSE images of thin sections. (a) zircon inclusion in PAY-6. (b) Muscovite mica inclusions in PAY-5.

**3.3 EMP analysis:** In order to obtain an average value, between 4 and 16 analyses (Table 2 illustrates oxide wt% sample) were carried out across the polished section of each sample. Number of analyses were randomly selected between core and rim. MgO and K<sub>2</sub>O were very low in first three analysed samples BA-1, PA-2 and FH-3. Hence, these elements were not measured in the other samples. The SiO<sub>2</sub> content of Brazilian beryls varies from 64.84 wt% (BAA-2) to 67.37 wt% (BA-1). BA-1 has maximum amount of Al<sub>2</sub>O<sub>3</sub> with 19.33 wt%. FeO in Brazilian beryls ranges from 0.17 wt% (BA-1) to 0.47 wt% (BAA-2). Total alkali content (Na<sub>2</sub>O+Cs<sub>2</sub>O) is 2.21 wt% in BAA-2 and lowest in BA-1 with 0.05 wt%. The data correspond to the commonly observed values of beryl and most of the crystals are homogeneous except BAA-2 (Fig. 3.3.1b).

Zoning in PA-2 is mainly due to the variation in the amount of Na and Cs. Lighter area is enriched in Na and Cs. This zone is observed close to the fracture (Fig. 3.3.1a).

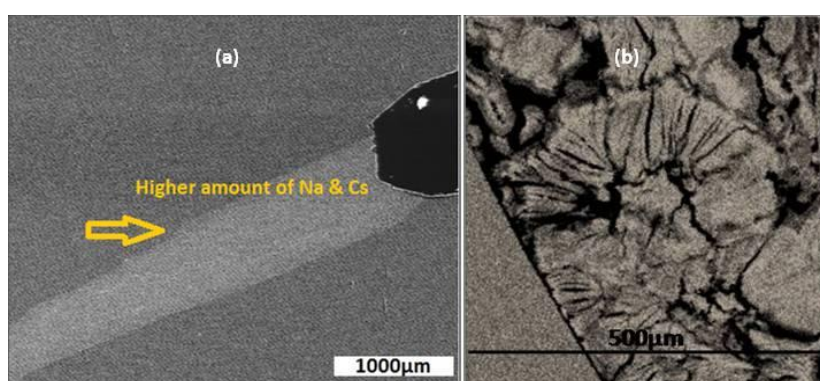


Fig. 3.3.1 BSE images of thin sections. (a) BSE image of zoning in PA-2. (b) Elemental mapping of Si around the rim of BAA-2.

SiO<sub>2</sub> and Al<sub>2</sub>O<sub>3</sub> of samples from Dassu mines and Yuno village range from 64.17 wt% to 67.17 wt% and 17.96 wt% to 18.82 wt% respectively. FeO varies between 0.06 wt% (PAY-1) and

0.54 wt% (PAD-8). PAD-8 has highest amount of alkali oxides with 0.94 wt% and PAD-3 with 0.18 wt% as lowest.

CA-1 has 64.42 wt% SiO<sub>2</sub> and 17.69 wt% Al<sub>2</sub>O<sub>3</sub> with 2.10 wt% alkalis. FH-3 has 67.03 wt% SiO<sub>2</sub>, 18.92 wt% Al<sub>2</sub>O<sub>3</sub>, 0.53 wt% FeO and 0.22 wt% alkalis.

Table 2 Oxides (wt%) in different samples

Sample	No. Obs	Oxides (Wt%)											
		SiO <sub>2</sub>	S.D	Al <sub>2</sub> O <sub>3</sub>	S.D	*BeO	FeO	S.D	Na <sub>2</sub> O	S.D	Cs <sub>2</sub> O	S.D	Total
<b>BA-1</b>	10	67.37	0.58	19.33	0.29	13.88	0.17	0.03	0.03	0.01	0.02	0.02	100.8
<b>BAA-1</b>	11	65.81	0.30	18.32	0.26	13.88	0.33	0.03	0.66	0.09	0.06	0.02	99.07
<b>BAA-2</b>	4	64.84	0.42	17.94	0.13	13.88	0.47	0.11	1.47	0.02	0.74	0.28	99.34
<b>CA-1</b>	4	64.42	0.69	17.69	0.11	13.88	0.20	0.11	1.58	0.05	0.42	0.15	98.14
<b>PA-2</b>	16	66.42	0.86	18.96	1.17	13.88	0.21	0.05	0.21	0.03	0.26	0.12	99.94
<b>PAD-1</b>	14	67.17	0.17	18.63	0.24	13.88	0.24	0.03	0.13	0.01	0.05	0.02	100.11
<b>PAD-3</b>	15	66.73	0.26	18.61	0.19	13.88	0.34	0.01	0.15	0.02	0.10	0.10	99.80
<b>PAD-4</b>	11	66.72	0.28	18.77	0.11	13.88	0.17	0.10	0.14	0.03	0.10	0.04	99.78
<b>PAD-5</b>	10	66.41	0.33	18.60	0.14	13.88	0.29	0.04	0.18	0.01	0.09	0.02	99.45
<b>PAD-6</b>	8	66.40	0.32	18.53	0.19	13.88	0.23	0.01	0.25	0.03	0.07	0.01	99.36
<b>PAD-7</b>	10	66.92	0.19	18.75	0.21	13.88	0.17	0.02	0.25	0.03	0.31	0.04	100.27
<b>PAD-8</b>	11	65.83	0.21	18.27	0.15	13.88	0.54	0.08	0.84	0.09	0.10	0.10	99.46
<b>PAD-9</b>	8	65.29	0.41	18.53	0.22	13.88	0.18	0.06	0.22	0.02	0.78	0.03	99.46
<b>PAD-10</b>	8	66.37	0.23	18.53	0.23	13.88	0.38	0.08	0.22	0.02	0.19	0.03	99.58
<b>PAY-1</b>	11	65.83	0.66	18.48	0.32	13.88	0.06	0.04	0.12	0.03	0.40	0.14	98.77
<b>PAY-2</b>	13	64.96	0.68	18.31	0.42	13.88	0.13	0.04	0.36	0.14	0.74	0.49	98.38
<b>PAY-3</b>	9	64.17	0.63	17.96	0.30	13.88	0.18	0.12	0.14	0.04	0.05	0.01	96.39
<b>PAY-4</b>	15	66.41	0.31	18.82	0.15	13.88	0.28	0.08	0.11	0.02	0.12	0.07	99.62
<b>PAY-5</b>	9	66.53	0.36	18.81	0.12	13.88	0.37	0.13	0.18	0.03	0.10	0.10	99.88
<b>PAY-6</b>	9	66.16	0.21	18.82	0.14	13.88	0.36	0.13	0.19	0.03	0.69	0.10	100.10
<b>FH-3</b>	12	67.03	0.58	18.92	1.17	13.88	0.53	0.04	0.11	0.02	0.11	0.05	100.58

Table 3 illustrates number of cations based on 18 oxygen atoms in each sample. Plots of average values of different elements in atoms per formula units are prepared in order to find out the substitution of cations in the samples. Fig. 3.3.2 to 3.3.7 illustrate the relationship between Si, Al; Si, Na+Cs; Al, Na+Cs; Al, Fe; Si, Fe and Na+Cs, Fe which are discussed in detail in Chapter 4.3.

Table 3 Number of cations based on 18 oxygen atoms

Sample	Number of cations												Total
	Si	S.D	Al	S.D	*Be	S.D	Fe	S.D	Na	S.D	Cs	S.D	
BA-1	5.99	0.02	2.02	0.03	2.96	0.02	0.01	0.00	0.01	0.00	0.00	0.00	11.00
BAA-1	5.97	0.01	1.96	0.02	3.03	0.02	0.03	0.00	0.12	0.02	0.00	0.00	11.11
BAA-2	5.93	0.02	1.94	0.02	3.05	0.01	0.04	0.01	0.26	0.01	0.03	0.01	11.24
CA-1	5.94	0.02	1.94	0.02	3.07	0.02	0.02	0.01	0.28	0.01	0.02	0.01	11.25
PA-2	5.97	0.08	2.01	0.12	3.00	0.02	0.02	0.00	0.04	0.01	0.01	0.00	11.04
FH-3	5.99	0.02	1.99	0.02	2.98	0.18	0.04	0.00	0.02	0.00	0.00	0.00	11.02
PAD-1	6.02	0.02	1.97	0.02	2.99	0.01	0.02	0.00	0.02	0.00	0.00	0.00	11.01
PAD-3	6.00	0.01	1.97	0.02	3.00	0.01	0.03	0.01	0.03	0.00	0.00	0.00	11.03
PAD-4	6.00	0.01	1.99	0.01	3.00	0.01	0.01	0.01	0.03	0.01	0.00	0.00	11.02
PAD-5	5.99	0.01	1.98	0.01	3.01	0.01	0.02	0.00	0.03	0.00	0.00	0.00	11.04
PAD-6	6.00	0.01	1.97	0.01	3.01	0.01	0.02	0.00	0.04	0.00	0.00	0.00	11.04
PAD-7	6.00	0.01	1.98	0.02	2.99	0.01	0.01	0.00	0.04	0.00	0.01	0.00	11.04
PAD-8	5.97	0.01	1.95	0.01	3.02	0.01	0.04	0.01	0.15	0.02	0.00	0.00	11.13
PAD-9	6.00	0.01	1.97	0.02	3.01	0.02	0.02	0.00	0.04	0.01	0.00	0.00	11.04
PAD-10	5.99	0.01	1.97	0.02	3.01	0.01	0.03	0.01	0.04	0.00	0.00	0.00	11.05
PAY-1	5.98	0.01	1.98	0.02	3.03	0.03	0.01	0.00	0.02	0.00	0.02	0.00	11.04
PAY-2	5.96	0.04	1.98	0.04	3.06	0.02	0.01	0.00	0.06	0.02	0.03	0.02	11.10
PAY-3	5.96	0.02	1.97	0.03	3.10	0.02	0.01	0.01	0.03	0.01	0.00	0.00	11.07
PAY-4	5.98	0.01	1.99	0.01	3.00	0.01	0.02	0.01	0.02	0.00	0.01	0.00	11.03
PAY-5	5.98	0.01	1.99	0.01	3.00	0.01	0.03	0.00	0.03	0.00	0.00	0.00	11.04
PAY-6	5.97	0.02	2.00	0.01	3.00	0.01	0.03	0.01	0.03	0.01	0.03	0.01	11.06

\*Be Not measured, calculated. Obs: Number of observations

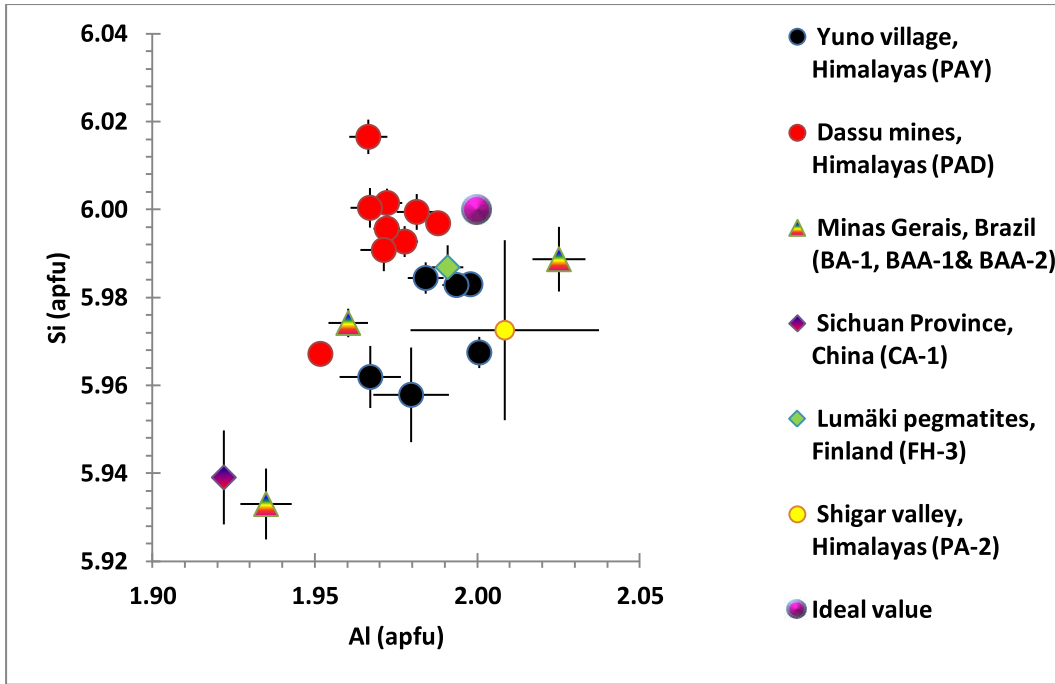


Fig. 3.3.2 Plot of Si (apfu) vs Al (apfu). The crosses around the data points show error bars.

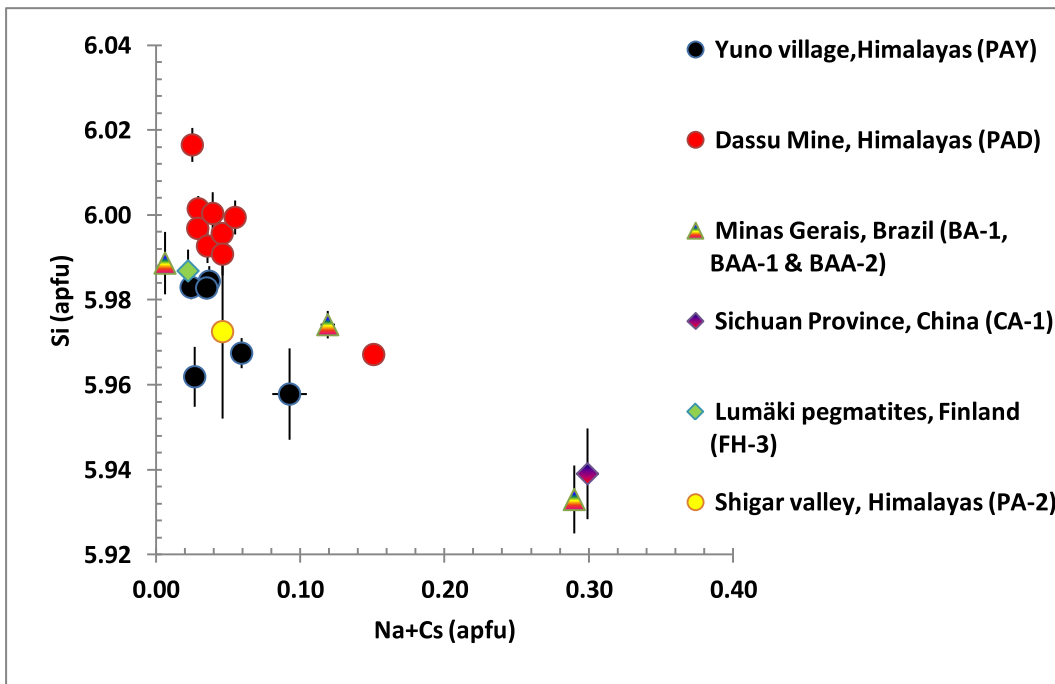


Fig. 3.3.3 Plot of Si (apfu) vs Na+Cs (apfu). The crosses around the data points show error bars.

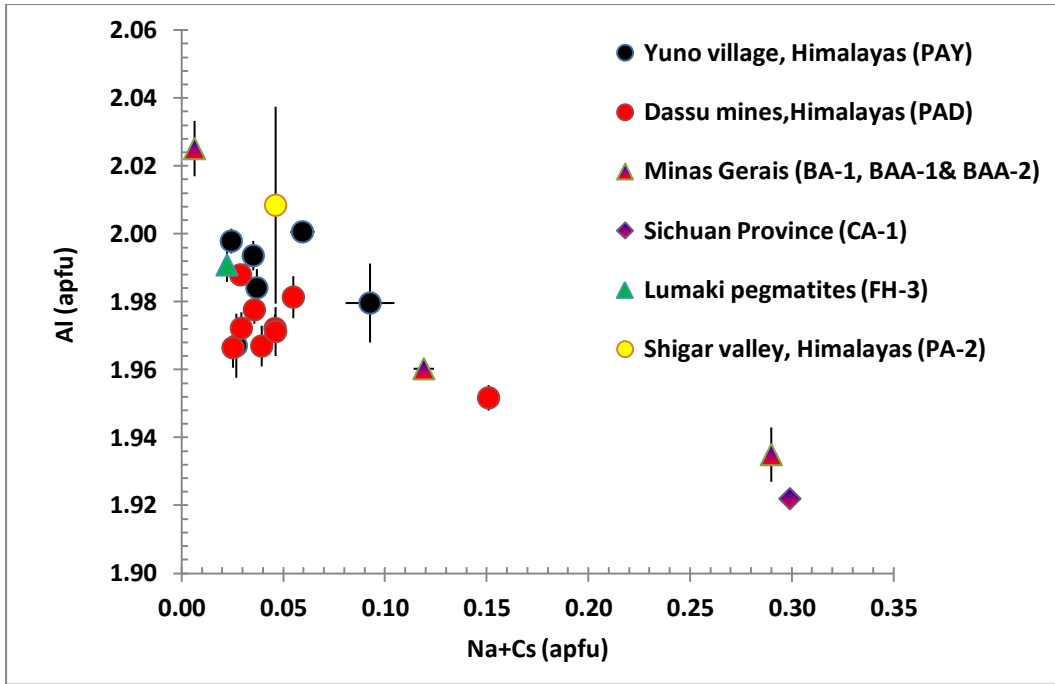


Fig. 3.3.4 Plot of Al (apfu) vs Na+Cs (apfu). The crosses around the data points show error bars.

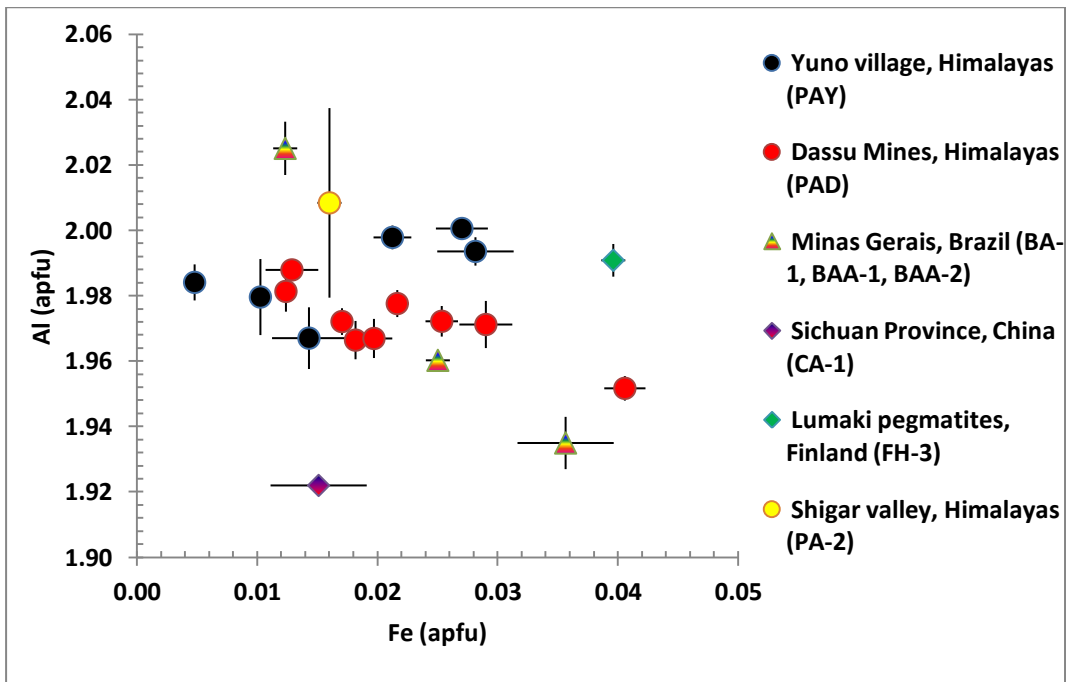


Fig. 3.3.5 Plot of Al (apfu) vs Fe (apfu). The crosses around the data points show error bars.

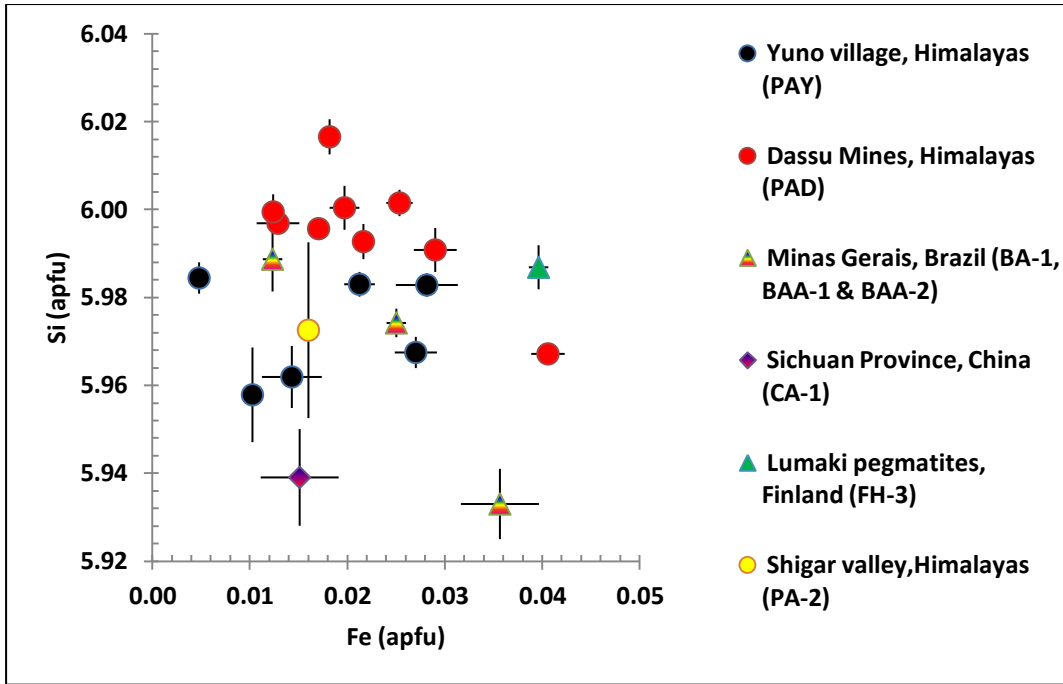


Fig. 3.3.6 Plot of Si (apfu) vs Fe (apfu). The crosses around the data points show error bars.

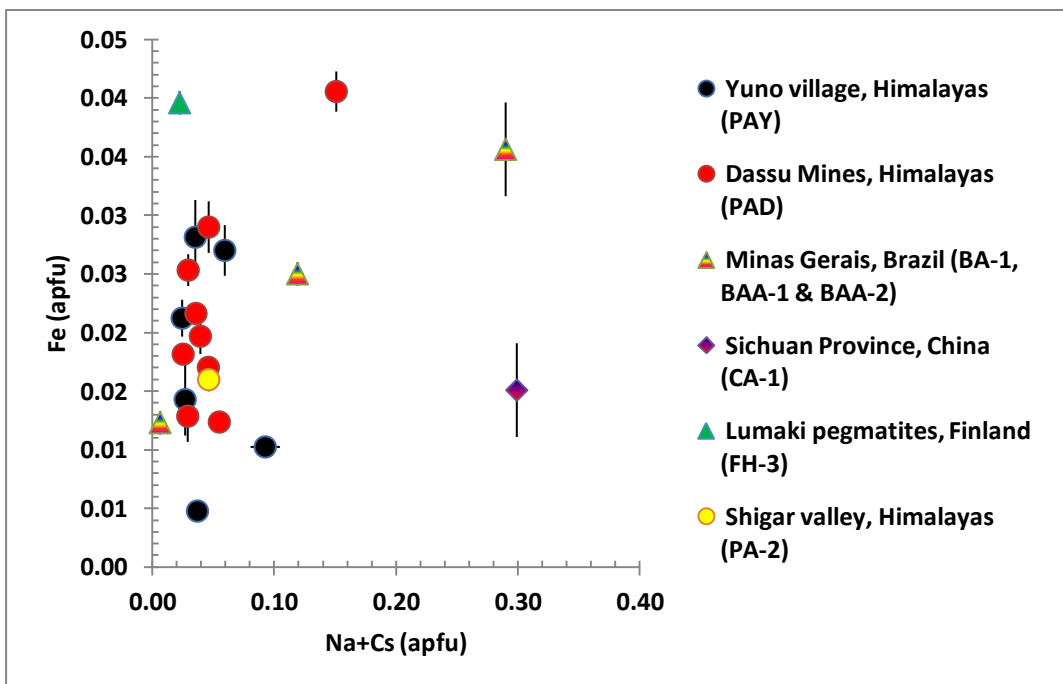


Fig. 3.3.7 Plot of Na+Cs (apfu) vs Fe (apfu). The crosses around the data points show error bars.

**3.4 Refractive indices determination:** Refractive indices  $\varepsilon$  of three representative samples lie in the range 1.570- 1.577 and  $\omega$  between 1.574 and 1.580. The birefringence  $\Delta n$  ranges from 0.003-0.004 and found to be uniaxially negative. A plot is prepared between refractive indices and alkali content (Fig.3.4.1).

Table. 4 Refractive indices,  $\Delta n$  and Na+Cs (apfu) per 18 oxygen atoms of samples from three different locations; standard deviation given for last digit

Sample	$\epsilon$	$\omega$	$\Delta n$	Na+Cs (apfu)
BA-1	1.570(1)	1.574(1)	-0.004	0.01
PA-2	1.574(1)	1.578(1)	-0.004	0.05
FH-3	1.577(1)	1.580(1)	-0.003	0.02

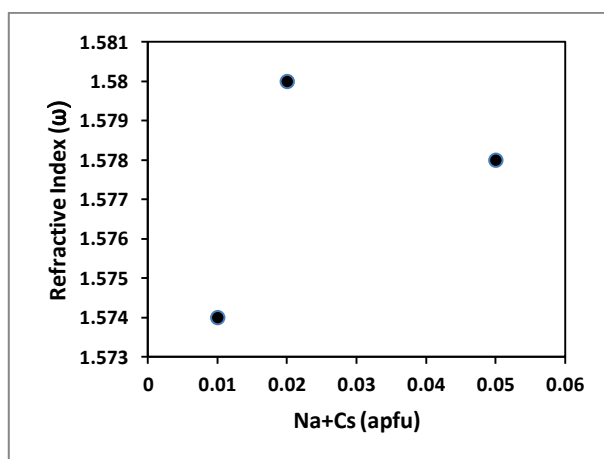


Fig. 3.4.1 Plot of refractive indices ( $\omega$ ) vs Na+Cs (apfu).

**3.5 XRD analysis:** Determination of ratio of lattice constants  $c$  and  $a$  by Rietveld refinement of XRD data of the samples show that  $c$ -parameter ranges from 9.1920 to 9.2201 Å and  $a$ - parameter ranges from 9.2087 to 9.2177 Å. Volume of unit cell in BA-1 is lowest with 675.357 (Å)<sup>3</sup> and CA-1 has the highest volume as 678.464 (Å)<sup>3</sup> (Table 5) .

Si-O Inter atomic distance varies from 1.591 Å (CA-1) to 1.598 Å (BA-1). Be-O bond length is found to be the lowest in BA-1 (1.666 Å) and highest in CA-1 (1.684 Å). Al-O distance ranges from 1.923 Å (CA-1) to 1.928 Å (BA-1) (Fig. 3.5.1a, b, Table 6).

Table 5 Lattice parameters, c/a ratio and volume of unit cell

Sample No.	Lattice parameters			
	c (Å)	a (Å)	c/a	Volume (Å) <sup>3</sup>
BA-1	9.1920(1)	9.2108(1)	0.9979	675.357
BAA-1	9.2033(1)	9.2160(1)	0.9986	676.952
BAA-2	9.2201(1)	9.2177(1)	1.0002	678.440
CA-1	9.2182(1)	9.2162(1)	1.0002	678.464
PA-2	9.1948(1)	9.2110(2)	0.9982	675.590
PAD-1	9.1927(1)	9.2121(1)	0.9979	675.602
PAD-3	9.1941(2)	9.2136(2)	0.9979	675.933
PAD-4	9.1921(1)	9.2087(1)	0.9982	675.055
PAD-5	9.1939(1)	9.2114(1)	0.9981	675.589
PAD-7	9.1966(1)	9.2131(1)	0.9982	676.031
PAD-8	9.2023(2)	9.2157(1)	0.9985	676.839
PAD-9	9.1959(2)	9.2107(2)	0.9984	675.632
PAD-10	9.1930(1)	9.2111(1)	0.9980	675.473
PAY-1	9.1950(1)	9.2112(1)	0.9982	675.629
PAY-2	9.1995(1)	9.2138(1)	0.9984	676.352
PAY-3	9.1920(1)	9.2112(0)	0.9979	675.426
PAY-4	9.1950(1)	9.2129(1)	0.9981	675.896
PAY-5	9.1930(4)	9.2122(1)	0.9979	675.643
PAY-6	9.1967(1)	9.2129(7)	0.9982	676.012
FH-3	9.1944(2)	9.2140(1)	0.9979	676.013

Table 6 Inter-atomic distances calculated by Rietveld method, coordination number and ionic radius of the cations in beryl samples.

Ion	Radius(Å) (Shannon, 1976)	CN	Mean atomic distance (M-O)		
			BA-1	FH-3	CA-1
Al <sup>3+</sup>	0.535	6	1.928 (2)	1.929 (2)	1.923 (2)
Be <sup>2+</sup>	0.27	4	1.666 (3)	1.679 (3)	1.684 (2)
Si <sup>4+</sup>	0.26	4	1.598 (2)	1.593 (2)	1.591 (2)

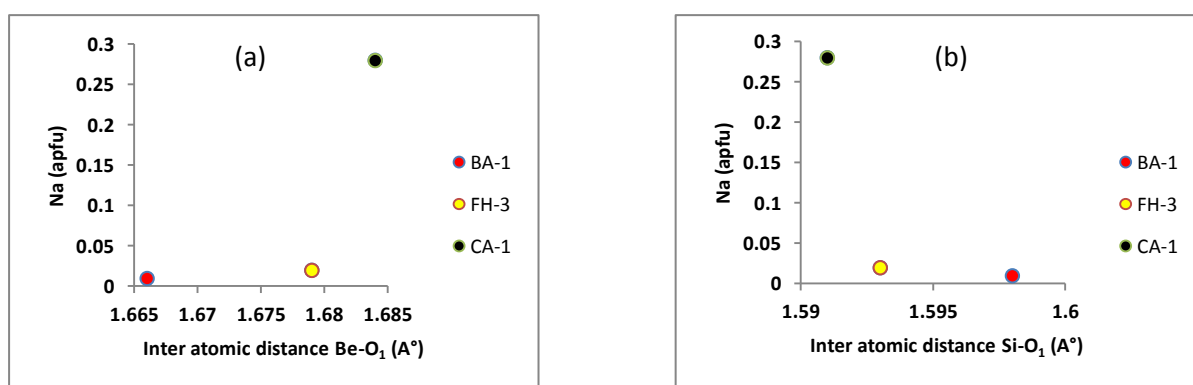


Fig. 3.5.1 Plot of inter atomic distances vs. Na(apfu). (a) Be-O<sub>1</sub> bond length vs. Na (apfu). (b) Si-O<sub>1</sub> bond length vs. Na(apfu).

Most of the analysed beryls have  $c/a$  ratio between 0.997 and 0.998. Two alkali rich beryls (CA-1 and BAA-2) have higher  $c/a$  ratio of 1.0002 (Fig. 3.5. 2, Table 5). The  $a$ -parameter has a slight negative trend with Al (Fig. 3.5.3) and a slight positive trend with Fe apfu (Fig. 3.5.4). The  $c$ - parameter has a direct correlation with Na+Cs (Fig. 3.5.5) and indirect correlation with Si apfu (Fig. 3.5.6). A positive trend is observed between  $c$ - parameter and  $a$ -parameter (Fig. 3.5.7).

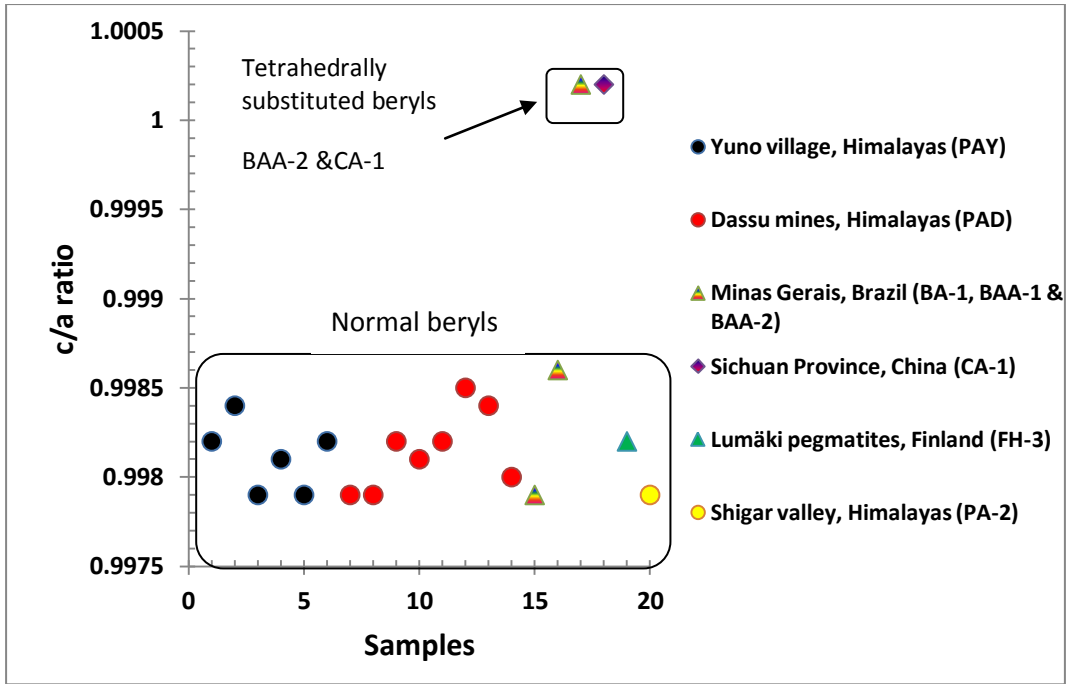


Fig. 3.5.2 Plot of samples vs. c/a ratio.

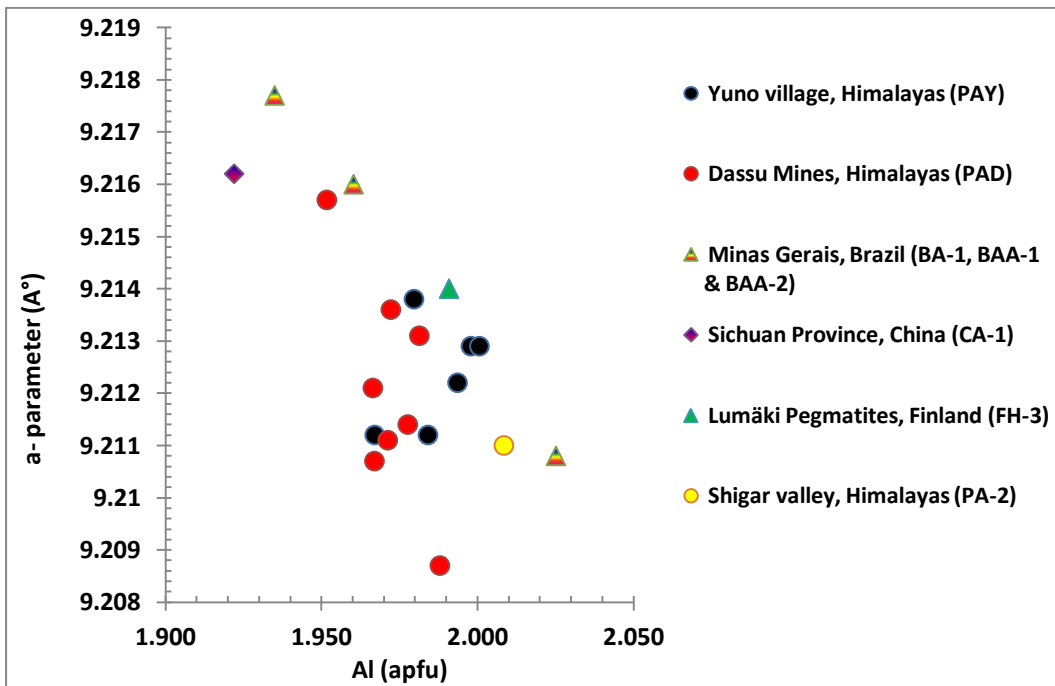


Fig. 3.5.3 Plot of Al (apfu) vs. a-parameter.

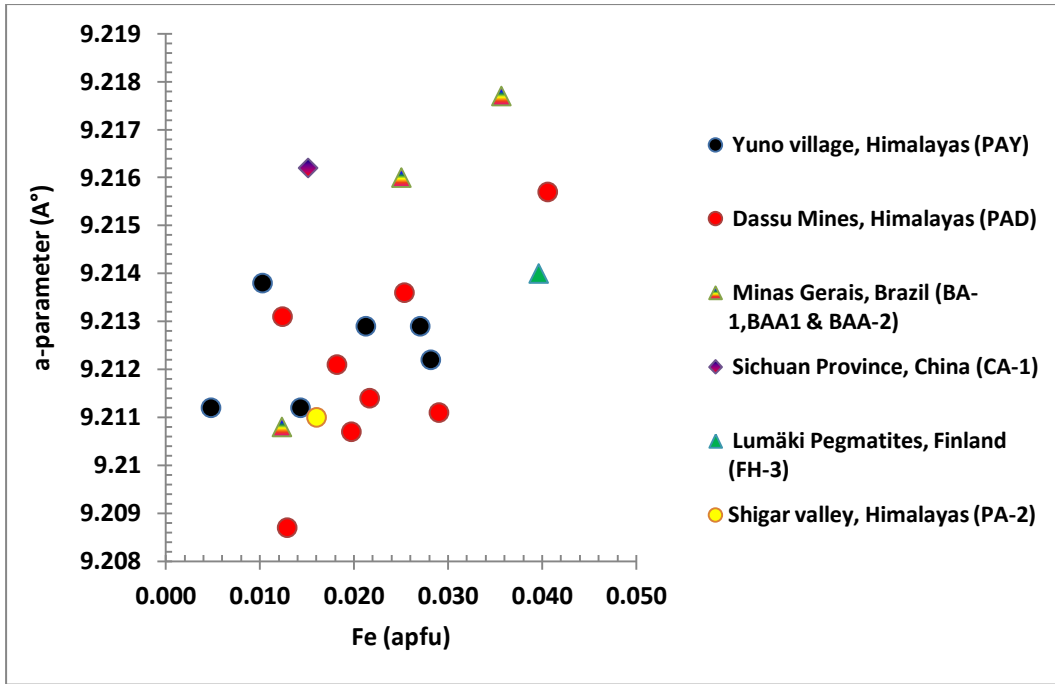


Fig. 3.5.4 Plot of a-parameter vs. Fe (apfu).

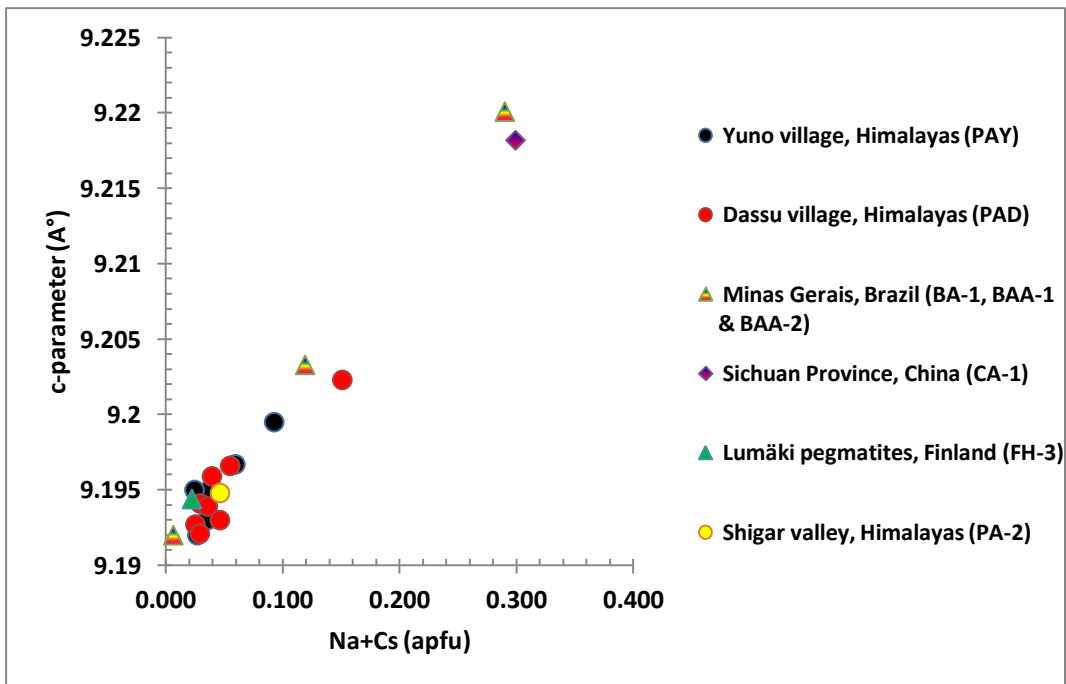


Fig. 3.5.5 Plot of c- parameter vs. Na+Cs (apfu).

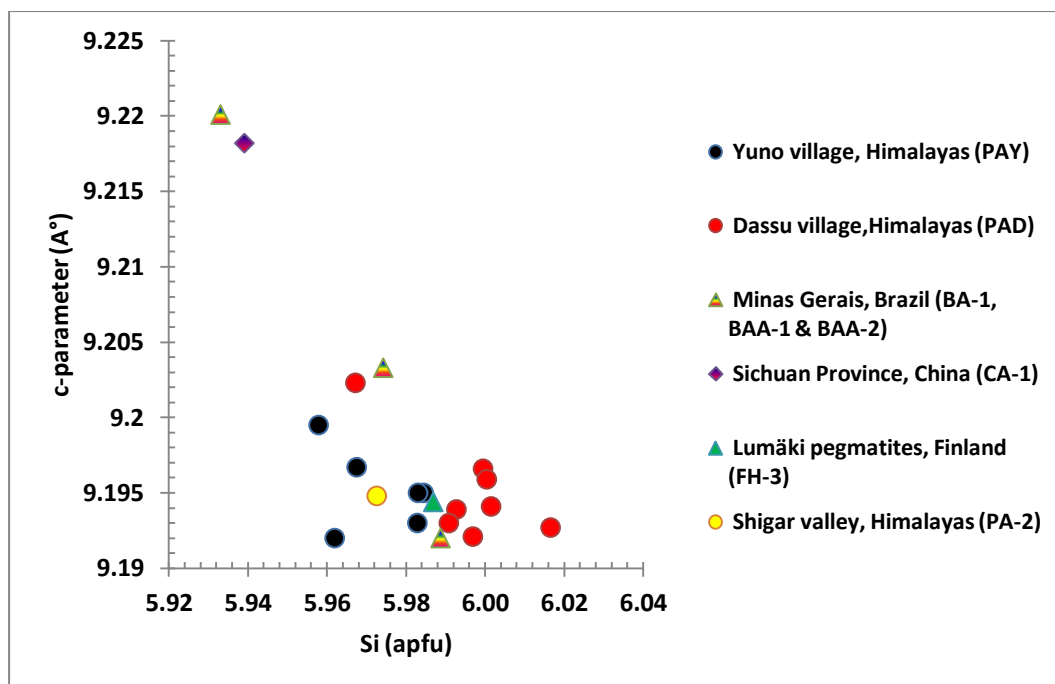


Fig. 3.5.6 Plot of c-parameter vs. Si (apfu).

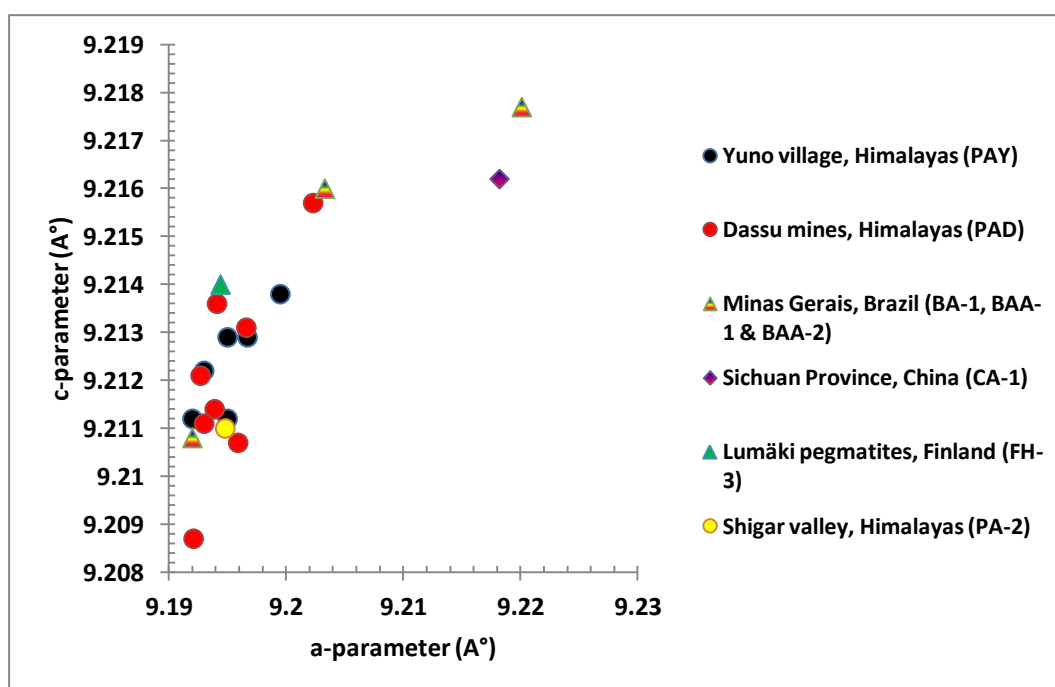


Fig. 3.5.7 Plot of c-parameter vs. a-parameter.

### 3.6 IR spectroscopic studies:

**Pellet method:** IR spectra of powdered beryl samples in the range  $400\text{ cm}^{-1}$  to  $1400\text{ cm}^{-1}$  show two main absorption bands at  $1200\text{ cm}^{-1}$  and  $960\text{ cm}^{-1}$ . The band at  $1206\text{ cm}^{-1}$  in BA-1 (Fig. 3.6.1) weakens and it shifts towards lower frequency ( $1179\text{ cm}^{-1}$ ) in CA-1 and BAA-2

(Fig. 3.6.3, 4). This band is sharp in BA-1 which becomes broader and smoother in CA-1 and BAA-2. The band at  $960\text{ cm}^{-1}$  is stronger than the band at  $1200\text{ cm}^{-1}$  and it shifts towards lower frequency in BAA-2 and CA-1; however the shift is negligible as compared to the band at  $1206\text{ cm}^{-1}$ . Besides that, the sharp band at  $1020\text{ cm}^{-1}$  in BA-1 becomes smoother and a shoulder develops on the flank around  $1060\text{ cm}^{-1}$  in CA-1 and BAA-2 (Fig. 3.6.3, 4). In BAA-1 weak shoulders appear at  $1063\text{ cm}^{-1}$  and  $1147\text{ cm}^{-1}$  (Fig. 3.6.2). In BAA-2 and CA-1, a small shoulder appears on the flank of the band at  $525\text{ cm}^{-1}$  (around  $560\text{ cm}^{-1}$ ) and  $440\text{ cm}^{-1}$ . The band which is at  $808\text{ cm}^{-1}$  in BA-1 shifts to higher frequency in BAA-2 and CA-1 ( $818\text{ cm}^{-1}$ ).

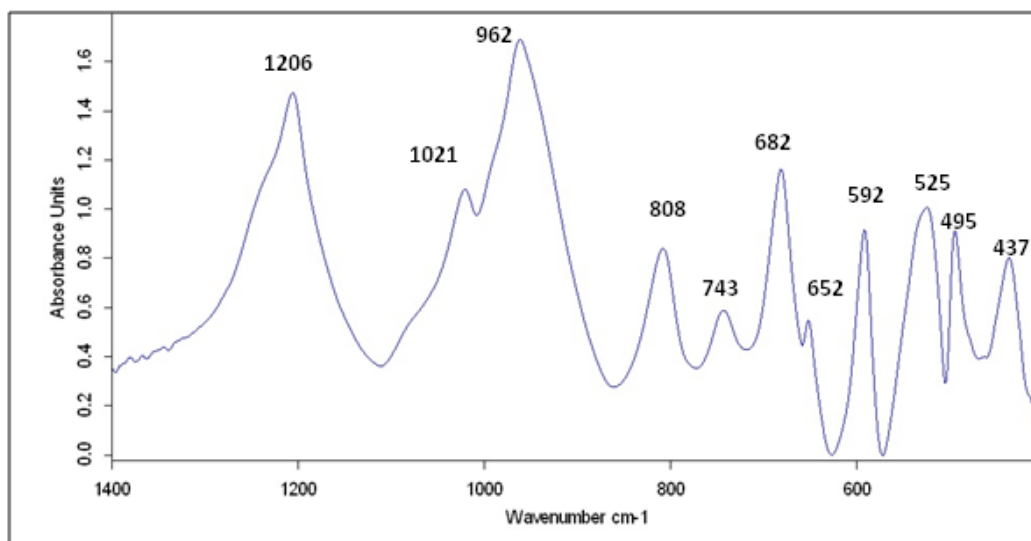


Fig. 3.6.1 Infrared spectrum of BA-1 in the frequency region from  $400\text{ cm}^{-1}$  to  $1400\text{ cm}^{-1}$ .

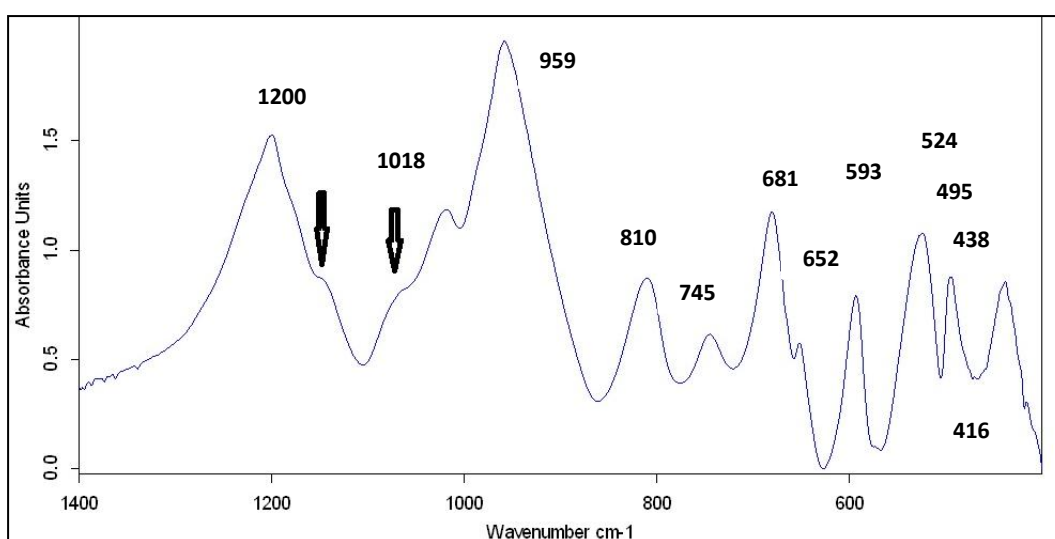


Fig. 3.6.2 Infrared spectrum of BAA-1 in the frequency region from  $400\text{ cm}^{-1}$  to  $1400\text{ cm}^{-1}$ .

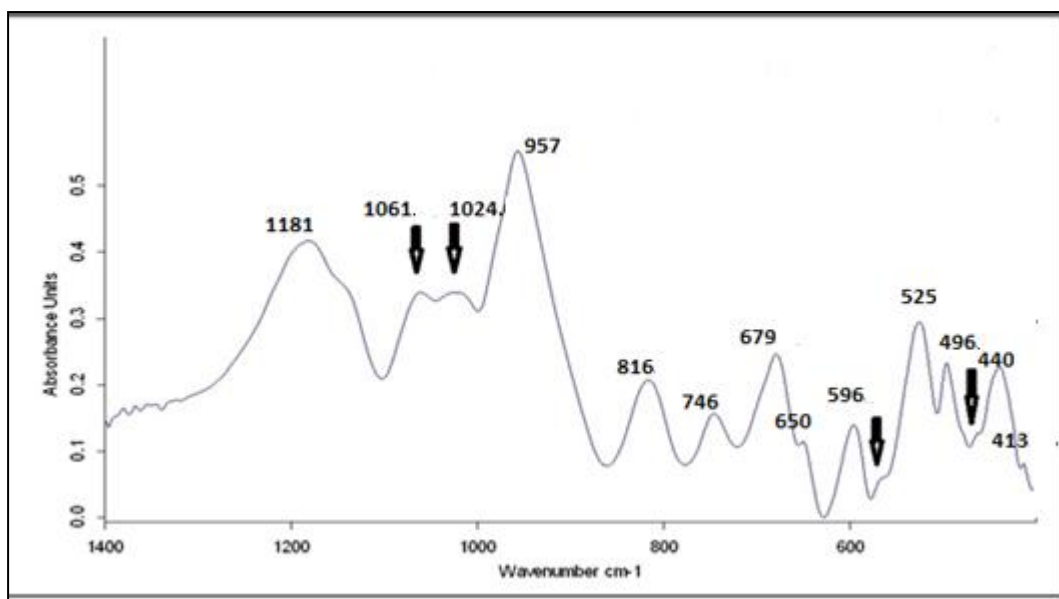


Fig. 3.6.3 Infrared spectrum of CA-1 in the frequency region from  $400\text{ cm}^{-1}$  to  $1400\text{ cm}^{-1}$ .

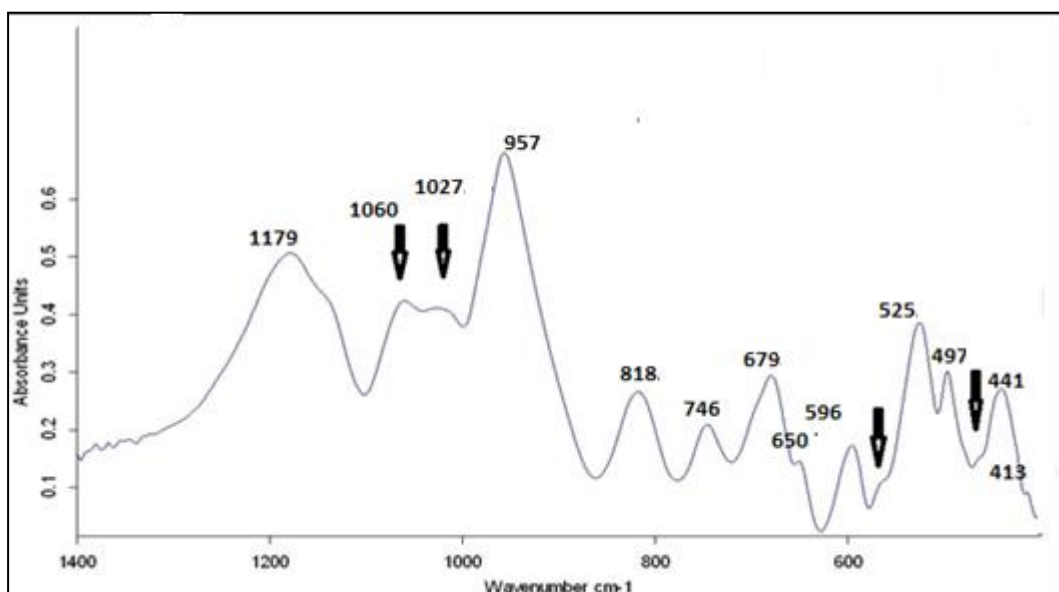


Fig.3.6.4 Infrared spectrum of BAA-2 in the frequency region from  $400\text{ cm}^{-1}$  to  $1400\text{ cm}^{-1}$ .

Plots of IR band positions and amounts of different elements have been prepared. Fig. 3.6.5, 3.6.6 and 3.6.7 indicate a direct correlation of Si (apfu) and Al (apfu) and an indirect correlation of Na+Cs with the band at  $1200\text{ cm}^{-1}$ . Fig. 3.6.8 shows a negative trend between Al (apfu) and the band at  $810\text{ cm}^{-1}$ . Na+Cs is directly correlated to the band at  $810\text{ cm}^{-1}$  (Fig. 3.6.9). Table 7 shows IR spectra band positions.

Table 7 IR spectra band positions of samples in wave numbers ( $\text{cm}^{-1}$ )

<b>BA-1</b>	1206	1021	962	808	743	682	652	592	525	495	437
<b>BAA-1</b>	1199	1018	959	810	745	680	652	593	524	495	438
<b>BAA-2</b>	1179	1061 1027	957	818	746	680	651	596	526	497	441
<b>CA-1</b>	1181	1062 1025	957	817	746	679	651	596	526	497	440
<b>FH-3</b>	1206	1020	962	809	743	682	652	592	526	495	439
<b>PA-2</b>	1203	1020	961	810	744	681	652	593	529	495	438
<b>PAD-1</b>	1204	1021	962	808	743	681	653	592	525	495	438
<b>PAD-3</b>	1205	1020	961	808	742	681	652	592	525	495	438
<b>PAD-4</b>	1205	1021	963	809	744	682	653	592	526	495	438
<b>PAD-5</b>	1204	1019	960	810	743	681	652	592	524	495	444
<b>PAD-6</b>	1204	1019	959	809	743	681	652	592	527	495	438
<b>PAD-7</b>	1205	1020	962	809	743	682	653	593	526	495	438
<b>PAD-8</b>	1198	1016	960	811	743	680	652	595	528	496	439
<b>PAD-9</b>	1204	1020	962	809	743	681	652	593	524	495	438
<b>PAD-10</b>	1203	1020	960	809	744	681	653	592	526	495	443
<b>PAY-1</b>	1204	1020	962	809	743	681	653	593	525	495	440
<b>PAY-2</b>	1203	1020	960	809	744	681	652	593	525	495	437
<b>PAY-3</b>	1204	1020	961	809	743	682	653	592	525	495	437
<b>PAY-4</b>	1205	1019	962	809	745	681	653	593	525	496	441
<b>PAY-5</b>	1205	1020	962	809	744	682	653	592	526	495	438
<b>PAY-6</b>	1204	1019	961	810	744	682	652	593	526	495	439

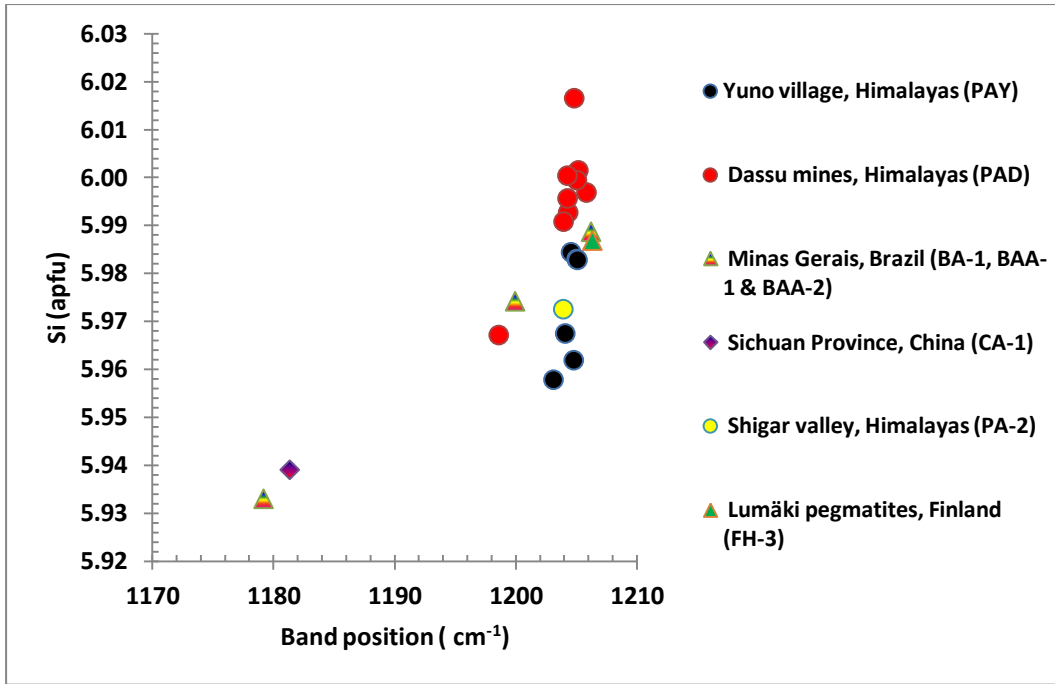


Fig. 3.6.5 Plot of IR band position around  $1200 \text{ cm}^{-1}$  vs. Si (apfu).

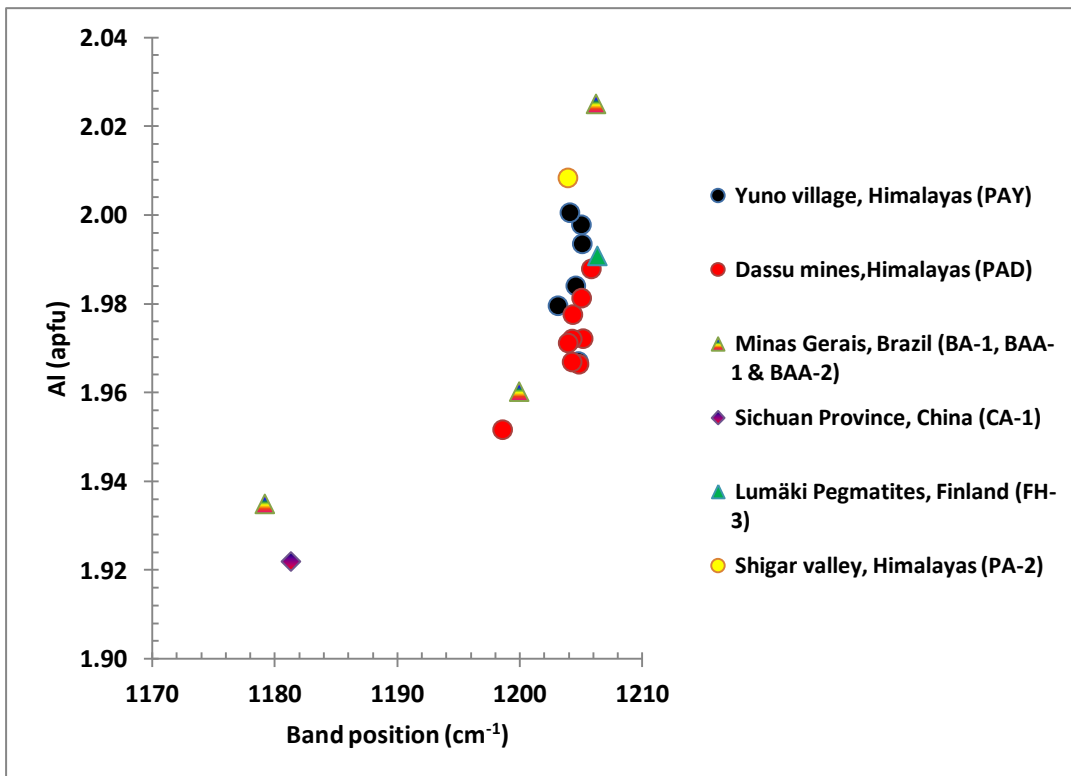


Fig. 3.6.6 Plot of IR band position around  $1200 \text{ cm}^{-1}$  vs. Al (apfu).

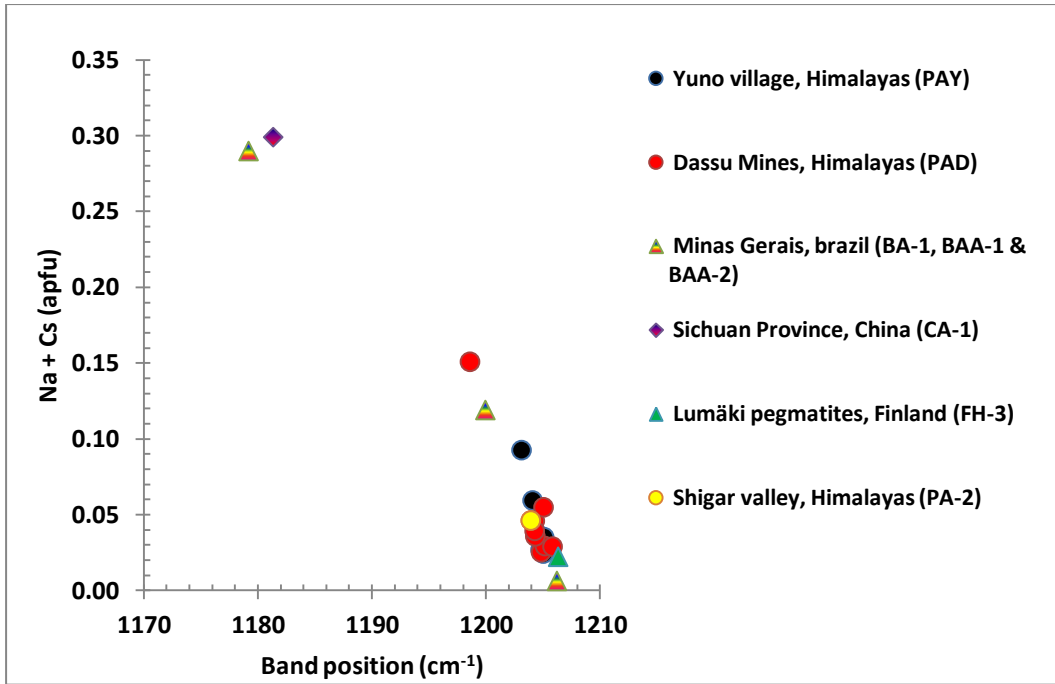


Fig. 3.6.7 Plot of IR band position around  $1200 \text{ cm}^{-1}$  vs. Na+Cs (apfu).

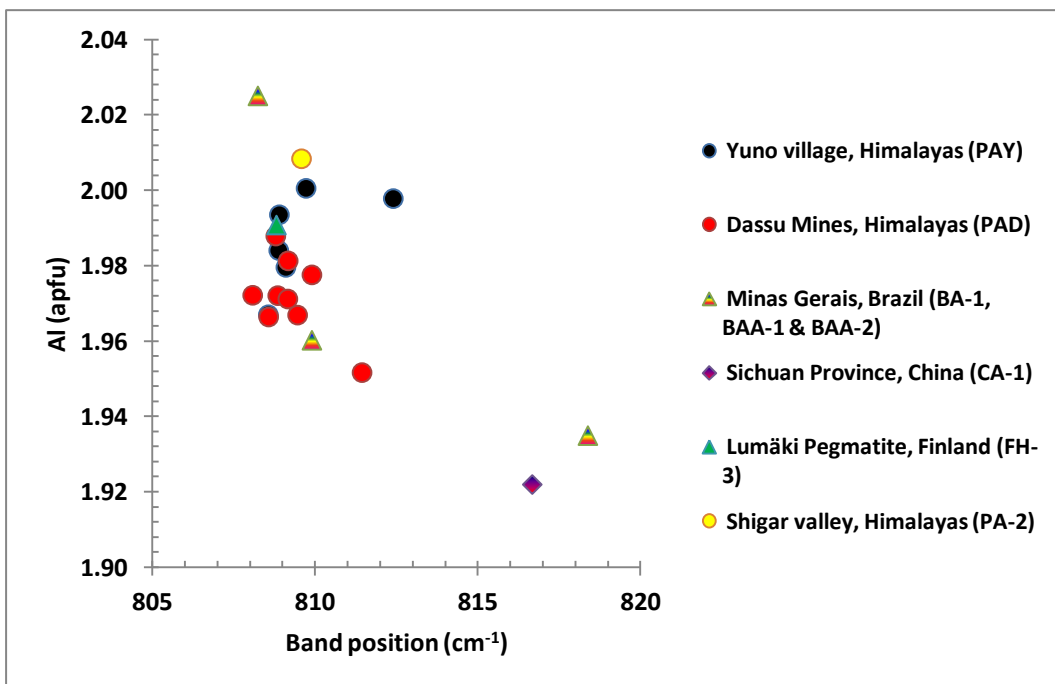


Fig. 3.6.8 Plot of IR band position around  $810 \text{ cm}^{-1}$  vs. Al (apfu).

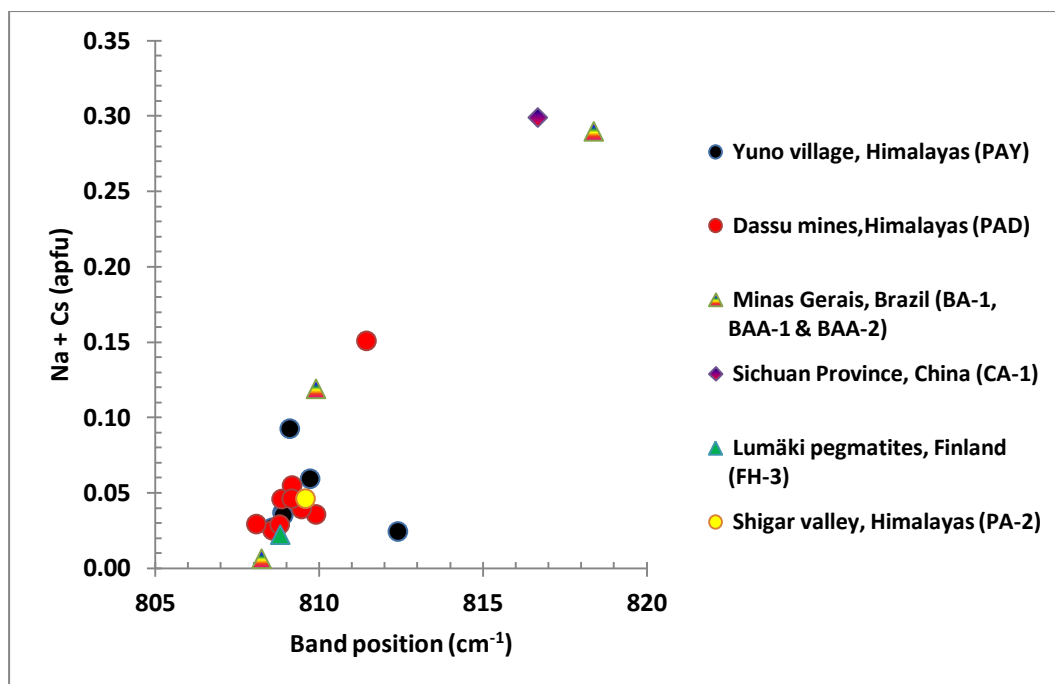


Fig. 3.6.9 Plot of IR band positions around  $810\text{ cm}^{-1}$  vs. Na+Cs (apfu).

**Infrared spectroscopic studies of single crystals under polarised light:** When the c-axis is oriented parallel to the electric vector, IR spectra in the region from  $3500\text{ cm}^{-1}$  to  $3800\text{ cm}^{-1}$  are characterised by two main bands around  $3600\text{ cm}^{-1}$  and  $3700\text{ cm}^{-1}$ . The intensity of these two bands are almost equal in PA-2 and PAD-1. However, in PAY-3 the intensity of the band at  $3600\text{ cm}^{-1}$  is almost half of the one at  $3700\text{ cm}^{-1}$ . In the lower frequency region a band is visible around  $1630\text{ cm}^{-1}$ . The band position is variable in different samples. A band is also observed at  $5270\text{ cm}^{-1}$  (Fig. 3.6.10, 11). The band around  $1940\text{ cm}^{-1}$  is perceptible in both orientations with different intensities. In Fig. 3.6.13 the IR spectrum of BA-1 under unpolarised light indicates the presence of 2 main bands  $3600$  and  $3698\text{ cm}^{-1}$  in the region from  $3500\text{ cm}^{-1}$  to  $3800\text{ cm}^{-1}$ . The intensity of the band at  $3698\text{ cm}^{-1}$  is double than at  $3600\text{ cm}^{-1}$ . The band at  $3660\text{ cm}^{-1}$  which is visible under  $E \perp c$  orientation in polarised light is also present under unpolarised light.

Under  $c \perp E$  orientation, a moderately strong band around  $2360\text{ cm}^{-1}$  was visible in most of the samples (Fig. 3.6.11, 12). The intensities are less compared to the parallel orientation in the range from  $3500\text{ cm}^{-1}$  to  $3800\text{ cm}^{-1}$ . At  $3860\text{ cm}^{-1}$ , the peak has a smooth and curved tip. The band at  $3657\text{ cm}^{-1}$  is sharp and more intense (Fig. 3.6.11). A sharp band is present at  $1598\text{ cm}^{-1}$  in PAY-3 (Fig. 3.6.12) and at  $1597\text{ cm}^{-1}$  in PA-2 (Fig. 3.6.10). An additional band is visible in PAY-3 which is at  $1283\text{ cm}^{-1}$  (red colour).

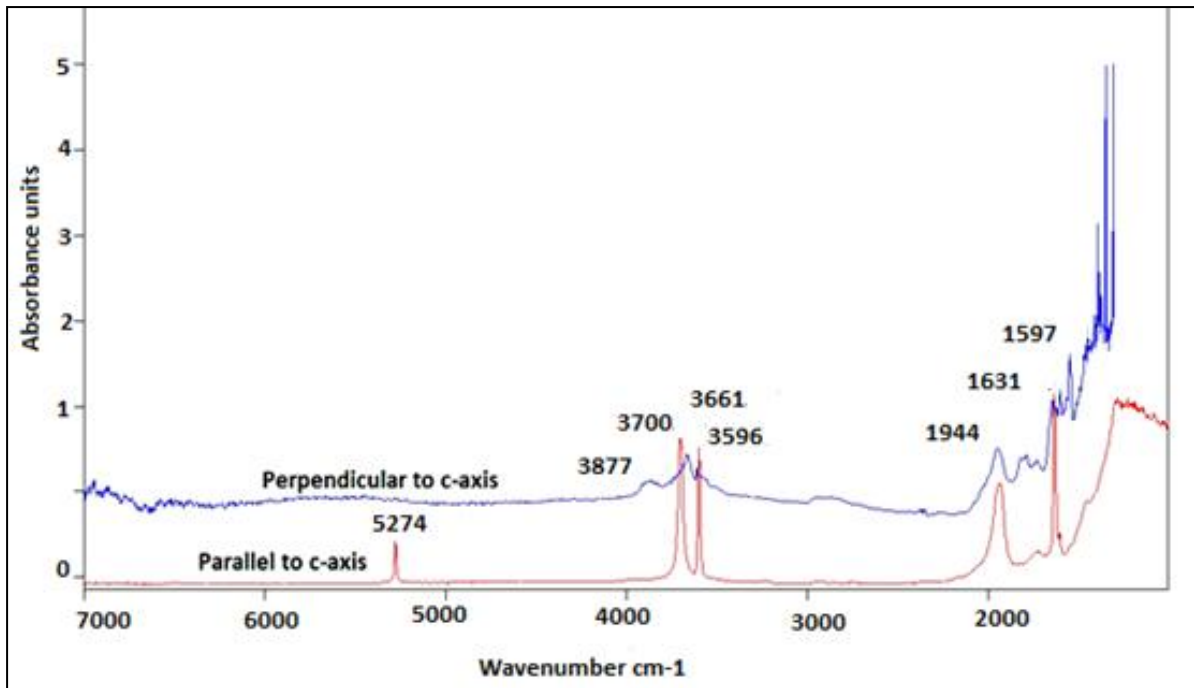


Fig. 3.6.10 Polarised IR spectra of PA-2 single crystal from  $1000\text{ cm}^{-1}$  to  $7000\text{ cm}^{-1}$ .

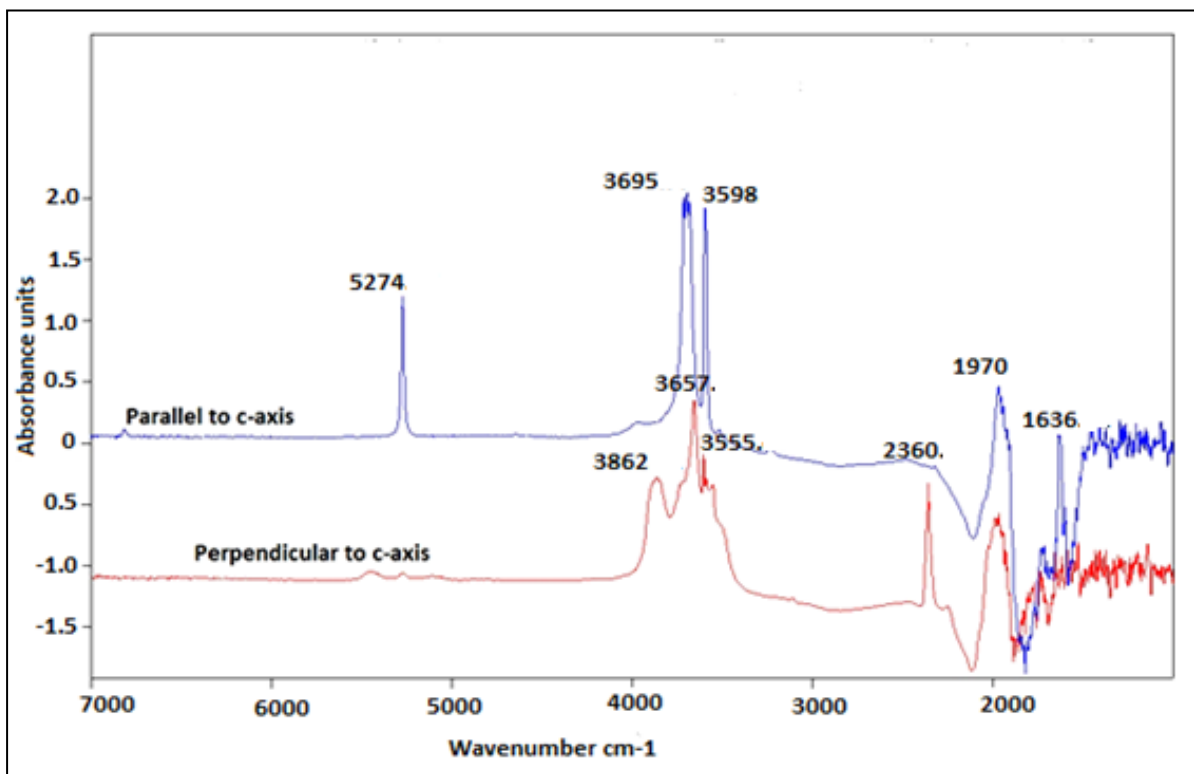


Fig. 3.6.11 Polarised IR spectra of PAD-1 single crystal from  $1000\text{ cm}^{-1}$  to  $7000\text{ cm}^{-1}$ .

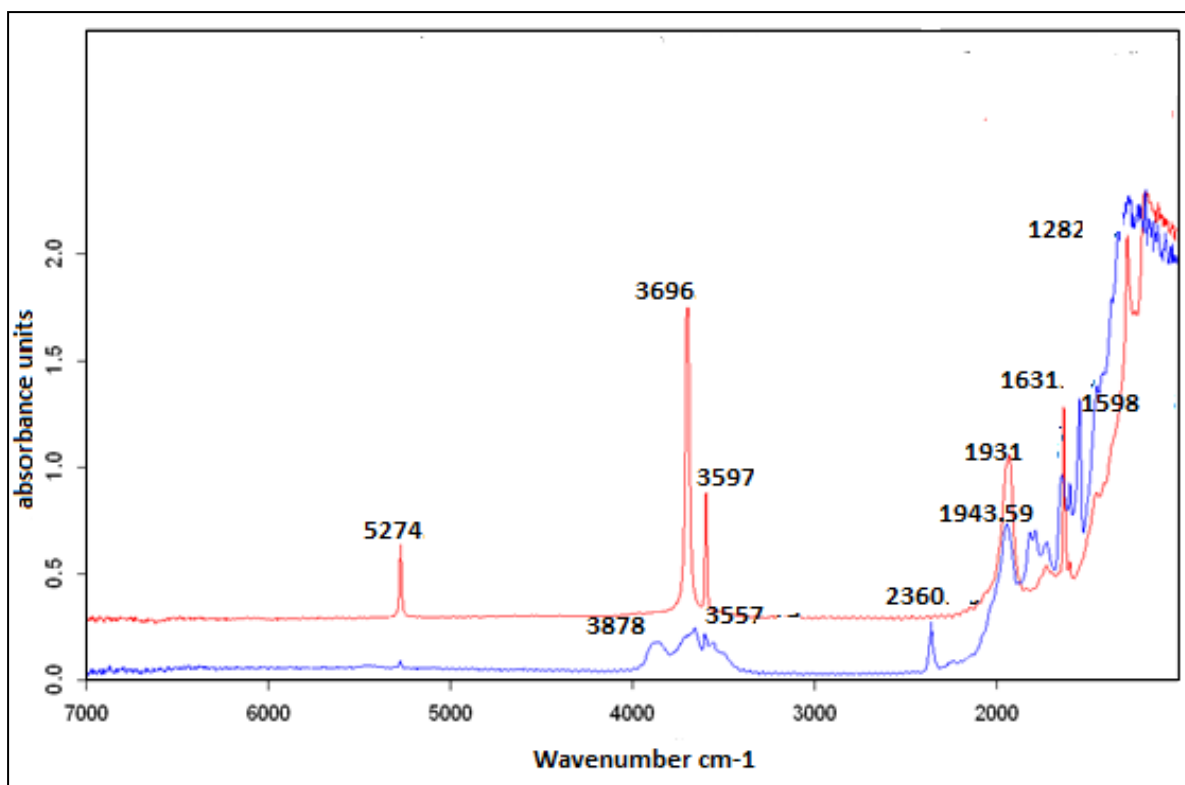


Fig. 3.6.12 Polarised IR spectra of PAY-3 single crystal from  $1000\text{ cm}^{-1}$  to  $7000\text{ cm}^{-1}$ . Blue line indicates  $E \perp c$  and red one, indicates  $E \parallel c$ .

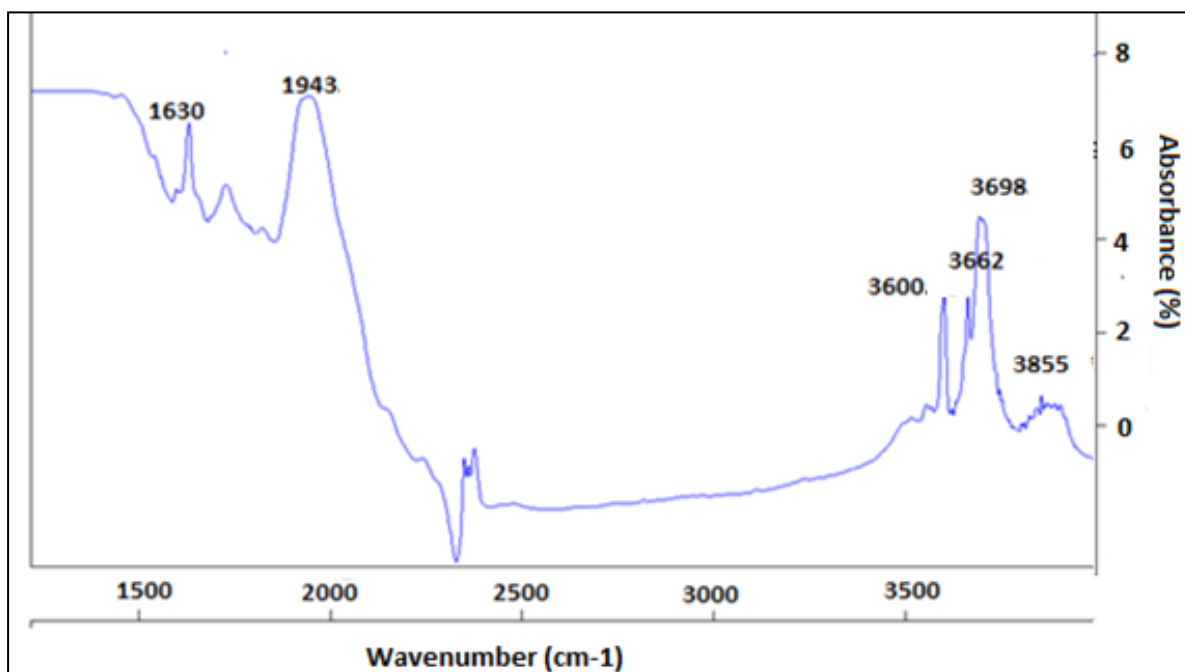


Fig. 3.6.13 IR spectra of BA-1 single crystal under unpolarised light from  $1000\text{ cm}^{-1}$  to  $4000\text{ cm}^{-1}$ .

**3.7 Raman spectroscopic studies:** The Raman spectra below show different polarisations of some important bands of beryl. When the electric vector is parallel to c-axis, two strong bands are distinctly visible around  $1066\text{ cm}^{-1}$  and  $686\text{ cm}^{-1}$  and two bands of weaker intensity are seen around  $324\text{ cm}^{-1}$  and  $396\text{ cm}^{-1}$  (Fig. 3.7.1, 2). In FH-3, apart from these four bands, broad shoulders are developed around  $788\text{ cm}^{-1}$ ,  $871\text{ cm}^{-1}$  and  $981\text{ cm}^{-1}$  (Fig. 3.7.2). The intensities of the bands at  $324\text{ cm}^{-1}$  and  $396\text{ cm}^{-1}$  are almost equal under  $E||c$  orientation. The spectra of PA-2 and PAD-8 under  $E\perp c$  orientation, the intensity of bands at  $324\text{ cm}^{-1}$  and  $1066\text{ cm}^{-1}$  reduces drastically (Fig. 3.7.3, 4). Additional bands are visible at  $424\text{ cm}^{-1}$ ,  $444\text{ cm}^{-1}$  and  $1243\text{ cm}^{-1}$  under this orientation. A weak band which is seen at  $1004\text{ cm}^{-1}$  in PAD-8 is observed at  $998\text{ cm}^{-1}$  in PA-2.

Raman spectra in the range  $3500\text{ cm}^{-1}$  to  $3700\text{ cm}^{-1}$  show only one band in most of the samples (Fig. 3.7.5). In PAD-8 with medium alkali content, a small band appears at  $3597\text{ cm}^{-1}$  and  $3608\text{ cm}^{-1}$ . The band position is at the same frequency in all the samples.  $E\perp c$  orientation of PA-2 and PAD-8 show the presence of a peak around  $1240\text{ cm}^{-1}$  (Fig. 3.7.3, 4).

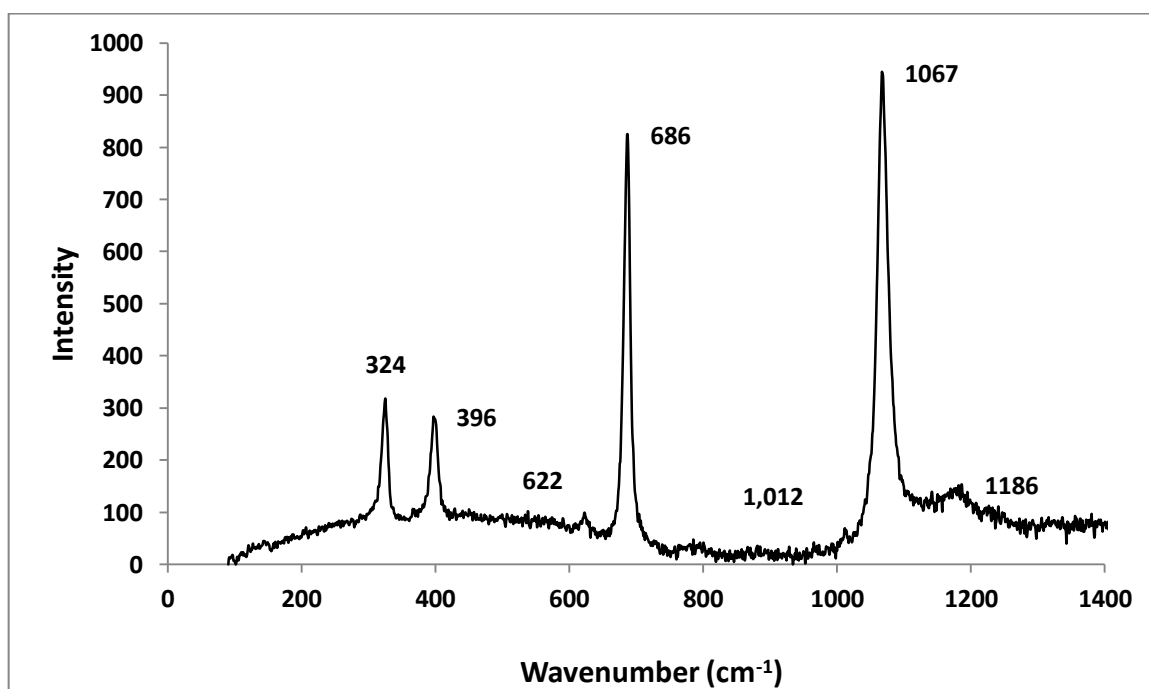


Fig. 3.7.1 Raman spectrum of alkali rich beryl BAA-1 ( $E||c$ ).

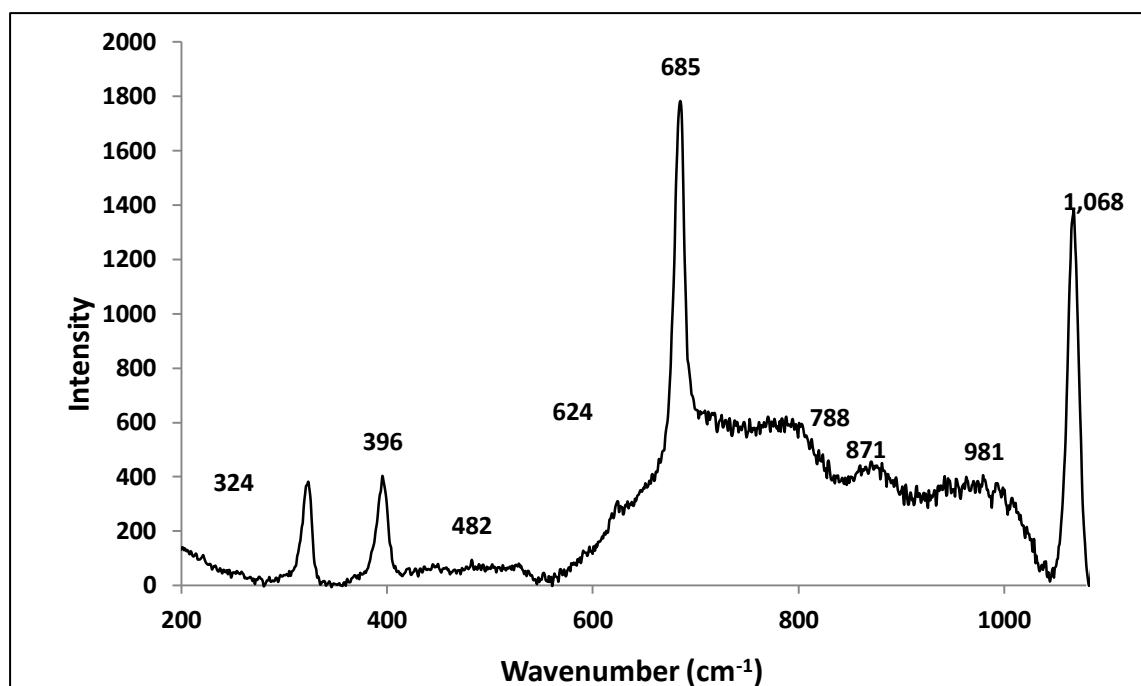


Fig. 3.7.2 Raman spectrum of FH-3 (E||c).

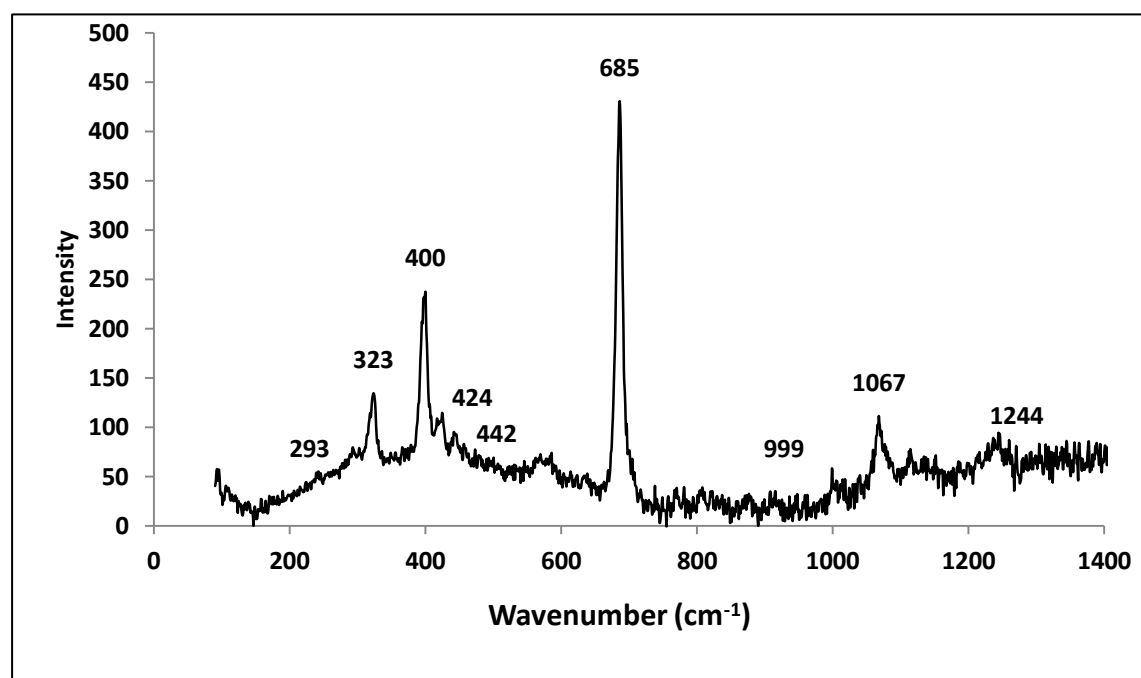


Fig. 3.7.3 Raman spectrum of PA-2 (E⊥c).

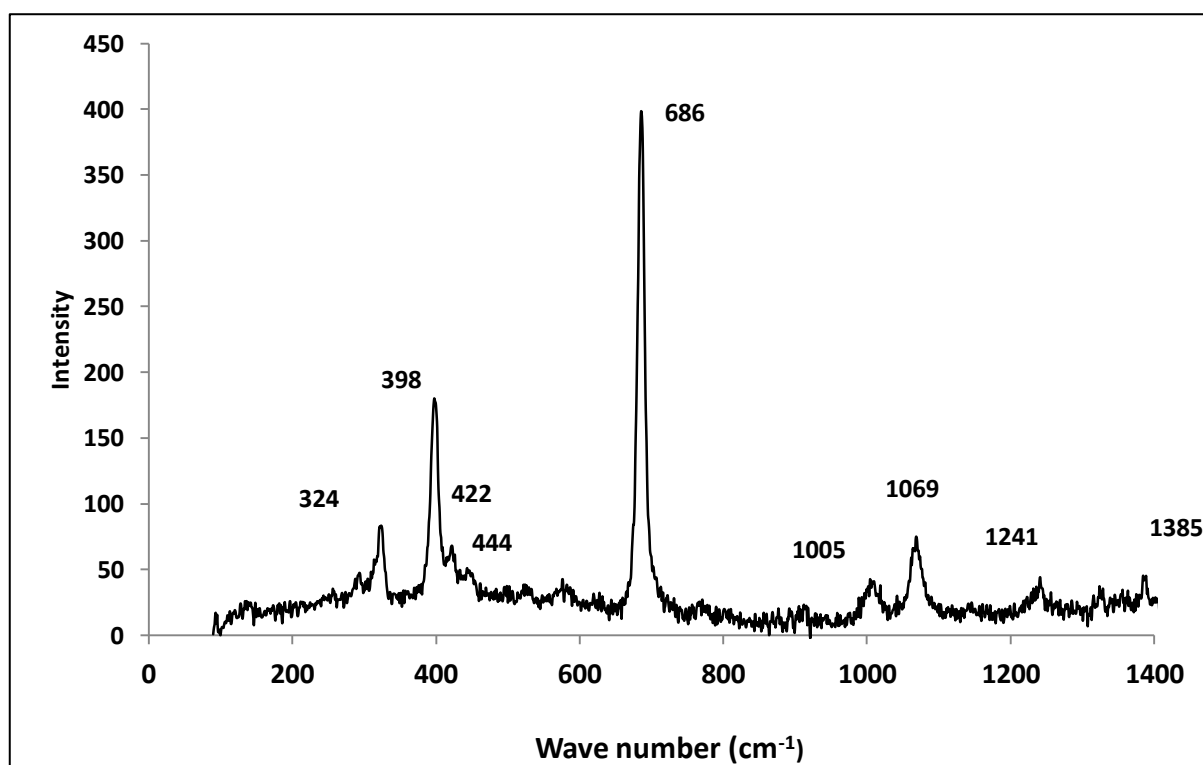


Fig. 3.7.4 Raman spectrum of PAD-8 (E.L c).

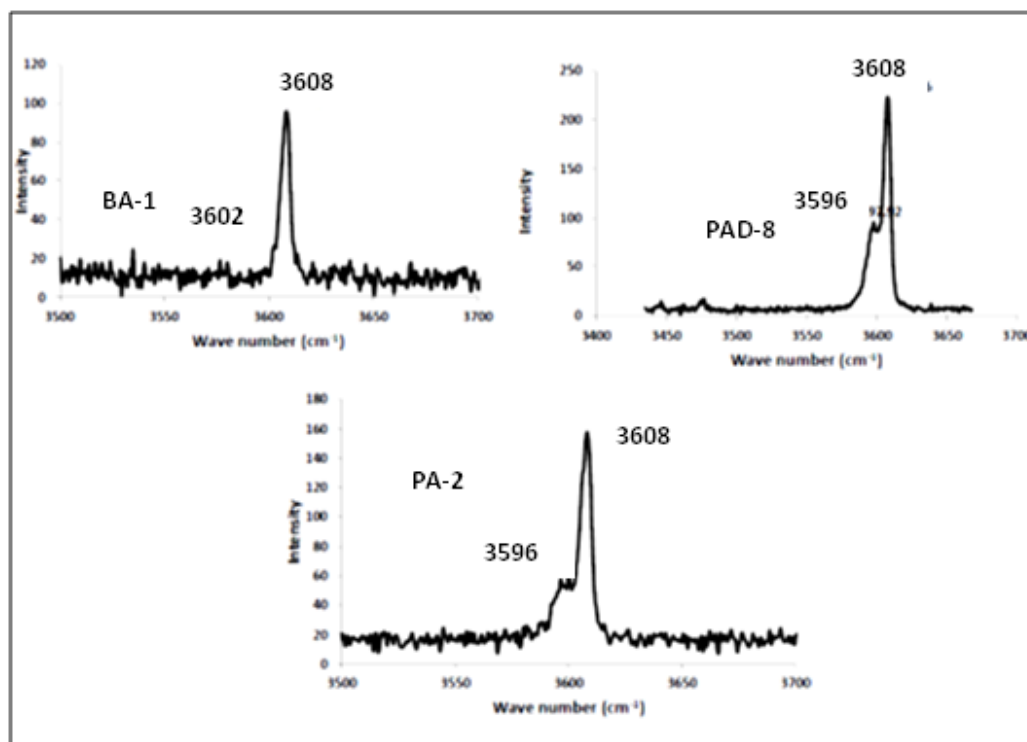


Fig. 3.7.5 Raman spectra of BA-1, PA-2 and PAD-8 in the range from 3500-3700  $\text{cm}^{-1}$ .

**3.8 NIR Spectroscopic Studies:** When  $E \parallel c$ , NIR spectra in the range 1000 nm to 2200 nm show two prominent bands; one around 1400 nm and other around 1895 nm. A small shoulder appears at 1409 nm in BAA-1 (Fig. 3.8.1) and it becomes stronger but splits in to two bands in BAA-2 and CA-1(Fig. 3.8.2, 3). In BAA-2, the band around 1410 nm is less intense than at 1399 nm whereas in CA-1, the band at 1410 nm becomes stronger than 1399 nm. Other bands which are weaker, are around 1148 nm, 1373 nm and 1466 nm. The spectrum of BAA-1 shows two shoulders at 1843 nm and 1794 nm. BAA-2 shows one band and CA-1 has a small shoulder at 1786 nm (Fig. 3.8.2,3).

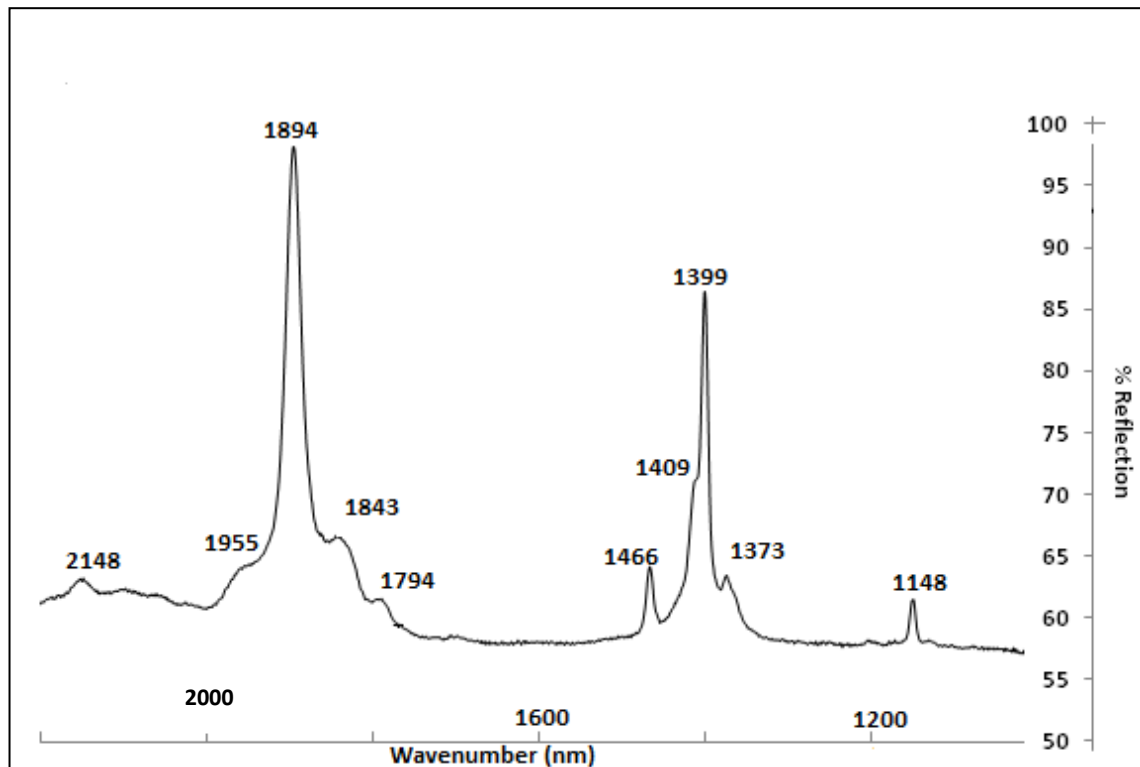


Fig. 3.8.1 NIR spectrum of BAA-1 from 1000 nm to 2200 nm.

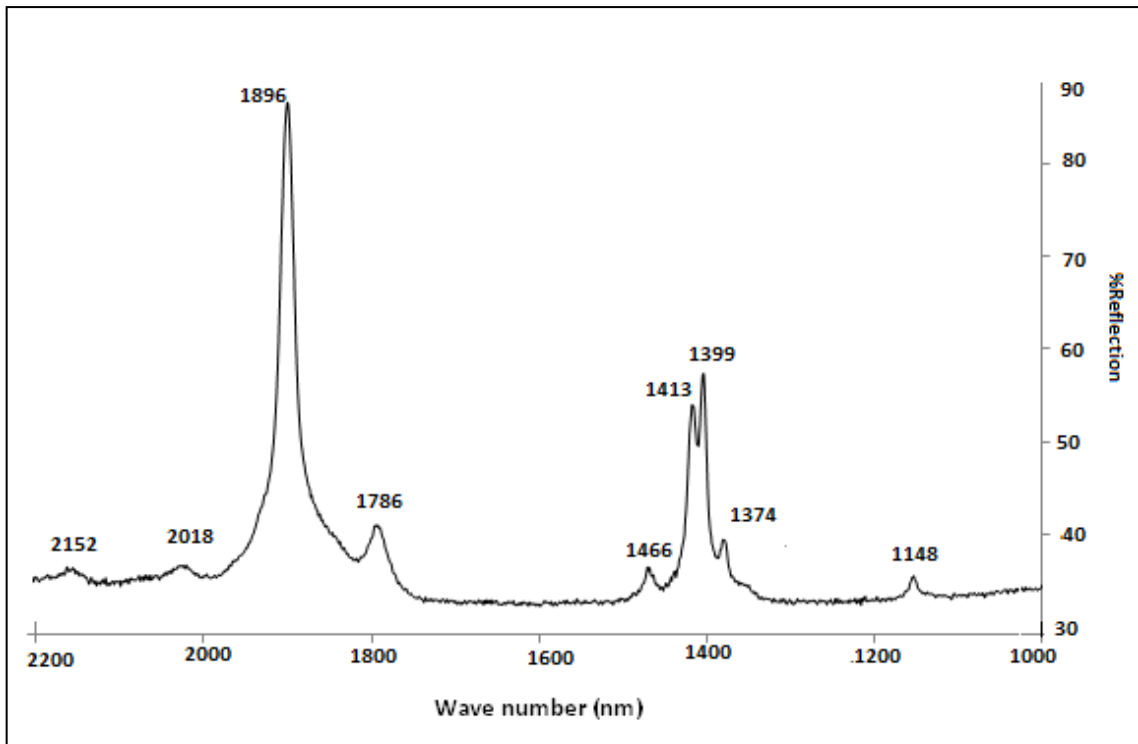


Fig. 3.8.2 NIR spectrum of BAA-2 in the range from 1000 nm to 2200 nm.

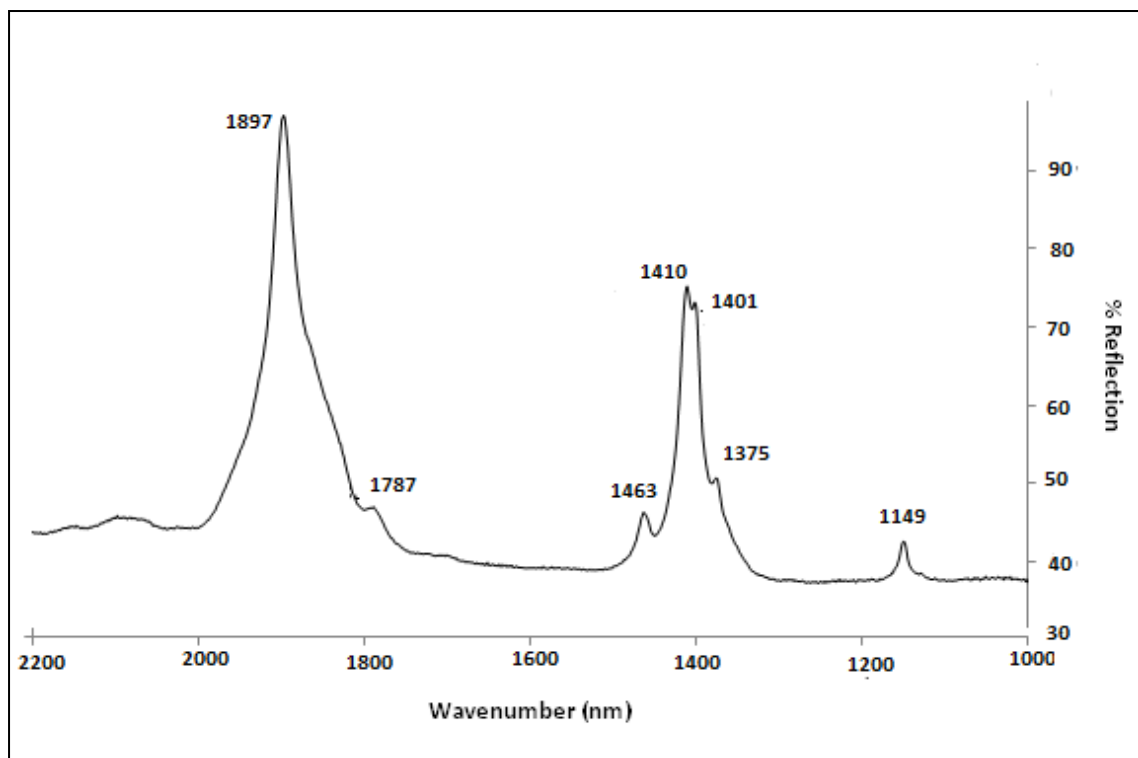


Fig. 3.8.3 NIR spectrum of CA-1 from 1000 nm to 2200 nm.

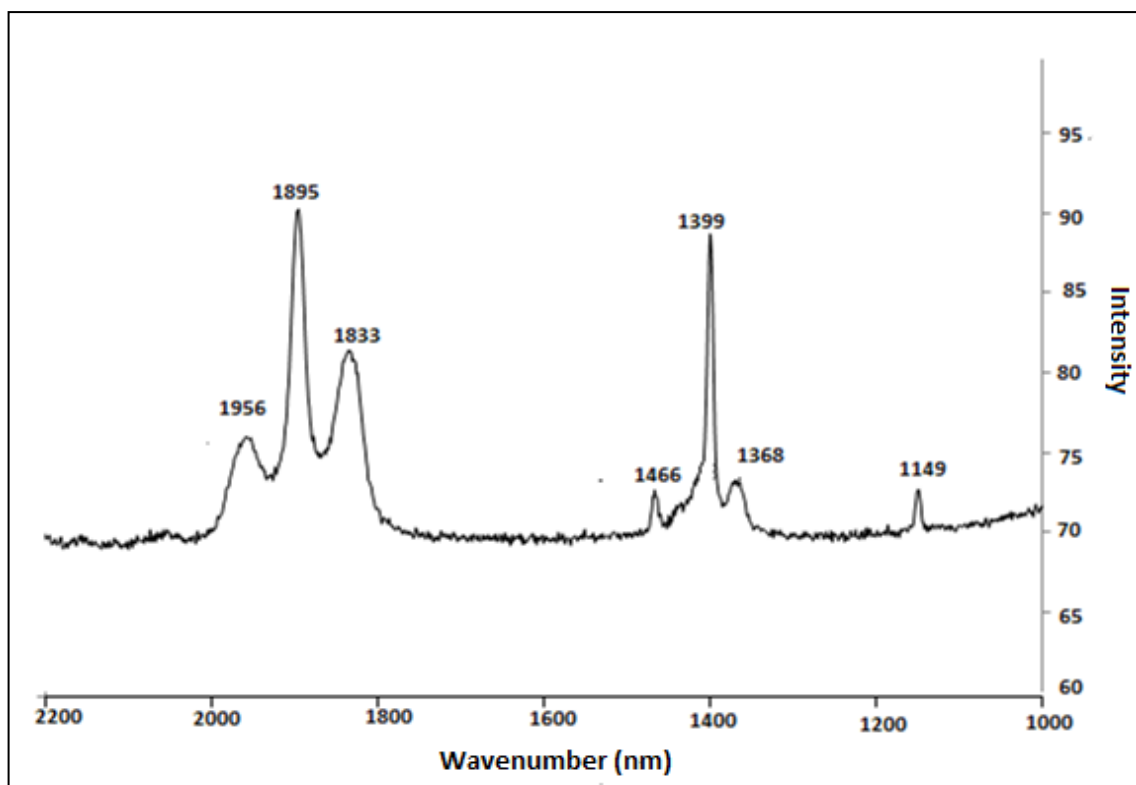


Fig. 3.8.4 NIR spectrum of PAD-1 (Transmission method) under E $\perp$ c orientation.

In Fig. 3.8.4, two extra bands are visible at 1833 nm and 1956 nm around the main band 1895 nm which are not seen in the spectra under unpolarised light in reflection method.

### 3.9 Scanning Electron Microscopic investigations:

#### 3.9.1. General description of SEM images:

**Basal pinacoid {0001}**: Basal pinacoids are characterised by the presence of hexagonally shaped etch pits. Some etch pits have a pointed base with inclined and steep faces (Fig. 3.9.1). Others are hollow where the bottom is not visible but with very steep faces almost perpendicular to {0001} (BA-1, BAA-1, Fig. 3.9.3, 4). These etch pits are characterised by the presence of flaky materials. Composition (see inset in Fig. 3.9.1; K-Al-Si) and shape indicate that they could be muscovitic mica. Apart from hexagonally shaped, triangular shaped hollow cores are also visible on the base of BA-1 (Fig. 3.9.5 a, b). In triangular shaped hollow cores, Fig. 3.9.5a shows that corners are sharper than in Fig. 3.9.5b. In BA-1, some hollow cores are filled with crumbling material; shape and composition indicate a clay mineral (Fig. 3.9.3c). A large number of hexagonally (irregular outline) to circular shaped etch pits are concentrated along the growth spirals (Fig. 3.9.2 a, b, c). There are sporadic occurrences of perfect hexagonal shaped etch pits on the base, in which one is filled with clay (Fig. 3.9.3a, c). Two samples have hexagonal hollow cores on their basal pinacoid (both from Minas Gerais, Brazil).

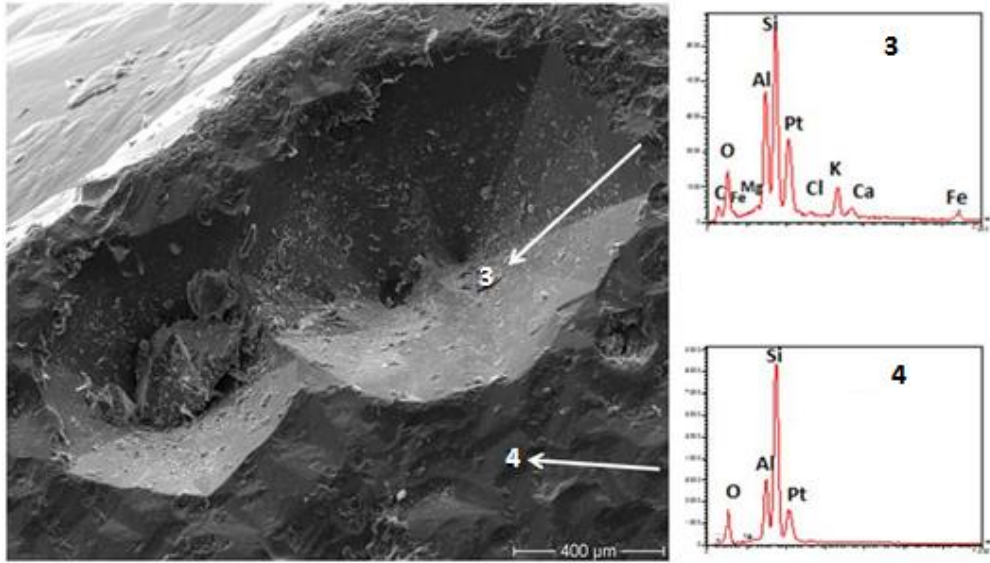


Fig. 3.9.1 SEM image of hexagonal etch pits with pointed base on  $\{0001\}$  of PA-2 from Shigar valley, Himalayas with the EDS of materials inside. Nos 3 and 4 in the figure indicate sites for EDS spectra. The spectrum of the flaky material (probably mica) inside the etch pit (No. 3) differs in composition from that of pure beryl (No. 4). A small amount of C and Ca (indicating  $\text{CaCO}_3$ ) are also present in the particle. Pt peak is due to the coating material.

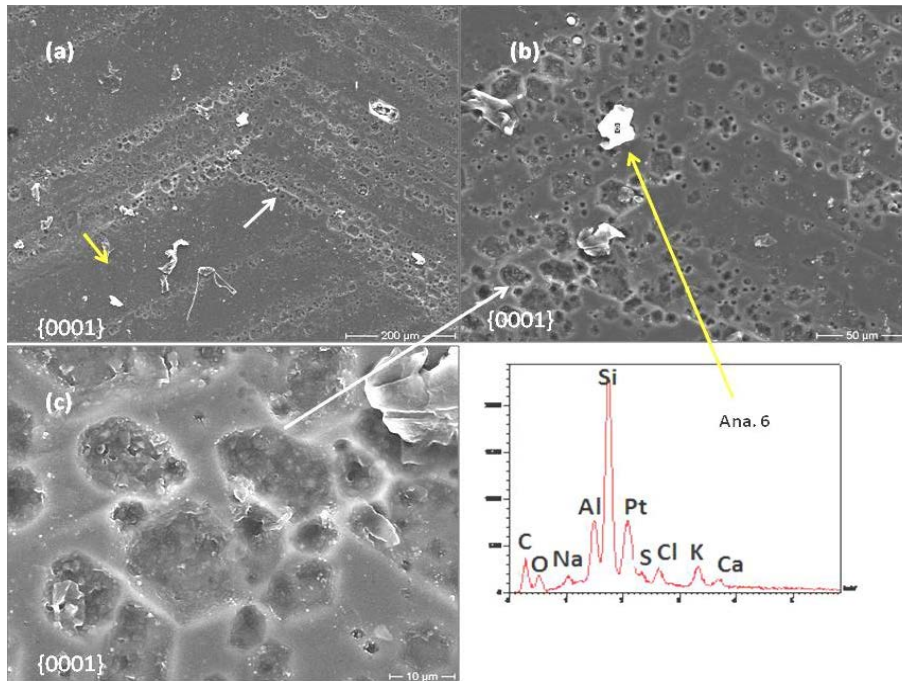


Fig. 3.9.2 SEM image of basal pinacoid  $\{0001\}$  of BA-1 from Minas Gerais, Brazil. (a) Concentration of flat bottomed, irregular to circular shaped etch pits along growth spirals (white arrows) and areas with less etch pit density (yellow arrow). (b) Magnified image of (a). (c) Enlargement of etch pits concentrated along the spirals in images (b) and (a).

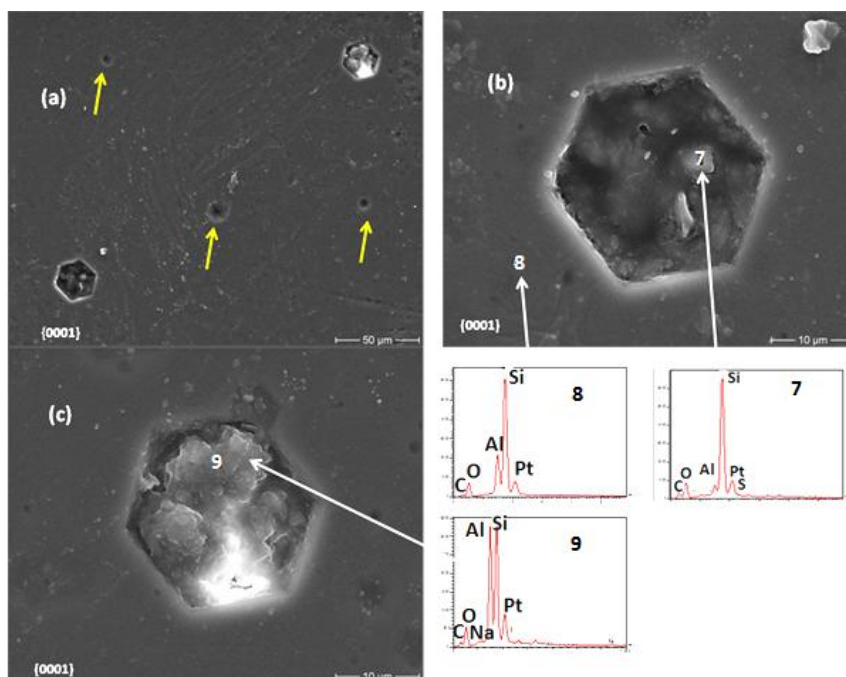


Fig. 3.9.3 SEM images of hollow cores on the basal pinacoid {0001} of BA-1. (a) Overview of hollow cores. Yellow arrows point to less developed etch pits giving an appearance of circular shape. (b) Enlarged part of (a), lower left: Hexagonal hollow core with the dissolution products. No. 7 indicates that the material inside the hollow core slightly differs by having less amount of Al from the composition of pure beryl (No. 8). (c) Enlarged part of (a), upper right: Analysis. 9 indicate a clay mineral.

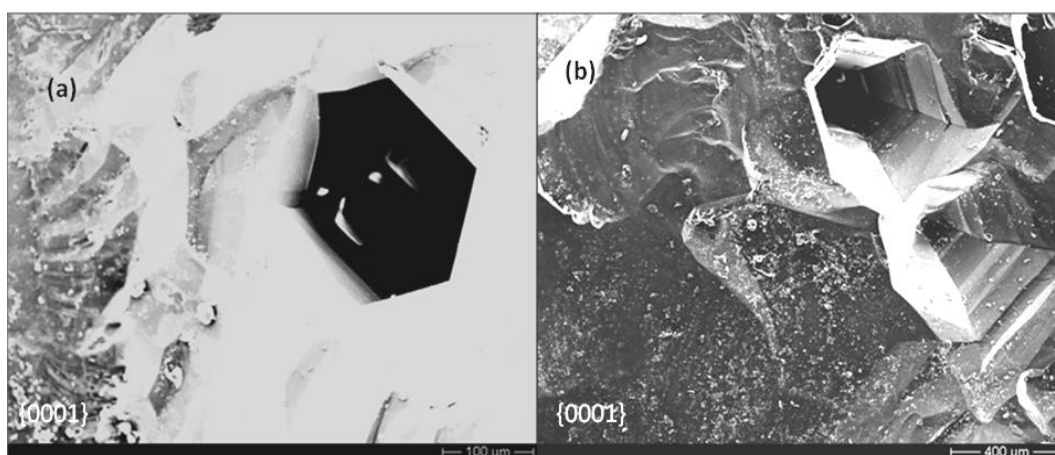


Fig. 3.9.4 SEM image of basal pinacoid {0001} of BAA-1 from Minas Gerais, Brazil. (a) Hexagonally shaped hollow core with steep walls. (b) Two kinds of etch pits, one with steep walls and a flat base (upper part; the base is not clearly visible, it could be hollow); the other one with steep but stepped walls and a pointed base (lower right).

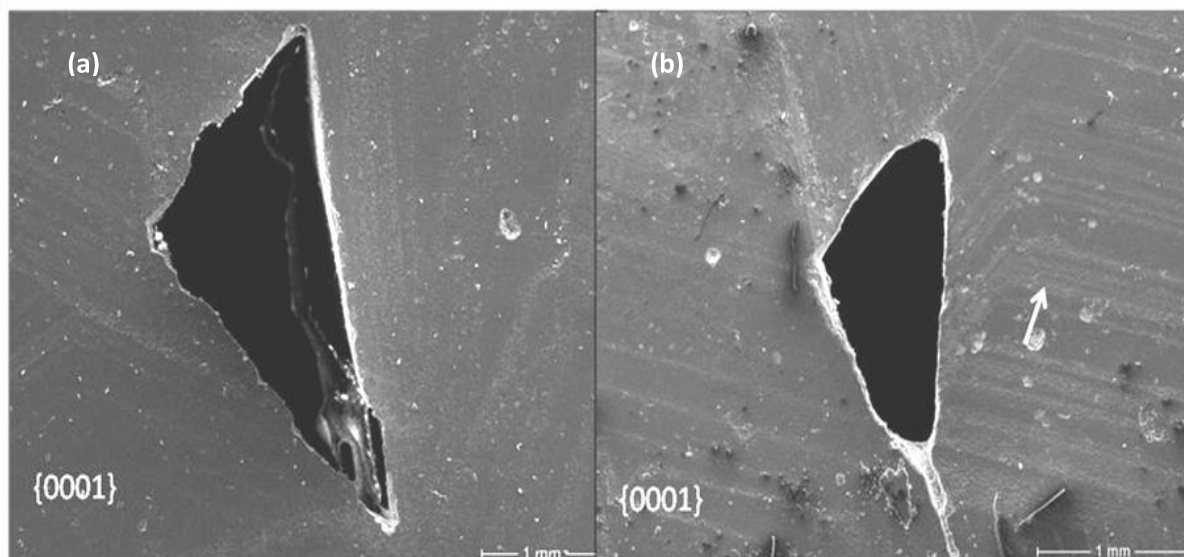


Fig. 3.9.5 Growth spirals (white arrow) and triangular shaped hollow cores on the base  $\{0001\}$  of BA-1 (Minas Gerais, Brazil). In (a) the corners of hollow core are sharper than in (b).

**Prism of first order  $\{10\bar{1}0\}$ :** Trapezoidal to nearly rectangular shaped etch pits oriented with their long axes perpendicular to the crystal's c-axis are observed. Four types of etch pits are visible on the prism face. 1) Deep etch pits with steep walls and square to pointed bottoms (P-type etch pit- Fig. 3.9.6, 7b, 8b, 9a, 10a); 2) shallow etch pits with flat rectangular bases (F-type etch pit- Fig. 3.9.6, 7c); 3) etch pits with steps (Stepped- Fig. 3.9.7a) and (4) canoe shaped etch pits with their long axes perpendicular to c-axis (Fig. 3.9.7c,d, 11). These etch pits are even visible in the already existing rectangular etch pits. Etch pits belonging to first three categories have an approximately rectangular geometrical shape. In Fig. 3.9.11, smaller canoe shaped etch pits are visible in large one giving a stepped appearance as in the third category of rectangular etch pits with steps.

Long edges of the etch pits are straight and short edges are curved and parallel to c-axis. This was observed on all the samples (Fig. 3.9.7a, b, 8b). The P-type etch pits on the sample from Lumäki, Finland are approximately rectangular and all four faces meet at the bottom along a line, instead of a point or flat base, resulting in two trapezoidal and two triangular faces in the etch pit bottom (Fig. 3.9.8). In some samples, the etch pits have merged together extending some area of crystal surface (Fig. 3.9.10b) and in some, smaller pits are found on the bases of larger pits (Fig. 3.9.8b). First order prism faces of PAY-1 shows etch pits with four long edges and two parallel short edges giving rhombus to diamond shaped (3.9.12a). In some places, these short edges become pointed (3.9.12a). Here these etch pits can also be grouped into two. The first one is deep with steep walls meeting at a point in the bottom and the second one has shallow and flat bottom as observed in BA-1. Fig. 3.9.13 demonstrates the etch pits on the sample CA-1 from Sichuan Province, China. Here, though etch pits are of rectangular shape, they are more elongated than those from other

provinces. Long edges are straight and short edges are curved. In some places, they join together in a line as in 3.9.13a and d. Chemical analysis of the materials inside the etch pit show that it is rich in K, Cl, C, Na with some amount of Ca and S (Fig. 3.9.9, ana. 12).

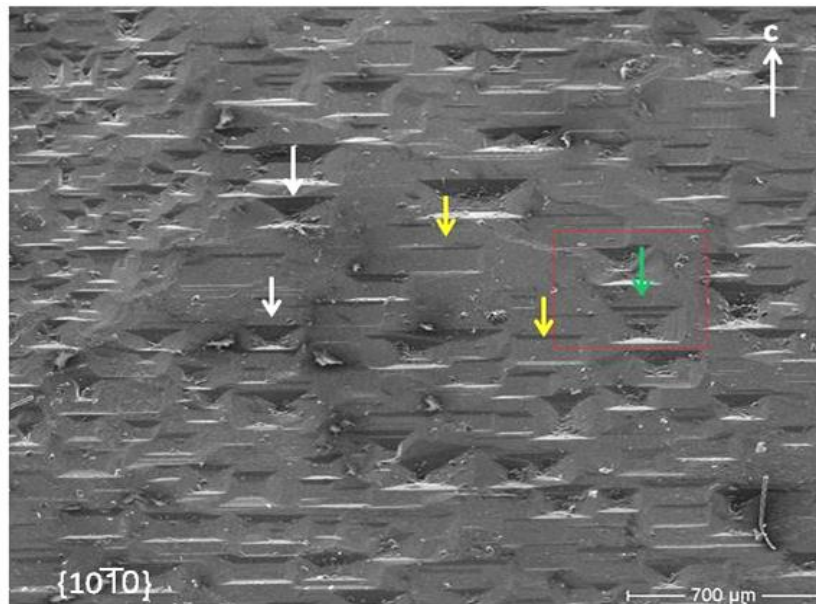


Fig. 3.9.6 Overview of prism face  $\{10\bar{1}0\}$  of BA-1 from Minas Gerais, Brazil with different kinds of etch pits. P-type etch pits (white arrow). Yellow arrows indicate F-type etch pits. Etch pits with steps is shown by green arrow.

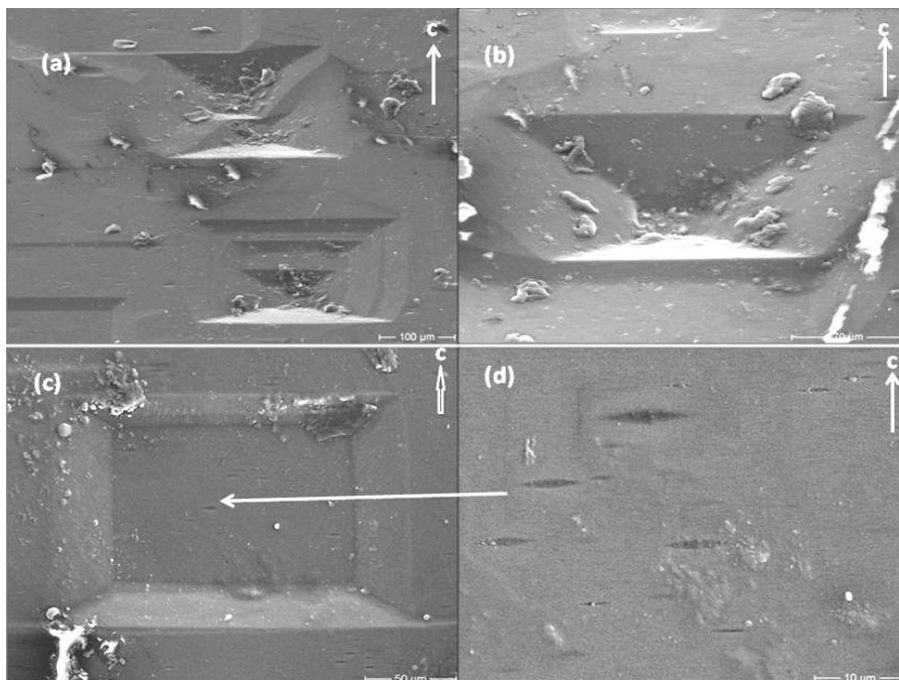


Fig. 3.9.7 Enlarged view of different kinds of etch pits on BA-1. (a) Etch pits with steps. (b) P-type etch pit. (c) F-type etch pit. (d) Higher magnification of canoe shaped etch pits in F-type etch pits.

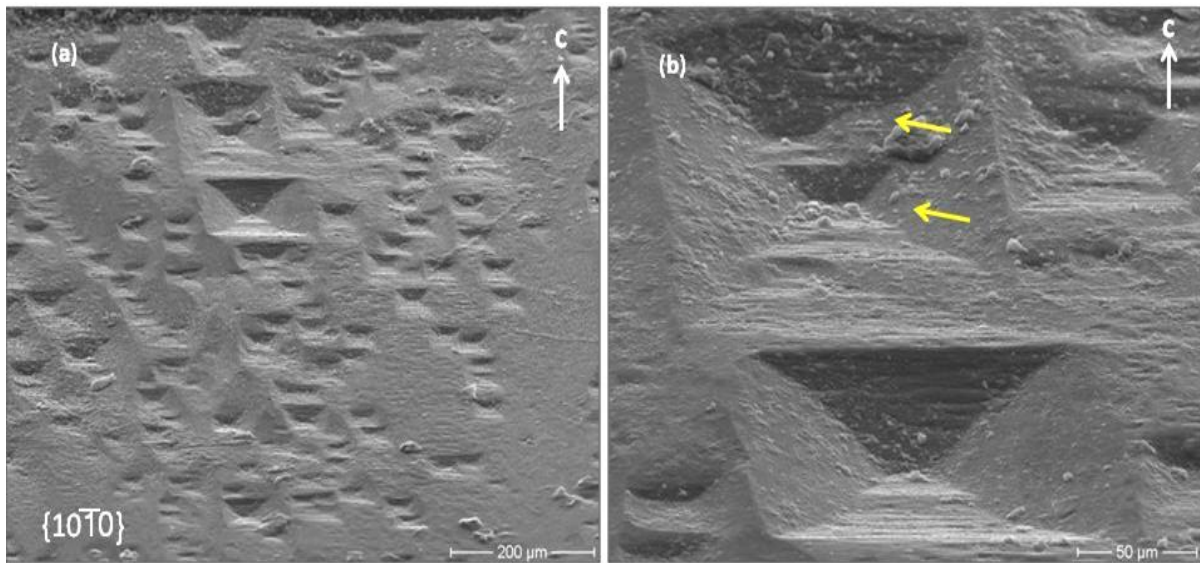


Fig. 3.9.8 SEM image of prism face of FH-3 (Lumäki pegmatites, Finland). (a) Overview. (b) P-type etch pits. Yellow arrows point to small etch pits in a larger etch pit.

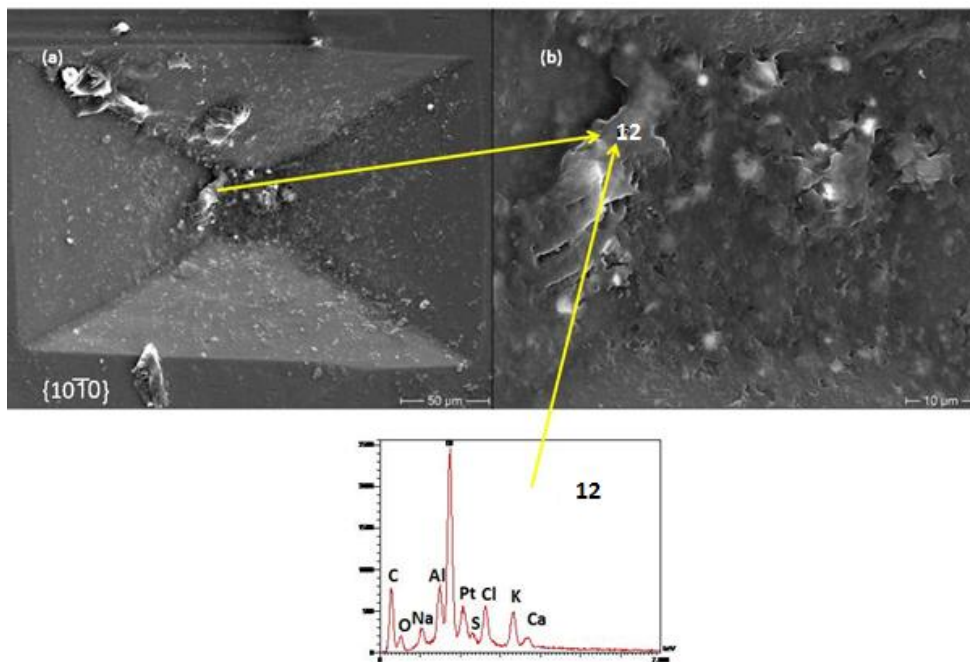


Fig. 3.9.9 SEM image of P-type etch pit with straight edges in BA-1. (b) Magnification of (a) with EDS spectra.

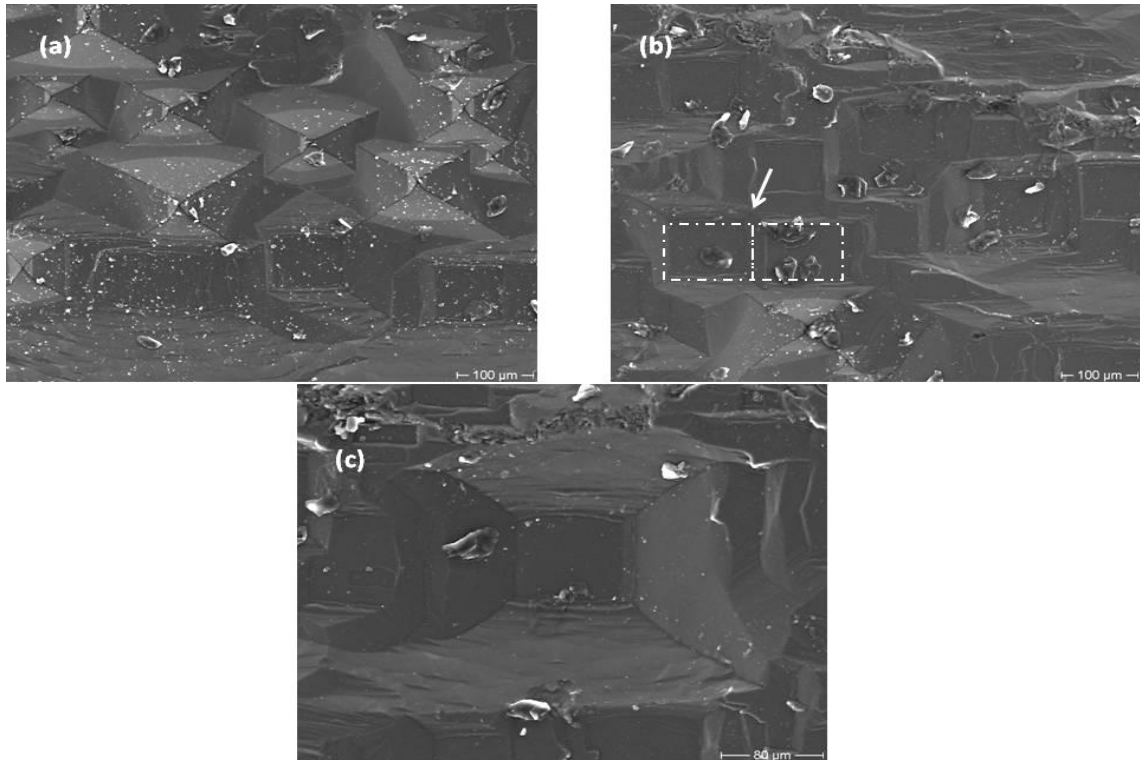


Fig. 3.9.10 SEM images of prism face of PA-2. (a) P-type and F-type etch pits. (b) Larger view of F-type etch pits. Dashed lines represent boundary of etch pits and arrow indicates the line of merge. Flaky materials are products of dissolution inside the etch pits (not analysed). (c) Magnified image of one of the etch pits with square bottom and sharp boundary.

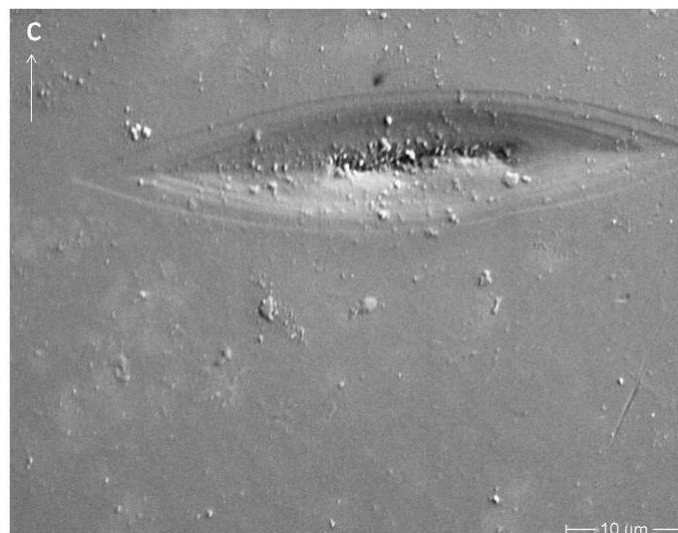


Fig. 3.9.11 Stepped Canoe shaped etch pit on the prism face of PAD-10 (Dassu mines, Himalayas).

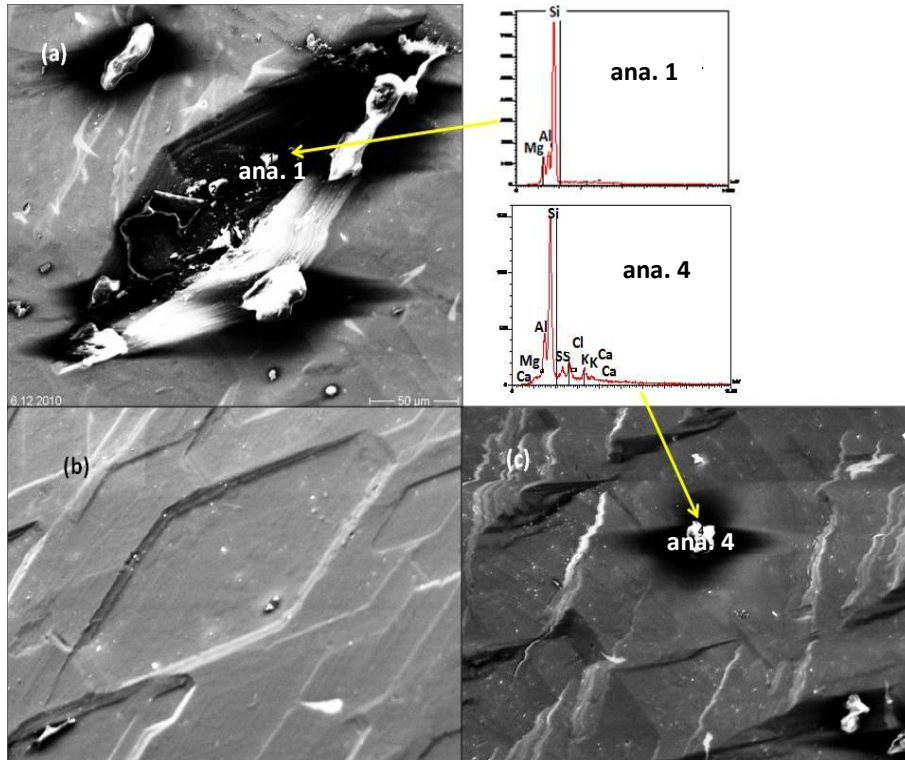


Fig. 3.9.12 Prism face of PAY-1 (Yuno village, Himalayas). (a) Rhombus shaped P- type etch pit. EDS spectra shows a slight enrichment of Mg in this etch pit. (b) Rhombus to elongated hexagonal shaped F-type etch pits (c) Merging of F-type etch pits. Ana. 4 shows small amount of K and S.

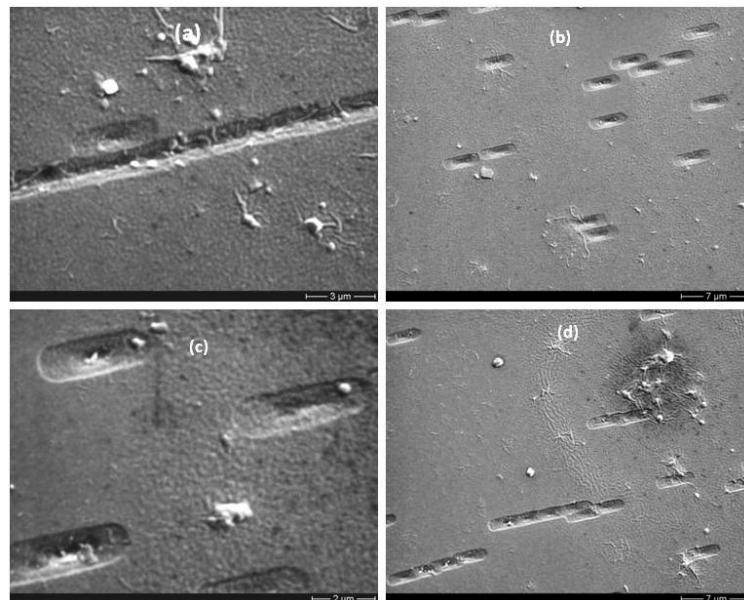


Fig. 3.9.13 Etch pits on the prism face of CA-1 from Sichuan Province, China. (a) Etch pits join together along a line. (b) P-type etch pits. (c) Magnification of image (b). (d) Etch pits join along a line.

**Prism of second order  $\{11\bar{2}0\}$ :** BA-1 from Minas Gerais, Brazil has been investigated to study etch pits on  $\{11\bar{2}0\}$ . This face is distinguished by the presence of canoe shaped etch pits with their long axes parallel to c-axis (Fig.3.9.14). Only this sample is found to be characterised by etch pits on this face. In rest of the samples, etch pits are not discernable.

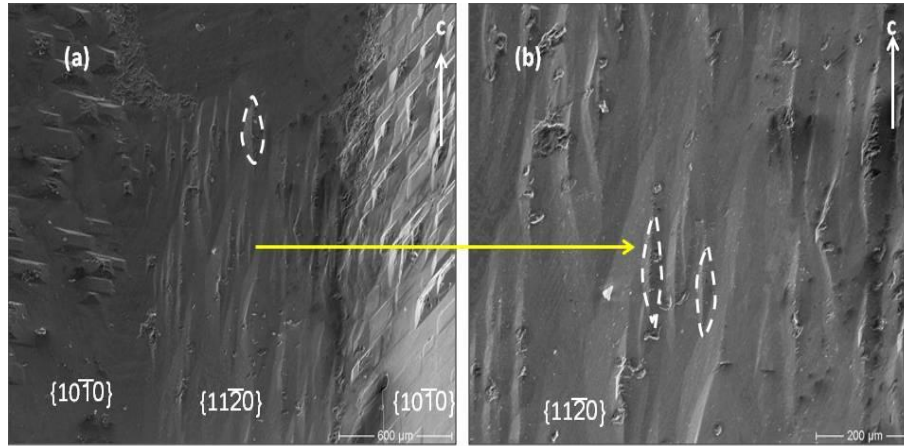


Fig. 3.9.14 SEM images of first and second order prism faces in BA-1. (a) Transition of faces  $\{10\bar{1}0\}$  and  $\{11\bar{2}0\}$  in BA-1. (b) Magnification of  $\{11\bar{2}0\}$  face. Dashed lines represent boundary of canoe shaped etch pits.

**Inner prism face of BA-1 at hollow core (BA-1b):** Since hollow core was found in BA-1, a small piece (BA-1b) was cut parallel to c-axis and subjected to SEM investigation. EDS spectra of the flakes on the prism face indicate the presence of newly precipitated beryl crystals as they have the same ratio of Si-Al as in normal beryl without any other element (Fig. 3.9.15, ana.1 & 2). Ana. 3 shows the flaky material is rich in K, Al, Si, Fe, and C with small amount of Ca. On the same face, canoe shaped structures with their long axes perpendicular to c-axis are detectable (Fig. 3.9.16).

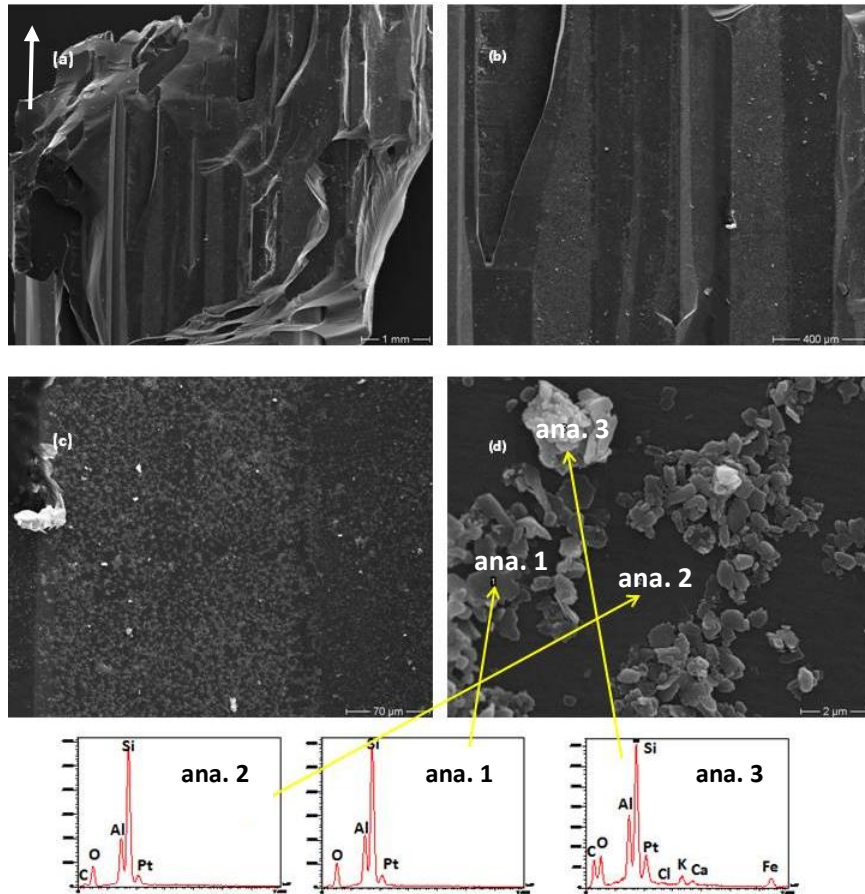


Fig. 3.9.15 Images of piece of BA-1 crystal from the inner side of the hollow core. (a) Overview of the crystal; white arrow indicates direction of c-axis. (b,c) Magnifications of image (a). (d) Higher magnification of image (c) with EDS spectra. Ana. 1 shows the composition of the flaky crystals are similar to that of ana. 2 indicating newly formed beryl crystals on the surface. Ana. 3 shows the enrichment of C, K and Fe with little Ca along with Si and Al in normal ratio found in beryl.

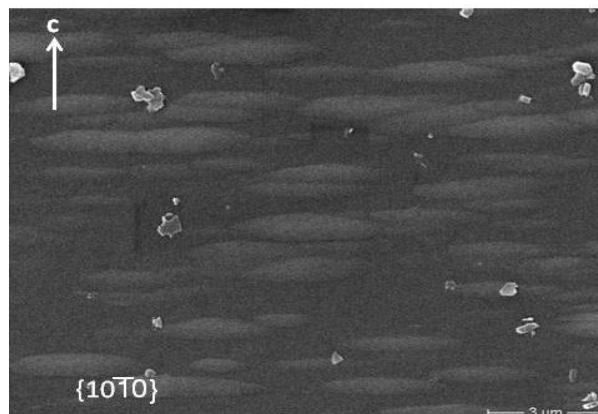


Fig. 3.9.16 Canoe shaped structures oriented perpendicular to c-axis on the inner prism face of hollow beryl (BA-1b).

**Pyramid  $\{10\bar{1}1\}$ :** Fig. 3.9.17 demonstrates an overview of transition from basal pinacoid  $\{0001\}$ , pyramid of second order  $\{11\bar{2}2\}$  and pyramid of first order  $\{10\bar{1}1\}$  in BA-1. On  $\{0001\}$ , the etch pits are concentrated along growth spirals and an etch pit free zone is found in between these spirals.

Triangular shaped etch pits are perceptible on pyramid of first order. Two kinds of etch pits are visible on this face. Some are triangles with flat and shallow triangular base while others are deeper with the quadrilateral base with equal adjacent sides giving kite shaped appearance (Fig. 3.9.18 a, b). Triangular shaped raised structures can be seen oriented in the opposite direction of etch pits (Fig. 3.9.18a).

Pyramid of second order  $\{11\bar{2}2\}$  is characterised by the presence of trapezoidal etch pits with steps (Fig. 3.9.18c, d). The longer side of the trapezium is found to be facing the base (Fig. 3.9.17, 18,d). The etch pits are densely populated along the edges in 3.9.19.

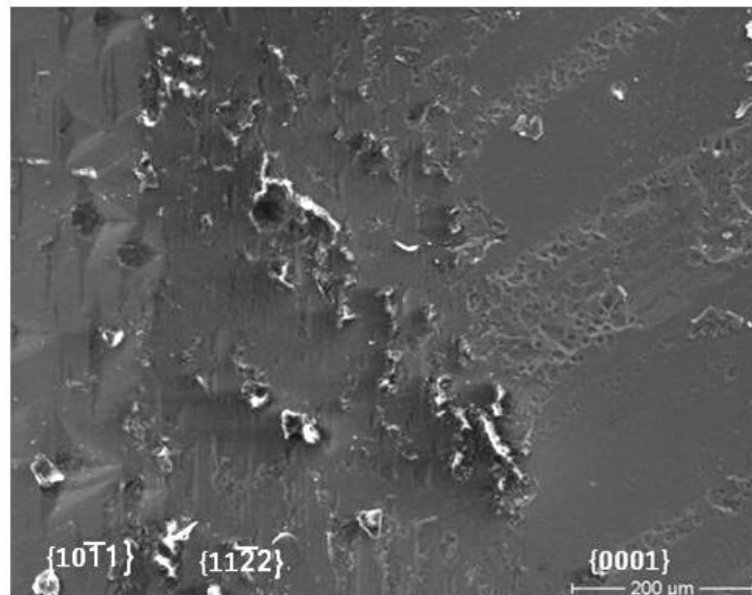


Fig. 3.9.17 Transition from basal pinacoid  $\{0001\}$ , pyramid of second order  $\{11\bar{2}2\}$  and pyramid of first order  $\{10\bar{1}1\}$  in BA-1.

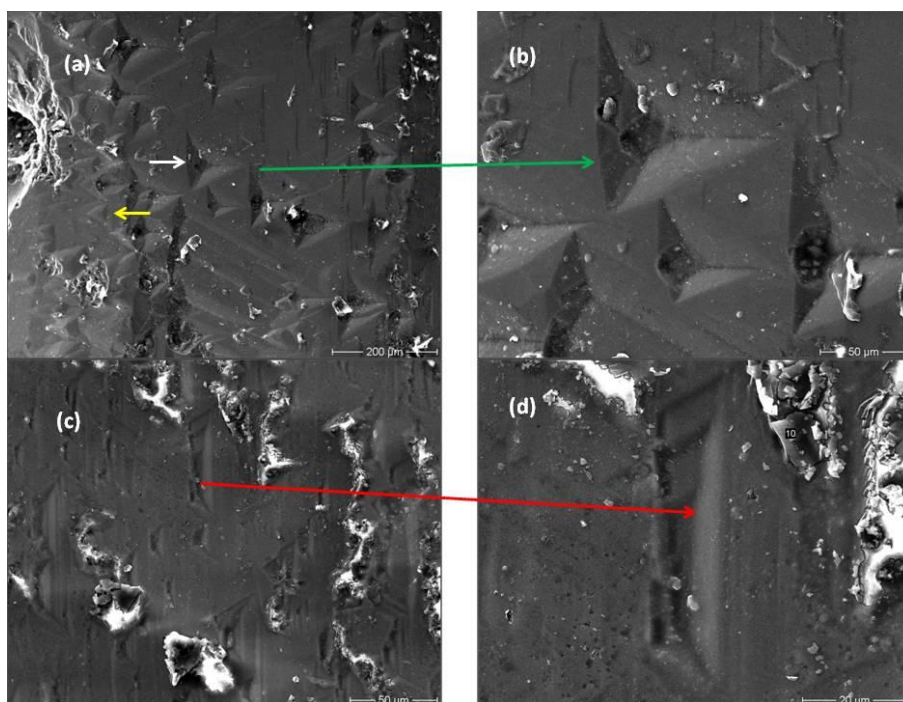


Fig. 3.9.18 SEM images of pyramid of first and second order faces of BA-1. (a) Enlarged image of Fig. 3.9.17. Triangular shaped etch pits (white arrow) and growth structures (yellow arrow) oppositely oriented on the pyramid of  $\{10\bar{1}1\}$  in BA-1 crystal (b) Higher magnification of  $\{10\bar{1}1\}$ . The bottom of the etch pit has a quadrilateral shape. (c) Trapezoidal etch pits with steps on  $\{11\bar{2}2\}$ . The longer edge of the trapezium is parallel to the edges of base and facing towards the base.

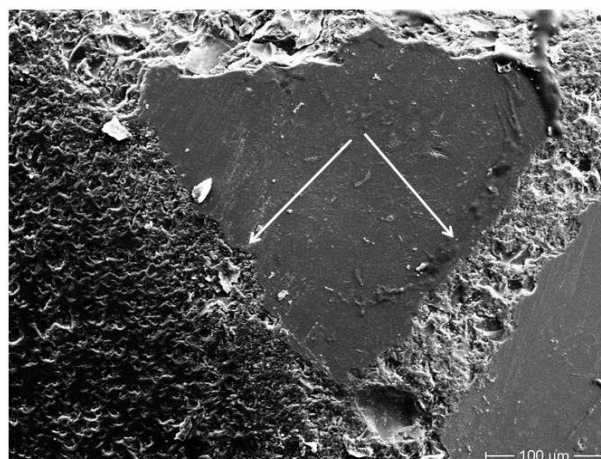


Fig. 3.9.19 Pyramidal face of PAD-9. Concentration of etch pits along the edges and faces are almost devoid of etch pits.

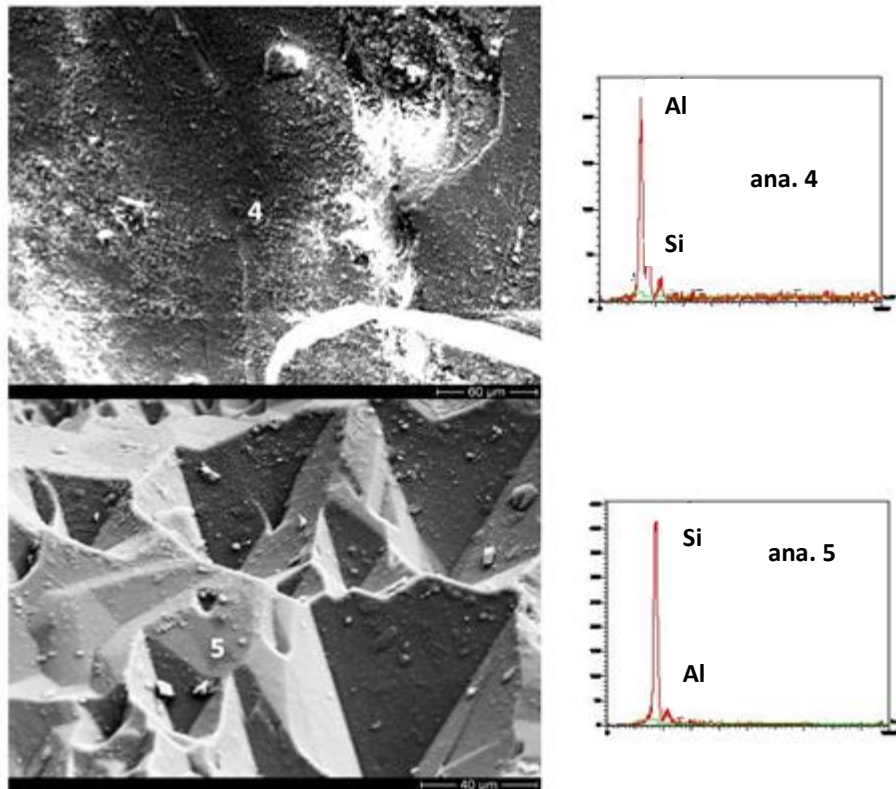


Fig. 3.9.20 SE images of sample BAA-2 from Minas Gerais, Brazil. Different parts of the sample show irregular Si and Al distribution.

### 3.9.2 SEM image analysis:

**Measurement of length of diagonals of etch pits:** Four etch pits on the prism face  $\{10\bar{1}0\}$  of BA-1 are selected for image analysis. The first stage was to determine the eccentricity of the etch pits by measuring the length of the diagonals.

The measurement of the sides' length of these etch pits indicate that two long edges are parallel to each other. They are of different lengths, which is the characteristic of trapezoid (Fig. 3.9.21). Geometrical reconstruction of a P-type etch pit shown in Fig. 3.9.22 point out that the legs are equal in length and parallel sides are not. We have found that diagonals are of equal length. Hence, this etch pit can be described as isosceles trapezoid. The etch pit shown in Fig. 3.9.23 has all sides of different length and of different angles. None of the sides are parallel indicating that it is just a quadrilateral or scalene trapezoid.

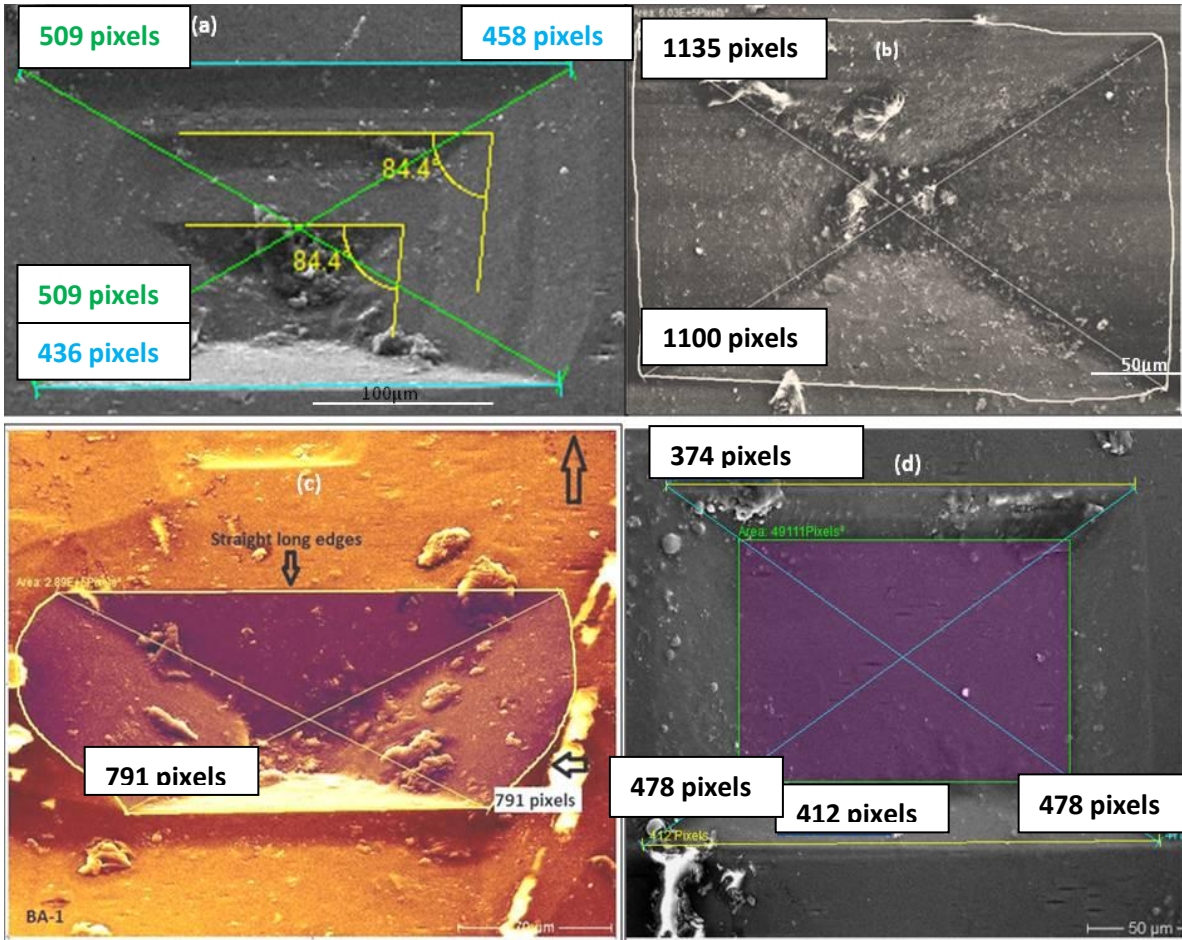


Fig. 3.9.21 SEM images of different etch pits on  $\{10\bar{1}0\}$  of BA-1 which are used to determine shape distribution, surface texture, fractal dimension and eccentricity by image analysis. (a) Stepped etch pit. Diagonals are of 509 pixels and are of the same length. Blue colour lines show the length of the edges. Upper one is 458 pixels and lower one is of 436 pixels. The edges of each step meet at an angle of  $84.4^\circ$ . (b) P-type etch pit. Here, diagonals are of different lengths (1135 pixels and 1105 pixels). (c) P-type etch pit. Short, curved edges are parallel to c-axis and diagonals are of same length (791 pixels). The length of the edges are not measured. From the figure, it is obvious that they are of unequal length. (d) F-type etch pit. Diagonals are of 478 pixels and opposite edges are of different lengths (374 pixels and 412 pixels).

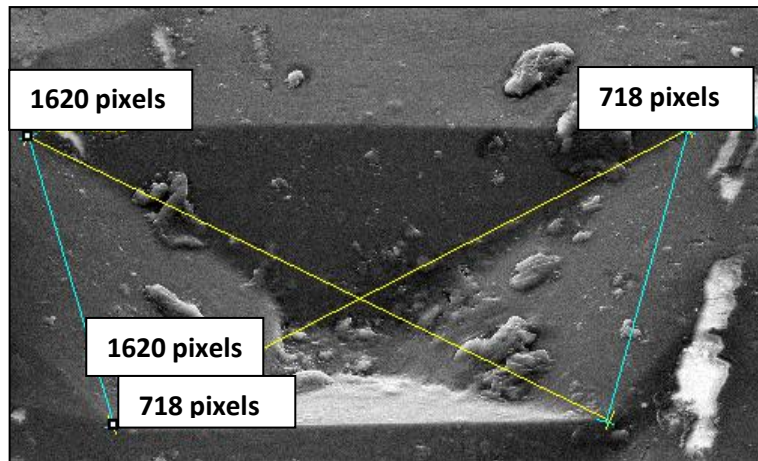


Fig. 3.9.22 Geometrical reconstruction of P-type etch pit on prism face of BA-1.

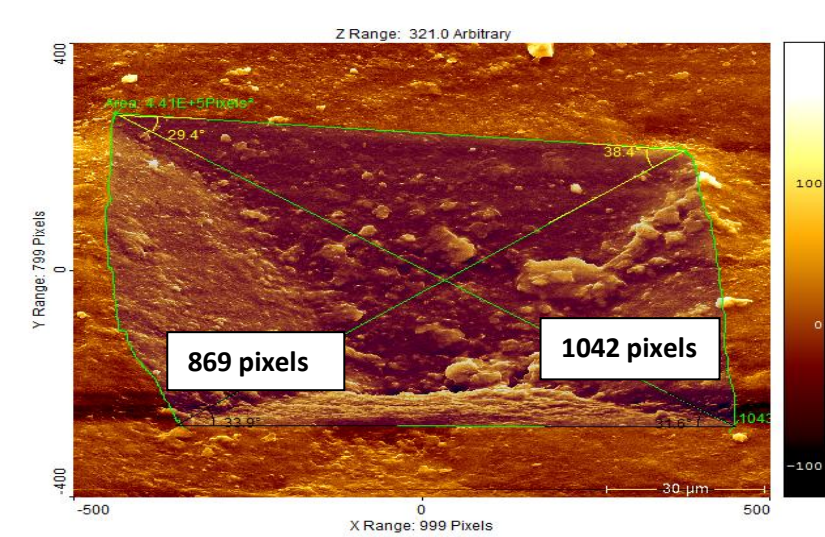


Fig. 3.9.23 Geometrical reconstruction of P-type etch pit in FH-3. The pit is of scalene trapezoidal shape with diagonals of different lengths (1042 & 869 pixels), un-parallel edges and angles of different value.

**Shape distribution analysis of etch pits:** The etch pits in Fig. 3.9.21 are used to find out etch pit shape factors. Shape factors include roundness, form factor, compactness and elongation. The plots of the shape factors of different kinds of etch pits are prepared to find out how the shape of an etch pit changes with dissolution. A progressive increase in roundness is observed from deep etch pit (P-type) to shallow etch pit (F-type). Form factor and compactness are also found to be highest in F-type etch pits. Elongation decreases from P-type to F-type (Table 8, Fig. 3.9.24). Fractal dimension is found to be highest in F-type with minimum surface texture value (Table 9, Fig. 3.9.25). The plot of surface texture vs fractal dimension shows an inverse relationship (Fig. 3.9.25c).

Table 8 Shape factors of different types of etch pits

Types of etch pits	Roundness	Form factor	Compactness	Elongation
P-type with short curved edges (1)	0.4359	0.6126	0.6602	0.6171
Stepped (2)	0.6158	0.6908	0.7847	0.4911
P-type with straight edges (3)	0.7666	0.7387	0.8756	0.3462
F-type (4)	0.8588	0.7583	0.9267	0.2914

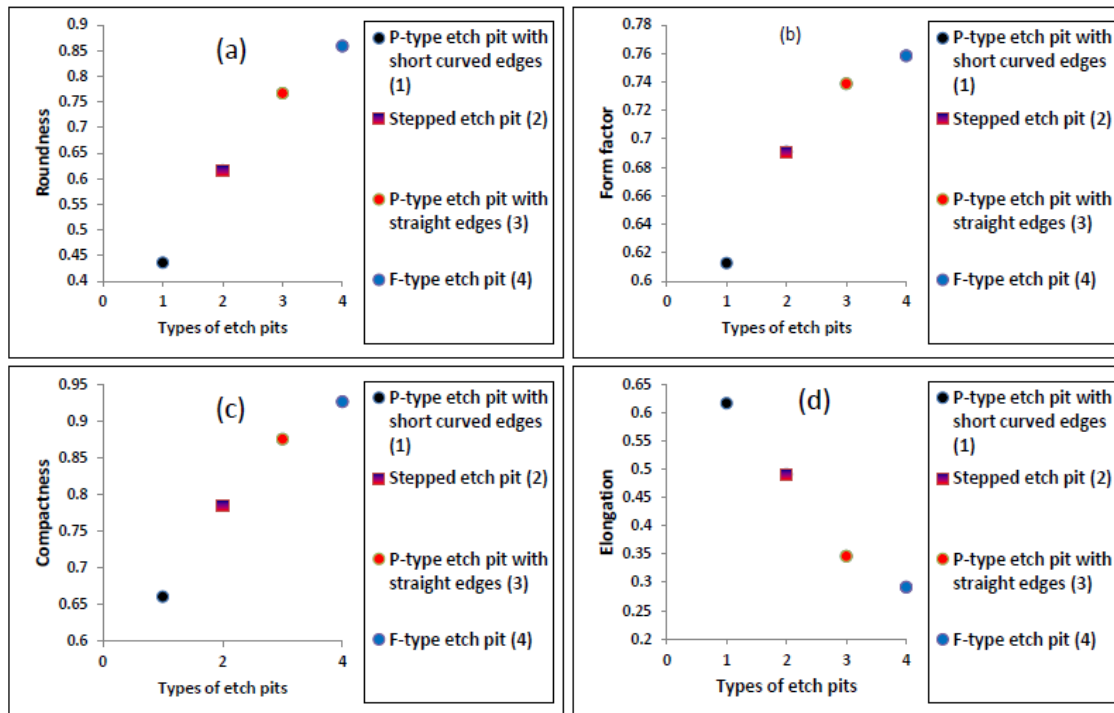


Fig. 3.9.24 Plots of shape factors of different kinds of etch pits.

Table 9 Fractal dimension and surface texture on different kinds of etch pits' surface

No.	Types of etch pits	Fractal dimension	Surface texture
1	F-type	3.16	50.3
2	Stepped	3.01	82.9
3	P-type with short, curved edge	2.9	92.3
4	P-type with straight edges	2.88	105.1

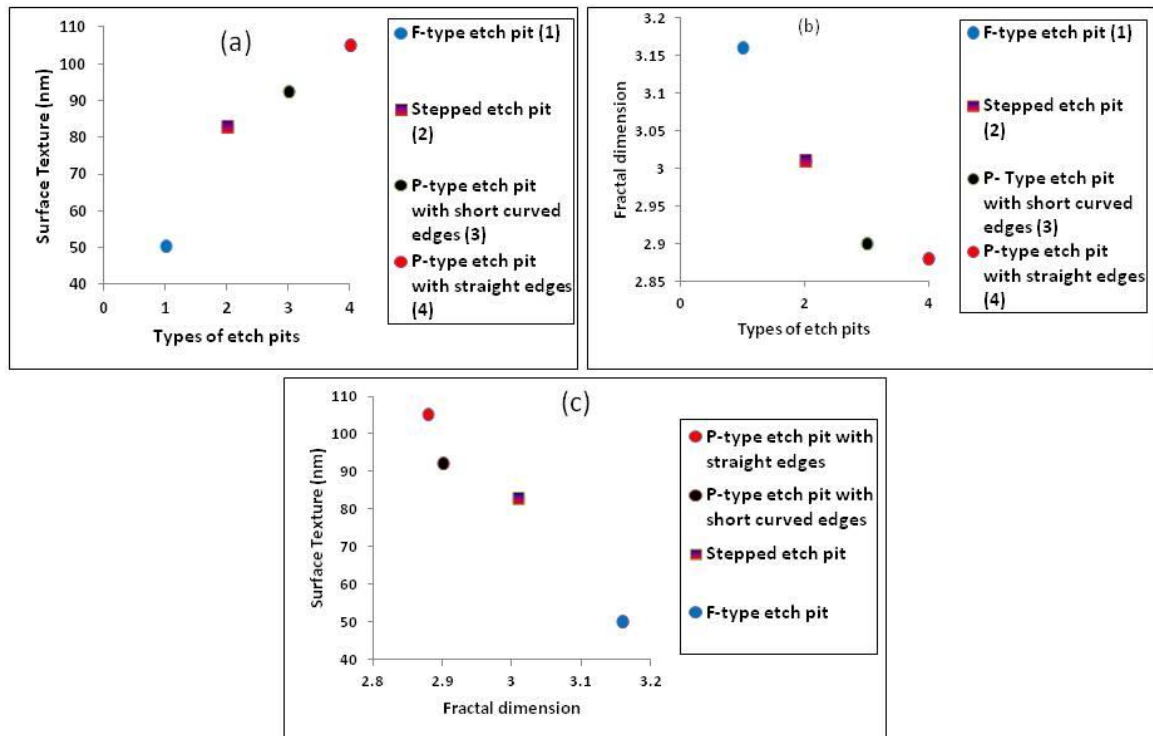


Fig. 3.9.25 Plots of values of fractal dimension and surface texture of etch pits shown in Fig. 3.9.21. (a) Surface texture vs. different kinds of etch pits. (b) Fractal dimensions vs. different kinds of etch pits. (c) Surface texture vs. fractal dimension of different etch pits.

**Micro hardness analysis:** Besides the etch pits shown in Fig. 3.9.21, one more P-type etch pit are subjected to Vickers hardness analysis and the values are compared with their surface texture by SPIP software. Vickers hardness is found to be minimum in P- type and maximum in F- type (Fig. 3.9.26, Table 10). Microhardness and surface texture have an inverse relationship as in the case of fractal dimension and surface texture.

Table 10 Vickers Hardness and surface texture at different kinds of etch pits

Hv(kg/mm <sup>2</sup> )	Ra (nm)	Type of etch pit
1.3886	22.9568	P-type with pointed bottom
11.745	9.22732	F-type
2.4298	17.8893	Stepped
3.2256	20.576	P-type with straight edges
4.091	14.6981	P-type with short curved edges

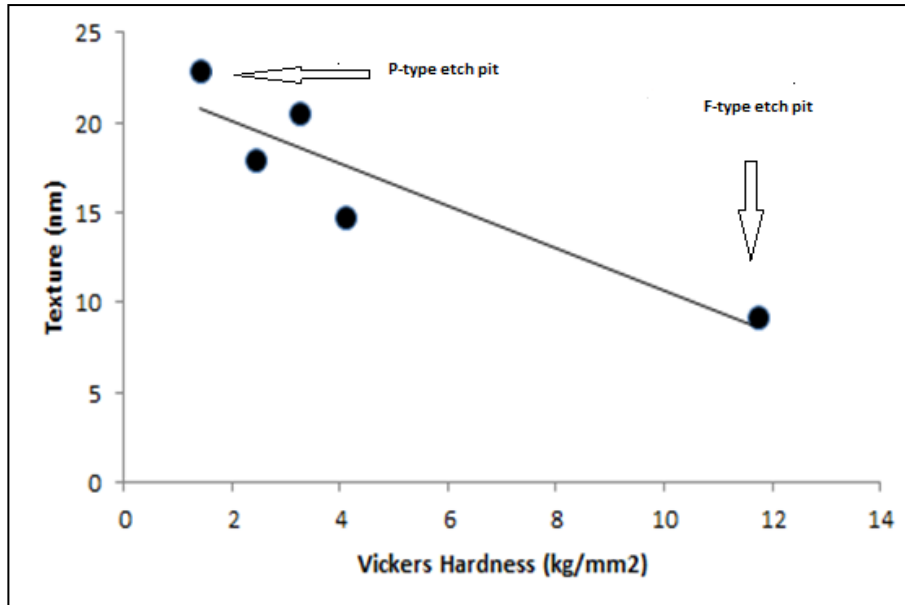


Fig. 3.9.26 Plot of Vickers hardness vs values of surface texture (Ra) in different etch pits.

**Determination of values of surface texture in different directions of etch pits:** Values of surface texture are measured along different directions of etch pits, mainly parallel and perpendicular to short edge and along the diagonals of etch pits with Gwyddion software to find out the most easily soluble direction in beryl. The value of surface texture is maximum parallel to short edges of the etch pits (Table 11, Fig. 3.9.27a,b,c,d). The etch pits used for analysis are shown in Fig. 3.9.21.

Table 11 Surface texture Ra ( $\mu\text{m}$ ) in different directions of the etch pit

Types of etch pits	to short edge	$\perp$ to short edge	Diagonal 1 (NW-SE)	Diagonal 2 (NE-SW)
P-type with straight edges	0.066	0.040	0.052	0.042
P-type with short curved edges	0.054	0.034	0.041	0.039
Stepped	0.050	0.046	0.043	0.038
F-type	0.024	0.012	0.017	0.016

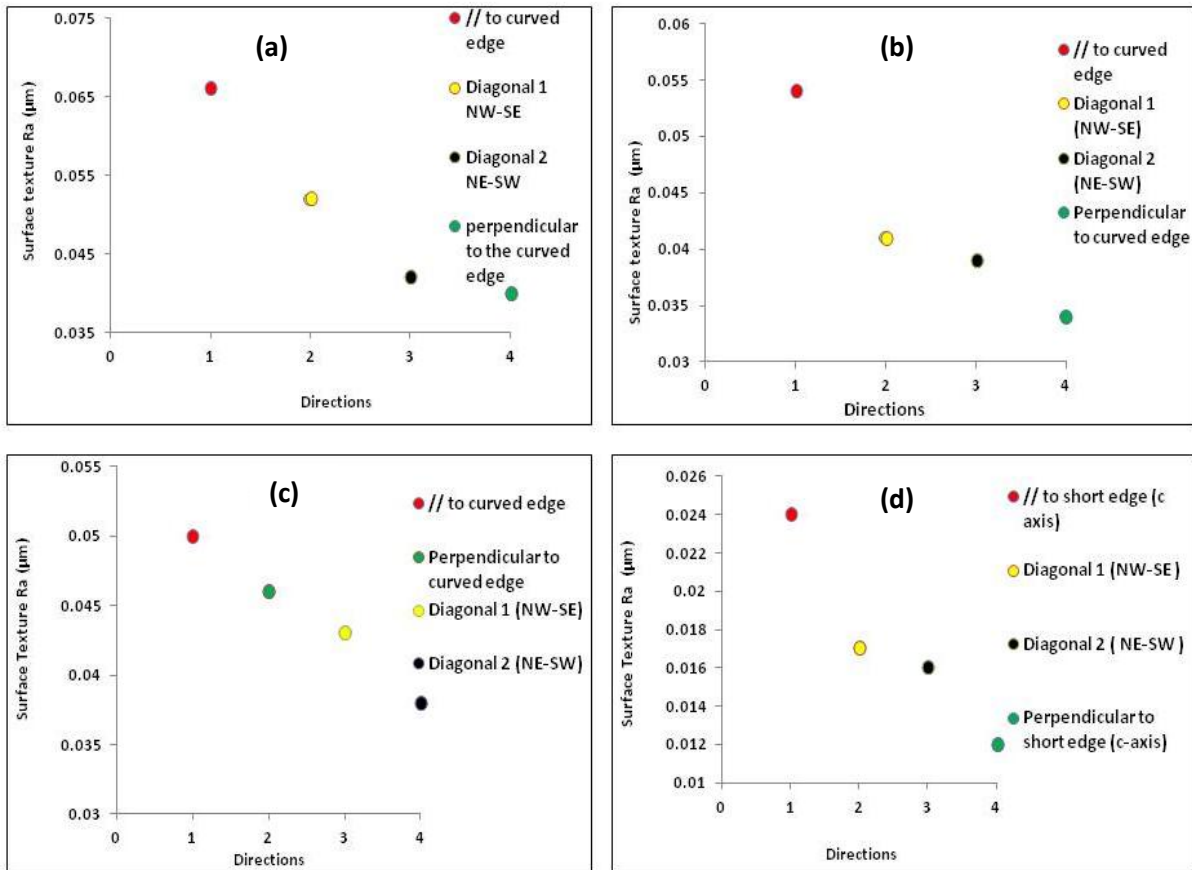


Fig. 3.9.27 Plots of values of surface texture in different directions of etch pits. **(a)** Surface texture along different directions of P- type etch pit with straight edges (Fig. 3.9.21b). **(b)** Surface texture values in stepped etch pit (Fig. 3.9.21a). **(c)** Values of surface texture in P- type etch pit with short curved edges (Fig. 3.9.21c). **(d)** Values of surface texture along different directions in F- type etch pit (Fig. 3.9.21d).

**Profile analysis of different kinds of etch pits:** Profiles are taken parallel to the longer edges of different kinds of etch pits (Fig. 3.9.28a, b,c,d).

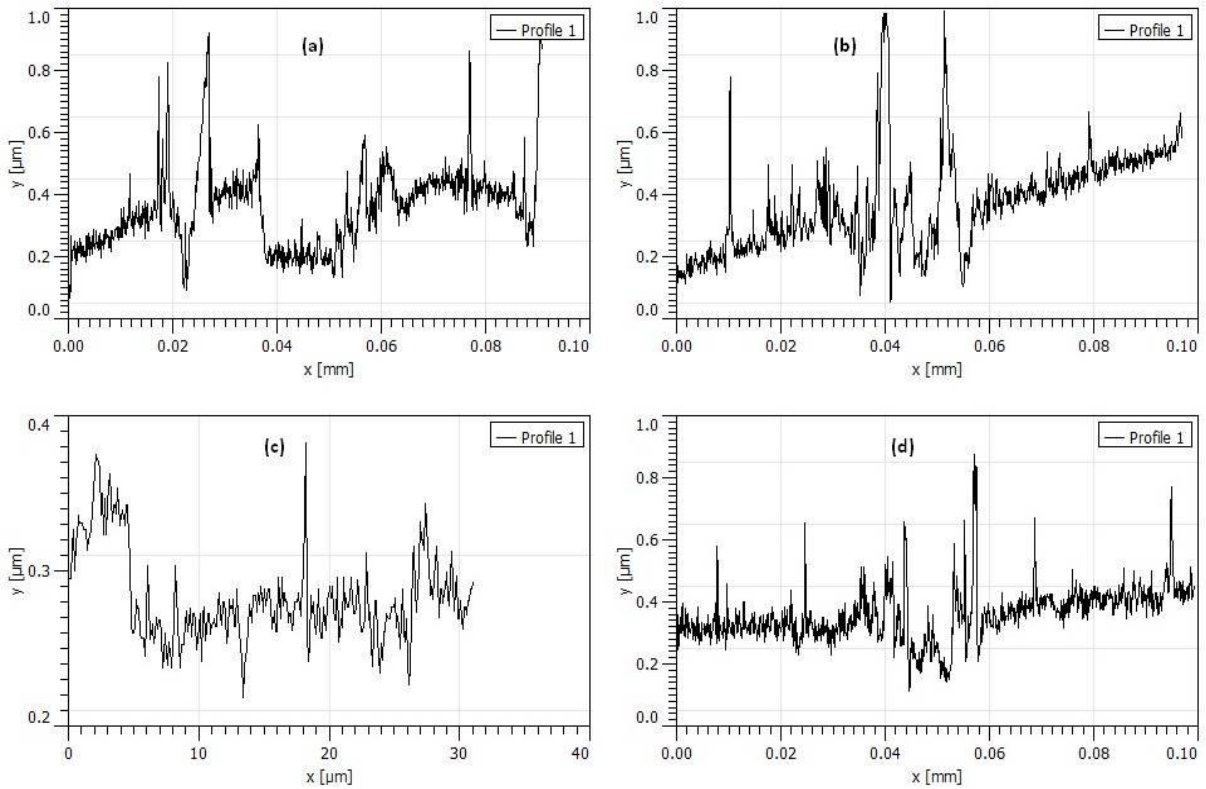


Fig. 3.9.28 Profile of texture along the length of different types of etch pits. **(a)** P-type with short curved edges (Fig. 3.9.21c). **(b)** P-type etch pit with straight edges (Fig. 3.9.21b). **(c)** F-type etch pit with shallow flat bottom (3.9.21d). **(d)** stepped etch pit (Fig. 3.9.21a).

**Determination of surface texture, fractal dimension and surface area of P- type etch pits in three representative samples:** The images of P-type etch pits on  $\{10\bar{1}0\}$  face of different samples are analysed in order to find out surface texture, fractal dimension and surface area of individual etch pits (Fig.3.9.29). Values are plotted to compare dissolution. PAY-1 has maximum surface texture value (Table 12, Fig. 3.9.30).

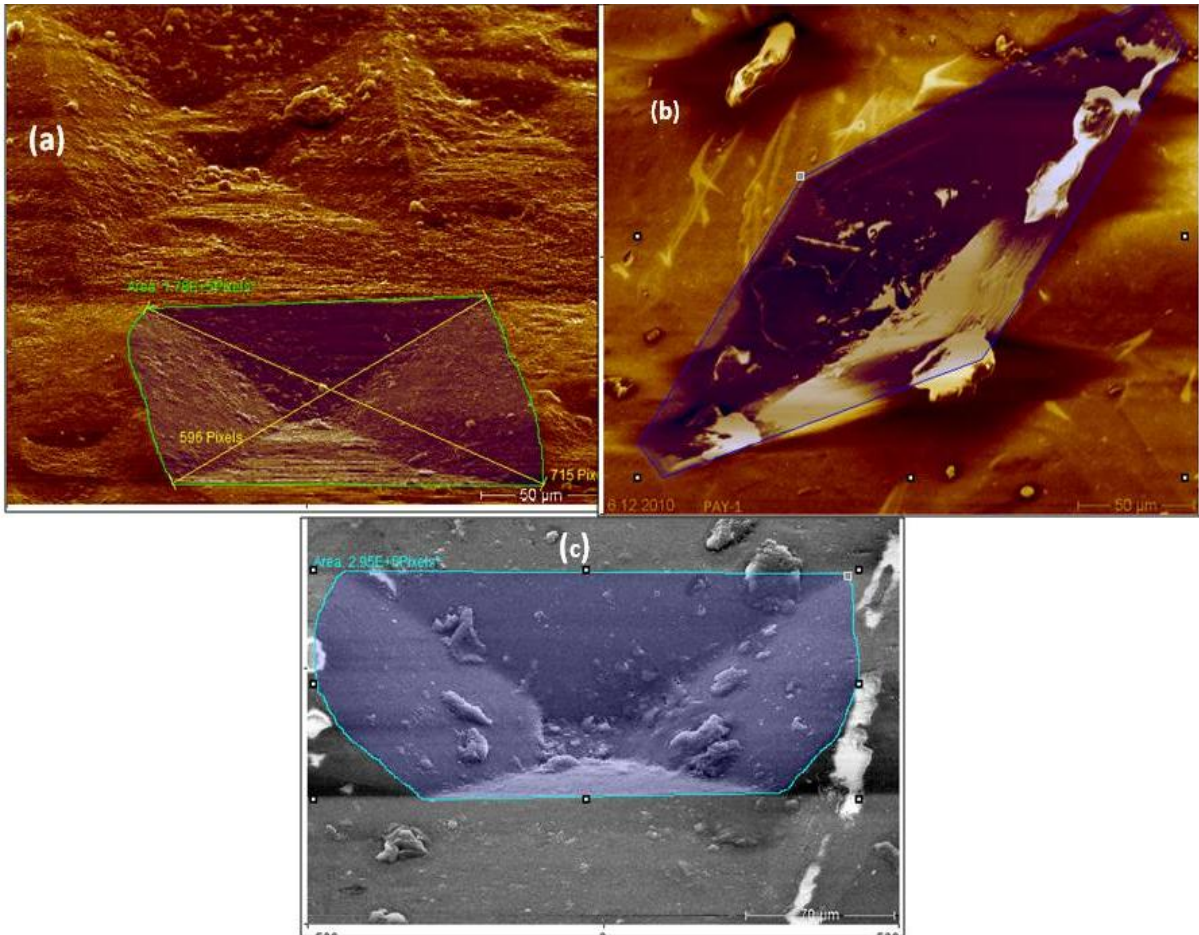


Fig. 3.9.29 Etch pits analysed to find out surface texture, fractal dimension and surface area. (a) P-type etch pit in FH-3. Yellow lines indicate diagonals of different lengths (596 pixels and 715 pixels). (b) P- type etch pit in PAY-1 in the form of rhombic to elongated hexagonal shape. (c) P- type etch pit in BA-1.

Table 12 Surface texture, fractal dimension and surface area of P-type etch pits in different samples.

Factors	PAY-1	FH-3	BA-1
Surface texture Ra( $\mu\text{m}$ )	0.2505	0.1043	0.0840
Fractal dimension	2.11	2.14	2.22
Surface area	$10.38 \times 10^{-9} \text{ m}^2$	$9.675 \times 10^{-9} \text{ m}^2$	$9.607 \times 10^{-9} \text{ m}^2$

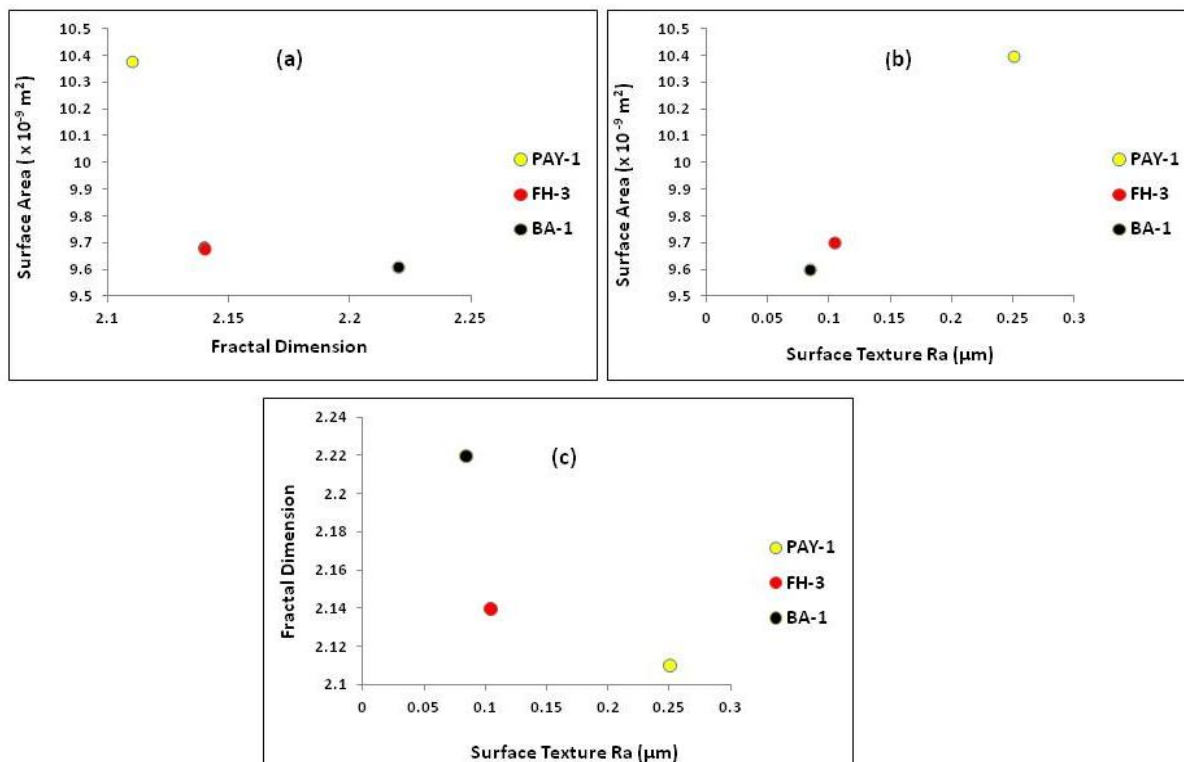


Fig. 3.9.30 Plots showing relationship between fractal dimension, surface area and surface texture in P-type etch pits of different samples.

**3.10 Hydrothermal experiments:** Two natural crystals (BA-1 and PAD-8) were used for the experiments. BA-1, the sample from Minas Gerais, Brazil is found to be poor in alkali content (0.05 wt%  $\text{Na}_2\text{O} + \text{Cs}_2\text{O}$ ) with high amount of  $\text{SiO}_2$  and  $\text{Al}_2\text{O}_3$ . PAD-8, the sample from Dassu mines with 0.24 wt%  $\text{Na}_2\text{O} + \text{Cs}_2\text{O}$  which is higher than that in BA-1. They were cut parallel to prism face ( $10\bar{1}0$ ), so that this face was exposed to the solution. We used four different types of solutions, chloridic with NaCl, KCl and HCl and one alkaline with NaOH. The aim of these exploratory experiments was to find out if similar features as on the natural crystals could be obtained. The results (Table 13) can serve as a guideline for further experiments.

Table 13 Run conditions and results for the hydrothermal experiments (at 600°C, 2 kbars)

Run No Sample	Sample weight	Solution weight	Duration	Observations	
				Etch pits	Products
RK 01 PAD-8	33.7 mg	2.66 mg 1N NaCl	5 days, 21 hours	strongly dissolved surface; deep etch pits	completely covered by reprecipitated  beryl, plagioclase, phenakite
RK 02 PAD-8	14.99 mg	1.64 mg 2N KCl	6 days	strongly dissolved surface; deep and shallow etch pits	completely covered by reprecipitated beryl, K- feldspar, phenakite; quench products rich in Fe, Cr
RK 01 BA-1	10.08 mg	5.05 mg 0.5 N NaOH	45 hours	long etch pits with their long axes perpendicular to c-axis; curved short edge	surface sporadically covered by quartz and euclase
RK 02 BA-1	15.27 mg	2.01 mg 0.5 N HCl	42 hours	no etch pits	surface sporadically covered by quench products rich in Na, K, Fe, Cr

**1N NaCl solution (PAD-8):** The prism face ( $10\bar{1}0$ ) of the sample was found to be covered with many long and short hexagonal prismatic crystals (Fig.3.10.1a,b,c). The shape and Si/Al ratio of the former one agree with that of beryl crystals (reprecipitated) which could have formed during quenching of the sample. In Fig. 3.10.2, analysis 7 has a high Na content, but no Cl; so it might be a Na-Ca-Si-mineral or a quench product. Crystal shape and analysis 18 indicate they could be phenakite crystals. Apart from these two minerals, another set of well shaped prismatic crystals are visible on the surface. The composition (Fig. 3.10.2, ana. 17) and shape imply they are plagioclase. Fig. 3.10.4 indicates the formation of phenakite and plagioclase (ana. 19,23,24).

Etch pits were not easily visible because of decomposed and reprecipitated crystals on the surface. Fine grained materials having a fibrous appearance were formed on the surface (Fig. 3.10.1a,c; not chemically analysed). Some parts of sample surface were unevenly covered with quenched products like NaCl along with Si and Al (Fig. 3.10.3, ana. 20, 21,22 ). After obtaining the EDS spectra, the sample was cleaned by boiling in HCl solution to eliminate the decomposed products and to get the images of etch pits. Cleaning in HCl solution helped to remove some products and as a result we could spot some etch pits under the decomposed products. These etch pits were found to be deep, elongated and alligned parallel to each other (Fig.3.10.5b).

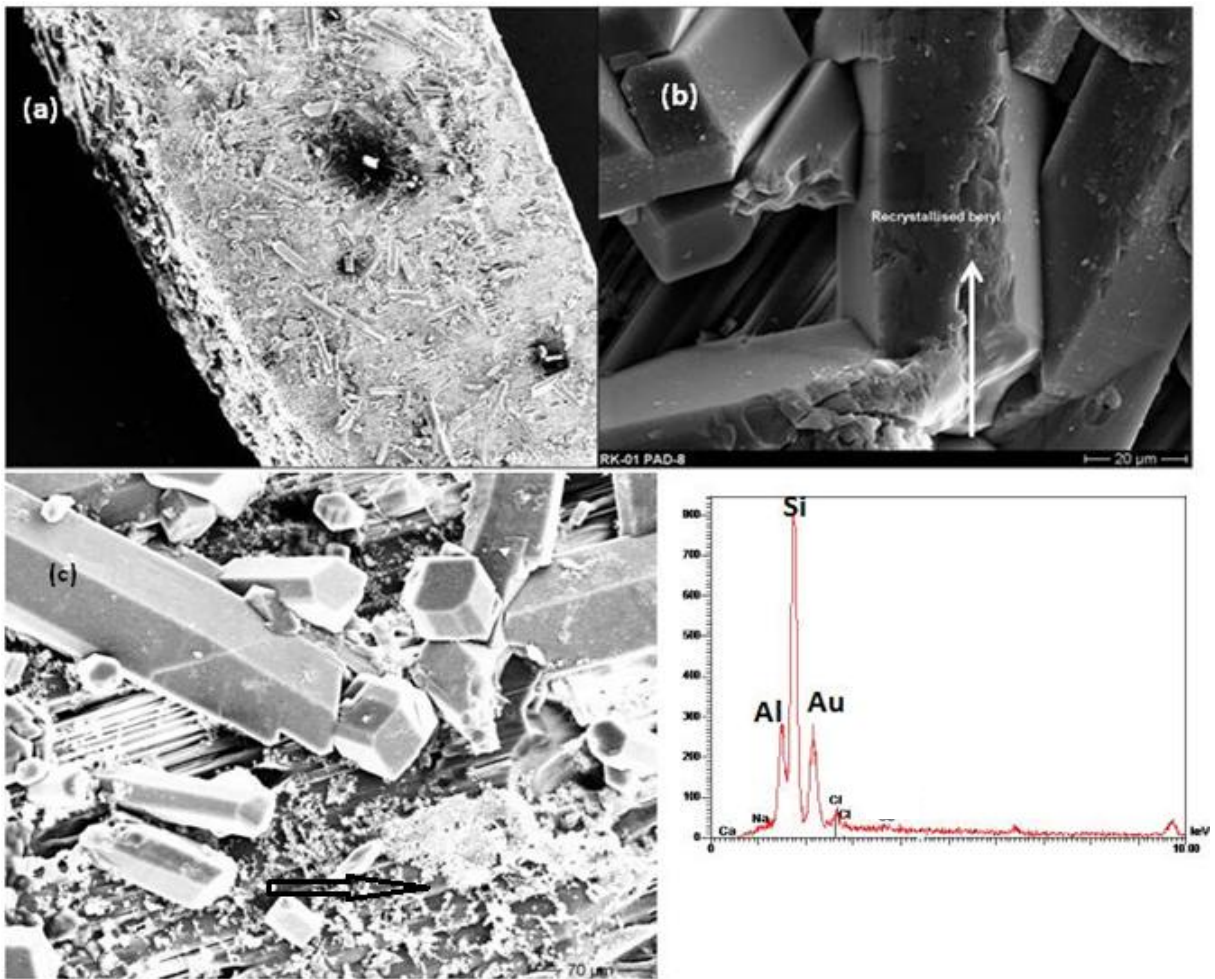


Fig. 3.10.1 SEM images of PAD- 8 hydrothermally treated in 1N NaCl solution. (a) Overview; the surface of the crystal is covered by newly precipitated beryl. (b) At higher magnification the hexagonal shape and EDS spectrum indicates reprecipitated beryl; the arrow points to place of analysis. (c) Surface irregularly covered with decomposed and reprecipitated crystals. The black arrow indicates fine grained and fibrous crystals.

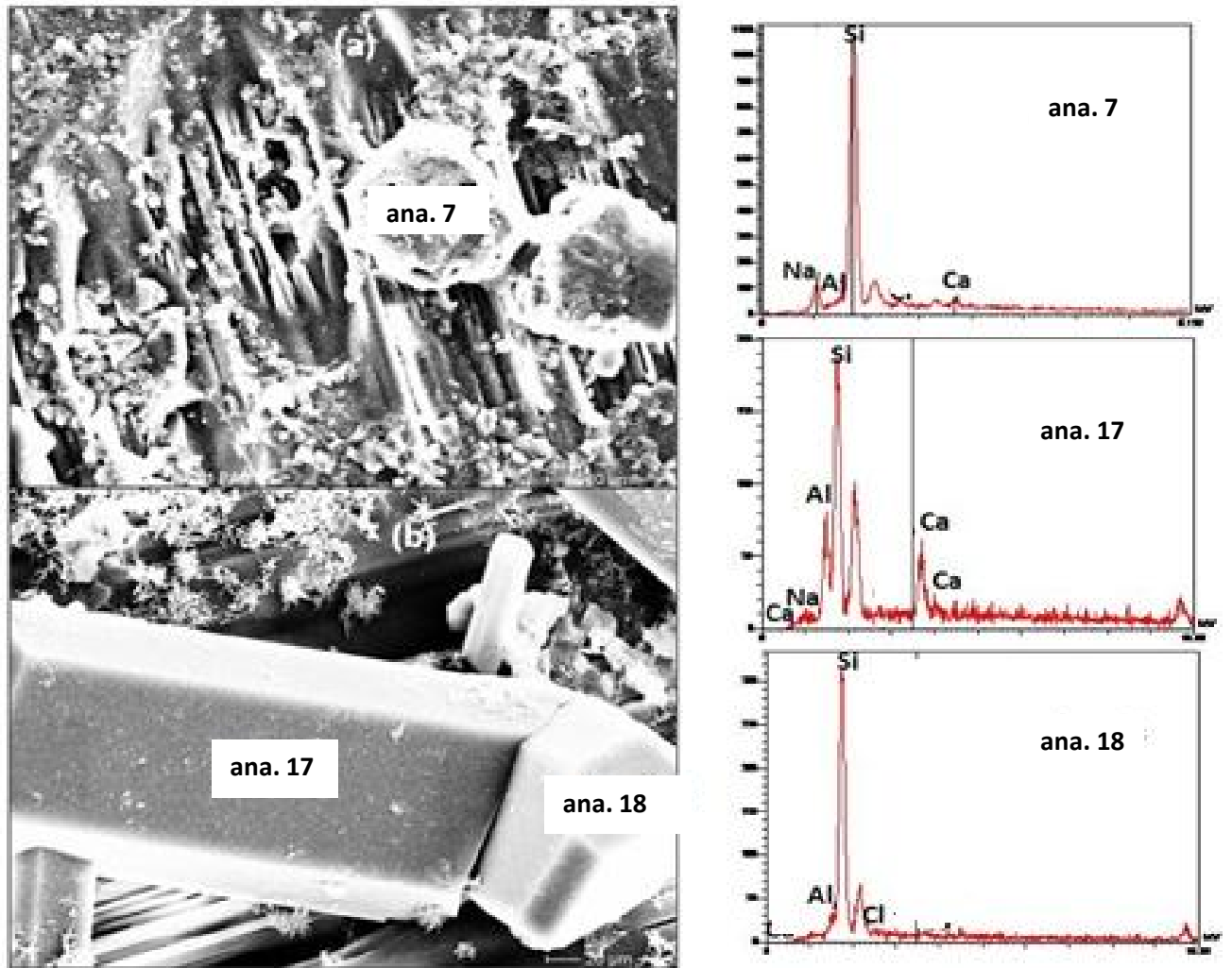


Fig. 3.10.2 SEM images of PAD-8 treated in NaCl solution. (a) Clearly shows the dissolved surface of the beryl and ana. 7 indicates that the product could be phenakite. The poorly developed shape and the Ca and Na content indicate quench products. (b) Shows two products. Ana. 17 indicates plagioclase and the shape of the crystals and composition of ana. 18 denotes phenakite.

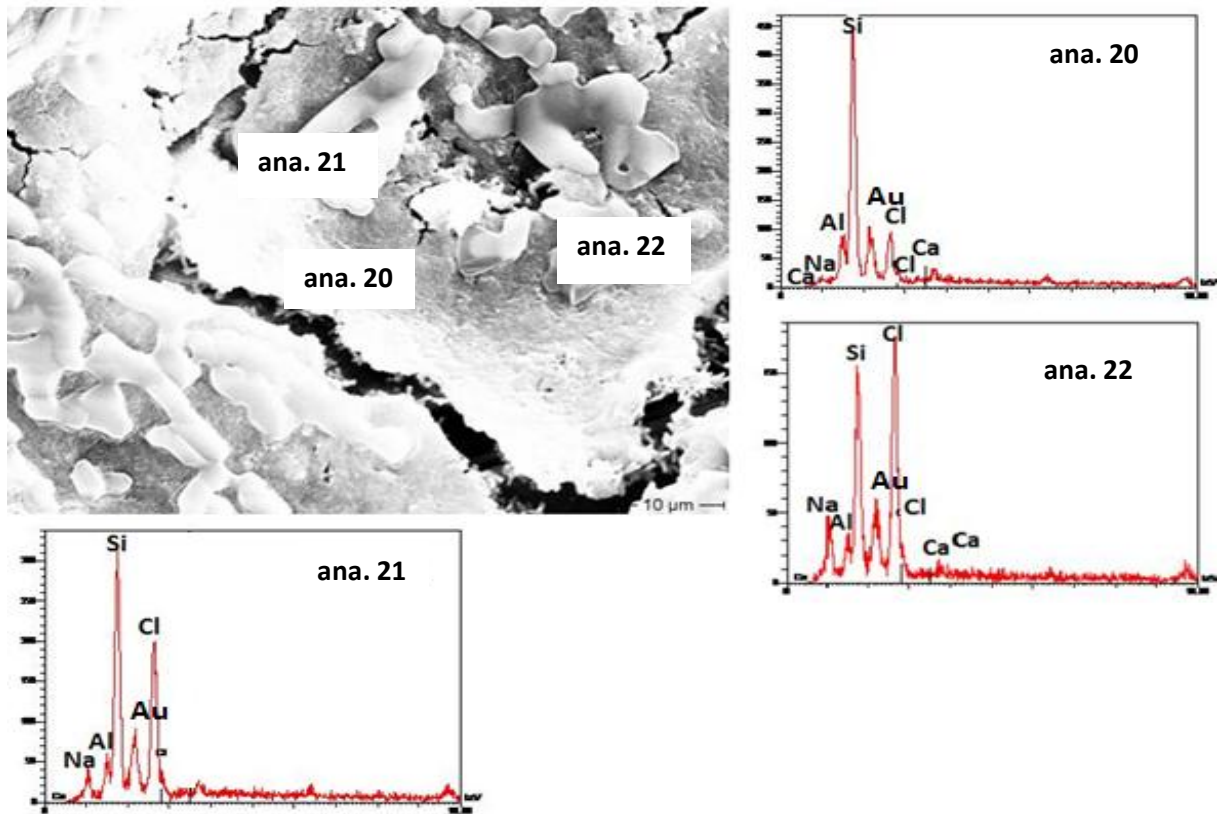


Fig. 3.10.3 SEM image of quench products with EDS spectra of PAD-8 treated in NaCl solution. The amount of Cl is variable in different analysis. Ana. 21 and 22 are from NaCl crystals precipitated after quenching, together with Si and Al in solution, forming the irregular cover on sample.

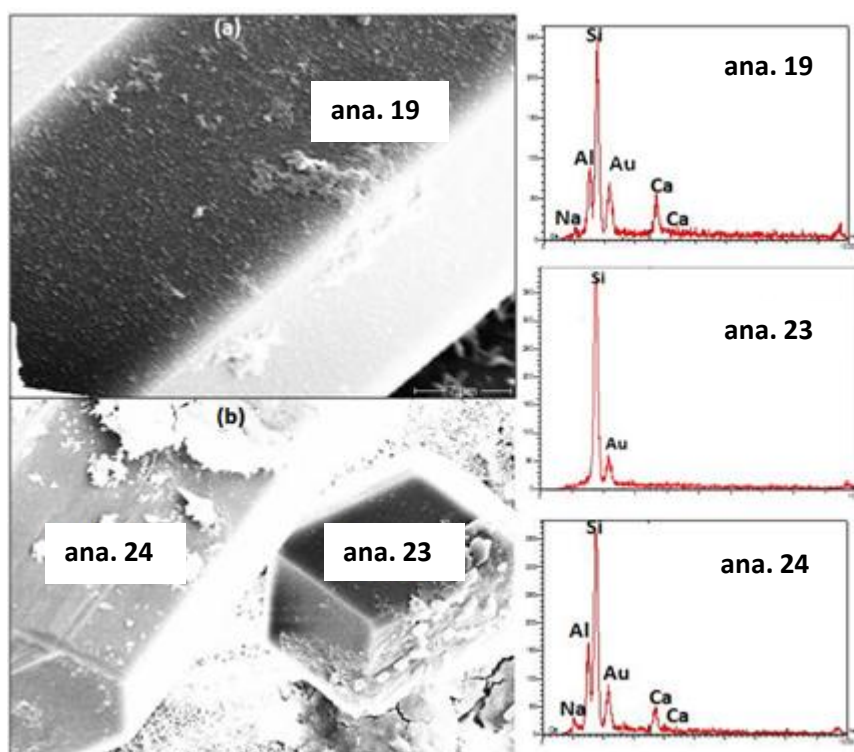


Fig. 3.10.4 SEM images of crystals on the surface of PAD-8 treated in NaCl solution. (a) Euhedral crystal formed at the surface of the sample; ana. 19 points towards the formation of Ca-rich plagioclase. (b) Ana.23 indicates the formation of phenakite and ana. 24 of beryl but rich in Ca.

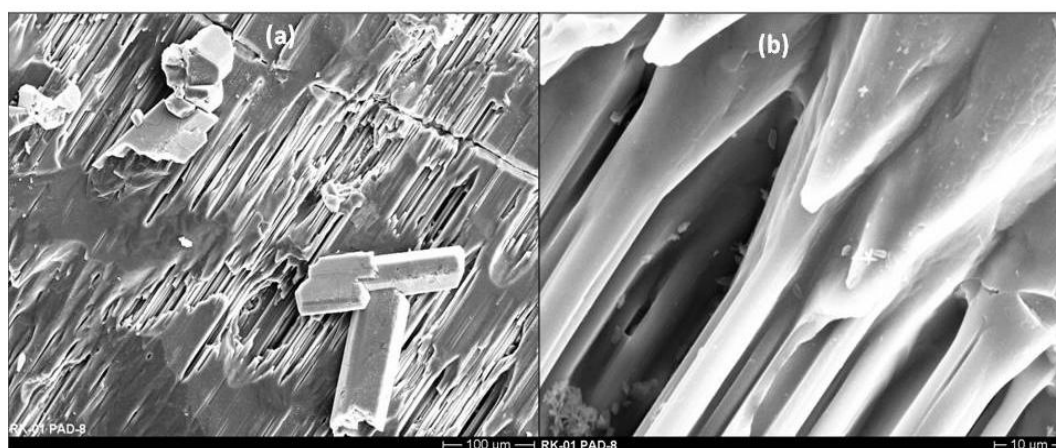


Fig. 3.10.5 Images of surface of NaCl-treated PAD-8 after cleaning. (a) The prism face  $\{10\bar{1}0\}$  is strongly dissolved and evidently elongated etch pits are observed parallel to c-axis along with hexagonal prismatic crystals. Shapes of these crystals indicate the formation of reprecipitated beryl crystals. (b) Magnification of image (a).

**2N KCl solution:** PAD-8 sample from Dassu mines cut parallel to c-axis was treated in 2N KCl solution at 600 °C and 2 kilobars for 6 days. As seen in NaCl treated sample, KCl treated

sample was also completely covered by decomposed products (Fig. 3.10.6a). Short-prismatic phenakite crystals and K-feldspar are found as decomposition products (Fig. 3.10.9a); analysis 12 has K and Al in almost equal amounts and Si almost three times of K and Al. Both minerals show well developed faces. At places, the surface is irregularly covered with fibrous materials rich in Fe and Cr (Fig. 3.10.7a, b). Fig. 3.10.8 indicates the formation of K-feldspar (ana. 12, 13). After cleaning of the sample in boiling HCl solution, SEM images were taken. Two kinds of etch pits were obtained after the treatment. 1) Deep, elongated, six sided etch pits were visible under these products. The edges are found to be straight and corners are sharp. 2) Elongated, rectangular shaped, shallow etch pits with curved short edges (Fig. 3.10.9b). However, deep etch pits are more prominent in the image.

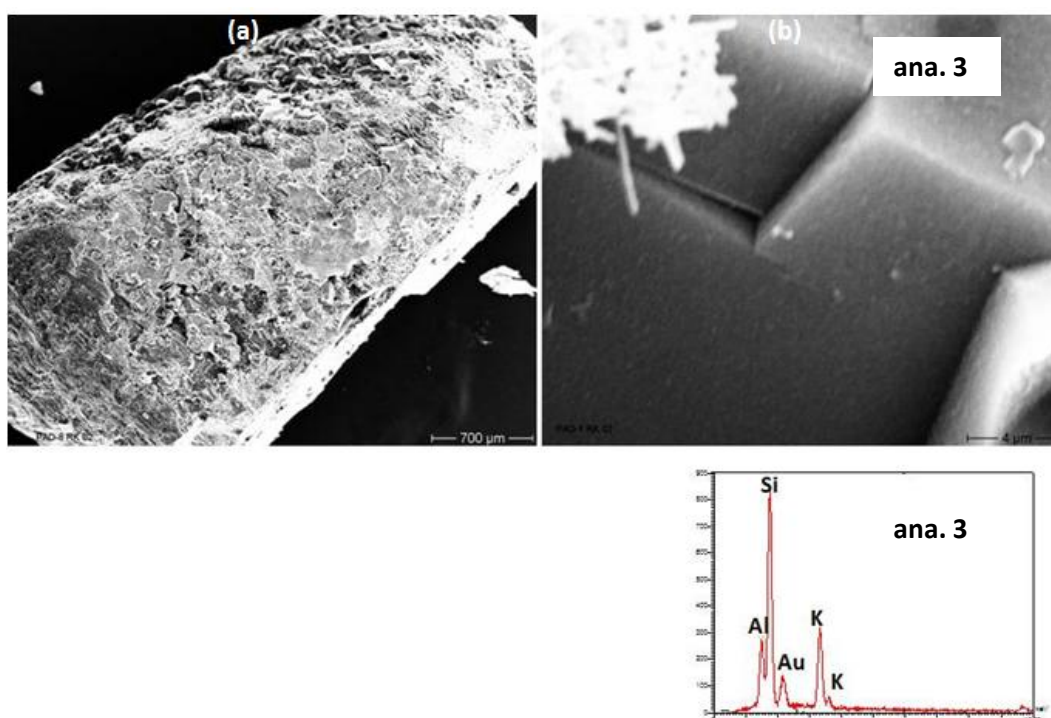


Fig. 3.10.6 SEM image of KCl treated PAD-8. (a) Overview. (b) Detail of surface, fibrous material in upper left of image is interpreted as quench products and ana. 3 reveals the presence of K, Al and Si as the major elements and the ratio implies the product could be K-feldspar.

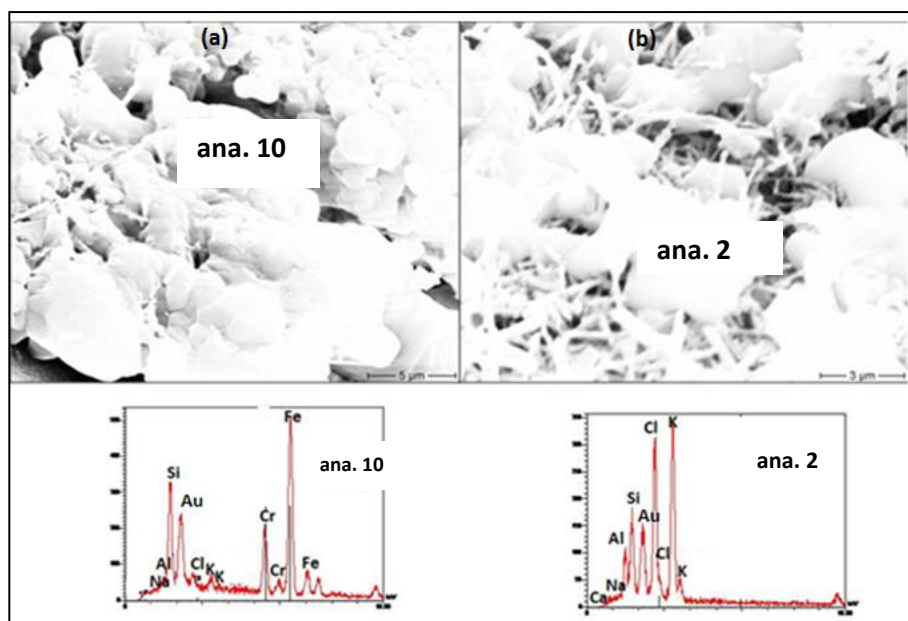


Fig. 3.10.7 SEM images of quench products in KCl treated PAD-8. (a) ana. 10 shows that some of the particles deposited on the surface are devoid of Al but rich in Fe, Si and Cr. Fe peak is much stronger than Si peak. K is also visible in small amount. Ana. 2 shows KCl along with back ground elements Si and Al from the sample.

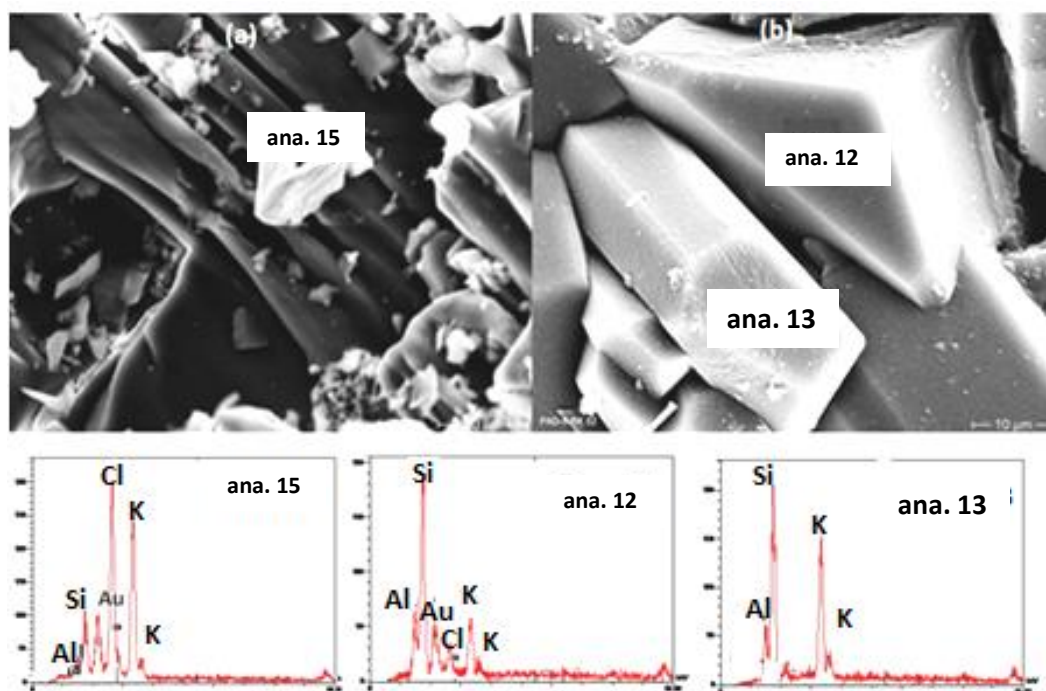


Fig.3.10.8 SEM images of strongly dissolved surface of KCl treated PAD-8. (a) Ana.15 has has higher amount of K and Cl (probably KCl plus element information from the background). (b) Well developed crystals on the surface, composition and shape indicate K-feldspar (ana. 12, 13). The variable K-content and some Cl is probably due to a mixture with quench products and/or due to different sample orientation.

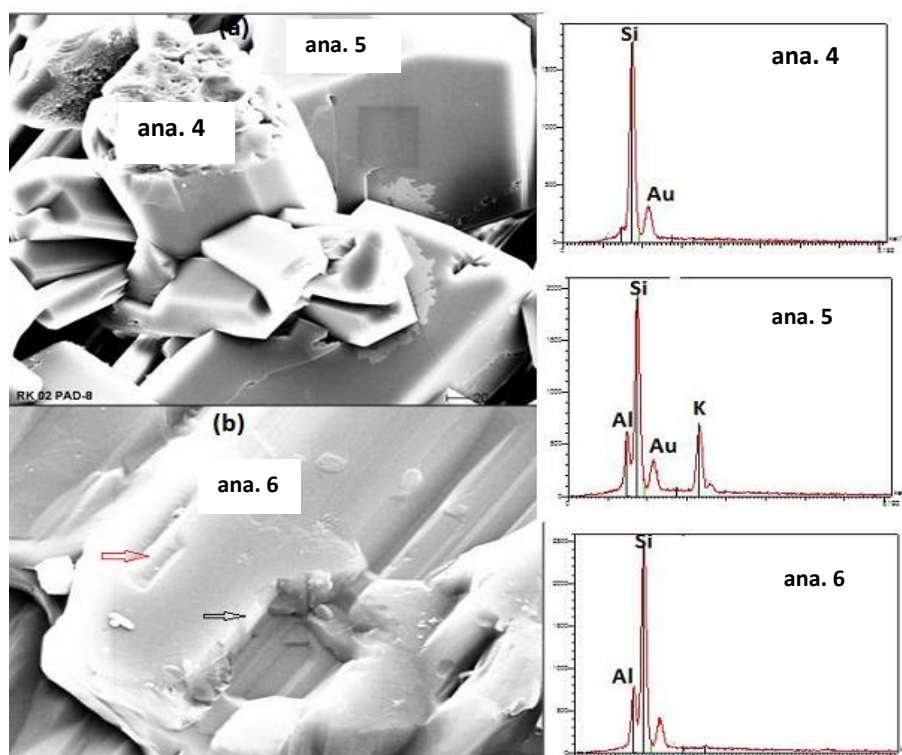


Fig. 3.10.9 SEM image of the surface of KCl treated PAD-8 after cleaning. (a) Euhedral crystals of phenakite and K-feldspar (ana. 4, 5). (b) Elongated, six-sided etch pits on the prism face ( $10\bar{1}0$ ) (black arrow) and long, rectangular, shallow etch pits with curved short edges (red arrow). Long direction of etch pits is perpendicular to c-axis. Ana. 6 is from the surface of the beryl.

**0.5N NaOH solution:** BA-1 cut parallel to c-axis was treated in 0.5N NaOH solution at 600 °C and 2 kilobar pressure for a duration of 45 hours. In contrast to NaCl- and KCl-bearing runs, the common decomposition products like feldspar and phenakite are not found in this run. However, clusters of reprecipitated beryl crystals are sparsely scattered on the surface (Fig. 3.10.13). Elongated etch pits are clearly visible with their long axes perpendicular to c-axis (Fig. 3.10.10). In Fig. 3.10.11a, the shape of the mineral is more like a rectangular prism than hexagonal prism. The EDS spectrum (ana. 1, Fig. 3.10.11a) shows that the mineral contains only Si. Hence, the mineral could be speculated either as bertrandite which crystallises in orthorhombic system or as quartz. However, the stability conditions of bertrandite do not comply with the run conditions used here. Bertrandite decomposes above 450 °C (Burt., 1978, Lebedev., 1980; Hsu., 1983 and Barton., 1986). The appearance as rectangular prism may be due to the angle from which the image is taken. Hence, the product could be quartz. Fig. 3.10.11b shows the presence of quartz. The fibrous material (Fig. 3.10.12) has Si and Al in equal proportion, which is either clay mineral or euclase. The shape of the mineral does not agree with clay. Hölscher et al (1986) reported the presence of euclase at up to 675°C and 25 kilobar, which nucleated spontaneously at 550°C and 20 kilobar. Hence, it can be

assumed that the product could be euclase. Franz and Morteani (2002) also found unidentified Al-Si rich phases in their experiments in the system  $\text{BeO-Al}_2\text{O}_3\text{-SiO}_2\text{-H}_2\text{O}$ .

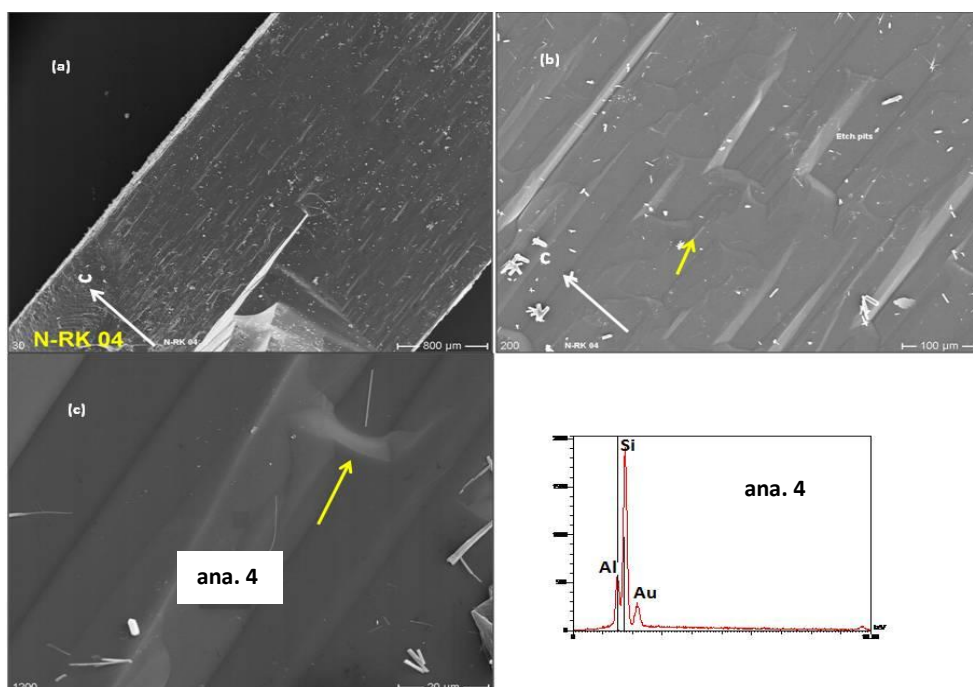


Fig. 3.10.10 SEM images of prism face  $\{10\bar{1}0\}$  of NaOH treated BA-1. (a) Overview. (b) Magnification of (a). The surface is characterized by the presence of long etch pits oriented perpendicular to c-axis (white arrow). Short edges are parallel to c-axis and are found to be slightly curved (yellow arrow). (c) Magnification of (b). Ana. 4 indicates the composition of beryl.

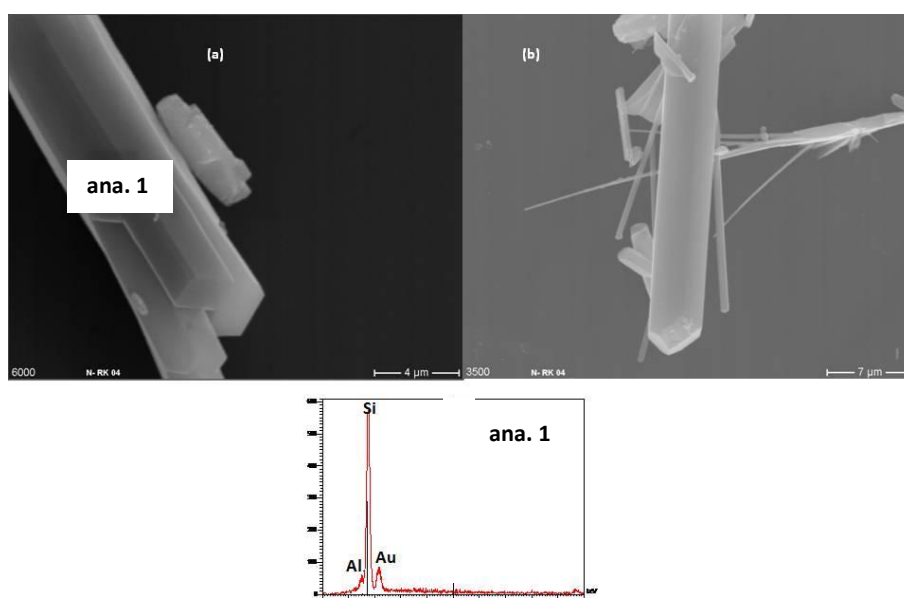


Fig. 3.10.11 SEM images of BA-1 treated in NaOH solution. (a) Columnar and prismatic decomposition products rich in Si, on the surface of BA-1. (b) Hexagonal prism with tapering end indicating quartz.

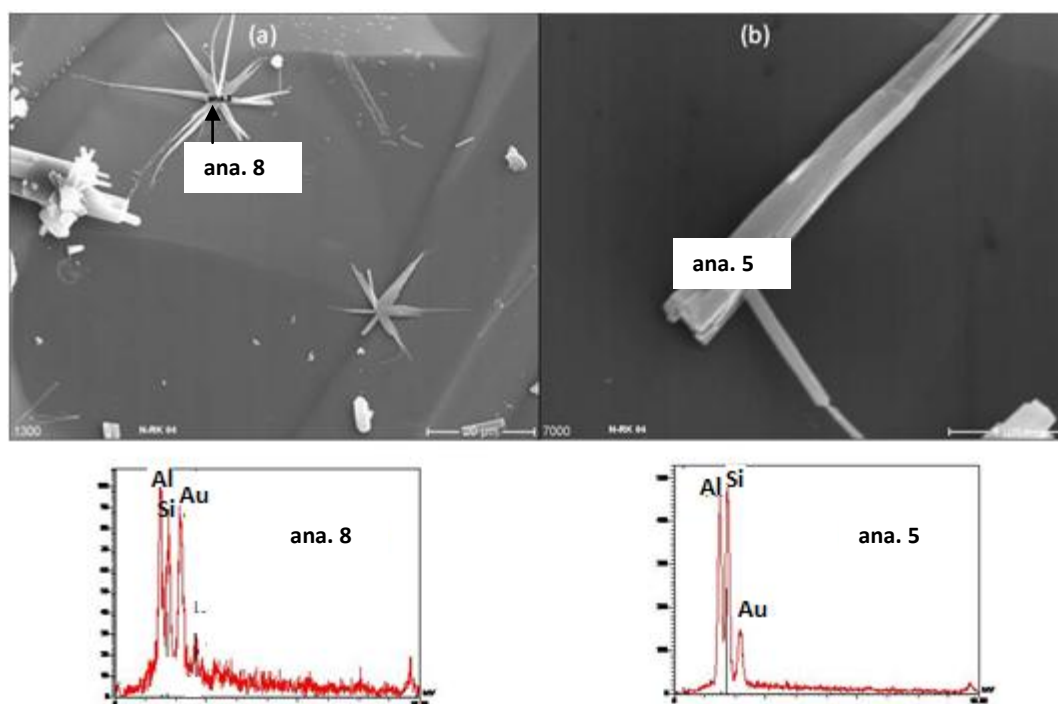


Fig. 3.10.12 SEM image of NaOH treated BA-1. (a) Flaky decomposition product rich in Al and Si in equal proportion point out the product could be euclase. (b) Magnification of image (a).

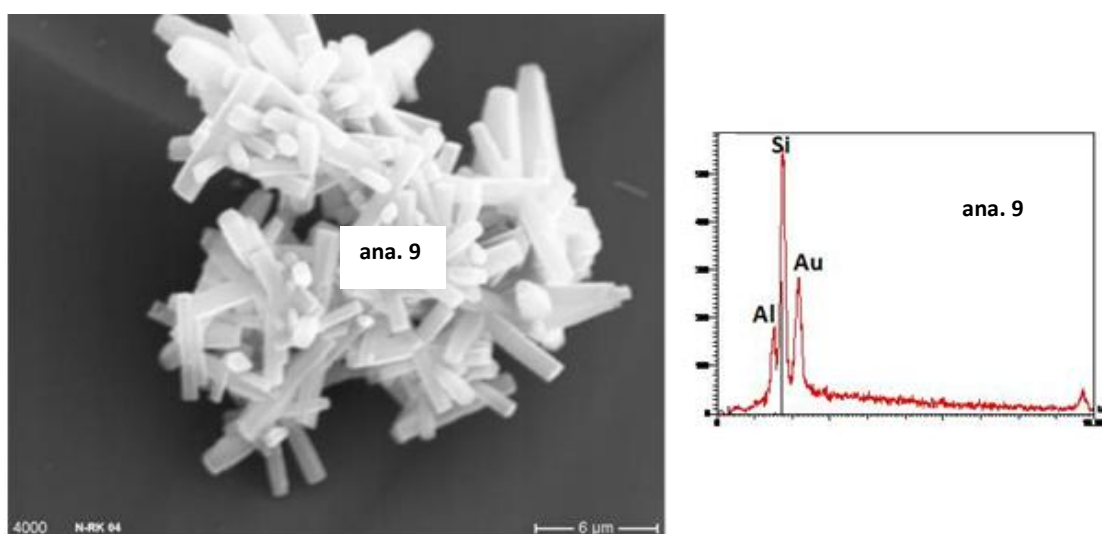


Fig. 3.10.13 SEM image of clusters of reprecipitated beryl on BA-1 treated in NaOH solution.

**0.5 N HCl solution:** BA-1 cut parallel to c-axis was polished and treated in 0.5 N HCl solution at 2 kilobars and 600°C for 40 hours. Unlike NaOH treated beryl, no etch pits are observed on the surface. Instead, a number of quench products during cooling to room temperature and 1 bar pressure are visible. All these irregularly shaped particles are found to be rich in Na, K, Fe, Cr and Cl along with the elements from background beryl. Scratches on the surface are remnants of polishing of the sample (Fig. 3.10.14, 15, 16).

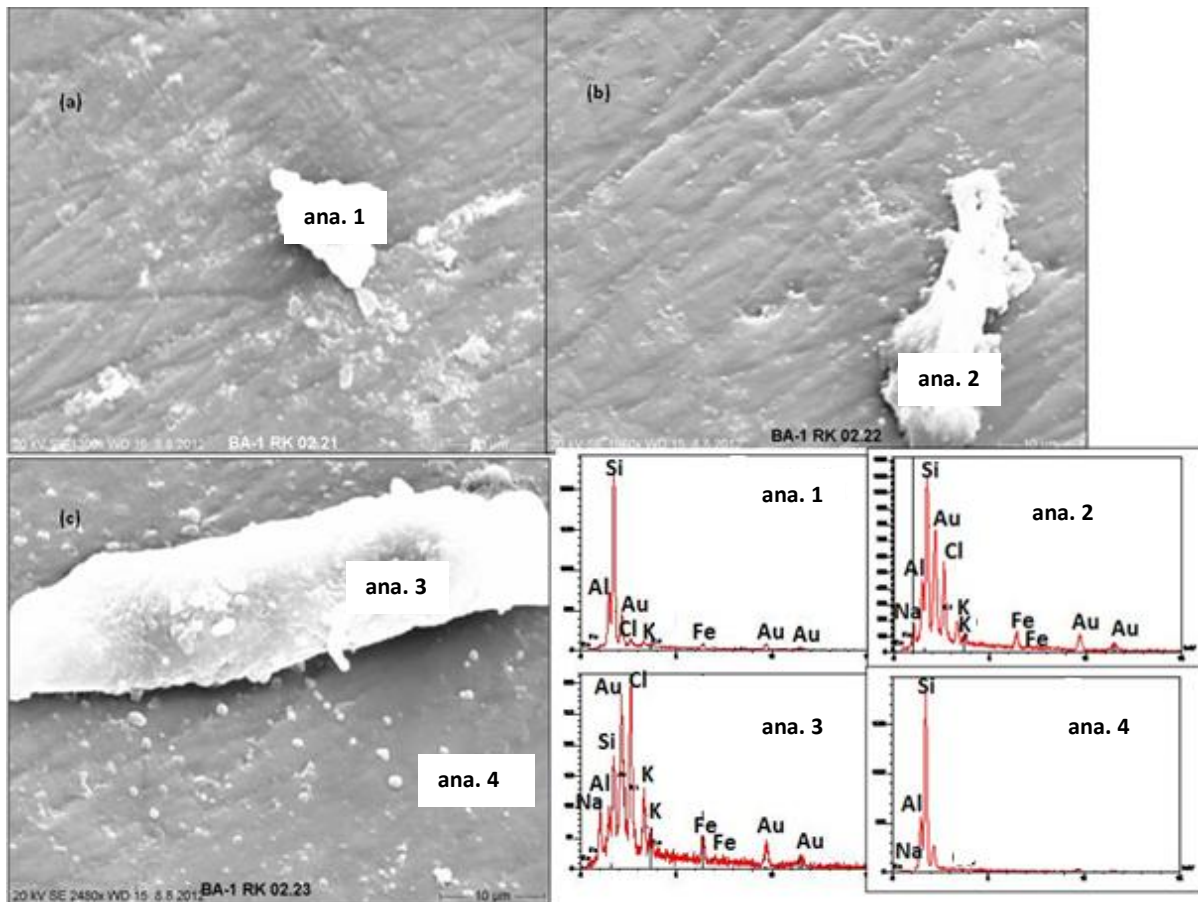


Fig.3.10.14 SEM image of HCl-treated BA-1. (a) Irregularly shaped quench product consisting of very small amounts of K-Cl-Fe with the background elements of beryl (ana. 1). (b) In ana. 2, the peaks of Fe and K are discernable in higher intensity apart from Al and Si in the same ratio as seen in beryl. (c) In ana. 3, K, Fe along with Na are perceptible. Si peak becomes feeble in this, indicating that it is not a dominant constituent of the quench product. Ana. 4 shows unaltered part of beryl.

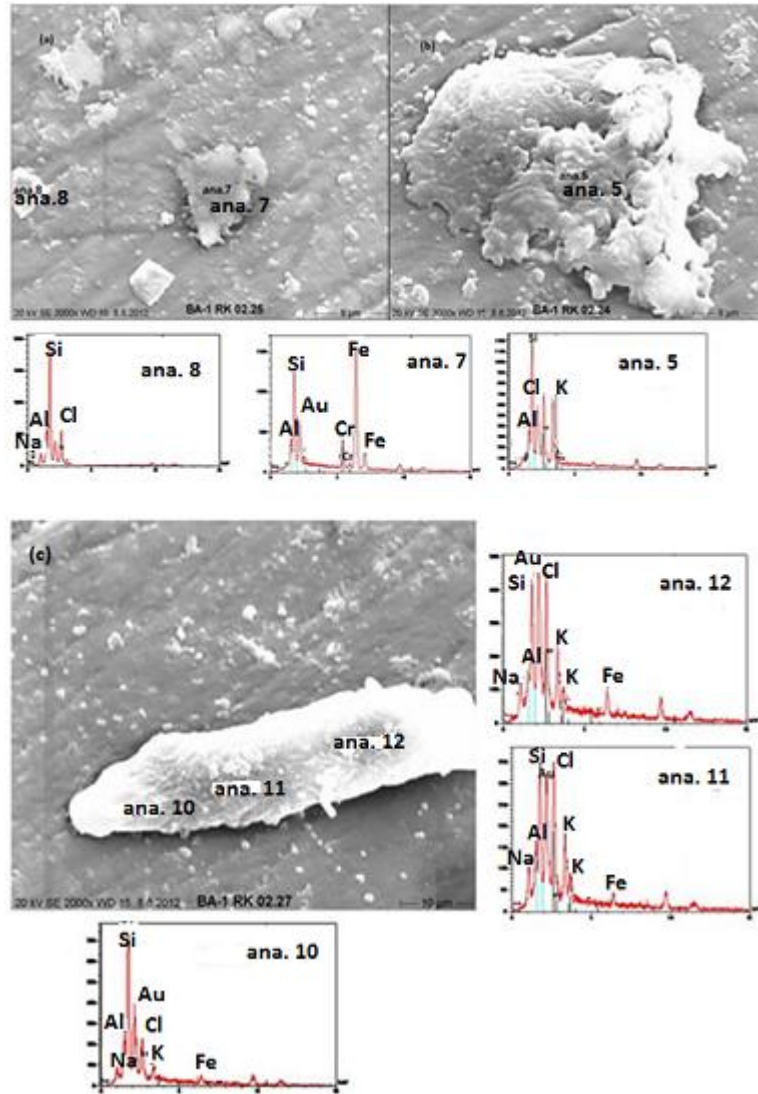


Fig. 3.10.15 SEM images of quench products in HCl treated BA-1. (a) Ana. 8 in (a) has a little amount of Na and Cl in the spectra with background analysis of beryl which can be interpreted as NaCl. Ana. 7 in (a) has a substantial amount of Fe and Cr without Na and K. (b) Ana. 5 in (b) has higher K content than in the other two analyses. The amount of Na and Fe are very little. (c) This image shows the slightly variable composition of the quench products rich in K-Na-Fe-Cl. A progressive enrichment in K, Na and Fe can be seen from ana. 10 to ana. 12.

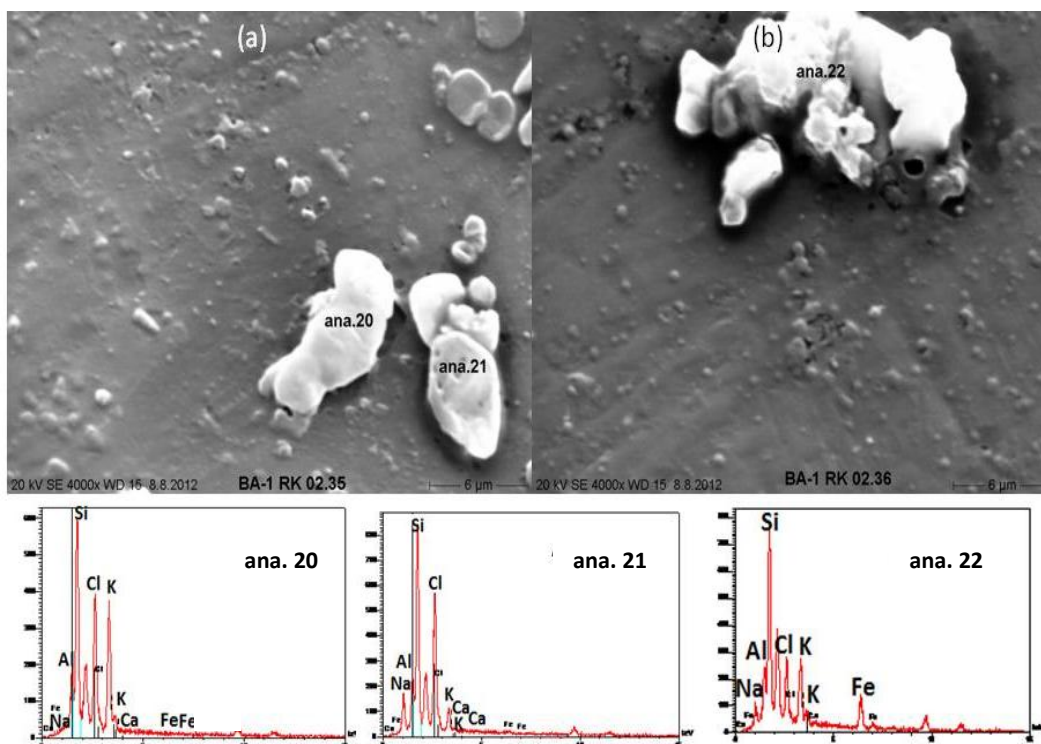


Fig. 3.10.16 SEM images of quench products on the surface of BA-1 treated in HCl solution. The products are with variable composition of K-Na-Fe-Cl.

**Infrared spectroscopic studies of hydrothermally treated beryl:** Infrared spectra of treated BA-1 in NaOH solution and HCl solution have similar bands in the finger print region. No extra bands are visible after the treatment. However, a shift in band positions towards higher frequency are observed in treated samples. The band at  $1206\text{ cm}^{-1}$  in untreated beryl (Fig. 3.10.17) shifts towards  $1209\text{ cm}^{-1}$  (Fig. 3.10.18, 19, Table 14) in treated beryls. The shift is almost similar in both alkaline and acidic medium (NaOH and HCl). The band at  $962\text{ cm}^{-1}$  in untreated beryl shifts towards  $965\text{ cm}^{-1}$  in HCl treated beryl. The band at  $435\text{ cm}^{-1}$  in untreated beryl also moves to higher frequency in both the treatments. Treated BA-1 in NaOH solution shows a broad shoulder around  $3400\text{ cm}^{-1}$  which is not shown by HCl treated beryl (Fig. 3.10.18, 19). The intensity of the band at  $3700\text{ cm}^{-1}$  in untreated BA-1 decreases after the treatment.

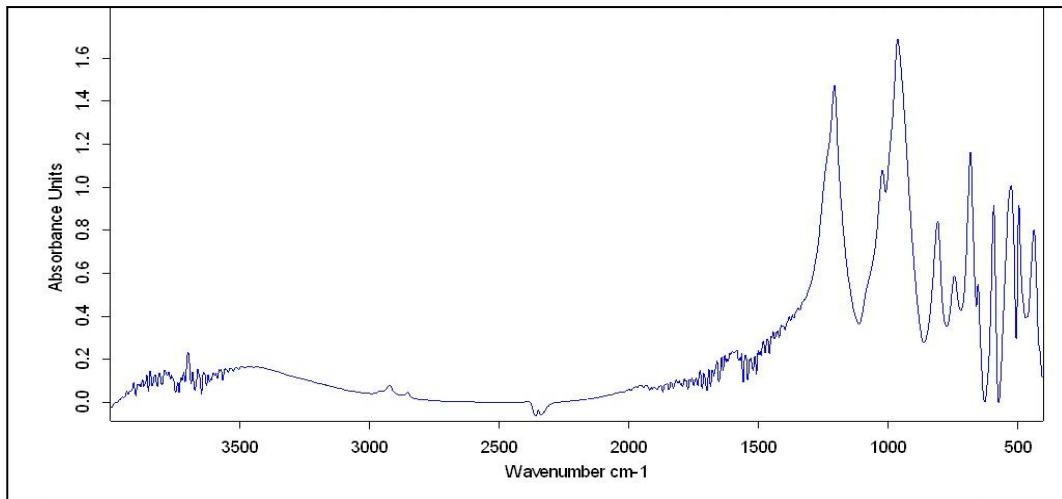


Fig. 3.10.17 IR spectrum of untreated BA-1 from 400 cm<sup>-1</sup> to 4000 cm<sup>-1</sup> wavenumber.

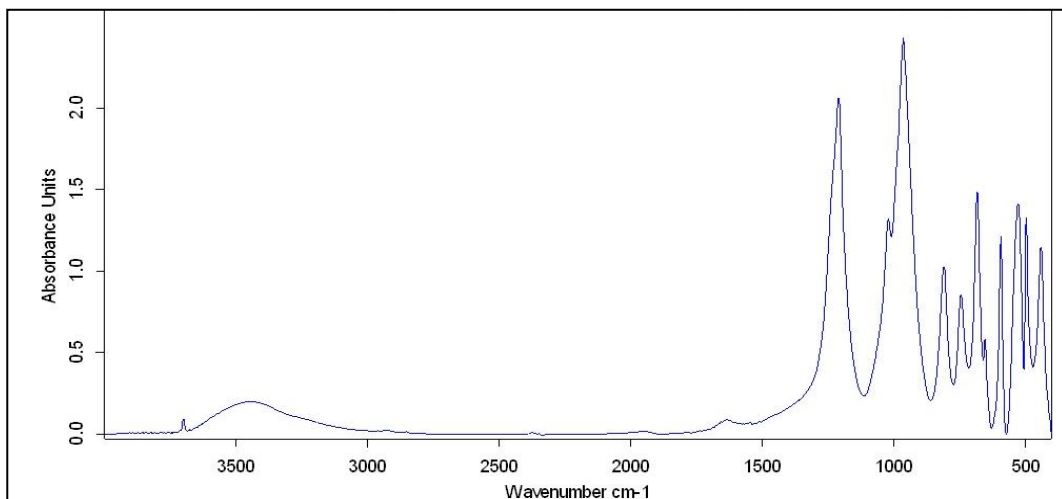


Fig. 3.10.18 IR spectrum of NaOH treated BA-1 from 400 cm<sup>-1</sup> to 4000 cm<sup>-1</sup> wavenumber.

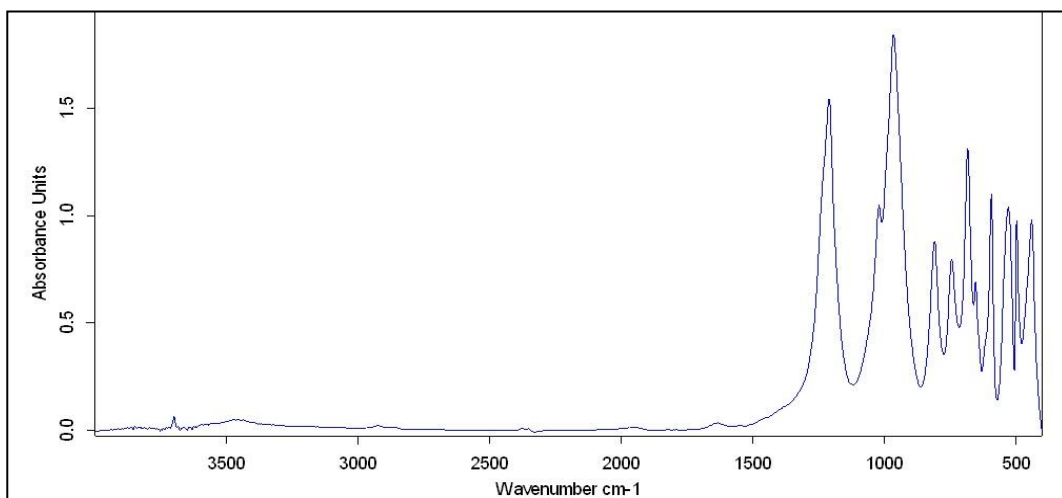


Fig. 3.10.19 IR spectrum of HCl treated BA-1 from 400 cm<sup>-1</sup> to 4000 cm<sup>-1</sup> wavenumber.

Table 14 Position of IR bands before treatment and after treatment in HCl and NaOH solutions

<b>Sample used</b>	<b>Band position before treatment</b>	<b>Band position HCl treated</b>	<b>Band position NaOH treated</b>
BA-1	1206 1021 962 808 524 435	1209 1019 965 808 528 439	1209 1020 963 808 527 440

## 4. Discussion

**4.1 Morphology:** The investigated sample suite manifests two morphological types of crystals. The majority of the samples are prismatic except three (BAA-1 and BAA-2 from Brazil, CA-1 from China) with a tabular habit. All prismatic samples have a low degree of substitution and are close to ideal stoichiometry, whereas the three tabular samples (Table 2) have between 0.72 wt% Na<sub>2</sub>O+Cs<sub>2</sub>O (BAA-1), 2.00 wt% Na<sub>2</sub>O+Cs<sub>2</sub>O (CA-1) and 2.18 wt% Na<sub>2</sub>O+Cs<sub>2</sub>O (BAA-2). In all samples, the faces {10 $\bar{1}$ 0} and {0001} are developed (Table 1). In BA-1 and PAD-4, 5, 6, the faces {10 $\bar{1}$ 1} and {10 $\bar{1}$ 2} are also observed. {21 $\bar{3}$ 0} is visible in PAD-5. CA-1 has a more complex morphology with small faces of dihexagonal pyramids like {11 $\bar{2}$ 1} and {31 $\bar{4}$ 3} (Table 1).

Variations in the habit in beryl are generally noted, but the specific cause of such variation is not well understood. Sinkankas, 1989 has shown that an increase in alkali content in beryl causes a transition from a columnar shape to stumpy to tabular. The aspect ratio of prism length to the diameter of pinacoidal faces is considered to decrease as beryl enriches in Cs, Na and Li creating flattened tabular crystals (Černý et al., 2003). This is also the case in our sample suite (CA-1, BAA-1 and BAA-2). The enrichment in alkalis changes the lattice parameters of the crystals, which are reflected in their tabular habit (variation in lattice parameter with the chemical composition will be discussed in detail in XRD section).

Beryl crystals are commonly prismatic with prominent growth in the direction {0001} of the hexagonal prism. The first order prism  $m$  {10 $\bar{1}$ 0} is the most common form found among beryls followed by pinacoids  $c$ {0001}. First order prisms are often present and well developed. Second order prism  $a$  {11 $\bar{2}$ 0} faces occur as narrow strips truncating squarely the edges where two faces of the first order prism meet. First order bipyramids  $p$ { $h_0\bar{h}$ l} and second order bipyramids  $s$ { $hh_2\bar{h}$ l} are also observed in beryls (Goldschmidt, 1913; Sinkankas, 1982 and Tröger, 1982). All these faces are present in the sample suite investigated by us (Fig. 3.1 and Table 1).

**4.2 RI determination:** Refractive index  $n_\epsilon$  of three representative samples BA-1, PA-2 and FH-3 varies between 1.570 and 1.577 and  $n_\omega$  between 1.574 and 1.580. Birefringence ( $\Delta n$ ) is -0.004 to -0.003 (Table 4). RI values agree with the reported values in the literature as  $n_\epsilon = 1.568$ -1.602 and  $n_\omega = 1.564$ -1.595. However, the  $\Delta n$  is slightly lesser than the published data which varies from 0.005 to 0.009 (Sinkankas, 1981). No correlation between RI and alkali amount is observed in our sample suite (Table 4 and Fig. 3.4.1).

Adams, 1953, determined  $n_\omega$  of more than 130 aquamarine-type beryls in order to establish a correlation between colour and RIs and thus to obtain some measure of BeO content of beryls, based on the fact that most aquamarines are richer in BeO than alkali rich beryls, in which Be has been replaced considerably. A correlation was established that RI decreases

with the increase in BeO. Generalisations have been made regarding the RIs, colour and chemical compositions. For example white, very pale blue and blue green are expected to have high RIs and low amount of BeO. Green, yellow green, golden yellow or pale brown varieties of beryl have low RIs and higher amount of BeO. As a rule, rose, pink, peach and apricot coloured varieties hold highest indices as they are rich in alkalis. Some emeralds possess high amount of alkalis and hence higher RIs than aquamarine varieties. However, there are also other explanations. Gibbs et al., 1968, Bakakin et al., 1969, 1970 and Morosin, 1972 have found that RIs are mainly affected by:

(a) Tetrahedral substitution of  $\text{Si}^{4+}$  by  $\text{P}^{5+}$  or  $\text{B}^{3+}$ , and possibly minor  $\text{Al}^{3+}$ . This kind of substitution in large amount is only on a small scale (Feklitchev and Razina, 1967). The real effect of this substitution mechanism on optical properties or RI cannot be predicted as this has not been sufficiently characterized.

(b) Octahedral substitution of  $\text{Al}^{3+}$  by  $\text{Fe}^{3+}$ ,  $\text{Cr}^{3+}$ ,  $\text{V}^{3+}$ ,  $\text{Sc}^{3+}$  and  $\text{Ti}^{4+}$ . This substitution is common in most genetic types of beryl and may attain considerable levels in some varieties (Feklitchev, 1964). The ionic refractivities of all these species are higher than that of  $\text{Al}^{3+}$  (Feklitchev, 1964). Hence, this type of octahedral substitution will give rise to an increase in the RIs of beryl.

(c) Octahedral substitution of  $\text{Al}^{3+}$  by  $\text{Mg}^{2+}$ ,  $\text{Mn}^{2+}$ ,  $\text{Ni}^{2+}$  and  $\text{Fe}^{2+}$ . As in (b), this substitution is also very common in many types of beryl. This substitution produces a charge imbalance in the structure that is generally compensated by mono valent cations entering the channel. As shown by Schaller et al, 1962, the increase in RIs is much steeper than for substitutions of type (b) because of the additional effect of the alkalis.

(d) Tetrahedral substitution of  $\text{Be}^{2+}$  by  $\text{Li}^{+}$ , coupled with alkalis,  $\text{Ca}^{2+}$ ,  $\text{Ba}^{2+}$  and  $\text{Sr}^{2+}$  in the channels to balance the charge deficiency produced by the substitution. Although  $\text{K}^{+}$ ,  $\text{Rb}^{+}$ ,  $\text{Li}^{+}$  and the alkaline-earth elements are generally minor components in the channels, both  $\text{Na}^{+}$  and  $\text{Cs}^{+}$  accomplish substantial levels. Most authors do not take  $\text{Ca}^{2+}$  into consideration when plotting alkali contents vs. RIs. However, Ca must occupy the channel sites in the beryl structure (Simpson, 1948; Feklitchev, 1964 and Yurgenson, 1965). Černý and Hawthorne, 1976 also included CaO and found a positive trend in the sum of alkali oxides vs. RIs. The ionic refractivity of Ca indicates that CaO should increase the RIs by three times the rate of  $\text{Na}_2\text{O}$  (Feklitchev, 1964).

(e) Hall and Walsh, 1971 noticed the effect of molecular water in the channels on RI which has not been recognized by most authors, although it has a prominent effect. In Mg-cordierite (Schreyer and Yoder, 1964),  $n_{\omega}$  is found to increase by 0.009 for each wt% of channel water. Pankrath and Langer, 2002 induced water in beryl channel at high P-T experimentally and found a positive correlation between RIs and water content. In order to

get a trend between RIs and different elements probably more samples should be investigated.

**4.3 EMPA:** Formula calculation from the partial analysis, obtained by EMPA is problematic, because of BeO as a major element, Li<sub>2</sub>O as a minor element and the valence state for Fe can not be determined. In first step, the total amount of Fe is assumed to be FeO and the formulae are calculated with the theoretical value of 13.88 wt% for BeO. This value might actually deviate according to tetrahedral substitutions, but all analyses calculated with this procedure yielded cation coefficients for Be between 2.96 and 3.10 (Table 3). Therefore we conclude that at least as a first approximation, the calculated cation coefficients can be evaluated in terms of crystal chemistry and possible substitutions.

All analysis except data from PAD-1 and BA-1 have values  $\leq 6.00$  for Si and  $\leq 2.00$  for Al (Fig. 3.3.2). This indicates that the substitution of Si+channel vacancy= Al+Na (or any other coupled substitution of Al for Si) is unlikely. A value of Si  $\geq 6.00$  as in the case of PAD-1 possibly indicates a minor amount of Si in the Be-tetrahedron. Si in Al-octahedral coordination is unlikely in samples of low pressure origin. Si-Al plots do not indicate a substitution of Al in Si tetrahedron or Si in Al octahedron (Fig. 3.3.2). All samples show both tetrahedral and octahedral substitution. Samples from Minas Gerais, Brazil show a negative trend in Si vs Na+Cs plot. This trend is slightly seen in the samples from Dassu Mines but not visible in the samples from Yuno village (Fig. 3.3.3). BSE image of PA-2 shows a zone (Fig. 3.3.1a) rich in Na and Cs. The alkali rich beryls are found to be depleted in Si and Al. A negative trend is observed in the Fe-Al (apfu) and Fe-Si (apfu) plots of the samples from Minas Gerais, Brazil (Fig. 3.3.5, 6) suggesting the substitution of Fe in Al octahedron and also Si tetrahedron. Al vs Na+ Cs plot (Fig. 3.3.4) has a negative trend which could be due to the substitution of divalent cations in the Al octahedron and the resulting charge deficiency is compensated by the incorporation of Na<sup>+</sup> and Cs<sup>+</sup> in the channel. As Be and Li are not measured in this work, the substitution in Be tetrahedra are not very clear. Many authors have established the fact that Li<sup>+</sup> is substituted in Be tetrahedra and the charge deficiency due to the substitution of monovalent cation in Be tetrahedra and Al octahedra is compensated by the incorporation of cations in the channel.

Chemical analyses of natural beryls generally deviate from the ideal chemical composition comprising of main elements Be, Al and Si and point to the presence of significant amounts of additional components particularly water and the alkali elements. The geochemical and paragenetic characteristics of parent pegmatites are strongly reflected through these variations in the chemical composition of beryl and this affects the physical as well as optical properties. Based on the alkali variation, Černý, 1975 modified a scheme proposed by Beus, 1960 to distinguish 1) alkali free beryl, 2) alkali-poor potassic and sodic-potassic beryl, 3) sodic beryl and 4) sodic-lithian beryl. He has shown that alkali content of beryl may be used quantitatively to further delineate the geochemical characterization of pegmatites and to identify petrogenetically related pegmatite groups. According to the chemical analysis, all

samples except CA-1, BAA-1 and BAA-2 can be classified into alkali free normal beryls which are typical of miarolitic pegmatites. BAA-2 and CA-1 can be grouped into alkali rich beryls. MgO and K<sub>2</sub>O were measured in BA-1, PA-2 and FH-3 and found below detection level. Hence these elements were not measured in other samples. As Li is not measured in this work, geochemical characterization of the parent pegmatites and to identify petrogenetically related parent pegmatites is complex.

**4.4 X-ray diffraction analysis:** By Rietveld refinement of XRD data, the lattice constants *c* and *a*-parameters were obtained. Table 5 shows that *c*-parameter ranges from 9.1920 (BA-1) to 9.2201 Å (CA-1) and *a*-parameter ranges from 9.2087 (PAD-4) to 9.2177 Å (BAA-2). According to Aurisicchio et al., 1987, based on the ratio of lattice parameters *c/a*, beryls can be classified into three groups: 1) octahedrally substituted beryls with their *c/a* ratio less than 0.997 with substitutions in the O site: Me<sup>3+</sup>Al<sub>-1</sub> or R<sub>f channel</sub><sup>+</sup> Me<sup>2+</sup>□<sub>-1</sub> Al<sub>-1</sub>, 2) tetrahedrally substituted beryls with their *c/a* ratio more than 0.999 to 1.003 with substitutions in T' site: R<sub>f channel</sub><sup>+</sup> Li<sup>+</sup>□<sub>-1</sub> Be<sub>-1</sub> and 3) normal beryl group with *c/a* ratio as 0.997-0.998 which shows a composition close to ideal stoichiometry with a very low degree of substitution in both sites. Based on this classification, out of 21 beryl samples 18 are normal beryls, 2 alkali rich beryls which are tetrahedrally substituted and the last BAA-1 being in the border line with its *c/a* ratio as 0.9987 (Fig. 3.5.2).

As shown in Fig. 3.5.3 and 3.5.4, there is a negative correlation between Al-content and the *a*-parameter and a slight positive correlation between Fe-content and *a*-parameter. Substitution of divalent ions, as their ionic radius is larger than Al<sup>3+</sup> radius, increases the cation-oxygen bond length in the octahedron; this octahedron, constrained by the short edges shared with Be tetrahedra, is flattened in the *c*-direction, and therefore the increase in length influences directly the value of the *a*-parameter (Aurisicchio et al., 1988). Fig. 3.5.5 shows that *c*-parameter increases with the increase in alkali content in the channel suggesting that the substitution of Li in Be tetrahedra increased the Be-O distance. As a result, the *c*-parameter also increased due to subsequent charge compensation by the incorporation of alkalis in channel.

Rietveld refinement of alkali rich beryl (CA-1) indicates that Na occupies 2b position (0, 0, 0) and water molecule 2a position (0, 0, 0.25) in the channel. Inter-atomic distances were determined using DISAGLE of GSAS software during the Rietveld refinement. It is observed that the increase in Na results in decrease of Si-O<sub>1</sub> bond length and increase in Be-O<sub>1</sub> bond length (Fig. 3.5.1a, b). This suggests that Li<sup>+</sup> could have been substituted in Be<sup>2+</sup> tetrahedra and the charge deficiency is compensated by Na incorporation in the channel.

Two models have been proposed in order to explain the alkali variations in beryl. A coupled substitution in the form Al<sup>3+</sup> is getting substituted by Li<sup>+</sup>, and Be<sup>2+</sup> substitutes in Al octahedra with additional alkalis entering the channel to compensate charge deficiency was proposed by Beus (1960). The equation  ${}^{\text{VI}}\text{Li}^{+} + {}^{\text{IV}}\text{Al}^{3+} + \square\text{Na} = {}^{\text{VI}}\text{Al}^{3+} + {}^{\text{IV}}\text{Be}^{2+} + \square$  represents the substitution mechanism. Evan and Mrose, 1966 supported this proposal on the basis of

preliminary refinements of pure synthetic beryl and Cs rich beryl. Belov, 1958 proposed substitution of  $\text{Be}^{2+}$  by  $\text{Li}^+$  and this was supported by Bakakin et al., 1969 through partial refinements of a Cs-Li beryl. Even though both mechanisms are supported by the refinement results, the problem is still unresolved.

Along with the alkali variation in beryl, the site occupancies of channel alkalis are also unanswered. Bakakin and Belov, 1962 proposed that Na, Ca and excess Li occupy the 2a site (in the plane of  $\text{Si}_6\text{O}_{18}$  rings) and Cs, Rb and K occur in the channel between 2a and 2b positions. Model proposed by Feklitchev, 1963 suggests that the alkalis occupy 2b position with channel water molecule in 2a position. Vorma et al., 1965 suggested that the channel alkalis and water molecule occupy the 2a position based on the ratio of intensities of reflections for a series of alkali rich beryls. Evan and Mrose, 1966 indicated that Cs occupy 2a position. Gibbs et al., 1968 and Morosin, 1972 suggested that water molecules in alkali free synthetic beryl occupy 2a position. Depending upon the presence or absence of alkalis, the role of water in the channel seems to vary. The current consensus places the three main alkali metals into three different sites.  $\text{Li}^+$  substitutes for  $\text{Be}^{2+}$  in the tetrahedra linking the six-membered  $\text{Si}_6\text{O}_{18}$  ring with  $\text{Na}^+$  and  $\text{Cs}^+$  in the channel to compensate the charge deficiency. Na is placed in the centres of individual rings of tetrahedra, but the larger  $\text{Cs}^+$  is located halfway between these centres (Hawthorne and Černý, 1977, Artioli et al., 1993, Sheriff et al., 1999, Černý, 2002 and Hawthorne and Huminicki, 2002).

The current study agrees with the proposal of Feklitchev, 1963 that Na occupies 2b position and water occupies 2a position in the channel and also the substitution mechanism proposed by Hawthorne and Černý, 1977, Artioli et al., 1993, Sheriff et al., 1999, Černý, 2002 and Hawthorne and Huminicki, 2002 ( $\text{Li}^+$  substitution in Be tetrahedra and charge deficiency is compensated by incorporation of alkalis in the channel). However, it contradicts observations of Aurisichhio, 1987 that Si-O<sub>1</sub> bond length increases with the increase in Na content.

**4.5 Inclusions:** Microscopic investigations of thin sections revealed the presence of number of inclusions in all the samples. The sample BA-1 from Minas Gerais is characterized by the presence of long growth tubes resulting into cavities at the top (Fig.3.2.1, 2.2a, b). The fluid inclusions are found to be concentrated at the boundary of these hollow channels (Fig. 3.2.2a, b) and a bunch of parallel inclusions terminate at these cavities (Fig. 3.2.2a) indicating the probability of the formation of hollow cavities by these fluid inclusions. These cavities are long and are running parallel to c-axis. In some places, they follow the symmetry of the basal pinacoid (Fig. 3.2.2b). Negative crystals (negative crystals are the general term for empty cavities in a crystal) and tubular inclusions parallel to c-axis were included in the oriented negative crystals group (Cameron et al., 1953). The black arrow in Fig. 3.2.2a gives an example of disseminated irregular inclusions which do not follow any crystallographic orientation. Fluid inclusions which are of round shape in FH-3 are enriched in Ca and S indicating  $\text{CaSO}_4$  daughter crystals and are aligned parallel to each other in bands. The bands

have higher content in Na, Cs and Mg too (Fig. 3.2.2c, 3.2.5b). As the sample was highly corroded, the faces were unrecognizable. It was not possible to determine the alignment of the inclusions with respect to crystallographic orientation. The shape of the inclusions in PA-2 (Fig.3.2.2d) varies from irregular to triangular. Irregular inclusions are distributed along a fracture suggesting secondary origin. Black arrow in Fig. 3.2.3a points to rectangular shaped two-phase inclusions oriented perpendicular to c-axis. These types of inclusions were present only in PAY-1. Elongated tubular inclusions in PAD-8 are crystallographically controlled as they are aligned parallel to c-axis indicating they are of primary origin (Fig. 3.2.4d). The fluid inclusions in PAD-4 (Fig.3.2.4a) are concentrated along a fracture suggesting secondary origin.

Most of the chemically analysed fluid inclusions are of two phases (liquid and gas) and are enriched in Ca and S and in some Na, K, Cl or Fe are also found. I conclude that the fluids and/or the daughter crystals in the fluid inclusions are rich in KCl, NaCl and  $\text{CaSO}_4$ . Among solid inclusions, clay, iron oxide and muscovite are found to be common. Thin, elongated and flaky muscovite in PAY-5 is found as clusters (Fig.3.2.6b). Zircon is also found as inclusion in PAY-6 (Fig.3.2.6a).

Fluid inclusions in the investigated samples can be categorized into 3 types based on classification of Cameron et al., 1952: 1) tubular inclusions with their long axes parallel to c-axis of the crystal (Fig. 3.2.4d), 2) round, elongated, polygonal or irregular inclusions un-oriented with respect to crystallographic elements (Fig. 3.2.2a,b,c) and 3) round, elongated, irregular inclusions along the fractures (Fig. 3.2.2d, 3.2.4a).

The study of inclusions is widely used by the gemmologists to recognise natural gem stones from the synthetic ones. Because of the fluids used in the synthesis of most gems in the laboratory usually are quite unlike those present in nature (Roedder, 1982). The inclusions manifest the identifying characteristics of the pegmatitic growth process. Aquamarine is often traversed by fine growth tubes parallel to c-axis in concurrence with the structural peculiarities of beryl having hollow channels between silicate rings (Gübelin, 1953). These inclusions known as "rain" are used as a positive identification of aquamarine by gemmologists. According to Gübelin, 1953, the beryl structure causes the development of growth tubes either hollow or filled with foreign substances.

## 4.6 Vibrational spectroscopy:

### 4.6.1 IR spectroscopy:

**Pellet method:** The IR spectra studies of beryl have been done by two methods in four different ranges to study the finger print region and presence of volatiles in the channel: 1)  $400\text{ cm}^{-1}$  to  $1400\text{ cm}^{-1}$  (KBr pellet method), 2)  $1400\text{ cm}^{-1}$  to  $1700\text{ cm}^{-1}$ , 3)  $2200\text{ cm}^{-1}$  to  $2400\text{ cm}^{-1}$  and 4)  $3500\text{ cm}^{-1}$  to  $3800\text{ cm}^{-1}$  (single crystals under polarised light). Here an attempt is made to find out a criterion to distinguish the spectra of alkali poor (normal) and alkali rich (tetrahedrally substituted) beryls from the spectra in the finger print region.

Infrared spectra of the samples show two strong peaks around  $1200\text{ cm}^{-1}$  and  $960\text{ cm}^{-1}$  in the finger print region. The peak at  $960\text{ cm}^{-1}$  has comparatively higher intensity than  $1200\text{ cm}^{-1}$ . The band around  $1200\text{ cm}^{-1}$  is seen in alkali poor samples at  $1206\text{ cm}^{-1}$  (BA-1 in Fig. 3.6.1 and Fig. 3.10.17, Table 14) and gradually shifts towards  $1178\text{ cm}^{-1}$  in alkali rich beryl CA-1 and BAA-2 (Fig. 3.6.3,4 ). This peak is stronger and sharper in alkali poor beryls than in alkali rich ones.

The negative trend in the amount of Na+Cs (apfu) and IR band position around  $1200\text{ cm}^{-1}$  shows that the increase in the amount of alkali greatly affects the band at  $1200\text{ cm}^{-1}$  which causes lengthening of the bond and as a consequence, it shifts towards lower frequency region (Fig 3.6.7). Hence the band around  $1200\text{ cm}^{-1}$  is found at  $1206\text{ cm}^{-1}$  in BA-1, which has a low alkali content and it shifts towards  $1176\text{ cm}^{-1}$  in alkali rich CA-1 and BAA-2. According to Hooke's law  $\nu = \left(\frac{1}{2\pi}\right)\sqrt{k/\mu}$  { $\nu$  is the frequency,  $k$  is the force constant and  $\mu = m_1m_2/(m_1 + m_2)$ }, the vibrations of bonds involving lighter elements will be found at higher frequency. The bond strength of Be-O vibration is higher than Al-O because the atomic mass of Be is 9 amu and that of Al is 26 amu. The atomic mass of Si is 29 amu which is much higher than Be. The Rietveld refinement and inter-atomic distances of the alkali rich and normal beryl show that increase in Na amount gives rise to the decrease of Si-O bond length and increase in Be-O bond length as explained before in the XRD results section (Fig. 3.5.1). The inter-atomic distance of Al-O in beryl is around  $1.9\text{ \AA}$  and that of Be-O is  $1.66\text{ \AA}$ . Hence we can rule out Al-O vibration to be at  $1200\text{ cm}^{-1}$ . Many authors have stated that the bands at higher frequency are difficult to be assigned as there is overlapping of Be-O and Si-O bands.

In addition, in BAA-1 (medium alkali oxide content) two shoulders are developed around  $1140\text{ cm}^{-1}$  and  $1060\text{ cm}^{-1}$  (Fig. 3.6.2). In alkali rich beryl, a broad shoulder develops at  $1020\text{ cm}^{-1}$  and splits into two bands causing a doublet at  $1020\text{ cm}^{-1}$  and  $1060\text{ cm}^{-1}$  (Fig 3.6.3,4). Plyusnina, 1964, 1967 has explained the presence of these bands due to the variation in the lengths of external bonds Si-O-Be and Si-O-Al. Huong, 2010 has explained that the shoulder at  $1140\text{ cm}^{-1}$  is due to M-O vibration where M is the cation which is substituted in Si tetrahedron.

The band at  $808\text{ cm}^{-1}$  is assigned to Be-O bond by Aurisicchio et al., 1994. The plot of the band at  $808\text{ cm}^{-1}$  vs. alkali amount shows a positive trend. In alkali poor beryl this band is found at  $808\text{ cm}^{-1}$  and in alkali rich beryls around  $820\text{ cm}^{-1}$  showing a shortening of bond in alkali rich beryl (Fig. 3.6.9). If the change in bond length is related to alkali substitution, there will be lengthening of bond instead of shortening as ionic radius of alkalies (extra frame work cations in the channel) are larger than Be. Here, shortening of bond could be due to the vacancy substitution from within the crystal structure. Hence, gradual shortening of the bond with increase in alkali, probably indicate the substitution  $2\text{Al}^{\text{IV}} + \square^{\text{IV}} = 3\text{Be}^{\text{IV}}$  or  $2\text{Be}^{\text{IV}} = \text{Si}^{\text{IV}} + \square^{\text{IV}}$ . The weak shoulder at  $560\text{ cm}^{-1}$  is due to the substitution of Li in Be tetrahedra (Aurisicchio et al., 1994). It appears initially as a shoulder and absorbance

increases progressively with the entry of  $^{IV}\text{Li}$  into the  $^{IV}\text{Be}$  site. This weak shoulder is also visible in CA-1 and BAA-2, which are rich in alkalis (Fig. 3.6.3, 4). Alkali rich samples have another weak shoulder around  $450\text{ cm}^{-1}$  and  $413\text{ cm}^{-1}$  (Fig.3.6.2,3,4), which are not reported so far, could be due to the M-O vibration. Table 15 summarises all the literature information on IR studies of beryl.

Table 15 IR vibration band assignment for beryl by different authors

Wave number $\text{cm}^{-1}$	Tarte, 1965	Plyusnina & Surzhanskaya, 1967	Gervais & Pirou, 1972	Adam & Gardner, 1974	Hofmeister et al, 1987	Manier Glavinaz et al, 1989	Auriscchio, 1994	Makresk & Jovanovski, 2009
1200		Be-O	Si-O	Si-O	Si-O	Si-O	Si-O	Si-O
1020			Si-O		Si-O	Si-O		Si-O
960		Si-O	Si-O		Si-O	Si-O	Si-O	Si-O
810		Be-O	Si-O	Si-O	Be-O		Be-O	Be-O
740					Be-O			Be-O
680					Be-O			Be-O
650								Ring
590	Li-O							Ring
520	Li-O	Si-O-Al	Si-O				Al-O	O-Si-O
490	Li-O	Si-O-Al	Si-O				Al-O	Al-O
438	Li-O	Si-O-Si					Al-O	$\text{SiO}_4$

Several authors have suggested Li substitution in Be tetrahedra and the charge deficiency is compensated by Na in the channel as it was discussed in XRD results. When we consider this argument and the inter-atomic distances obtained from the refinement of alkali rich CA-1 and alkali poor beryl BA-1, the band at  $1200\text{ cm}^{-1}$  could be assigned to Be-O vibration as described by Plyusnina and Surzhanskaya, 1967 instead of Si-O vibration as most of the authors have proposed. The incorporation of channel cations in the channel could be mainly due to Li substitution in Be tetrahedra and or divalent cations into Al octahedra as is evidenced by interatomic distance and IR spectra. The  $c/a$  ratios of CA-1 and BAA-2 (1.002) show that they are tetrahedrally substituted beryls (substitution in Be tetrahedra; Auriscchio et al., 1994) and hence it can be recommended that in tetrahedrally substituted beryl, the band at  $1200\text{ cm}^{-1}$  is found at lower frequency. With the increase in the tetrahedral substitution, Be-O bond length increases consequently bond strength decreases and the band is found around  $1180\text{ cm}^{-1}$ . In synthetic flux grown beryl normally the peak at  $1200\text{ cm}^{-1}$  is observed around  $1206\text{-}1207\text{ cm}^{-1}$  as they were formed in alkali free environment. It was used as a criterion to identify natural emeralds from the synthetic by Huang, 2008.

From this work it can be concluded that out of 21 samples, BAA-2 and CA-1 are tetrahedrally substituted alkali rich samples. Tetrahedral substitution can be evidenced by the presence of two split bands at  $1020\text{ cm}^{-1}$  and  $1060\text{ cm}^{-1}$  instead of one band at  $1020\text{ cm}^{-1}$ . Also the

band at  $1200\text{ cm}^{-1}$  can be used as a criterion to distinguish between tetrahedrally substituted and normal beryls. The band at  $1200\text{ cm}^{-1}$  could be assigned to Be-O vibration.

**Single crystal investigation:** IR spectroscopy is a very useful method in identifying the kind of treatment used in beryl especially emerald to enhance its gemmological value by fracture filling with different types of organic materials. Organic materials have peaks in the region from  $2000$  to  $3000\text{ cm}^{-1}$  frequency. Here this method is applied on beryl to study vibrations of bonds and substitution in crystal lattice and also to locate  $\text{H}_2\text{O}$  and  $\text{CO}_2$  in the channel.

$E||c$  polarised spectra show two sharp absorption bands around  $3700$  and  $3600\text{ cm}^{-1}$  (Fig. 3.6.10,11,12,13). According to Wood and Nassau, 1967 and 1968, these bands can be assigned to  $\nu_3$  (asymmetric stretching) and  $\nu_1$  (symmetric stretching) vibration modes of type I and type II  $\text{H}_2\text{O}$  respectively (Fig. 4.1).  $\nu_3$  shifts from  $3695\text{ cm}^{-1}$  to  $3700\text{ cm}^{-1}$  and  $\nu_1$  mode is more or less constant at  $3596.7\text{ cm}^{-1}$  except in PAD-1 at  $3600\text{ cm}^{-1}$ . The band at  $1631\text{ cm}^{-1}$  is assigned to  $\nu_2$  vibration (bending frequency) of type II  $\text{H}_2\text{O}$ . In most of the samples,  $\nu_2$  band of type II  $\text{H}_2\text{O}$  is seen around  $1631\text{ cm}^{-1}$  (Fig. 3.6.10,12,13).

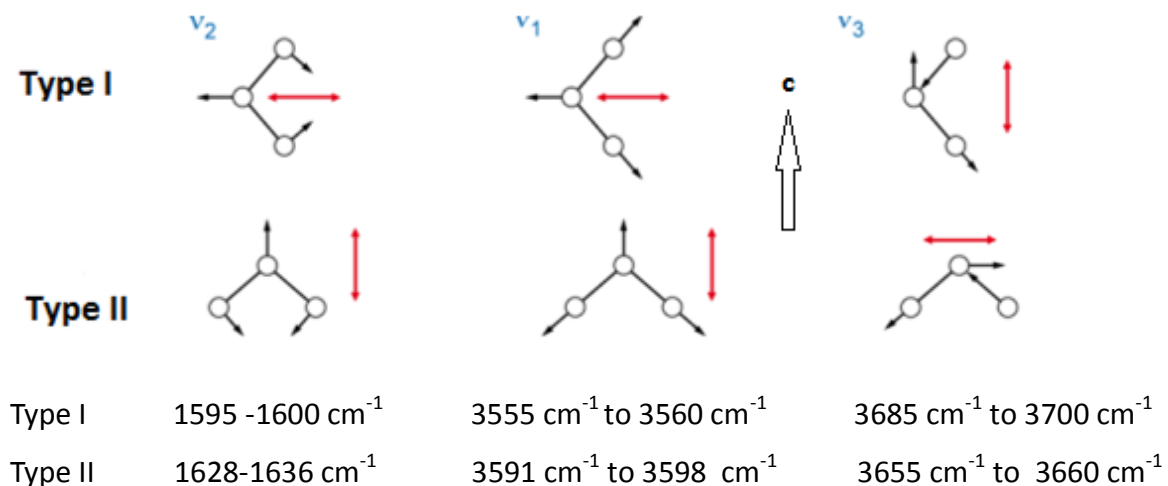


Fig. 4.1 Vibrations of type I and type II  $\text{H}_2\text{O}$  molecules in the channel of beryl.  $\nu_2$ - bending mode,  $\nu_1$  - symmetric stretching mode  $\nu_3$ - asymmetric stretching mode. Red arrows indicate changes in the dipole moment in order to be visible by optical spectroscopy (modified from Wood and Nassau, 1967, Lodzinski et al., 2005) and large black arrow points to the c-direction.

$E||a$  polarised spectra showed absorption around  $3660\text{ cm}^{-1}$  and  $3865\text{ cm}^{-1}$ . Aurisicchio et al., 1994 suggested that the band at  $3660\text{ cm}^{-1}$  is mainly due to  $\nu_3$  mode of type II  $\text{H}_2\text{O}$  molecule. Wood and Nassau, 1967 have found most of the  $\pi$  polarised lines are accompanied by two  $\sigma$  polarised lines approximately separated by  $170\text{ cm}^{-1}$ . They assigned the band at  $3865\text{ cm}^{-1}$  to combined vibration-rotation energy "sum" level of  $\nu_3$  mode of type I  $\text{H}_2\text{O}$  molecule.  $E||a$  polarised spectra also show a strong absorption around  $2360\text{ cm}^{-1}$  (Fig.

3.6.10, 11) except PA-2. This band was assigned by Wood and Nassau, 1967 to asymmetric stretching vibration mode ( $\nu_3$ ) of  $\text{CO}_2$  molecule. In all the samples investigated here, the band is seen in the range 2359 and 2361  $\text{cm}^{-1}$  and no other band was found in this region at 2340  $\text{cm}^{-1}$ . A band is also visible at 1590  $\text{cm}^{-1}$  which is assigned to  $\nu_2$  mode of type I  $\text{H}_2\text{O}$  molecule.

The band around 1940  $\text{cm}^{-1}$  is present irrespective of the orientation; however the intensity varies depending on the orientation (Fig. 3.6.10, 11, 12). This band can be assigned to the first overtone absorption of a lattice mode, Si-O band at 960  $\text{cm}^{-1}$  agreeing the observations of Wood and Nassau, 1968 and Aines and Rossman, 1984.

The band at 5274  $\text{cm}^{-1}$  with electric vector parallel to c-axis, which is equivalent to 1896 nm found in NIR spectra, has been assigned to the vibrations of combination of  $\nu_2$  and  $\nu_3$  (bending and asymmetric stretching) modes of type I  $\text{H}_2\text{O}$  molecule by Wood and Nassau, 1967. In all the samples, irrespective of chemical composition this band is observed at 5274  $\text{cm}^{-1}$  (Fig. 3.6.10, 11, 12).

$\text{CO}_2$  features were recorded by Leung et al., 1983 and Stockton, 1987 in the range 2200  $\text{cm}^{-1}$  and 2400  $\text{cm}^{-1}$ . Leung et al., 1983 noticed that synthetic emeralds do not show any band of  $\text{CO}_2$  around 2360  $\text{cm}^{-1}$ . Stockton, 1987 found two bands at 2340  $\text{cm}^{-1}$  and 2358  $\text{cm}^{-1}$  of  $\text{CO}_2$  in this region in both natural and synthetic, and proved that the band at 2358  $\text{cm}^{-1}$  is always stronger in natural emeralds. All literature information on IR studies of beryl in the water region is summarised in Table 16.

In current studies, the bands in alkali poor (BA-1 with  $\text{Na}_2\text{Owt}\%$  0.03) as well as alkali rich beryl are visible at 3596 to 3600  $\text{cm}^{-1}$  and 1631  $\text{cm}^{-1}$ . According to Aurisicchio et al., 1994, the samples with no Na has a maximum absorbance at 3600  $\text{cm}^{-1}$ . In samples with medium to high Na content, it shifts to 3588  $\text{cm}^{-1}$  and the presence of both Na and Cs causes the absorption band to be close to 3595  $\text{cm}^{-1}$  to 3597  $\text{cm}^{-1}$ . In the current work, even though most of the samples have very little or no Cs, the absorption bands are found around 3596  $\text{cm}^{-1}$ . However, the ratio of intensity of the bands around 3600 and 3700  $\text{cm}^{-1}$  could be used as a criterion to associate with Na content as suggested by Aurisicchio et al., 1994 and Huong, 2008. Fukuda and Shinoda, 2008 assigned the band at 1625  $\text{cm}^{-1}$  to doubly coordinated ( $\text{H}_2\text{O-Na-OH}_2$ ) and the band 1631  $\text{cm}^{-1}$  to singly coordinated ( $\text{H}_2\text{O-Na-}\square$ ) type II  $\text{H}_2\text{O}$  molecule. In the investigated samples above, the absorption bands are around 1630  $\text{cm}^{-1}$  probably indicating the presence of singly coordinated type II  $\text{H}_2\text{O}$  molecules or in other words alkali poor samples might be having singly coordinated type II  $\text{H}_2\text{O}$  molecules. Alkali poor samples have peak with higher intensity around 3700  $\text{cm}^{-1}$  as compared to alkali rich beryl (Fig.3.6.12, 13).

From the above results we can conclude that both alkali poor and rich samples have type I and type II H<sub>2</sub>O molecules. Further studies are required to establish the relationship between water band position and alkali amount. However, the intensity ratio of the bands around 3600 cm<sup>-1</sup> and 3700 cm<sup>-1</sup> vary according to the amount of type of H<sub>2</sub>O molecules present in the channel.

Table 16 IR studies of beryl samples in the water region by different authors

No	Authors	Experimental conditions	Observations and conclusions
1	Wood and Nassau, 1967,68	Natural beryl	Studied 1500 cm <sup>-1</sup> to 1700 cm <sup>-1</sup> and 3400 cm <sup>-1</sup> to 3800 cm <sup>-1</sup> . They have assigned deformation modes in the range 1400 cm <sup>-1</sup> to 1700 cm <sup>-1</sup> and stretching modes in the range 3400 cm <sup>-1</sup> to 3800 cm <sup>-1</sup> as discussed in the above paragraph.
2	Kodaira et al., 1983	Flux grown water free beryl crystals in 0.1 N NaOH solution at 600°C and 10 kilobar pressure for 24 hours	Infrared spectra showed two sharp (OH) stretch bands at 3680 and 3590 cm <sup>-1</sup> .
3	Schmetzer and Kiefert, 1990	Natural and synthetic emeralds	Water molecules can either exist alone or with alkalis (mainly Na). If there is an alkali ion nearby, H <sub>2</sub> O type II may be associated with this ion in two ways; H <sub>2</sub> O-Na-OH <sub>2</sub> or H <sub>2</sub> O-Na-□, in which □ represents a vacancy of water in the channel sites. Additionally, they found that hydroxyl ions (OH <sup>-</sup> ) can also be associated with alkali ions in a sequence like HO-Na-□.
4	Fukuda and Shinoda, 2008, 10	Anhydrous synthetic beryl hydrated at 150MPa and 700°C for 30hours and one natural beryl to determine dehydration temperature and coordination of H <sub>2</sub> O type II and Na <sup>+</sup> cation	Hydrated synthetic beryl: Intense absorption band at 3700 cm <sup>-1</sup> due to ν <sub>3</sub> asymmetric stretching mode of type I water Natural beryl: Type I H <sub>2</sub> O molecule (ν <sub>3</sub> mode) disappeared after annealing for 8 hours. The bands at 3600 and 1625 cm <sup>-1</sup> survived after annealing at 850°C and shifted to 3589 and 1631 cm <sup>-1</sup> respectively after 24 hours of annealing. They assigned the band at 1625 cm <sup>-1</sup> to doubly coordinated type II H <sub>2</sub> O molecule (H <sub>2</sub> O-Na-OH <sub>2</sub> ) and with annealing it changed to singly coordinated (H <sub>2</sub> O-Na-□) and shifted to higher frequency of 1631 cm <sup>-1</sup> . Fukuda and Shinoda, 2010 suggested that this band could be due to the coordination of H <sub>2</sub> O type II with Li <sup>+</sup> .

**4.6.2 Raman spectroscopy:** Present work shows the position of important Raman bands of beryl under different orientations. Raman spectra are characterised by the presence of four main peaks around 1066, 685, 395 and 325 cm<sup>-1</sup>. It is observed that the band at 1066 cm<sup>-1</sup> has more intensity than that at 685 cm<sup>-1</sup> under E||c orientation (Fig. 3.7.1, 2). Under

E⊥c orientation, the intensity of the band at 1066 cm<sup>-1</sup> reduces and the band at 395cm<sup>-1</sup> is found to be stronger than at 325 cm<sup>-1</sup> (Fig. 3.7.3, 4). Adam and Gardener, 1974 assigned the bands at 1066 cm<sup>-1</sup> and 1008 cm<sup>-1</sup> to Si-O vibration. The stronger peak at 685 cm<sup>-1</sup> is assigned to Be-O vibration and the one around 325 cm<sup>-1</sup> is attributed to the vibration of ring. All Raman bands are visible in all the samples with different intensities according to the orientation. Apart from two main bands, other bands are seen around 295, 420-423, 441-445 and 1008-1010 cm<sup>-1</sup> (Si-O).

Raman spectra of beryl have been studied by many scientists. Powder Raman spectra were studied by Griffith, 1969 and he assigned some main bands to stretching vibrations of silicate rings. As predicted by Factor Group Analysis, Adam and Gardner, 1974 identified all the bands in single crystal spectra and assigned all the peaks to different vibrations. Hofmeister et al., 1987 analysed vibrational spectra of several beryllium aluminium silicates including beryl and came to a conclusion that assignment of modes in higher frequency is still not certain as both Si-O and mixed Be-O, Si-O vibration modes can exist at higher frequencies. Kim et al., 1990 calculated normal modes for beryl. Charoy et al., 1996 characterised alkali poor beryl and also channel occupancy by different spectroscopic methods. They identified that irrespective of the orientation, the intensity and position of H<sub>2</sub>O signal are similar. The bands are visible at 3606 cm<sup>-1</sup> and 3597 cm<sup>-1</sup>. The latter one is found as a shoulder. Moroz et al., 2000 used Raman spectroscopy not only for identifying natural from synthetic but also to determine the locality. Huong, 2008 has used the peak at 1067 cm<sup>-1</sup> and full width at half maximum (FWHM) in order to distinguish natural emeralds from synthetic and schist emeralds from non-schist emeralds. She found that in hydrothermal and flux emeralds, the band is seen at lower frequency (1067-1068 cm<sup>-1</sup>) and FWHM (11 to 14 cm<sup>-1</sup>) is found to be lower than natural (in schist type the values are 1069 - 1072 cm<sup>-1</sup> and 19 - 26 cm<sup>-1</sup> and in non-schist type at 1068 - 1070 cm<sup>-1</sup>). Table 17 summarises all literature information on Raman spectroscopic studies on beryl.

Table 17 Band positions in the Raman spectra of samples, their assignments by different authors, orientation and their intensities

Band position cm <sup>-1</sup>	Adam and Gardener, 1974	Kim et al., 1995	Charoy et al., 1996	Moroz et al., 2000	Huong and Hofmeister, 2008	Orientations and the intensity of the bands
295	Ring				--	Weak
325	Ring	Ring	Ring	Ring	--	Moderately strong
395	Ring	Ring	Ring	Ring	--	E⊥c orientation, the band at 395 is stronger than 325 cm <sup>-1</sup>
685	Be-O		Be-O	--	--	Strong
1006	Si-O	Ring	Si-O	Ring	--	Weak
1065	Si-O		Si-O		Si-O	Very strong when E  c, weak when E⊥c

In the water region (3500-3700  $\text{cm}^{-1}$ , Fig. 3.7.5) of the spectra, all samples have a peak at 3608  $\text{cm}^{-1}$ , which does not change its position. BA-1 which is alkali free or poor has a strong peak at 3608  $\text{cm}^{-1}$  and a dent is developed at 3602  $\text{cm}^{-1}$  (Fig. 3.7.5). However, this band develops a shoulder at 3596-3598  $\text{cm}^{-1}$  and it intensifies with the increase in alkali content in PAD-8 (Fig. 3.7.5). Raman spectrum of PA-2 shows two small bands at 3596  $\text{cm}^{-1}$  and 3599  $\text{cm}^{-1}$ .

Wood and Nassau, 1967, 68 suggested that the band at 3608  $\text{cm}^{-1}$  is due to type I  $\text{H}_2\text{O}$  molecule (without alkali) and the band at 3598  $\text{cm}^{-1}$  is associated with the vibration of type II  $\text{H}_2\text{O}$  molecules (linked to alkali cation). Huong and Hofmeister, 2008 have demonstrated in their studies on emeralds that flux grown beryl does not have the peak in this region. Hydrothermally grown beryl is characterised by the peak at 3608  $\text{cm}^{-1}$  and all natural beryls show two peaks at 3608  $\text{cm}^{-1}$  and 3598  $\text{cm}^{-1}$  with the varying ratios of intensities. In non-schist type beryl, the peak at 3608  $\text{cm}^{-1}$  is stronger than at 3598  $\text{cm}^{-1}$ . The situation is reversed in schist type beryl. Huong and Hofmeister, 2008 have found three peaks in Raman spectra in the lower temperature ranges and studied FWHM of this broad band and suggested the possibility of existence of type IIa and type IIb  $\text{H}_2\text{O}$  molecule. Type IIa  $\text{H}_2\text{O}$  molecule is where Na is linked with water molecules on both sides and IIb is when Na is linked to water molecule on one side and other side vacant. However, they concluded that the proposals need further experimental confirmation.

Under  $E \perp c$  orientation, the spectra show a band at 1241  $\text{cm}^{-1}$  (Fig. 3.7.3, 4) and in some, a peak with much less intensity at 1385  $\text{cm}^{-1}$  (Fig. 3.7.4). These peaks are assigned to  $\text{CO}_2$ . Charoy et al., 1996 noticed reversal in intensity with orientation between the above mentioned peaks. The reason for the above phenomenon is not clear.

Raman spectra of samples with low to medium content alkali show a strong peak at 3608  $\text{cm}^{-1}$  which is due to the vibration of type I  $\text{H}_2\text{O}$  molecule and a small shoulder at 3596-3598  $\text{cm}^{-1}$  due to type II  $\text{H}_2\text{O}$  molecule which is in agreement with the previous studies.

**4.6.3 NIR spectroscopy:** Near-IR spectroscopy measures the broad overtone and combination bands of some of the fundamental vibrations and is an excellent technique for rapid and accurate quantification. The spectra of the samples in the NIR range were obtained to study overtones and combinations of vibrations of  $\text{H}_2\text{O}$  molecules in the channel with UV-Vis-NIR spectrometer.

Under  $E \parallel c$  orientation in transmitted and reflected unpolarised light, the spectra is characterised by two main bands around 1895 nm and 1399 nm (Fig. 3.8.1, 2, 3). Alkali poor beryl has only one peak without shoulder at 1399 nm showing the presence of combination of  $\nu_1$  and  $\nu_3$  modes of type I  $\text{H}_2\text{O}$  molecule (Table 18). In alkali rich beryls, a shoulder is developed at 1410 nm and the intensity increases gradually with the alkali content. In alkali

rich CA-1, the band at 1410 nm is stronger than at 1399 nm (Fig. 3.8.3). This peak at 1410 nm is due to the combination of  $\nu_1$  and  $\nu_3$  modes of type II H<sub>2</sub>O molecule (Wood and Nassau, 1967). The intensity of peaks at 1399 nm and 1895 nm are much higher in alkali rich beryl than in alkali poor samples. This could be due to the presence of type II H<sub>2</sub>O molecule and can be used as a criterion to differentiate alkali rich from alkali poor beryl.

Table 18 Band positions in NIR spectra of the samples and assignment to various vibrations

Band position in present work (nm)	Assignment of bands	Comments
1958 (5107 cm <sup>-1</sup> )	Combination of $\nu_2$ and $\nu_3$ mode of type I H <sub>2</sub> O molecule	E $\perp$ c
1895 (5274 cm <sup>-1</sup> )	Combination of $\nu_2$ and $\nu_3$ mode of type I H <sub>2</sub> O molecule Combination of $\nu_2$ and $\nu_3$ mode of type II H <sub>2</sub> O molecule	E  c E $\perp$ c. In alkali rich beryls this band is intense indicating the presence of type II H <sub>2</sub> O molecule. Same band is also visible under E  c orientation
1832 (5458cm <sup>-1</sup> )	Combination of $\nu_2$ and $\nu_3$ mode of type I H <sub>2</sub> O molecule	E $\perp$ c
1786 (5599 cm <sup>-1</sup> )	-----	E  c
1466 (6821 cm <sup>-1</sup> )	2 $\nu_2$ + $\nu_3$ of type I H <sub>2</sub> O molecule 2 $\nu_2$ + $\nu_1$ of type II H <sub>2</sub> O molecule	E  c and E $\perp$ c
1399 (7148 cm <sup>-1</sup> )	Combination of $\nu_1$ and $\nu_3$ mode of type I H <sub>2</sub> O molecule. Combination of $\nu_1$ and $\nu_3$ mode of type II H <sub>2</sub> O molecule	A shoulder develops around 1410nm and gets strengthened with increase in alkali. The band splits into two and in CA-1 (highest Na content of all the samples) the newly developed band has more intensity than at 1399 nm.

Hunt and Salisbury, 1970 observed that whenever water is present in the mineral, two characteristic bands appear at 1400 nm due to 2 $\nu_3$  mode and 1900 nm due to  $\nu_2$  +  $\nu_3$  mode and the presence of both bands indicate un-dissociated water molecules trapped in the channel. Wood and Nassau, 1967 had also assigned the band at 1895 nm to type I H<sub>2</sub>O molecule and the band at 1399 nm to combination of  $\nu_1$  and  $\nu_3$  modes of type I H<sub>2</sub>O molecules. The band at 1895 nm can also be attributed to  $\nu_2$  and  $\nu_3$  mode of type II water molecule. They also attributed bands at 1466 nm to the combination of vibrations of 2 $\nu_2$  and  $\nu_3$  and 1362 nm to the combination of vibrations of  $\nu_1$  and  $\nu_3$  of type I H<sub>2</sub>O molecule. The sharp peaks on both sides of 1895 nm which gets intensified under E $\perp$ c orientation, are ascribed to sum and difference bands involving rotational frequencies (Hunt and Salisbury, 1970). According to Wood and Nassau, 1967, the band at 1958 nm and 1832 nm arise due to the combination of vibrations of  $\nu_2$  and  $\nu_3$  of type I H<sub>2</sub>O molecule. Wood and Nassau, 1967 and Hunt and Salisbury, 1970 assigned the band at 1148 nm to the

combination of  $\nu_1$ ,  $\nu_2$  and  $\nu_3$  vibration of type I  $\text{H}_2\text{O}$  molecule. Hence in alkali rich beryls this peak gets intensified. Mashkovtsev and Lebedev, 1993 noticed the presence of band at 1413nm in Li and Na containing beryls.

NIR spectroscopic studies indicate that we can differentiate tetrahedrally substituted alkali rich samples from the normal beryls by the presence of an extra band around 1410 nm which gets stronger with the increase in alkali amount. The vibrational spectroscopic studies of beryl in the finger print region and also from the study of volatiles in the channels from different sources, we can differentiate alkali poor samples from the rich ones which in turn are the geochemical signatures of the parent pegmatites.

## 4.7 Scanning Electron Microscopy:

**4.7.1 Results of the current study:** The SEM images of all the samples were investigated. However,  $\{10\bar{1}0\}$  faces are given more importance based on the fact suggested by Honess, 1927 that the fundamental crystal forms of simple index are most susceptible to corrosion. He has also found that in beryl, unit prisms and base are much more soluble than other faces (Honess, 1917). Here also, the studies of natural etch pits on beryl demonstrated that the etch pit density is much higher on  $\{10\bar{1}0\}$  as compared to other faces. Hence, locating etch pits and comparison of the morphologies of the etch pits on this face of the samples from different provenances were effortlessly carried out. However, all the faces of BA-1 are studied as it showed etch pits on all the faces. Etch pits are observed on basal pinacoid  $\{0001\}$ , prism of first order  $\{10\bar{1}0\}$ , prism of second order  $\{11\bar{2}0\}$ , pyramid of first order  $\{10\bar{1}1\}$  and pyramid of second order  $\{11\bar{2}2\}$  on BA-1 Minas Gerais, Brazil (Table 19). The characteristic etch pits are not visible on all the above mentioned faces of all the samples. Hence, focus was mainly on  $\{10\bar{1}0\}$  as in most of the samples, this face showed etch pits. From the images, it is obvious that the etch pits on  $\{10\bar{1}0\}$  of the samples from different localities are different (Table 19, Fig. 3.9.13, 29, Fig. 4.2). BA-1 from Minas Gerais has isosceles trapezoidal etch pits with curved short edges, steep walls and square shaped bottom. FH-3 from Lumäki pegmatites has scalene trapezoidal etch pits with steep walls and pointed bottom, where as PAY-1 from Yuno village, Himalayas has elongated six sided to diamond shaped etch pits. Most of the samples from Yuno village and Dassu mines, Himalayas have either diamond or canoe shaped etch pits or deep solution channels parallel to c-axis.

Table 19 Etch pits on different faces of representative samples from different locations

Location	Basal pinacoid {0001}	First order prism {10 $\bar{1}$ 0}	Second order prism {11 $\bar{2}$ 0}	First order pyramid {10 $\bar{1}$ 1}	Second order pyramid {11 $\bar{2}$ 2}
<b>Minas Gerais, Brazil (BA-1, BAA-1 and BAA-2)</b>	1) Deep, hexagonal with pointed base 2) Hexagonal hollow core, deep, base not visible 3) Triangular hollow core, deep, base not visible	1) Trapezoidal to nearly rectangular, shallow etch pits with flat and broad base, centric (F-type) 2) Isosceles trapezoidal to scalene trapezoidal, deep etch pits with steep walls from square to pointed bottom (P-type) 3) Isosceles trapezoidal stepped etch pits 4) Canoe shaped etch pits with their long axes perpendicular to c-axis	1) Canoe shaped etch pits with their long axes oriented parallel to c-axis	1) Shallow triangular shaped etch pits with flat base 2) Deep triangular etch pits with steep walls and kite shaped to pointed bottom	1) Trapezoidal etch pits with steps
<b>Himalayas, Shigar valley, Yuno village and Dassu mines (PA-2, PAY suite and PAD suite)</b>	Hexagonal shaped, steep walls with pointed base	1) Nearly square shaped etch pits with square and pointed bottom. The curved edges parallel to c-axis 2) Stepped canoe shaped etch pits with long axes perpendicular to c-axis 3) Diamond shaped etch pits (F-type, P-type and stepped). 4) Many solution channels running parallel to c-axis			
<b>Lumäki pegmatites, Finland (FH-3)</b>	-----	1) Scalene trapezoidal shaped, eccentric and curved, short edges parallel to c-axis 2) Small etch pits in larger pit			
<b>Sichuan Province, China (CA-1)</b>		Very few etch pits visible. Elongated almost rectangular etch pits with curved short edges. Joining of these pits along a line at some places			



Fig. 4.2. Geometrical reconstruction of P-type etch pits on the prism face  $\{10 \bar{1} 0\}$  of the samples from different localities.

Honess, 1927 had described that the etch pits become more angular as the dissolution proceeds and the etch pits in early stages do not represent the actual symmetry of the face. Hence, the six-sided etch pits might be representing an early stage of dissolution, with increasing dissolution they would have turned into diamond shaped (Fig. 3.9.12). On the same face stepped etch pits are also discernable. Etch pits on  $\{10 \bar{1} 0\}$  of PA-2 from Shigar valley, Himalayas (Fig. 3.9.10) are more or less square shaped which is quite different from those of BA-1 and FH-3. CA-1 from Sichuan Province, China has elongated rectangular etch pits with curved short edges (Fig.3.9.13). Feklitchev, 1963 studied dissolution forms in molten alkaline and acidic solutions and found that crystals of different fields can be characterised by different sets of simple dissolution forms. The shape distribution of etch figures according to Honess, 1927 is directly attributable to the solvent and to the molecular configuration of the faces upon which they occur. The current study supports arguments by Honess, 1927 and Feklitchev, 1963 that the etch pits reflect their provenances.

All the SEM images show that the etch pits observed on the crystal faces differed based on their symmetry and provenance. However, in each etch pit morphology whether it is quadrilateral, triangular or hexagonal, the etch pits can be classified into three:

(1) etch pits with shallow, flat and broad bases (F-type); (2) etch pits which are deep with narrow bases and some places changing into pointed (P-type) and (3) stepped etch pits (Fig. 3.9.7c, b, a).

On the same crystal face, P-type etch pits and F-type etch pits can be seen (Fig. 3.9.6). Canoe shaped dissolution forms are observable on prism of second order of BA-1 (Fig. 3.9.14a, b) oriented parallel to c-axis. Only BA-1 demonstrated etch pits on  $\{11 \bar{2} 0\}$ .

On the basal pinacoid  $\{0001\}$  hexagonal etch pits are observed and are found mainly in three forms: (1) irregular to circular turning into hexagonal shallow etch pits with flat base (Fig. 3.9.2, 3a); (2) deep etch pits with steep walls meeting at a point (Fig. 3.9.1a, b); (3) deep etch pits with steep walls where bottom is hollow or not visible which are termed as hollow core (Fig. 3.9.3, 4). In some places, hollow cores (the etch pits belonging to second category) are filled with dissolution products (Fig.3.9.3b, c). Triangular shaped hollow cores are also visible on  $\{0001\}$  face of BA-1 crystal.

Canoe shaped etch pits on the prism faces are seen mainly in two forms: (1) with pointed bottoms (Fig. 3.9.7d) and (2) stepped (Fig. 3.9.11). The first category is found in quadrilateral shape (F-type etch pits) whereas shallow ones with broad and flat base are not seen among canoe shaped etch pits.

Further investigation of etch pits on the crystal faces by image analysis through etch pit shape distribution analysis on prism of first order  $\{10\bar{1}0\}$  also supports the classification of etch pits into three different groups, i.e. (1) shallow etch pits with flat bottom (F-type); (2) deep etch pits with square to pointed bottoms (P-type) and (3) stepped. The approximately rectangular etch pits on prism faces as described by Wilk, 1887 are found to be trapezoidal through their geometrical reconstruction. These trapezoids can be isosceles (Fig. 3.9.22) and scalene or quadrilateral (Fig. 3.9.23).

In BA-1, pipe-like tubular inclusions parallel to the c-axis are visible under the stereoscopic and microscopic investigations (Fig. 3.2.1, 2a, 2b). In all these images, it is quite clear that the inclusions surround hollow cores or cavities. Furthermore, a group of inclusions terminates at these cavity edges. Petersson, 1881 noticed tubular cavities running parallel to c-axis, each terminating in an etch pit made him to believe that the tubes themselves were greatly elongated solution cavities. By SEM image investigation, it is found that they outcrop at the basal pinacoids  $\{0001\}$  exhibiting in two morphologies namely triangular and hexagonal (Fig. 3.9.3, 4, 5). In the sample BAA-1, channels are not perceptible.

Griffin, 1951 observed hollow core for the first time in beryl. Extensive studies have been done on the formation of hollow crystals on cadmium iodide, silicon carbide etc. Hollow cores are often observed in vapour grown crystals. However, enough studies were not carried out in beryl. Griffin applied theory of crystal growth on beryl also. Trapping of solid inclusions on the surface at the onset of re-growth can cause the formation of tubes like two phase inclusions and this can generate dislocations (Sunagawa, 1987). Beryl has a lattice parameter approximately of 9.1 Å. This is the minimum possible Burger vector for screw dislocations to be hollow. Frank, 1951 has shown that silicates having lattice spacings of 10 Å form border line cases for the dislocations to have hollow core. Concentration of stress at the screw dislocation would result into change in velocity and orientation of the growth spiral or creation of hollow core (Sunagawa, 1987). Canoe shaped growth marks on the sides of hollow core are visible in a-axis direction (Fig. 3.9.15, 16). According to London, 2008, mineral growth in beryl and mica is forced or advances at a faster rate owing to changes in pegmatitic environment and beryl would preferentially grow along one of its a-axes. Similar kind of pipe-like hollow channels and hollow cores were observed by Tempesta et al., 2011 in the beryls from Minas Gerais, Brazil. They studied these structural defects by X-ray diffraction topography and concluded that hollow cores are mainly due to dissolution around branches of dislocations.

Formation of hollow cores could be due to growth rather than dissolution based on the above arguments. The presence of second generation beryl crystals on the inside walls of hollow cores (Fig. 3.9.15d, ana.1) support this observation. However, the clay mineral in these hollow cores indicates that they are affected later by dissolution as dislocations are preferential sites for dissolution. On BA-1, etch pits are concentrated along the spirals suggesting that growth spirals are subjected to faster dissolution than other parts, the etch pits along the spirals are shallow and flat (Fig. 3.9.2a,b,c).

On the pyramidal face  $\{10\bar{1}1\}$  of BA-1, triangular shaped etch pits are found in two forms: (1) with flat and shallow base and (2) slightly deeper with kite shaped bottom (Fig. 3.9.18b). Trapezoidal etch pits on pyramid of second order are stepped (Fig. 3.9.18c, d). A close look at the images show that continued dissolution on this face would lead to the formation of triangular shapes.

Eccentricity of a pit is a measure of the direction of the dislocation line with respect to the etching (observation) plane (Sangwal, 1987). The lengths of the diagonals of the etch pits are used here to determine the eccentricity of etch pits. Based on that, an effort is made to classify etch pits. Two groups of etch pits are found: (1) centric etch pits with two diagonals of equal length meeting at the centre of the etch pit and (2) excentric etch pits with diagonals which do not meet at the centre and hence the lengths are not equal. Eccentricity can be determined with the help of angle measurements also. Out of 4 etch pits shown in Fig. 3.9.21, three have diagonals of equal length and can be classified as centric etch pits. Most of the flat bottomed etch pits which are found on point defects are centric etch pits (Fig. 3.9.21d). According to Motzer and Reichling, 2010 and Szurgot, 2010, they can be excentric too. The etch pits can be formed due to combination of point defect and line defect (Fig. 4.3). The presence of deep etch pits with square base (P-type) are explained by this argument (Fig. 3.9.21b).

Eccentricity is mainly due to the inclination of dislocation to the perpendicular striking at the surface. With the help of information on depth of the etch pit, the angle of inclination of dislocation to the surface can be calculated. However, since the images are taken with reference to only two dimensions (height was not measured), the inclination of dislocation to the etched surface is not calculated. From the work of Motzer and Reichling, 2010 (Fig. 4.3) and this work,  $\alpha$  excentric and  $\beta$  centric can be classified into P-type etch pit,  $\gamma$  and  $\delta$  etch pit with kinked wall into stepped etch pit with pointed bottom and flat bottom respectively. P-type etch pit can be centric when it is formed above a local defect and it becomes excentric when it is formed above a dislocation. The structure of kinked wall (stepped etch pit) is explained by Motzer and Reichling, 2010 as initiated due to localised defect beneath the surface which changed the etching behaviour at a certain point of etching process. In this classification, F-type etch pit (Sunagawa, 1987) is not included.

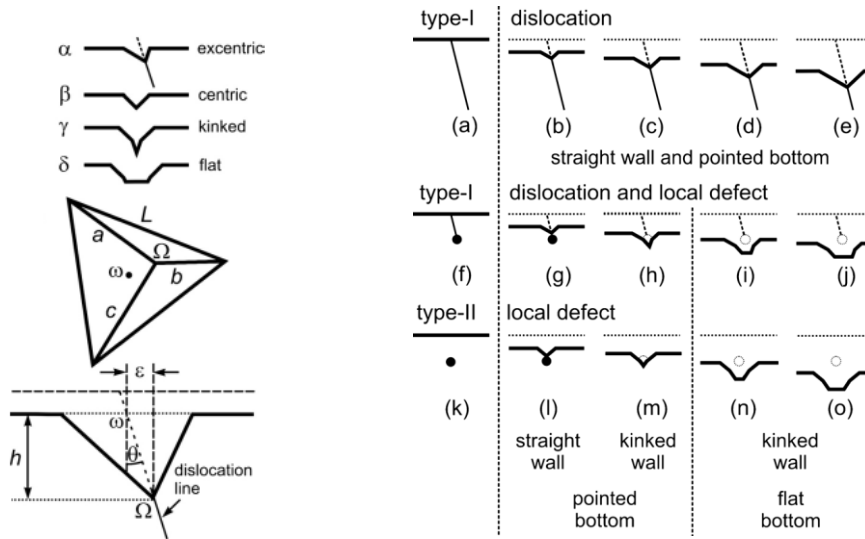


Fig. 4.3 Schematic representation of formation of different kinds of etch pits after Motzer and Reichling, 2010.

SEM can be used in the characterization of surface topography and nanoscale sub-micron particles. Since SEM images are not taken with reference to height, the characterisation of surface topography is done by texture instead of roughness which can be done in two principal planes (Thomas, 1999). Using a sinusoidal curve as a simplified model of the surface profile, the roughness can be measured at right angles to the surface in terms of wave amplitude and parallel to the surface in terms of surface wavelength. The latter one is recognised as texture. Image measurements are very useful to feature textured regions for the purposes of classification. Many natural images, especially the images of minerals subjected to dissolution show structures at all scales or high degree of roughness.

Etch pit shape distribution analysis, surface texture analysis and fractal dimension analysis of etch pits have been done by Scanning Probe Image Process software (SPIP) and Gwyddion image analysis software.

The software SPIP had calculated the values based on the following definitions: (1) Roundness (defined as:  $4 \times \text{area} / \pi \times \text{length}^2$ ) describes shapes resemble to a circle. The roundness value of a shape approaches 1, the closer the shape resembles a circle. (2) Form factor provides a measure that describes shape of a feature and is defined as  $4 \times \pi \times \text{area} / \text{perimeter}^2$ . (3) Compactness is a measure expressing how compact a feature is and defined as compactness = diameter/length. A circle will have a compactness value as 1. The compactness of a square is 1.1284. Elongated irregular features results in the value  $< 1$ . (4) Elongation (defined as length-breadth/length) is the measure of indicating how elongated a shape is. A square or a circle will retain the value zero. As these shapes change towards a long rectangle or ellipse the value converges towards 1.

From the etch pit shape distribution analysis, a clear trend is observed in different kinds of etch pits. Roundness of the etch pits decreases from F-type to P-type (Fig. 3.9.24a). It is obvious that dissolution on the locations of F-type etch pit is minimum as compared to P-type etch pits. According to Honess, 1927, the increasing dissolution causes the etch pit to be more angular. In this work also a gradual reduction in the roundness of the etch pits is observed as it progresses from F-type to P-type. A positive trend is observed in the elongation of the etch pits from F-type to P-type (Fig. 3.9.24d). Form factor and compactness decrease from F-type to P-type (Fig. 3.9.24b, c). The higher the intensity of dissolution, the higher the angularity and elongation and the lower the form factor and compactness of the etch pits.

Texture can be defined as irregularities in the topography of surface. Surface texture (Ra) analysis of different kinds of etch pit establishes the fact that the values of texture increases from F-type to P-type (Fig.3.9.25a, the higher the dissolution, the higher the value of texture). Fractal geometry was proposed by Mandelbrot, 1975. This was initially applied in nature for mountains, trees etc. which is applicable for self-similar objects (Mandelbrot, 1989). A fractal dimension is a ratio providing a statistical index of complexity comparing how detail in a fractal pattern changes with the scale at which it is measured. There are a few methods to determine fractal dimension: box counting, triangulation, power spectrum method etc. Here, the concept of fractal geometry is applied based on the assumption that dissolution causes the deposition of self-similar particles on the surface of the sample. Power spectrum method is mainly used to find out fractal dimension in this work.

Image analysis of P- type etch pits from different samples indicate that there is a direct correlation between surface texture (Ra) and surface area (Fig. 3.9.29). It also demonstrates that the surface area increases with increase in dissolution. Analysis of many etch pits show that P-type etch pits have higher texture value and lower fractal dimension (Fig. 3.9.25a, b). It also elucidates the fact that fractal dimension decreases with increase in dissolution. Care was taken to use the images of same scale to determine fractal dimension. The relationship between surface texture, surface area and fractal dimension are shown in Fig. 3.9.30. Fractal dimension decreases with the increase in value of surface texture and surface area. Hence surface texture analysis and fractal dimension analysis can be used to get an indication of rate of dissolution and to compare rates of dissolution of different samples. The shape distribution of the etch pits along with fractal dimension, surface texture and surface area can be good tools to determine the rate of dissolution and hence the crystal defects.

The shape distribution of etch figures according to Honess, 1927 is directly attributable to the solvent and to the molecular configuration of the faces upon which they occur. Hence, the faces will show different degrees of resistance to the chemical action. Microhardness analysis at different etch pits indicate that P-type etch pits have the minimum hardness (Fig. 3.9.26, Table 10). Here, the hardness is calculated by the software SPIP with the formula Force/ Area. Force is kept as a constant (10mN). The value of surface texture has an indirect

relationship with the microhardness (Fig. 3.9.26). The values obtained from SPIP are different from what Gallagher and Lebedeva, 1963 have measured. They reported Vickers hardness of beryl approximately at  $1300 \text{ kg/mm}^2$  with varying values on different faces. As the indents in the crystal are not man made with known loads but naturally made during the process of dissolution after the crystallisation of the minerals, the values of microhardness from the image analysis do not depict exact hardness. However, the minimum hardness values in P-type etch pits and maximum in F-type etch pits confirm that the dissolution leads to a decline in the microhardness. The concept of microhardness can be very useful in gem industry to find out the internal defects of crystals.

Honess, 1927 has stated that the shape of the etch pits is directly related with intermolecular forces within the crystal. In etch pits of all the samples, long edges are straight and short ones are curved contradicting the observations of Honess, 1917 and Medina et al., 1987 (Fig. 3.9.7,8). Surface texture analysis parallel and perpendicular to short curved edges and along the diagonals of different kinds of etch pits (Fig. 3.9.27, Table 11) show that the texture value is maximum  $\parallel$  to short curved edges indicating maximum unevenness of topography in this direction and hence weaker bonds. Hence it is evident that the dissolution is higher along this direction. Texture values  $\perp$  to short curved edges (along long straight edges) are lower than diagonals. This supports the argument of Wooster, 1976 that in all the crystals, straight edges of the etch pits are parallel to chain of strong bonds. In complicated structures, the chains parallel to different zone axes often have atoms in common. The curved edges of etch pits are explained by switching from dissolution along one chain to the inclined one. In the case of beryl, curved edges correspond to weaker bonds; the channels in beryls, which contain larger cations like Na, Ca, K etc and volatiles like  $\text{H}_2\text{O}$ ,  $\text{CO}_2$ . Hence in beryl, rate of dissolution is maximum along c-axis than in other parts which contradicts the views of Feklitchev, 1963 that the directions of maximum dissolution coincides with diagonals of the etch pits.

We can summarise the different stages of formation of etch pits on principal faces of beryl crystals through the schematic diagram below (Fig. 4.4).

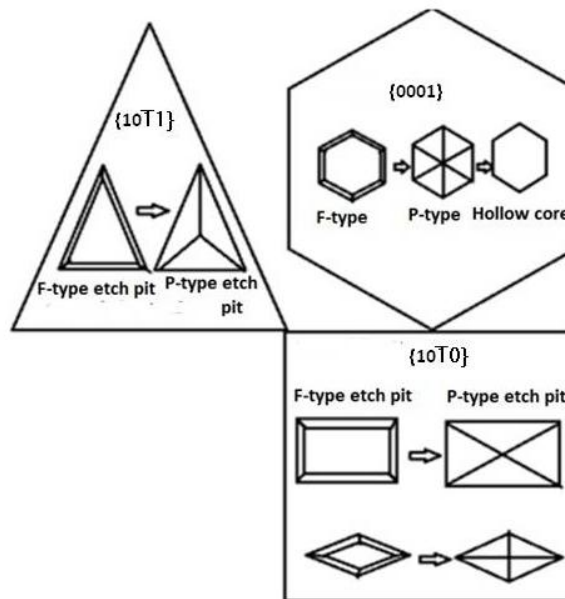


Fig. 4.4 Schematic diagram showing different stages of formation of etch pits.

**Chemical analysis of the materials in and around the etch pits:** Energy Dispersive Spectra (EDS) of the materials inside the etch pits of BA-1 indicates the presence of C, K, Cl, Na and Ca besides Si and Al in the normal ratio (Fig. 3.9.2, ana. 6). Fig. 3.9.9 ana.12 in BA-1 shows the materials inside P-type etch pit rich in C, K, Cl, Na and small amount of S and Ca indicating the materials could be KCl, NaCl,  $\text{CaSO}_4$  and  $\text{CaCO}_3$ . Since the shape of this material in the etch pit is more or less like that of a fibrous, platy clay like material, the analysis represents a combination of dissolution products and the fluid inclusions trapped in beryl during dissolution. Analysis of a small part of sample from inside the hollow core (Fig. 3.9.15) manifests two kinds of materials: (1) ana. 1 indicates the composition of a pure beryl and (2) ana. 3 could be considered as mixture of two phases; a platy crystal with K, Al, Fe, Si, a clay mineral, probably illite and the other phase with Ca and C which is carbonate with some amount of Fe in it. C probably indicates the presence of  $\text{CO}_2$  during dissolution. PAY-1 indicates the presence of S and K (Fig. 3.9.12c, ana. 4). EDS spectra of dissolution products in the rhombus shaped P-type etch pit on the prism face of PAY-1 indicates a product rich in Mg (Fig. 3.9.12a, ana. 1). When the spectra of ana. 1 and of pure beryl are compared, it is observed that the amount of Al is less in comparison with beryl composition indicating Mg and Al clay mineral.

BSE images of the thin sections indicate that most of the fluid inclusions are found to be enriched in Ca and S (Fig. 3.2.4a,b,c,d,3.2.5b); some also with K and Fe. I conclude that the fluids and/or the daughter crystals in the fluid inclusions are rich in KCl, NaCl and  $\text{CaSO}_4$ . Similar composition of inclusions and the materials inside the etch pits possibly suggest that the fluid responsible for creation of the etch pits had a similar composition as the fluid, which was captured in the inclusion. Material inside the pits might be; (1) remnants of the dissolution process, i.e; inclusions which did not dissolve and were set free during

dissolution, (2) newly formed phases during incongruent dissolution and (3) materials brought into the crystal from an external fluid which precipitated within the crystal.

**4.7.2 Literature review on formation of etch pits:** Sunagawa, 1987 has explained the reasons for the changes in the morphology of dissolution figures from circular to polygonal due to the control of stronger bonds on the etching face. When the face is rough there is no control of stronger bonds on the etching face and the etching advances isotropically and circular etch pits are formed. When the face becomes smooth, it advances anisotropically and etching rate is controlled by the strong bond directions within the face and the dissolution figure takes polygonal morphology.

The presence of two types of etch pits was explained by different authors on different faces of the crystal subjected to dissolution. When a crystal without any linear or planar defect is subjected to dissolution, shallow dissolution forms with flat bottoms are formed. These are grouped into category 1 which do not deepen with time and are produced on point defects. Different terminologies have been used by various authors to describe different kinds of etch pits. Mikio Yamamoto, 1957 used the word temporary or short time etch pits and Sunagawa, 1987 as F-type etch pits. The point defects can be due to either a substituting impurity atom, vacancy, self interstitial atom or interstitial impurity atom. In laboratory, F-type etch pits either disappear or extend all over the surface with increasing dissolution instead of deepening with time. Sunagawa, 1962 described this process as two dimensional developments after their depth has reached two or three unit cell heights. Honess, 1927 argued that pits cannot deepen after attaining the stability solution form. However, etch pits of a second generation can be formed in the same etch pit (maybe with different morphology) with increasing dissolution, eg: canoe shaped etch pits in the broad and shallow etch pits (Fig. 3.9.7c, d).

Category 2 (deep etch pits having small base) are permanent (P- type etch pits), in which dissolution occurred at the sites of line defects or dislocations. These etch pits deepen with time (Yamamoto, 1957, Joshi et al., 1978, Sangwal, 1987). According to Honess, 1927 flat bottomed etch pits represent early stages of formation and etch pits with pointed bottoms represent late stages of dissolution.

**4.7.3 Literature review about the morphology of etch pits on beryl:** Wilk, 1887 studied etch pits on Ukrainian beryls and found that all the faces are not subjected to dissolution at the same intensity. He described the etch pits on prism face  $m\{10\bar{1}0\}$  as approximately rectangular and suggested that beryl consists of three rhombic part-molecules by measuring etch pits on prism face goniometrically.

Petersson, 1891 studied etch figures on six wine-yellow crystals from Mursinka in the Urals and found many rhombohedral pits on the first order bi-pyramid, second order bi-pyramid  $s\{11\bar{2}1\}$  and prism faces. Triangular pits were found on the first order bipyramid face  $p\{10\bar{1}$

1}; this one being obliterated because of extensive dissolution. He found the density of etch pits on pinacoid  $c\{0001\}$  faces were low. Tubular cavities were found parallel to c-axis, each terminating in an etch pit and led him to believe that the tubes themselves were greatly elongated solution cavities.

Penfield and Sperry, 1888 investigated a severely corroded beryl crystal from Willimantic, Connecticut. They observed etch pits on a steep dihexagonal pyramid, prism of first and second order but rarely on pyramid of first order  $p\{10\bar{1}1\}$  and  $n\{31\bar{4}1\}$ . They also described etch figures on pale green and blue aquamarine crystals from Mount Antero, Colorado. The crystals were simple in form but sometimes severely corroded on their terminations, which had the very steep faces of the dihexagonal bipyramid.

Traube, 1895 was the first to etch beryls artificially to study the pits made by molten KOH as a solvent. He was able to develop regular six sided pits on the pinacoidal faces, bound by forms in the zone between  $c\{0001\}$  and  $m\{10\bar{1}0\}$ , as well as more or less regular triangular pits on the faces of the first order bipyramid  $p\{10\bar{1}1\}$ , curved pits elongated along the horizontal axis direction on faces of the second order bipyramid  $s\{11\bar{2}1\}$  and rectangular to curved pits on the faces of the first order prism  $m\{10\bar{1}0\}$  elongated along c-axis. These pits became complex and diverse in form when ammonium bifluoride was used as the etchant.

Kohlmann, 1907 studied Brazilian beryls and described etch marks found on natural specimens. Characteristic rectangular etch pits (some with bulged outlines) were found on  $m\{10\bar{1}0\}$ . Numerous canoe-shaped pits were found on the second order prism  $a\{11\bar{2}0\}$ , with their long dimension parallel to the c-axis. Triangular pits were found on  $m\{10\bar{1}0\}$  of only one crystal, but similar triangular depressions were abundant on the second order bipyramid  $s\{11\bar{2}1\}$ . As in the previous findings, etch pits on the pinacoidal faces were hexagonal in outline. Kohlmann, 1907 also noted hexagonal tubes oriented parallel to c-axis.

Honess, 1917 produced etch figures on beryls by immersing them in molten sodium hydroxide and found that only fifteen seconds were required to obtain satisfactory results. He was also successful in getting etch figures using potassium hydroxide and a mixture of two hydroxides where as failed to produce etch figures after boiling in hydrofluoric acid for more than an hour.

Zedlitz, 1941 studied natural etch figures on gem quality aquamarines from Minas Gerais, Brazil. He found narrow canoe shaped etch pits on  $m\{10\bar{1}0\}$  oriented both parallel and normal to c-axis.

Feklitchev, 1963 analyzed the morphology of experimentally produced etch figures on natural beryl crystals, in both alkaline and acidic media at atmospheric pressure with fused solids as etchants. He found that beryl from different fields can be characterised by a

different set of simple dissolution forms or etch figures. He compared the morphology of etch pits formed in an alkaline medium with the formation of albite replacing beryl and in acidic medium with kaolinite replacing beryl. The acid-alkaline properties of natural solutions affecting beryl result in different forms and alignments of etch figures and they can be used in reconstruction of acidity-alkalinity of the solutions.

Medina et al., 1983 were the first to use SEM to investigate natural etch pits on beryl and found that the morphology of etch pits on different beryl faces depend largely on the structural arrangement of the Al-O-Be chains on each face.

Honess, 1927 and Feklitchev, 1963 observed that the samples from different provenances are characterised by etch pits of different morphologies which is governed by the composition of the solution (Fig. 4.2). This agrees with our observations. The classification proposed by Sunagawa, 1987 can be applied on beryl crystal faces too. Whatever may be the morphology of etch pit, it can be classified into F-type (on point defects), P-type (on line defects) and stepped. The studies on quartz and gypsum by Joshi et al., 1978 and Raju, 1980 revealed that the morphology of etch pits are controlled by crystal defects. Point defects can be inclusions as observed in the chemical analysis of the products inside the etch pits. The etch pit studies on beryl in this work also substantiates the role of defects in etch pit formation. Surface texture value is maximum in P-type etch pit indicating maximum dissolution. Fractal dimension and surface texture have indirect relationship and P-type has minimum fractal dimension value. Surface texture value is higher parallel to short curved edges of the etch pits on prism of first order. As these curved edges run parallel to the c-axis, I conclude that dissolution rate is higher parallel to c-axis. Different kinds of etch pits observed on  $\text{CaF}_2$  crystal classified by Motzer and Reichling, 2010 by artificial etching are applicable on natural etch pits in natural beryls also. The morphology of etch pits reflect the symmetry of the faces as observed by previous authors. From the above studies it can be concluded that the dissolution in beryl is mainly controlled by crystal chemistry, structure, provenance and internal defects.

## **4.8 Hydrothermal Experiments:**

**4.8.1 SEM studies:** Hydrothermal treatment of beryl at 600 °C and 2 kbar pressure for 4 days in NaCl solution caused decomposition of beryl. Most of the decomposition products are phenakite and a phase approaching the composition of feldspar (Fig. 3.10.2, ana. 18). In some parts of recrystallised beryl, the particles deposited on the surfaces are rich in Ca (Fig. 3.10.2, ana. 17) suggesting  $\text{Ca}^{2+}$  ions could be from solid or fluid inclusions. The inclusions especially in PAD-8 used for hydrothermal treatment with NaCl have a substantial amount of Ca. Etch pits were formed, however the surface was completely covered by reprecipitated beryl and decomposition products. After removing these products, almost canoe shaped deep etch figures were observed (Fig. 3.10.5a, b).

KCl treatment of beryl at 600°C and 2 kbar had given rise to the formation of not only K-feldspar but also phenakite (Fig. 3.10.6, 8, 9). The surface of beryl became enriched in Fe and Cr (Fig. 3.10.7, ana. 10) which is explained as quench products. The chemical analysis of PAD-8 indicates a higher amount of Fe. Though Cr is not measured, beryl varieties not belonging to emerald do not have high Cr content. The concentration of Fe and Cr in the quench products could be the solid inclusions rich in Fe and Cr as inclusions are preferential sites for dissolution. This phenomenon cannot be satisfactorily explained on the basis of our data. KCl treated sample surface also showed etch figures under the decomposed products. Some are deep and long, hexagonal shaped with straight edges and sharp corners. Some are shallow, long with flat base and curved edges (Fig. 3.10.9).

Hydrothermal treatment of beryl in NaOH solution at 600°C and 2 kilobars has so far not been reported. But in the present work under these conditions, elongated etch pits with short and curved edges parallel to c-axis are formed (Fig. 3.10.10) which is similar to that of natural etch pits on un-treated samples. Fig. 3.10.11 shows a prismatic decomposition product rich in Si, possibly quartz. Fig. 3.10.12 shows extremely fibrous decomposition product with Si/Al ratio close to 1 which could possibly be euclase,  $\text{BeAlSiO}_4(\text{OH})$ . It might have formed metastably or during quenching of the experiment. However, Franz and Morteani, 2002 mentioned that during synthesis experiments, they found a number of unidentified phases in the system with Be-Al-Si and it is possible that such unknown phases are also formed in the current experiments.

SEM images of beryl treated in HCl solution at 600°C and 2 kilobars show an interesting stage in the dissolution of beryl. Many particles deposited on the surface are found to be enriched in Na and K (Fig. 3.10.14, 15). The only source of K, Na and Ca are the leached out cations from the channel or solid inclusions. The quench product on the surface (Fig. 3.10.15, 16) has a higher amount of Fe and Cr as in the KCl treated beryl.

Syromyatnikov et al., 1972 used single crystals of beryl to study the stability of beryl in aqueous solutions at high temperature and pressure. They used 0.5 M NaCl, KCl, NaF, KF,  $\text{Na}_2\text{CO}_3$  and  $\text{K}_2\text{CO}_3$  solutions, distilled water and HCl solution. Pressure was between 0.49 to 0.98 kilobars and temperature varied from 300°C to 800°C for a period of 5 to 6 hours. Beryl decomposed into phenakite in NaCl solution and orthoclase and kalsilite in KCl solution (no Be compounds were present). At 800°C beryl undergoes fusion. Syromyatnikov et al., 1972, treated beryl in HCl solution at 500°C and 600°C and fine crystals of chrysoberyl were found as the decomposed products.

In the current study, hydrothermal treatment of beryl in NaCl, it decomposed into feldspar and phenakite as observed by Syromyatnikov et al., 1972. However, treatment in KCl solution produced phenakite crystals along with feldspar which is in contrast to the observation of Syromyatnikov et al., 1972. The analysis of quench products and fluid inclusions show similar composition suggesting inclusions are preferable sites for dissolution strengthening the argument that one of the controlling factors of dissolution is point defects (inclusions).

**4.8.2 IR spectroscopic studies of hydrothermally treated beryl:** IR spectra of HCl and NaOH treated powdered beryls are obtained at room temperature. KCl and NaCl treated samples are not subjected to IR investigation as the concentrations of the solvents used and duration of the treatment are not comparable and the samples are completely coated with dissolution products after the experiment.

The following changes were observed in the different regions of spectra:

In the domain  $900\text{ cm}^{-1}$  to  $1210\text{ cm}^{-1}$ : The absorption bands observed at  $1206\text{ cm}^{-1}$  and  $962\text{ cm}^{-1}$  in the untreated alkali poor BA-1 crystal gets shifted to  $1209\text{ cm}^{-1}$  and  $965\text{ cm}^{-1}$  after the treatment in HCl and NaOH solutions at  $600^\circ\text{C}$  and 2 kilobars (Fig.3.10.17, 18, 19). This could be due to the leaching of larger cations from the channel resulting into shortening of bond which is observed as a shift to higher frequency. The flanks between the wavenumbers  $1206\text{ cm}^{-1}$  and  $1021\text{ cm}^{-1}$  becomes broad after the hydrothermal treatment. The shoulder at the flank of  $965\text{ cm}^{-1}$  which was at  $1021\text{ cm}^{-1}$  in untreated crystal shifted around  $1020\text{ cm}^{-1}$  in both treatments.

In the domain  $400\text{ cm}^{-1}$  to  $600\text{ cm}^{-1}$ : A shift is observed in the band at  $435\text{ cm}^{-1}$  in untreated sample to  $439\text{ cm}^{-1}$  (HCl) and  $440\text{ cm}^{-1}$  (NaOH) after the treatment. Here also, the shift is towards higher frequency indicating a shortening of the bond and an increase in bond energy. The band at  $524\text{ cm}^{-1}$  also shifts to higher frequency after the treatment. These bands were assigned to Al-O vibration by Aurisicchio, 1994. Shift to higher frequency indicates leaching of larger substituted divalent cations from the Al octahedron resulting in shortening of bond.

NaOH treated beryl did not show the symptom of incorporation of Na in the channel. This spectrum showed a broader shoulder in the water region, which could be due to the absorbed water from the pellet as it was not dried before the measurement. The intensity of the band at  $3699\text{ cm}^{-1}$  due to the vibration of type I  $\text{H}_2\text{O}$  molecule in untreated sample gets reduced in the treated samples as observed by Galvianz et al., 1989 (Fig. 3.10.17, 18, 19).

The only available infrared spectroscopic study of hydrothermally treated beryls was by Galvianz et al., 1989. In order to find out the behaviour of alkali cations in beryl channel, they treated powdered natural Li-Cs rich beryl in NaCl, LiCl and CsCl for duration of 22 days, 31 days and 42 days at  $600^\circ\text{C}$  and 1.5 kilobars. They observed in NaCl treated samples: (1) an increase in Na content of the sample and solution and (2) a decrease of Li and Cs in the sample and increase in the solution. Albite was crystallised and they suggested that Li substitution should also have taken place in the channel sites of beryl. They also used aqueous HCl solution for duration of 18 to 42 days at the same P-T conditions and the treated beryl was investigated under IR spectroscopy. They observed that a steady state was reached after 17 days. There was a significant reduction of Na in the channel as compared to Li and Cs. Their observation was that Be does not take part in the leaching process. Generally, a sharpening of the bands was observed in IR spectrum and Si-O peaks shift to

higher frequencies with progressive leaching. No changes were visible in Be-O bonds except in  $820\text{ cm}^{-1}$  band which shifts to lower frequency. Galvianz et al., 1989 did not mention the changes in the bands which are in the low frequency region. In  $2500$  to  $4000\text{ cm}^{-1}$  region, stretching bands of type II  $\text{H}_2\text{O}$  molecules disappear as the dissolution progresses.

The shifts in the frequencies after the treatment in present study are not as large as in the study by Galvianz et al., 1989. This can be attributed to two reasons: (1) the sample used for the current dissolution experiment is BA-1 which has less amount of substitution in Be-tetrahedron and Al-octahedron evidenced by Rietveld and chemical analysis and (2) the experiment was conducted for a shorter duration as the present work focuses on the formation of etch pits.

IR spectra results point to the fact that dissolution of beryls start from leaching of cations from the channels followed by removal of larger divalent and trivalent cations from Al octahedron and dissolution process commences with strengthening of the bond initially. The incorporated cations in the channel and the Al- octahedron are also categorised into point defects along with inclusions. Hence, it can be concluded that larger cations in the channel and substituted cations in the structure which are point defects have an important role in the dissolution of beryl.

## 5. Summary and Conclusion

The chemical analysis of 21 natural beryl samples selected for this study show that most of them are normal beryls with minor substitution, except two tabular samples (BAA-2 and CA-1) which are rich in alkalis, BAA-1 exhibits tabular morphology but with medium alkali content.  $\text{Si}^{+4}$ - $\text{Al}^{+3}$  substitutions are not prominent in the samples, except in PAD-1 and BA-1.

Rietveld refinement shows that the majority of the samples have a ratio of their lattice parameters  $c/a$  between 0.998-0.999, indicating that they belong to the normal beryl group. The alkali rich beryls have a higher  $c/a$  ratio of 1.000, inferring a tetrahedral substitution. Inter-atomic distances obtained from Rietveld refinement indicate  $\text{Na}^+$  incorporation in the channel causes an increase in the bond length of  $\text{Be-O}_1$  and a decrease in  $\text{Si-O}_1$  bond length. Refractive indices do not have a collinear relationship with the alkali content.

IR spectroscopic investigations reveal the presence of type I and type II  $\text{H}_2\text{O}$  molecules in the spectra of alkali poor and alkali rich samples. Alkali rich tetrahedrally substituted beryls can be differentiated from the normal beryl by the intensity ratio of water bands at 3600 and 3700  $\text{cm}^{-1}$ , with a stronger prominent band at 3600  $\text{cm}^{-1}$ . A band at 2350  $\text{cm}^{-1}$  was observed in all samples, which is assigned to the vibration of  $\text{CO}_2$ .

The presence of a band at 1206  $\text{cm}^{-1}$  in the IR spectra of two alkali poor samples demonstrates that it could be used to separate them from the tetrahedrally substituted alkali rich samples. In tetrahedrally substituted beryls, this band is observed at lower frequency around 1180  $\text{cm}^{-1}$  and the band at 1020  $\text{cm}^{-1}$  splits into two bands (1060  $\text{cm}^{-1}$  and 1020  $\text{cm}^{-1}$ ). Rietveld refinement of alkali rich beryl indicates the possibility of substitution of a larger  $\text{Li}^+$  cation into  $\text{Be}^{+2}$  tetrahedra and charge balance by incorporation of  $\text{Na}^+$  into the channel. The combination of XRD and IR spectra results infer that the absorption band around 1200  $\text{cm}^{-1}$  could be assigned to the vibration of  $\text{Be-O}$ . Raman spectra of the studied samples demonstrate that the increase in alkali content creates a shoulder at 3597  $\text{cm}^{-1}$  which is due to the vibration of type II  $\text{H}_2\text{O}$  molecule. The main Raman bands are observed at 327  $\text{cm}^{-1}$ , 392  $\text{cm}^{-1}$ , 687  $\text{cm}^{-1}$  and 1067  $\text{cm}^{-1}$  and the intensity of the band at 1067  $\text{cm}^{-1}$  drastically reduces when the electric vector is perpendicular to  $c$ -axis.

NIR spectra, when electric vector is parallel to  $c$ , are characterised by two main spectral bands at 1399 nm and 1865 nm, the intensity of which increases in alkali rich beryls. A band around 1410 nm is found only in alkali rich samples which becomes prominent with the increase of alkali content.

SEM investigations show that the morphology of etch pits reflects the internal symmetry of the crystals which differ significantly on prism of first order of samples from different localities. The crystal faces are characterised by three kinds of etch pits based on their general morphology: (1) Shallow etch pits with broad bottom: F-type etch pits (on point

defects), (2) deep etch pits with narrow or pointed bottom: P-type etch pits (on line defects) and (3) stepped etch pits.

Etch pits are also classified into centric and excentric based on the inclination of dislocations to the surface. Shape factors of the etch pits indicate that the value of roundness, form factor and compactness decrease from F-type etch pits to P-type etch pits with an increase in the value of elongation. SEM image analysis shows that dissolution changes the surface roughness and texture. The surface texture is maximum in P-type etch pits, which are found on line defects. F-type etch pits are observed on point defects and show a minimum texture value. This could be a useful criterion to identify line defects and point defects. Fractal dimension is minimum in P-type etch pits and maximum in F-type etch pits and show an inversely proportional relation with surface texture. Surface area and surface texture reflect a linear relationship and they in turn have an inverse relationship with fractal dimension. A hollow core in one crystal (BA-1) could largely be attributed to a dislocation induced growth phenomenon rather than to a dissolution phenomenon.

The chemical (qualitative) analysis of the materials in and around the etch pits show that they are rich in C, K, Cl, Na and small amounts of S and Ca indicating the presence of KCl, NaCl, CaSO<sub>4</sub> and CaCO<sub>3</sub>. The analysed inclusions and the materials inside the etch pits have similar composition probably suggesting the same solvent responsible for dissolution and the fluid inside the inclusions. It can be concluded that the materials inside the pits might be: (1) the inclusions (2) newly formed phases during incongruent dissolution and (3) materials brought into the crystal by an external fluid, which precipitated within the crystal.

Hydrothermal experiments at 600°C and 2 kilobars in variable concentrations of NaCl and KCl solutions produced different minerals as decomposition products and etch pits. Phenakite, besides feldspar is a common dissolution product in both experiments. NaOH solution produced quartz and euclase. Beryl crystals show elongated etch pits with short and curved edges parallel to c-axis. A sample treated with HCl does not show any decomposition products and their surfaces are marked by sporadic occurrences of irregularly shaped quench products rich in Na and K which are the combinations of inclusions and the leached out cations from the channel. However, more experiments under different controlled variables are required in order to strengthen the argument.

The surface texture analysis of etch pits on first order prism face shows a maximum value parallel to its short edges and minimum parallel to its long edges. The short edges of the etch pits on prism faces coincide with the direction of the c-axis and maximum surface texture value along this direction indicates higher rate of dissolution. The hydrothermal experiments in NaOH solution, which led to the formation of etch pits, in which short and curved edges are parallel to the c-axis as in natural etch pits confirm this observation. Hydrothermal treatment of beryl in HCl solution shows quench products rich in alkalis, suggesting leaching of alkalis from the channels. The dissolution of beryl is initially marked by an increase in bond strength as evidenced in the infrared spectrum of hydrothermally

treated beryls due to shortening of the bonds because of the removal of larger cations from the channel. IR bands in the lower frequency region which are assigned to Al-O vibration, after the treatment, shift to higher frequency due to the shortening of bond. This shows the removal of the larger divalent and trivalent cations (Point defects) from Al-octahedron. Surface texture varies in different etch pits with its maximum value in P-type etch pits. This indicates maximum dissolution in this type of etch pits underlining the importance of crystal defects on the dissolution behaviour. A similar composition of inclusions and the materials inside the etch pits of natural beryl suggest that point defects have a large effect on dissolution.

It can be concluded that the internal factors like crystal structure, chemistry, defects (point defects in the form of inclusions and line defects in the form of dislocations), substitution of cations, symmetry and external factors like the types of solvent, their concentration and duration of the exposure of crystal to dissolution are the controlling factors of dissolution of beryl. A higher rate of dissolution was observed along c-axis, attributed to its distinctive crystal structure and dissolution process commences by the removal of larger cations from the channel followed by the removal of substituted cations from the Al-octahedron. The prism of first order of the samples from different geographical locations are characterised by either canoe, diamond and square shaped etch pits or solution channels parallel to c-axis (Himalayas), by isosceles trapezoidal etch pits with curved, short edges along with canoe shaped etch pits (Brazil), with characteristic scalene trapezoidal etch pits with curved, short edges (Finland) and with elongated rectangular etch pits with curved, short edges (China).

This demonstrates that the morphology of etch pits of natural beryl samples from different localities differ considerably, which could be a useful parameter in provenance study for source rocks. However, detailed analysis of a large number of samples from each provenance is required to substantiate the argument. The morphology of etch pits mirrors the symmetry of the faces, which is consistent with the earlier studies. They could be used as effective tools in detecting crystal defects in beryl.

## 6. References

- Adams, J. W (1953): Beryllium deposits of the Mount Antero region, Chaffee County, Colorado: *U. S. Geol. Survey. Bull.* 982D, 106-107.
- Adams, D.M and Gardner, I.R. (1974): Single-crystal vibrational spectra of beryl and diopside. *Journal of the Chemical Society - Dalton Transactions*, 1502-1505.
- Agheem M. H., Shah, M. T., Khan, T., Laghari, A and Dars, H (2011): Field features and petrography used as indicators for the classification of Shigar valley pegmatites, Gilgit-Baltistan region of Pakistan. *Journal of Himalayan Earth Sciences* 44(2) 1-7.
- Aines, R.D. and Rossman, G.R. (1984): The high temperature behaviour of water and carbon dioxide in cordierite and beryl. *American Mineralogist*, Vol.69, 319-327.
- Akatsuka, M., Sueoka, K and Yamamoto, T (2000): Classification of etch pits at silicon wafer surface using image processing instrument *J. Cryst. Growth* 210, 366-369.
- Anbeek, C. (1992): Surface roughness of minerals and implications for dissolution studies. *Geochimica et cosmochimica Acta* 56 1461–1469
- Andersson, L.O. (2006): The positions of H<sup>+</sup>, Li<sup>+</sup> and Na<sup>+</sup> impurities in beryl. *Physics and Chemistry of Minerals*, 33, 403-416.
- Artioli, G., Rinaldi, R., Stahl, K and Zanazzi, P.F. (1993): Structure refinements of beryl by single-crystal neutron and X-ray diffraction. *American Mineralogist*, Volume 78, pages 762-768.
- Atlas der Kristallformen, (1913): vol. 1 Adamin-Buntkupfererz. 244 pp, Carl Winters Universitätsbuchhandlung; Heidelberg.
- Aurischio, C., Fioravanti, G., Grubessi, O., Zanazzi, P.F. (1988): Reappraisal of the crystal chemistry of beryl. *American Mineralogist*, 73, 826-837
- Aurischio, C., Grubessi, O and Zecchini, P. (1994): Infrared and crystal chemistry of the beryl group. *Canadian Mineralogist*, 32, 55-68.
- Avnir, D., Farin D and Pfeifer, E (1984): Molecular fractal surfaces. *Nature* 308:261-263.
- Bakakin, V. V and Belov, N. V. (1962): Crystal chemistry of beryl. *Geokhimiya* 1962, 484-500.
- Bakakin, V.V., Rylov, G.M and Belov, N.V. (1967): Correlation between the chemical composition and unit cell parameters of beryls. *Dokl. Akad. Nauk. SSSR* 173, 1404-1407. In Filho and Sighinolfi (1973) Contribution to the crystal chemistry of beryl. *Contr. Mineral. Petrol.*, 38, 279-290.
- Bakakin, V.V., Rylov, G.M and Belov, N.V. (1969): On the crystal structure of lithium bearing beryl *Dokl. Akad. Nauk SSSR* 188, 659-662. (in Russ). In Černý, P., and Hawthorne, F.C., (1976): Refractive indices versus alkali contents in beryl. General limitations and applications to some pegmatitic types. *Canadian mineralogist*, 14: 491–497.

Bakakin, V.V., Rylov, G.M and Belov, N.V. (1970): X-ray identification of isomorphous varieties of beryl. *Geokhimiya*, 1302-1311 (in Russ). In Černý, P., and Hawthorne, F.C., (1976): Refractive indices versus alkali contents in beryl. General limitations and applications to some pegmatitic types. *Canadian mineralogist*, 14: 491–497.

Barton, M.D. (1986): Phase equilibria and thermodynamic properties of minerals in the BeO-Al<sub>2</sub>O<sub>3</sub>-SiO<sub>2</sub>-H<sub>2</sub>O (BASH) system, with petrologic applications. *Amer. Mineral.*, 71, 277-300.

Belov, N. V. (1958): Essays on Structural Mineralogy IX. Mineral. Sbornik Geol. Soc. Lvov. 12, 15-42.

Belov, N.V. and Matveeva, R.G. (1951): The determination of structural parameters of beryl by the method of bounded projections. *Doklady Akad. Nauk SSSR*, 6, 69-82.

Berner, R. A and Schott, J. (1982): Mechanisms of pyroxene and amphibole weathering; II. Observations of soil grains, *American Journal of Science*, 282, 1214-1231.

Bershov, L.V. (1970): Methane and atomic hydrogen in some natural minerals. *Geochemistry International*, p. 853-856.

Beus, A. A. (1960): Geochemistry of beryllium genetic types of beryl deposits. *Izdanie kademii Nauk SSSR*, Moscow.

Birch, F. (1950): A simple technique for the study of elasticity of crystals. *American Mineralogist* 35: 644-650. In Sinkankas J. (1981) Emerald and other beryls. Chilton Book Company, Radnor.

Bose, R. (1936): Optische und spektrographische Untersuchungen an Beryllen, insbesondere bei höheren Temperaturen. *Neues Jahrbuch für Mineralogie* Abt. A. Beilage-Bd. 70. Pp. 467-570.

Bragg, W.L and West, J. (1926): The structure of beryl, Be<sub>3</sub>Al<sub>2</sub>Si<sub>6</sub>O<sub>18</sub>. *Proceeding of the Royal Society of London* A-111, p. 691-714. In Sinkankas J. (1981) Emerald and other beryls. Chilton Book Company, Radnor.

Brotzen, O. (1959): Outline of mineralization in zoned granitic pegmatites. *Geologiska Foreningers*, Stockholm Forhandlingar, 496, 2-98.

Burt, D.M. (1978): Multisystem analysis of beryllium mineral stabilities: The system BeO-Al<sub>2</sub>O<sub>3</sub>-SiO<sub>2</sub>-H<sub>2</sub>O. *Am Mineral* 63:664-676

Cameron, E. N., Rowe, R. B and Weis, P. L. (1953): Fluid inclusions in beryl and quartz from pegmatites of the Middletown district, Connecticut: *Am. Mineral*.36, 906-910.

Cassedanne, J.P and Lowell, J. (1982): Famous mineral localities: The Virgem da Lapa pegmatites. *Mineralogical Record*, Vol.13, No.1, 19-28.

Cemič, L., Langer, K and Franz, G. (1986): Experimental determination of melting relationship of beryl in the system BeO-Al<sub>2</sub>O<sub>3</sub>-SiO<sub>2</sub>-H<sub>2</sub>O between 10 and 25 kbar. *Mineralogical Magazine*, vol. 50, 55-61

Černý, P. (1975): Alkali variation in pegmatitic beryl and their petrogenetic implications. *Neues Jahrb. Mineral. Abh.* 123, 198-212.

Černý, P and Hawthorne, F.C. (1976): Refractive indices versus alkali contents in beryl. General limitations and applications to some pegmatitic types. *Canadian mineralogist*, 14: 491-497.

Černý, P. (2002): Mineralogy of beryllium in granitic pegmatites. *Reviews in Mineralogy and Geochemistry*, 2002, v. 50, 405-444.

Černý, P., Anderson, A.J., Tomascak, P.B and Chapman, R. (2003) Geochemical and morphological features of beryl from the Bikita granitic pegmatite, Zimbabwe. *Canad Mineral* 41: 1003-1011

Charoy, B and Noronha, F. (1996): Multistage growth of a rare element, volatile rich microgranite at Argemala (Portugal). *Journal of Petrology*, 37, Issue 1, 73-94

Charoy, B., de Donato, P., Barres, O and Pinto-Coelho, C. (1996): Channel occupancy in an alkali-poor beryl from Serra Branca (Goias, Brazil): Spectroscopic characterization. *American Mineralogist*, 81, 395-403.

Chemical Rubber Company (1966): *Handbook of Chemistry and Physics*. 47<sup>th</sup> ed. Boca Raton, Fla.: Chemical Rubber Company. In International Gem Society

Curie, J. (1889): Recherche sur le pouvoir inducteur spécifique et la conductibilité des corps cristallisés. *Annales de Chimie et de Physique* 17 : 385-434 ; 18 : 203-69. In Sinkankas J. (1981) Emerald and other beryls. Chilton Book Company, Radnor.

Dam, B., Koeman, N. J., Rector, J. H., Stauble Pumpin, B., Poppe, U and Griessen, R. (1996): Growth and etching phenomena observed by STM/AFM on pulsed-laser deposited YBa<sub>2</sub>Cu<sub>3</sub>O<sub>7- $\delta$</sub>  films, *Physica C* 261, 1-11.

Deer, W.A., Howie, R. A., and Zussman, J. (1962): Rock forming minerals. Vol. 1. London: Longmans. pp. 256-67.

Dirac, F and Ebert, H. (1967): Isotopic age from the pegmatite province of Eastern Brazil, *Nature*, 215, 948-949.

De Almeida Sampaio Filho, H and Sighinolfi, G. P. (1973): Contribution to the crystal chemistry of beryl. *Contribution to Mineral and Petrology*, 38, 279-290.

Ehrnrooth, E.K and Tuovinen P. (1989): Heat treatment of the Lumäki beryls. *Gemmologian Työsaralta (publication of the Gemmological Society of Finland)*, 18, 4-19. (in Finnish)

Emsley, J. (2001): Nature's building blocks. An A-Z guide to the elements. Oxford University Press, Oxford

Ernst, V. E. (1926): Über echte Ätzhügel und Lösungskörperformen am brasilianischem Beryll. *Z. Krist. Mineral.*, 63, 153-156.

Evans, H.T., Jr and Mrose, M.E. (1968): Crystal chemical studies of cesium beryl. *Geological Society of America Special Paper* 101. Abstracts for 1966. 63.

Everest, D.A. (1973): Beryllium. In Bailar JC, Emeléus HJ, Nyholm R, Trotman-Dickenson AF (eds) *Comprehensive Inorganic Chemistry*, vol. 1. Pergamon, Oxford, New York, p 531-590

Feklichev, V.G. (1963): Chemical composition of minerals of the beryl group, character of isomorphism, and position of principal isomorphous elements in the crystal structure. *Geochemistry* no. 4, 410-21

Feklitchev, V.G. (1964): Beryl, Morphology, Composition, and Structure of Crystals. Nauka, Moscow (in Russ.).

Feklithev, V.G and Razina, I.S. (1964): On phosphorus bearing beryl. *Mem. Mineral. Museum Acad.Sci. U.S.S.R.*, 15, 247-250 (in Russ.).

Filho and Sighinolfi (1973): Contribution to the crystal chemistry of beryl. *Contr. Mineral. Petrol.* 38, 279-290.

Fizeau, H. (1866): Mémoire sur la dialation des corps solides par la chaleur. *Compte Rendu de l'Academie des Sciences* (Paris) 62 : 1101-1106, 1133-48 In Sinkankas (1981) Emerald and other beryls. Chilton Book Company, Radnor.

Flanigen, E.M., Breck, D.W., Mumbach, N.R and Taylor, A.M. (1967): Characteristics of synthetic emeralds. *American Mineralogist*, 52, 744-772.

Frank, F.C. (1951): Capillary equilibria of dislocated crystals. *Acta crystallographica* Vol. 4, Part 6. 497-501.

Franz, G and Morteani, G. (2002): Be-minerals: Synthesis, stability, and occurrence in metamorphic rocks. In E.S. Grew, Ed., Beryllium: Mineralogy, Petrology, and Geochemistry, 50, p. 551–589. Reviews in Mineralogy and Geochemistry, Mineralogical Society of America, Chantilly, Virginia.

Fukuda, J and Shinoda, K. (2008): Coordination of water molecules with Na<sup>+</sup> cations in a beryl channel as determined by polarized IR spectroscopy. *Physics and Chemistry of minerals*, 35, 347-357.

Fukuda, J and Shinoda, K. (2011): Water molecules in beryl and cordierite: High temperature vibrational behaviour, dehydration and coordination to cations. *Physics and Chemistry of minerals*.38:469-481.

Gervais, F. and Piriou, B. (1972): Étude des spectres de réflexion infrarouge du beryl dans les région 280-1400 cm<sup>-1</sup>. *Comptes rendus de l'Académie des Sciences Paris*, B274, p. 252-255

Gibbs, G.V., Breck, D.W and Meagher, E.P. (1968): Structural refinement of hydrous and anhydrous synthetic beryl, Be<sub>3</sub>Al<sub>2</sub>Si<sub>6</sub>O<sub>18</sub> and emerald Be<sub>3</sub>Al<sub>1.9</sub>Cr<sub>0.1</sub>Si<sub>6</sub>O<sub>18</sub>. *Lithos*1, 275-285

Goldman, D.S., Rossman, G.R and Parkin, K.M. (1978): Channel constituents in beryl. *Physics and Chemistry of Minerals*, 3, 225-235.

Gorshunov, B.P., Zhukova, E.Z., Torgashev, V.I., Lebedev, V.V., Shakurov, G. S., Kremer, R.K., Pestrjakov, E.V., Thomas, V.G., Fursenko, D.A and Dressel, M. (2013): Quantum behavior of Water Molecules Confined to Nanocavities in Gemstones. *J. Phys. Chem. Lett.*, 4, 2015–2020.

Greenwood, N.N and Earnshaw, A. (1997): Chemistry of the Elements, 2nd edn. Butterworth-Heinemann, Oxford, Woburn.

Grew, E. S. (2002): Mineralogy, Petrology and Geochemistry of Beryllium: An Introduction and List of Beryllium Minerals. Reviews in Mineralogy and Geochemistry, Mineralogical Society of America, Chantilly, Virginia.

Griffin, L.J. (1951): Microscopic studies on beryl crystals. II. Dislocation and growth of (10 $\bar{1}$ 0) prism faces. *Philosophical Magazine* (London) 42: 1337-52.

Griffith, W.P. (1969): Raman studies on rock-forming minerals. Part 1. Orthosilicates and cyclosilicates. *Journal of the Chemical Society A*, 1372-1377

Gübelin, E. J. (1953): Inclusions as a mean of Gemstone Identification, Los Angeles: *Gemological Inst. Of America*.

Gübelin, E. J and Koivula, J. I. (2005): Photoatlas of Inclusions in Gemstones, Vol. 2. *Opinio Publishers*, Basel, Switzerland.

Hagemann, A., Lucken, A., Bill, H., Gysler-Sanz, J and Stalder, H.A. (1990): Polarized Raman spectra of beryl and bazzite. *Physics and Chemistry of Minerals*, 17, 395-401.

Hall, A and Walsch, J. N. (1971): The beryls of the Rosses district, Donegal. *Mineral. Mag.* 38, 328-334.

Hänni, H. A. (1982). A contribution to the separability of natural and synthetic emeralds. *J. Gemm.*, 18(2), 138-44

Hawthorne, F.C and Černý, P. (1977): The alkali-metal positions in Cs-Li Beryl. *Canadian Mineralogist*, 15, p. 414-421.

Hawthorne, F.C and Huminicki, D.M.C. (2002): The Crystal Chemistry of Beryllium. *Reviews in Mineralogy & Geochemistry*. 50, 333-403.

Hazen, R. M., Au A.Y and Finger, L. W. (1986): High-pressure crystal chemistry of beryl (Be<sub>3</sub>Al<sub>2</sub>Si<sub>6</sub>O<sub>18</sub>) and euclase (BeAl-SiO<sub>4</sub>OH). *Am Mineral* 71:977–984

Heald, M. T. (1956): Cementation of Simpson and St. Peter sandstones in parts of Oklahoma, Arkansas and Missouri. *J. Geology*. 64, 16-30 in Meakin, P and Rosso, K. M. (2008): Simple kinetic Monto Carlo Models for dissolution pitting induced by crystal defects. *The Journal of Chemical Physics* 129, 1-19.

- Hofmeister, A.M., Hoering, T.C and Virgo, D. (1987): Vibrational spectroscopy of beryllium aluminosilicates: Heat capacity calculation from band assignments. *Physics and Chemistry of Minerals*, 14, p. 205-224.
- Hölscher, A., Schreyer, W and Lattard, D. (1986): High-pressure, high-temperature stability of surinamite in the system MgO-BeO-Al<sub>2</sub>O<sub>3</sub>-SiO<sub>2</sub>-H<sub>2</sub>O, *Contrib Mineral Petrol* 92: 113-127.
- Honess, A. P. (1917): On the etching figures of beryl. *American Journal of Science- fourth series*, Vol. 43, p. 223-236.
- Honess, A. P. (1927): The nature, origin and interpretation of the etch figures on crystals, New York J. Wiley & Sons; London Chapman & Hall.
- Hsu, L.C. (1983): Some phase relationships in the system BeO-Al<sub>2</sub>O<sub>3</sub>-SiO<sub>2</sub>-H<sub>2</sub>O with comments on the effect of HF. *Geol Soc China Memoir* 5:33-46
- Hunt, G.R and Salisbury, J. W. (1970): Visible and Near Infra red spectra of minerals and rocks: I silicate minerals. *Modern Geology*, Vol. 1 pp. 283-300.
- Huong, L.T.T. (2008): Microscopic, chemical and spectroscopic investigations on emeralds of various origins. PhD thesis. University of Mainz (Germany).
- Huong, L. T., Häger, T and Hofmeister, W. (2010): Confocal Micro-Raman Spectroscopy: A Powerful Tool to Identify Natural and Synthetic Emeralds. *Gems & Gemology*, Spring 2010, Volume 46, no. 1
- Isotani, S., Furtado, W. W., Antonini, R and Dias, O. L. (1989): Line-shape and thermal analysis of the Fe<sup>2+</sup> band in Brazilian green beryl. *Am Mineral* 74: 432-438
- Jannettaz, E. (1873) : Sur la propagation de la chaleur dans les corps Cristallisés. Paris : Gauthier-Villars. 82 pp. In Sinkankas J. (1981) Emerald and other beryls. Chilton Book Company, Radnor.
- Jahns, R. H. (1953): The genesis of pegmatites; 1. Occurrence and origin of giant crystals. *American Mineralogist*, 38, 563-598.
- Jahns, R. H. (1955): The study of pegmatites. *Economic Geology*, 50th Anniversary, 1025-1130.
- Joshi. M. S., Kotru. P. N and Ittyachen. M. A. (1978): Revelations of stepped dislocations in amethyst crystals by hydrothermal etching. *American Mineralogist*, Vol. 63, 744-746.
- Kane, R. E and Liddicoat, R.T. (1985): The Biron hydrothermal synthetic emerald. *Gems & Gemology*, 21(3), 156-70.
- Kazmi, A. H., Peters, J. J and Obodda, H. P. (1985): Gem- pegmatites of the Shingus- Dassu area, Gilgit, Pakistan. *Mineral. Rec.*, 16, 393-411.
- Khaibullin, R.I., Lopatin, O.N., Vagizov, F.G., Bazarov, V.V., Bakhtin, A.I., Khaibullin, I.B., and Aktas, B. (2003): Coloration of natural beryl by iron ion implantation. *Nuclear Instrument and Methods in Physics Research Section B: Beam Interactions with Material and Atoms*, 26, p. 277-281

- Kim, C., Bell, M.I., McKeown, D.A. (1990): Vibrational analysis of beryl ( $\text{Be}_3\text{Al}_2\text{Si}_6\text{O}_{18}$ ) and its constituent ring ( $\text{Si}_6\text{O}_{18}$ ). *Physica B*, 205, p. 193-208.
- Kodaira, K, Iwase, A., Tsunashima, A and Matsushita, T. (1983): High pressure hydrothermal synthesis of beryl crystals. *Journal of Crystal Growth*. Vol. 60, pp. 172-174.
- Kohlmann, H. (1907): Beiträge zur Kenntniss der brasilianischen Berylls. In Sinkankas J. (1981) Emerald and other beryls, Chilton Book Company, Radnor.
- Kolesov, B.A and Geiger, C.A. (2000): The orientation and vibrational states of  $\text{H}_2\text{O}$  in synthetic alkali-free beryl. *Physics and Chemistry of Mineral*, 27, p. 557-564.
- Larsen, A.C. and Von Dreele, R.B. (2004): Generalized structure analysis system. Los Alamos National Laboratory Report LAUR 86-748.
- Lathi and Kinnuen. (1993): A new gem beryl locality: Lumäki, Finland. *Gems & Gemology*, Vol. 29, No.1, pp. 30-37
- Laurs, M. B., Dillas, J.H., Wairrach, Y and Kausar, A.B. (1998): Geological setting and petrogenesis of symmetrically zoned, miarolitic granitic pegmatites at Stak Nala. Nanga Parbat-Haramosh massif, Northern Pakistan. *Canad. Mineral.*, 36, 1-47
- Lebedev, A.S. (1980): The lower temperature boundary of beryl crystallization at hydrothermal conditions. In Be-Minerals: Synthesis, Stability, and Occurrence in Metamorphic Rocks,
- Leung, C.S., Merigoux, H., Poirot, J.P and Zecchini, P. (1983): Sur l'identification des pierres fines et de synthèse par spectroscopie infrarouge. *Association française de gemmology*, ISSN 0398-9011, 75, p. 14-15.
- Leung, C.S., Merigoux, H., Poirot, J.P and Zecchini, P. (1986): Use of infrared spectrometry in gemmology. In: *Proceedings of the 13th General Meeting of the International Ineralogical Association*, Varna, 1982, Vol. 2, publ. Sofia 1986, 441-8
- Lin, C. T. (1994): Screw dislocations of  $\text{YBa}_2\text{Cu}_3\text{O}_{7-y}$  single crystal revealed by chemical etching. *J. Cryst. Growth*. 143, 110-114.
- Liu Yan., Deng Jun., Li ChaoFeng., Shi GuangHai and Zheng AiLi. (2007): REE composition in scheelite and scheelite Sm-Nd dating for the Xuebaoding W-Sn-Be deposit in Sichuan Chinese Science Bulletin, vol. 52, no. 18, 2543-2550
- Lodzinski M., Sitarz, M., Stec K., Kozanecki M., Fojud Z and Jurga, S. (2005): ICP, IR, Raman, NMR investigations of beryls from pegmatites of the Sudety Mts. *J Mol Struct* 744: 1005- 1015.
- London, D. (1986): Formation of tourmaline-rich gem pockets in miarolitic pegmatites. *Am. Mineral*. 71, 396-405.
- London, D. (2008): Pegmatites. *Can Mineral Spec Publ* 10, Mineralogical Association of Canada, Quebec, pp 54

- Makreski, P and Jovanovski, G. (2009): Minerals from Macedonia. XXII. Spectroscopic and Structural Characterization of Schorl and Beryl Cyclosilicates, *Spectrochim. Acta*, 73A 460–467.
- Mandelbrot, B. B. (1975): Les objets fractals : forme, hasard et dimension, *Flammarion*, Paris, 1975.
- Mandelbrot, B. B. (1989): Fractal Geometry: What is it and what does it do? *Proc. R. Soc. Lond. A* 423, 3-16.
- Manier-Glavinaz, V., Couty, R and Lagache, M. (1989): The removal of alkalis from beryl: Structural adjustments. *Canadian Mineralogist*, 27, p. 663-671.
- Markl, G and Schumacher, J. (1997): Beryl stability in local hydrothermal and chemical environments in a mineralised granite. *Amer. Mineral.* 82, p. 195-203.
- Mashkovtsev, R.I and Lebedev, A.S. (1993): Infrared spectroscopy of water in beryl. *Journal of Structural Chemistry*, p. 930-933.
- Mashkovtsev, R.I., Stoyanov, E.S and Thomas, V.G. (2004): State of molecules and ions in the structural channels of synthetic beryl with an ammonium impurity. *Journal of Structural Chemistry*, 45, 1, p. 56-63.
- Mathew, G., Karanth, R. V., Gundu Rao, T. K. and Deshpande, R. S. (1997): Cause of colour in colourless beryl: A ESR and OA investigation. *Proceedings of DAE Solid State Physics Symposium*. 40, 26-27.
- Mathew, G., Karanth, R. V., Gundu Rao, T. K. and Deshpande, R. S. (1998): Maxixe type colour centre in natural colourless beryl from Orissa, India: An ESR and OAS spectroscopic investigation. *Journal of Gemology*. 26, 238 - 251.
- Mathew, G., Karanth, R. V., Gundu Rao, T. K and Deshpande, R. S. (2000): Colouration in natural Beryls: A Spectroscopic investigation. *Journal of Geological Society of India*, 56, 285-303.
- Medina J. E., Morante M and Leguey, S. (1983): Natural etch pits in beryl related with the structure. *Bulletin de Mineralogie*, 106, 293-297.
- Middlemiss, C.S and Parshad, L.J. (1918): Note on the aquamarine mines of Dassu on the aquamarine mines of Dassu on the Braldu River, Shigar valley, Baltistan. *Rec. Geol. India*. 45, 160-172.
- Morosin, B. (1972): Structure and thermal expansion of beryl. *Acta Crystallogr B* 28: 1899-1903.
- Moroz, I., Roth, M., Boudeulle, M and Panczer, G. (2000): Raman microspectroscopy and fluorescence of emeralds from various deposits. *Journal of Raman Spectroscopy*, 31, p. 485-490.
- Motzer, C and Reichling, M. (2010): Morphological classification and quantitative analysis of etch pits *Journal of Applied Physics*, 108.

- Mukherjee, B. (1951): Colour of beryl. *Nature* 167, 602.
- Nassau, K., Prescott, B.E and Wood, D.L. (1976): The deep blue Maxixe-type color center in beryl. *Am. Mineral.*, 61, 100–7
- Newnham, R.E and Yoon, H.S. (1973): Elastic anisotropy in minerals. *Mineralogical Magazine*, 39, 7 8-84.
- O' Donoghue, M. (1990): *Gemstones of Pakistan*. Gemstone Corp. Pakistan. 146p.
- Parkin, K.M., Loeffler, B.M and Burns, R.G. (1977): Mössbauer spectra of kyanite, aquamarine and cordierite showing intervalence charge transfer. *Phys Chem Miner* 1: 301–311
- Pecora, W. T., Klepper, M. R and Larrabec, D. M. (1950a): Mica deposits in Minas Gerais, Brazil. *USGS Bull.* 964-c., Wasington, D. C., 305 pages.
- Penfield, S. L and Sperry, E. S. (1888): Mineralogical notes. *American Journal of Science* 36: 317-31. In. Sinkankas J. (1981) *Emerald and other beryls*. Chilton Book Company, Radnor.
- Petersson, G.W. (1891): Natürliche Lösungerscheinungen an Beryll. *Zeitschrift für Kristallographie und Mineralogie* (Leipzig) 63: 153-6. In. Sinkankas J. (1981) *Emerald and other beryls*. Chilton Book Company, Radnor.
- Pitkänen, R. (1991): The lumäki gem beryl pegmatite. In Lathi and Kinnunen (1993) *A new gem beryl locality: Lumäki, Finland*. *Gems and Gemology*, Vol. 29, No.1, pp.30-37
- Plyusina, I.I. (1964): Infrared absorption spectra of beryls. *Geokhimiya*, 1, p. 31-41.
- Plyusina, I.I and Surzhanskaya, E.A. (1967): IR spectrum of beryl. *Zhurnal Prikladnoi Spektroskopii*, 7, 6, p. 917-923
- Pouchou, J. L and Pichoir, F. (1984): Un nouveau modèle de calcul pour la microanalyse quantitative par spectrométrie de rayons X. *La Recherche Aérospatiale*, 3, 167-192
- Price, D.C., Vance, E.R., Smith, G., Edgar, A and Dickson, B.L. (1976): Mössbauer effect studies of beryl. *J Phys* 37(C) 6: 811–817
- Proctor, K. (1984): Gem pegmatites of Minas Gerais, Brazil: Exploration, occurrence, and aquamarine deposits. *Gems & Gemology*, Vol. 20, No. 2, 78-100
- Proctor, K. (1985): Gem pegmatites of Minas Gerais Brazil: The tourmalines of the Aracuai districts. *Gems & Gemology* 2 (1): 3-19.
- Proctor, K. (1985b): Gem pegmatites of Minas Gerais Brazil: The tourmalines of the Governador Valadares District. *Gems & Gemology* 21 (2): 86-104.
- Raju, K. S. (1980): Evidence of edge and screw dislocations in gypsum single crystals. *Bull. Mater. Sci.* 2, 139-144
- Read, P.G. (1986): *Beryl*. Butterworth Gem Books, London, 225 p

- Roedder, E. (1982): Fluid inclusions in gemstones: valuable defects; *Proc. Int. Gemol. Symp.*, 1, Santa Monica, 479-502.
- Rosenhotz, J. L and Smith, D. T. (1936): The dielectric constant of mineral powders; *American Mineralogist*, 21, pp. 115-120.
- Sanders, I. S and Doff, D. H. (1991): A blue sodic beryl from southeast Ireland. *Mineral Mag* 55: 167–172
- Sangwal, K. (1987): Etching of crystals: Theory, Experiment and Applications. North-Holland, Amsterdam
- Schaller, W. T., Stevens, R. L. and Jahns R. H. (1962): An unusual beryl from Arizona. *Amer. Mineral.* 47,681-699
- Schmetzer, K. (1989): Types of water in natural and synthetic emerald. *Neues Jahrbuch für Mineralogie Monatshefte*, p. 15-26
- Schmetzer, K and Kiefert, L. (1990): Water in beryl – a contribution to the separability of natural and synthetic emeralds by infrared spectroscopy. *Journal of Gemmology*, 22, 4, p. 215-223.
- Schreyer, W and Yoder, H.S. Jr. (1964): The system Mg-cordierite-H<sub>2</sub>O and related rocks. *Neues Jahrb. Mineral. Abh.* 101, 271-342.
- Schwarz, S and Stockhert. (1996): Pressure solution in siliciclastic HP-LT metamorphic rocks-constraints on the state of stress in deep levels of accretionary complexes. *Tectono physics*, 255: 203-209.
- Shannon, R. D. (1976): Revised effective ionic radii and systematic studies of interatomic studies in halides and chalcogenides. *Acta Crystallographica*, A32, 751-767.
- Sherriff, B.L., Grundy, H.D., Hartman, J.S., Hawthorne, F.C and Černý, P. (1991): The incorporation of alkalis in beryl: Multi-nuclear MAS NMR and crystal-structure study. *Canadian Mineralogist*, 29, p. 271-285.
- Shigley, J. E and Kampf, A. R. (1984): Gem bearing pegmatites: A review. *Gems and Gemology*, Vol.20, No:2, pp.64-77.
- Simonen, A. (1987): Pre-Quaternary rocks of the map-sheet areas of the rapakivi massif in SE Finland, *Geological Survey of Finland*.
- Simpson, E. S. (1948): Minerals of Western Australia. I. W. A. Perth, 479
- Sinkankas, J. (1981): Emeralds and other beryls. Chilton Book Company, Radnor.
- Sinkankas, J. (1989): Emerald and other beryls. Geoscience Press
- Stockton, C.M. (1984): The chemical distinction of natural from synthetic emeralds. *Gems & Gemmology*, 20, 3, p. 141-145.

- Stockton, C.M. (1987). The separation of natural from synthetic emeralds by infrared spectroscopy. *Gems & Gemology*, **23**(2), 96-9
- Stuart, B. (2014): Infrared spectroscopy: Fundamentals and applications. John Wiley and Sons, Ltd
- Sunagawa, I. (1962b): Mechanism of natural etching of Hematite crystals. *Amer. Miner*, **47**, 1332-1345.
- Sunagawa, I. (1981): Observations of the influence of stress fields on the shape of growth and dissolution spirals. *Journal of Crystal growth*, **53**, 490-504.
- Sunagawa, I. (1987): Surface microtopography of crystal faces; Morphology of crystals pp.321-365.
- Syromyatnikov, F. V., Makarova, A. P and Kupriyanova II (1972): Experimental studies of stability of beryl and phenacite in aqueous solutions. *Intl Geol Rev* **14**:837-839.
- Szurgot, M. (2010): Investigations of distributions of point defect clusters in lopezite crystals by etch topography. *Microscopy: Science, Technology, Applications and Education A. Méndez-Vilas and J. Díaz (Eds)* 2137-2144.
- Tarte, P. (1965): Effet isotopique Li6-Li7 dans le spectre infra-rouge de composés inorganiques du lithium. 1. Carbonate, chromoferrite, tungstate, molybdate et nitrate de lithium. *Spectrochimica Acta*, **21**, 2, p. 313-319.
- Tempesta, G, Scandale, E and Agrosi, G. (2011): Striations and hollow channels in rounded beryl crystals, *Periodico di Mineralogia* **79**, 1 (Special Issue), 75-87
- Thomas, T. R. (1999): Rough Surfaces, 2nd ed., Imperial College Press, London, U.K.
- Traube, H. (1895): Über die Ätzfiguren einiger Minerale. Neues Jahrbuch für Mineralogie Beilage-Bd. 10, pp. 454-69. In J. Sinkankas (1981) Emerald and other beryls. Geoscience Press, Prescott, Arizona.
- Tröger, W. E. (1982): Optische bestimmung der gesteinsbildenden Minerale. P.38, E. Schweitzerbert'sche Verlagsbuchhandlung, Stuttgart.
- Tutton, A. E. H. (1922): Crystallography and Practical Crystal measurement. Vol. 2. London: Macmillan and Co. In Sinkankas (1981) Emerald and other beryls. Chilton Book Company, Radnor.
- Twells, R. (1922): Beryl as a constituent in high tension insulator porcelain. *Journal of the American Ceramic Society* Vol. 5, Issue. 5, 228-234.
- Uher, P., Chudík, P., Bacík, P., Vaculovič, T and Galiová, M. (2010): Beryl composition and evolutionary trends: An example from granitic pegmatites of the beryl- columbite subtype, western Carpathians, Slovakia. *Journal of Geosciences*, **55**, 69-80
- Vaasjoki, M. (1977): Rapakivi granites and other postorogenic rocks in Finland. In Lathi and Kinnunen (1993) A new gem beryl locality: Luumaki, Finland; *Gems & Gemology*, Vol.29, No.1, pp.30-37

- Vianna, P., da Costa, G., Grave, E., Evangelista, H and Stern, W. (2002a): Characterisation of beryl (aquamarine variety) by Mossbauer spectroscopy. *Physics and Chemistry of Minerals*, Volume 29, pages 78-86
- Vianna, R., Jordt- Evangelista, H., da Costa, G. and Stern, W. (2002b): Characterization of beryl (aquamarine variety) from pegmatites of Minas Gerais, Brazil, Volume 29, pages 668-679
- Voigt, J. H. (1887): Bestimmung der Elästicitäts Constantanen von Beryll und Bergkrystall. *Neues Jahrbuch für Mineralogie (Stuttgart) Beilage-Bd.5* p.84. In Sinkankas (1981) *Emerald and other beryls*. Chilton Book Company, Radnor.
- Vorma, A., Sahama, Th. G and Happala, I. (1965): Alkali position in the beryl structure. *Soc.Geol. Fin.* 37, 119-129.
- Wang, R.C., Che, X.D., Zhang, W.L., Zhang, A.C and Zhang, H. (2009): Geochemical evolution and late re-equilibrium of Na-Cs- rich beryl from the Koktokay #3 pegmatite (Atlai, NW China). *Eur J Mineral* 21: 795-809.
- Wickersheim, K.A and Buchanan, R.A. (1959): The near infrared spectrum of beryl. *American Mineralogist*, 44, p. 440-445.
- Wickersheim, K.A and Buchanan, R.A. 1965): Some remarks concerning the spectra of water and hydroxyl groups in beryl. *Journal of Chemical Physics*, 42, 1468-1469.
- Wilk, F. J. (1887): Mineralogische und petrographische Mitteilungen. In Sinkankas, J. (1981) *Emerald and other beryls*. Chilton Book Company, Radnor.
- Wheeler, E. K., Fluck, R., Woods, B and Whitman, P. K. (2003): Effect of Surface Degradation on Optical Performance of Potassium Dihydrogen Phosphate Optics. *Appl. Opt.* 42, 5545-5550.
- Wood, D.L and Nassau, K. (1967): Infrared spectra of foreign molecules in beryl. *The Journal of Chemical Physics*, 47, 7, p. 2220-2228.
- Wood, D.L and Nassau, K. (1968): The characterization of beryl and emerald by visible and infrared absorption spectroscopy. *Am Mineral* 53: 777-800
- Wooster, W. A. (1976): Etch figures and crystal structures. *Kristall und Technik* 11, 6, 615-623.
- Yamamoto, M. (1957): A note on the formation of etch pits on crystals. The 895<sup>th</sup> report of the Research Institute for Iron, Steel and Other Metals.
- Yonenaga, I., Taishi, T., Huang, X and Hoshikawa, K. J. (2001): Dynamic characteristics of dislocations in highly boron-doped silicon. *Appl. Phys.* 89, 5788.
- Yurgenson, G. A. (1965): Calcium-bearing vorobyevite-a new variety of beryl. *Vestn. Nauchn.Inf. Zabaikalsk. Otd. Geogr. Obschest. U.S.S.R.*, 45-48.
- Zedlitz, O. (1941): Goniometrische Untersuchungen der Lösungs- und Aetzerscheinungen an einem Beryllkristall von Minas Gerais, Brasilien. *Neues Jahrbuch Mineralogie, Abt A.*, pp.98-108

Zhou, J., Reddic, J. E., Sinha, M., Ricker, W. S., Karlinsey, J., Yang, J. W., Khan, M. A and Chen, D. A. (2002): Surface morphologies of MOCVD-grown GaN films on sapphire studied by scanning tunneling microscopy. *Appl. Surf. Sci.* 202, 131-138.

## 7. Appendix

### Contents

Table of oxides of individual samples and inclusions

Infrared spectra of powdered samples

Infrared spectra of single crystals under polarised light

Raman spectra of samples

NIR spectra of samples under different orientations

Three dimensional reconstruction of P-type and stepped etch pit

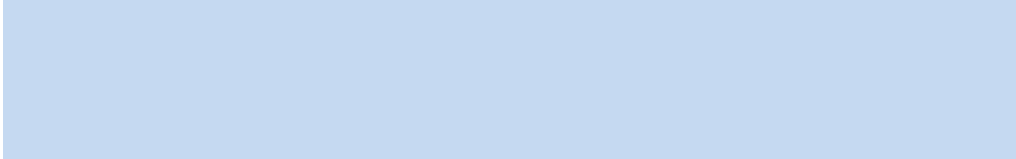
SEM images

AFM image of polished thin section of BA-1

### FH-3

W%BeO	W%Na2O	W%MgO	Al2O3	W%SiO2	Ox%(Ca)	Ox%(Mn)	Ox%(Fe)	Ox%(Rb)	Ox%(Cs)	total
13.88	0.09	0.05	18.85	66.90	0.03	0.02	0.54	0.12	0.10	<b>100.58</b>
13.88	0.07	0.05	19.01	67.17	0.03	0.00	0.51	0.13	0.11	<b>100.95</b>
13.88	0.11	0.07	18.93	67.23	0.01	0.00	0.54	0.08	0.16	<b>101.01</b>
13.88	0.09	0.08	18.63	67.11	0.01	0.01	0.55	0.12	0.13	<b>100.61</b>
13.88	0.10	0.04	19.11	67.03	0.01	0.00	0.50	0.08	0.14	<b>100.88</b>
13.88	0.09	0.08	18.90	66.79	0.00	0.00	0.53	0.09	0.08	<b>100.43</b>
13.88	0.12	0.06	18.91	65.45	0.00	0.00	0.44	0.10	0.00	<b>98.95</b>
13.88	0.15	0.03	18.95	67.08	0.00	0.00	0.55	0.08	0.18	<b>100.89</b>
13.88	0.12	0.05	18.98	67.31	0.00	0.00	0.61	0.07	0.10	<b>101.12</b>
13.88	0.12	0.04	18.69	67.09	0.00	0.00	0.50	0.11	0.09	<b>100.52</b>
13.88	0.10	0.06	19.08	67.26	0.00	0.01	0.54	0.12	0.09	<b>101.13</b>
13.88	0.10	0.09	18.90	67.96	0.02	0.00	0.57	0.12	0.10	<b>101.73</b>
<b>13.88</b>	<b>0.54</b>	<b>0.00</b>	<b>17.55</b>	<b>61.87</b>	<b>3.73</b>	<b>0.00</b>	<b>0.50</b>	<b>0.03</b>	<b>0.11</b>	<b>98.23</b>
<b>13.88</b>	<b>0.31</b>	<b>0.60</b>	<b>18.24</b>	<b>64.69</b>	<b>2.76</b>	<b>0.00</b>	<b>0.51</b>	<b>0.07</b>	<b>0.12</b>	<b>101.18</b>
					<b>PA-2</b>					
13.88	0.18	0.00	18.60	66.80	0.00	0.02	0.26	0.10	0.21	<b>100.04</b>
13.88	0.22	0.00	18.99	66.91	0.00	0.00	0.21	0.07	0.23	<b>100.52</b>
13.88	0.25	0.00	18.89	66.62	0.00	0.01	0.17	0.10	0.21	<b>100.13</b>
13.88	0.24	0.00	18.50	66.86	0.03	0.01	0.16	0.10	0.24	<b>100.01</b>
13.88	0.19	0.02	18.50	66.31	0.01	0.00	0.19	0.09	0.25	<b>99.44</b>
13.88	0.22	0.01	18.61	66.93	0.00	0.01	0.20	0.12	0.17	<b>100.16</b>
13.88	0.22	0.00	18.49	66.97	0.00	0.00	0.19	0.11	0.21	<b>100.07</b>
13.88	0.23	0.01	18.33	66.50	0.03	0.00	0.32	0.10	0.46	<b>99.85</b>
13.88	0.23	0.03	17.72	66.06	0.00	0.03	0.25	0.10	0.54	<b>98.84</b>
13.88	0.19	0.00	18.74	67.01	0.00	0.04	0.26	0.11	0.45	<b>100.67</b>
13.88	0.18	0.01	17.30	66.79	0.01	0.00	0.24	0.09	0.20	<b>98.70</b>
13.88	0.16	0.00	19.06	67.36	0.01	0.00	0.23	0.10	0.19	<b>100.97</b>
13.88	0.18	0.04	21.50	63.76	0.07	0.02	0.25	0.08	0.21	<b>99.99</b>

13.88	0.19	0.00	21.87	65.44	0.00	0.02	0.15	0.10	0.15	<b>101.80</b>
13.88	0.71	0.03	18.71	66.17	0.00	0.01	0.04	0.12	1.35	<b>101.01</b>
13.88	0.70	0.02	18.59	65.98	0.00	0.00	0.04	0.08	1.26	<b>100.55</b>
13.88	0.20	0.00	19.23	66.46	0.00	0.00	0.15	0.12	0.26	<b>100.29</b>
13.88	0.21	0.00	18.95	65.95	0.00	0.00	0.17	0.10	0.19	<b>99.46</b>
13.88	0.60	0.01	18.59	66.40	0.02	0.00	0.11	0.10	1.22	<b>100.93</b>
					<b>BA-1</b>					
13.88	0.02	0.01	19.16	66.11	0.01	0.01	0.16	0.13	0.00	<b>99.48</b>
13.88	0.02	0.01	19.25	66.12	0.01	0.01	0.17	0.11	0.05	<b>99.63</b>
13.88	0.01	0.02	19.70	67.11	0.00	0.01	0.16	0.10	0.02	<b>101.01</b>
13.88	0.04	0.00	19.52	67.46	0.02	0.00	0.20	0.07	0.00	<b>101.17</b>
13.88	0.06	0.01	19.16	67.96	0.00	0.01	0.12	0.12	0.00	<b>101.31</b>
13.88	0.02	0.00	19.57	67.83	0.02	0.00	0.16	0.10	0.01	<b>101.59</b>
13.88	0.04	0.00	19.47	67.86	0.03	0.00	0.15	0.09	0.00	<b>101.53</b>
13.88	0.04	0.03	19.17	67.60	0.00	0.02	0.15	0.12	0.00	<b>101.00</b>
13.88	0.02	0.01	18.73	67.40	0.00	0.02	0.15	0.06	0.00	<b>100.28</b>
13.88	0.04	0.01	19.57	68.23	0.02	0.00	0.24	0.09	0.07	<b>102.15</b>
0.00	0.01	0.01	0.29	0.73	0.01	0.01	0.03	0.02	0.02	<b>Std.dev</b>
13.88	0.03	0.01	19.33	67.37	0.01	0.01	0.17	0.10	0.02	<b>100.92</b>
<b>Solid Inclusion</b>	<b>0.02</b>	<b>0.15</b>	<b>32.85</b>	<b>40.33</b>	<b>0.10</b>	<b>0.00</b>	<b>0.53</b>	<b>0.00</b>	<b>0.00</b>	<b>87.86</b>



**PAD-1**

Ox%(Be)	Ox%(Na)	Ox%(Al)	Ox%(Si)	Ox%(Fe)	Ox%(Cs)	<b>total</b>
13.88	0.13	18.48	67.00	0.27	0.06	<b>99.82</b>
13.88	0.11	18.55	67.17	0.25	0.09	<b>100.05</b>
13.88	0.14	18.16	67.48	0.27	0.04	<b>99.95</b>
13.88	0.12	18.47	67.19	0.24	0.05	<b>99.95</b>
13.88	0.14	18.76	66.83	0.27	0.08	<b>99.97</b>
13.88	0.15	18.53	67.40	0.25	0.04	<b>100.27</b>
13.88	0.13	18.58	67.04	0.25	0.05	<b>99.92</b>
13.88	0.12	18.43	67.23	0.18	0.05	<b>99.90</b>
13.88	0.13	18.74	67.23	0.22	0.06	<b>100.26</b>
13.88	0.11	18.81	67.25	0.19	0.02	<b>100.27</b>
13.88	0.15	19.05	67.22	0.25	0.07	<b>100.63</b>
13.88	0.14	19.01	67.26	0.21	0.05	<b>100.56</b>
13.88	0.15	18.71	67.02	0.26	0.01	<b>100.02</b>
13.88	0.15	18.52	67.06	0.28	0.08	<b>99.96</b>
13.88	0.13	18.63	67.17	0.24	0.05	<b>100.11</b>

			<b>PAD-3</b>			
13.88	0.14	18.46	66.84	0.27	0.14	<b>99.73</b>
13.88	0.16	18.33	66.39	0.33	0.12	<b>99.21</b>
13.88	0.14	18.39	67.37	0.27	0.07	<b>100.12</b>
13.88	0.15	18.56	67.08	0.33	0.12	<b>100.11</b>
13.88	0.17	18.49	66.58	0.39	0.23	<b>99.74</b>
13.88	0.17	18.42	66.38	0.50	0.27	<b>99.63</b>
13.88	0.18	18.39	66.76	0.48	0.34	<b>100.02</b>
13.88	0.12	18.73	66.74	0.31	0.01	<b>99.80</b>
13.88	0.13	18.51	66.66	0.33	0.05	<b>99.56</b>
13.88	0.13	18.88	66.82	0.35	0.00	<b>100.04</b>
13.88	0.13	18.82	66.92	0.34	0.01	<b>100.11</b>
13.88	0.14	18.88	66.62	0.32	0.05	<b>99.89</b>
13.88	0.15	18.74	66.70	0.29	0.02	<b>99.78</b>
13.88	0.15	18.76	66.60	0.28	0.04	<b>99.70</b>
13.88	0.14	18.73	66.49	0.29	0.00	<b>99.54</b>
13.88	0.15	18.61	66.73	0.34	0.10	<b>99.80</b>
			<b>PAD-4</b>			
13.88	0.09	18.92	66.92	0.06	0.07	<b>99.95</b>
13.88	0.13	18.84	66.75	0.08	0.10	<b>99.78</b>
13.88	0.18	18.80	66.73	0.22	0.22	<b>100.04</b>
13.88	0.16	18.79	66.42	0.23	0.11	<b>99.59</b>
13.88	0.17	18.76	66.65	0.22	0.11	<b>99.79</b>
13.88	0.12	18.65	66.06	0.08	0.09	<b>98.87</b>
13.88	0.10	18.85	67.03	0.07	0.08	<b>100.02</b>
13.88	0.12	18.85	66.89	0.07	0.07	<b>99.88</b>
13.88	0.18	18.74	66.71	0.28	0.10	<b>99.89</b>
13.88	0.16	18.62	66.80	0.27	0.08	<b>99.81</b>
13.88	0.18	18.60	66.93	0.30	0.07	<b>99.95</b>
13.88	0.14	18.77	66.72	0.17	0.10	<b>99.78</b>

**PAD-5**

<b>13.88</b>	<b>0.18</b>	<b>18.70</b>	<b>66.76</b>	<b>0.34</b>	<b>0.09</b>	<b>99.96</b>
<b>13.88</b>	<b>0.19</b>	<b>18.50</b>	<b>66.45</b>	<b>0.32</b>	<b>0.09</b>	<b>99.43</b>
<b>13.88</b>	<b>0.19</b>	<b>18.37</b>	<b>66.17</b>	<b>0.34</b>	<b>0.07</b>	<b>99.02</b>
<b>13.88</b>	<b>0.17</b>	<b>18.53</b>	<b>65.89</b>	<b>0.24</b>	<b>0.10</b>	<b>98.81</b>
<b>13.88</b>	<b>0.16</b>	<b>18.66</b>	<b>66.05</b>	<b>0.27</b>	<b>0.08</b>	<b>99.11</b>
<b>13.88</b>	<b>0.19</b>	<b>18.55</b>	<b>66.90</b>	<b>0.22</b>	<b>0.13</b>	<b>99.86</b>
<b>13.88</b>	<b>0.18</b>	<b>18.43</b>	<b>66.48</b>	<b>0.28</b>	<b>0.09</b>	<b>99.33</b>
<b>13.88</b>	<b>0.19</b>	<b>18.80</b>	<b>66.18</b>	<b>0.28</b>	<b>0.07</b>	<b>99.39</b>
<b>13.88</b>	<b>0.18</b>	<b>18.71</b>	<b>66.51</b>	<b>0.30</b>	<b>0.12</b>	<b>99.69</b>
<b>13.88</b>	<b>0.20</b>	<b>18.72</b>	<b>66.75</b>	<b>0.29</b>	<b>0.10</b>	<b>99.93</b>

		<b>PAD-6</b>				<b>99.45</b>
13.88	0.23	18.64	66.46	0.22	0.06	99.48
13.88	0.23	18.55	66.76	0.22	0.05	99.69
13.88	0.24	18.83	66.72	0.23	0.07	99.97
13.88	0.26	18.32	66.25	0.23	0.07	99.00
13.88	0.24	18.29	66.11	0.25	0.06	98.82
13.88	0.22	18.56	66.41	0.24	0.07	99.38
13.88	0.30	18.47	65.92	0.20	0.08	98.84
13.88	0.27	18.60	66.61	0.23	0.07	99.66
		<b>PAD-7</b>				<b>99.36</b>
13.88	0.28	18.41	66.85	0.14	0.37	99.93
13.88	0.28	18.37	67.15	0.14	0.35	100.17
13.88	0.25	18.90	66.98	0.20	0.28	100.49
13.88	0.24	18.96	67.04	0.17	0.28	100.57
13.88	0.23	18.73	67.03	0.17	0.27	100.31
13.88	0.23	18.71	66.82	0.16	0.29	100.09
13.88	0.22	18.99	67.11	0.17	0.31	100.68
13.88	0.20	18.76	66.73	0.15	0.29	100.00
13.88	0.28	18.79	66.94	0.17	0.35	100.42
13.88	0.26	18.90	66.54	0.17	0.32	100.07

**PAD-8**

13.88	0.68	18.25	66.01	0.45	0.13	99.40
13.88	0.84	18.35	65.66	0.45	0.06	99.25
13.88	0.68	18.42	65.68	0.44	0.40	99.48
13.88	0.90	18.33	66.06	0.65	0.05	99.86
13.88	0.89	18.42	65.86	0.55	0.05	99.65
13.88	0.89	18.33	65.99	0.61	0.09	99.78
13.88	0.86	18.29	66.14	0.50	0.08	99.75
13.88	0.80	17.97	65.59	0.48	0.11	98.83
13.88	0.91	18.06	65.76	0.62	0.07	99.29
13.88	0.90	18.40	65.93	0.56	0.03	99.71
13.88	0.85	18.16	65.50	0.58	0.07	99.04

**PAD-9**

13.88	0.21	18.73	66.76	0.17	0.07	99.83
13.88	0.20	18.68	66.52	0.31	0.03	99.62
13.88	0.20	18.21	66.55	0.35	0.02	99.21
13.88	0.22	18.33	65.73	0.23	0.10	98.49
13.88	0.19	18.32	66.76	0.28	0.04	99.47

13.88	0.27	18.47	66.01	0.29	0.04	98.96
13.88	0.21	18.76	66.89	0.24	0.04	100.02
13.88	0.21	18.44	66.63	0.22	0.02	99.40
13.88	0.22	18.80	66.95	0.19	0.12	100.16
13.88	0.31	18.20	65.29	0.18	0.78	98.64
		PAD-10				
13.88	0.23	18.24	65.91	0.30	1.01	99.57
13.88	0.27	18.55	66.31	0.23	0.30	99.55
13.88	0.19	18.85	66.37	0.40	0.09	99.78
13.88	0.21	18.60	66.63	0.48	0.04	99.83
13.88	0.21	18.64	66.53	0.44	0.00	99.71
13.88	0.21	18.47	66.42	0.42	0.02	99.42
13.88	0.23	18.72	66.22	0.44	0.04	99.53
13.88	0.22	18.18	66.60	0.36	0.00	99.24

## PAY-1

13.88	0.09	18.54	65.51	0.04	0.32	98.38
13.88	0.10	18.74	66.74	0.03	0.31	99.79
13.88	0.09	18.98	66.98	0.03	0.27	100.23
13.88	0.09	18.78	65.83	0.04	0.25	98.87
13.88	0.13	18.37	66.23	0.06	0.41	99.08
13.88	0.12	18.45	65.23	0.07	0.49	98.25
13.88	0.18	18.65	65.83	0.00	0.26	98.80
13.88	0.18	18.06	65.89	0.00	0.28	98.30
13.88	0.13	17.77	64.40	0.09	0.55	96.82
13.88	0.12	18.45	65.76	0.10	0.59	98.90
13.88	0.11	18.39	65.67	0.13	0.57	98.75
13.88	0.14	18.57	65.84	0.10	0.55	99.06
		PAY-2				98.77
13.88	0.47	18.37	63.66	0.10	1.11	97.57
13.88	0.46	18.46	64.42	0.12	1.11	98.44
13.88	0.48	18.36	64.67	0.12	1.15	98.67
13.88	0.50	18.52	64.54	0.11	1.13	98.69
13.88	0.50	18.43	64.56	0.10	1.15	98.61
13.88	0.51	18.34	64.56	0.13	1.17	98.60
13.88	0.31	18.43	64.97	0.11	0.79	98.48
13.88	0.34	18.52	64.98	0.12	0.86	98.70
13.88	0.34	18.06	64.85	0.12	0.92	98.17
13.88	0.16	16.98	65.64	0.17	0.04	96.88

13.88	0.17	18.72	65.91	0.15	0.05	98.89
13.88	0.20	18.50	66.00	0.18	0.04	98.80
13.88	0.19	18.38	65.68	0.22	0.09	98.44
		PAY-3				98.38
13.88	0.11	17.66	64.64	0.34	0.06	96.70
13.88	0.11	17.92	64.72	0.29	0.07	96.99
13.88	0.12	17.88	63.95	0.21	0.03	96.06
13.88	0.10	17.42	63.22	0.24	0.06	94.91
13.88	0.18	18.18	63.07	0.04	0.06	95.41
13.88	0.19	18.28	64.35	0.04	0.06	96.80
13.88	0.18	18.33	64.46	0.04	0.04	96.94
13.88	0.15	18.09	64.43	0.19	0.05	96.79
13.88	0.10	17.90	64.70	0.28	0.05	96.92
						96.39

## PAY-4

13.88	0.09	19.07	66.02	0.18	0.18	99.42
13.88	0.08	19.11	66.70	0.17	0.18	100.13
13.88	0.14	18.93	66.06	0.40	0.07	99.48
13.88	0.14	18.69	66.46	0.37	0.09	99.62
13.88	0.10	18.87	66.77	0.26	0.09	99.97
13.88	0.09	18.83	66.63	0.26	0.16	99.84
13.88	0.09	18.65	65.88	0.19	0.22	98.91
13.88	0.10	18.71	66.10	0.20	0.22	99.21
13.88	0.12	18.89	66.52	0.29	0.09	99.78
13.88	0.10	18.91	66.79	0.23	0.09	99.99
13.88	0.14	18.76	66.56	0.33	0.05	99.71
13.88	0.12	18.84	66.69	0.36	0.11	100.00
13.88	0.11	18.61	66.66	0.23	0.24	99.72
13.88	0.13	18.74	66.06	0.38	0.05	99.24
13.88	0.13	18.64	66.23	0.38	0.04	99.30
		PAY-5				
13.88	0.19	18.81	66.69	0.22	0.27	100.06
13.88	0.20	18.53	66.24	0.24	0.26	99.36
13.88	0.15	18.78	66.52	0.38	0.04	99.75
13.88	0.15	18.91	66.58	0.40	0.03	99.95
13.88	0.15	18.90	66.76	0.38	0.04	100.12
13.88	0.17	19.03	66.21	0.21	0.14	99.64
13.88	0.22	18.75	66.58	0.49	0.07	99.98
13.88	0.19	18.82	66.45	0.51	0.04	99.88
13.88	0.19	18.76	66.77	0.54	0.04	100.19
		PAY-6				
13.88	0.12	18.77	66.30	0.33	0.16	99.56
13.88	0.14	19.05	66.77	0.28	0.19	100.30

13.88	0.19	18.72	65.90	0.45	1.08	100.22
13.88	0.23	18.80	65.89	0.38	0.86	100.04
13.88	0.21	18.77	66.29	0.32	0.53	99.99
13.88	0.21	18.94	66.41	0.28	0.63	100.35
13.88	0.20	18.92	66.42	0.26	0.59	100.27
13.88	0.20	18.76	65.83	0.50	1.08	100.26
13.88	0.20	18.65	65.63	0.42	1.09	99.87

### BAA-1

13.88	0.55	18.43	65.72	0.38	0.04	99.00
13.88	0.55	18.57	65.63	0.38	0.05	99.05
13.88	0.58	18.04	65.25	0.30	0.02	98.08
13.88	0.66	17.66	65.42	0.33	0.08	98.04
13.88	0.71	18.48	66.00	0.35	0.09	99.51
13.88	0.70	18.40	65.91	0.30	0.05	99.23
13.88	0.75	18.24	65.93	0.30	0.06	99.17
13.88	0.80	18.37	65.83	0.33	0.08	99.29
13.88	0.77	18.49	65.88	0.31	0.09	99.41
13.88	0.61	18.44	66.14	0.35	0.07	99.48
13.88	0.62	18.43	66.25	0.31	0.03	99.53
		<b>BAA-2</b>				
13.88	1.46	17.88	64.98	0.50	0.93	99.63
13.88	1.46	17.80	64.92	0.52	0.92	99.50
13.88	1.45	18.06	65.22	0.31	0.78	99.69
13.88	1.50	18.04	64.24	0.54	0.34	98.55

### CA-1

13.88	1.53	17.76	65.18	0.09	0.28	<b>98.72</b>
13.88	1.58	17.78	64.83	0.10	0.31	<b>98.48</b>
13.88	1.66	17.64	63.86	0.29	0.51	<b>97.84</b>
13.88	1.56	17.56	63.80	0.29	0.58	<b>97.67</b>

Table 1 Oxide wt% of the individual samples. Figures in red colour indicate the composition along fluid inclusions

## Muscovite

Ox%(Na)	Ox%(Al)	Ox%(Si)	Ox%(K)	Ox%(Ca)	Ox%(Fe)	Ox%(Cs)	total
0.29	31.94	45.09	11.36	0.00	1.82	0.05	90.56
0.30	32.58	45.20	11.31	0.01	1.96	0.06	91.42

Table 2 Oxide wt% of muscovite associated with CA-1

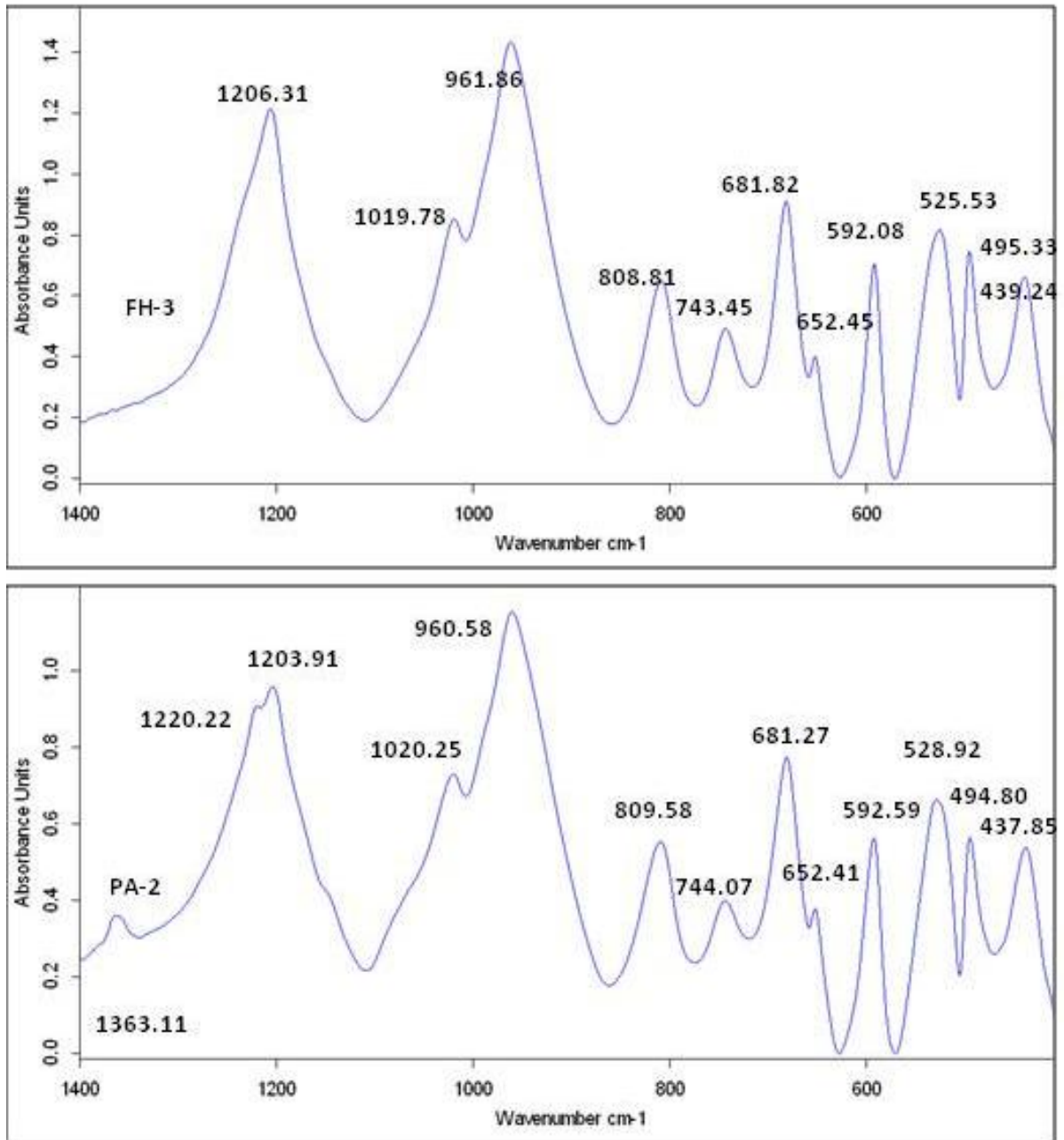


Fig. 1 Infrared spectra of the powdered samples FH-3 and PA-2 in the finger print region from 400 cm<sup>-1</sup> to 1400 cm<sup>-1</sup>.

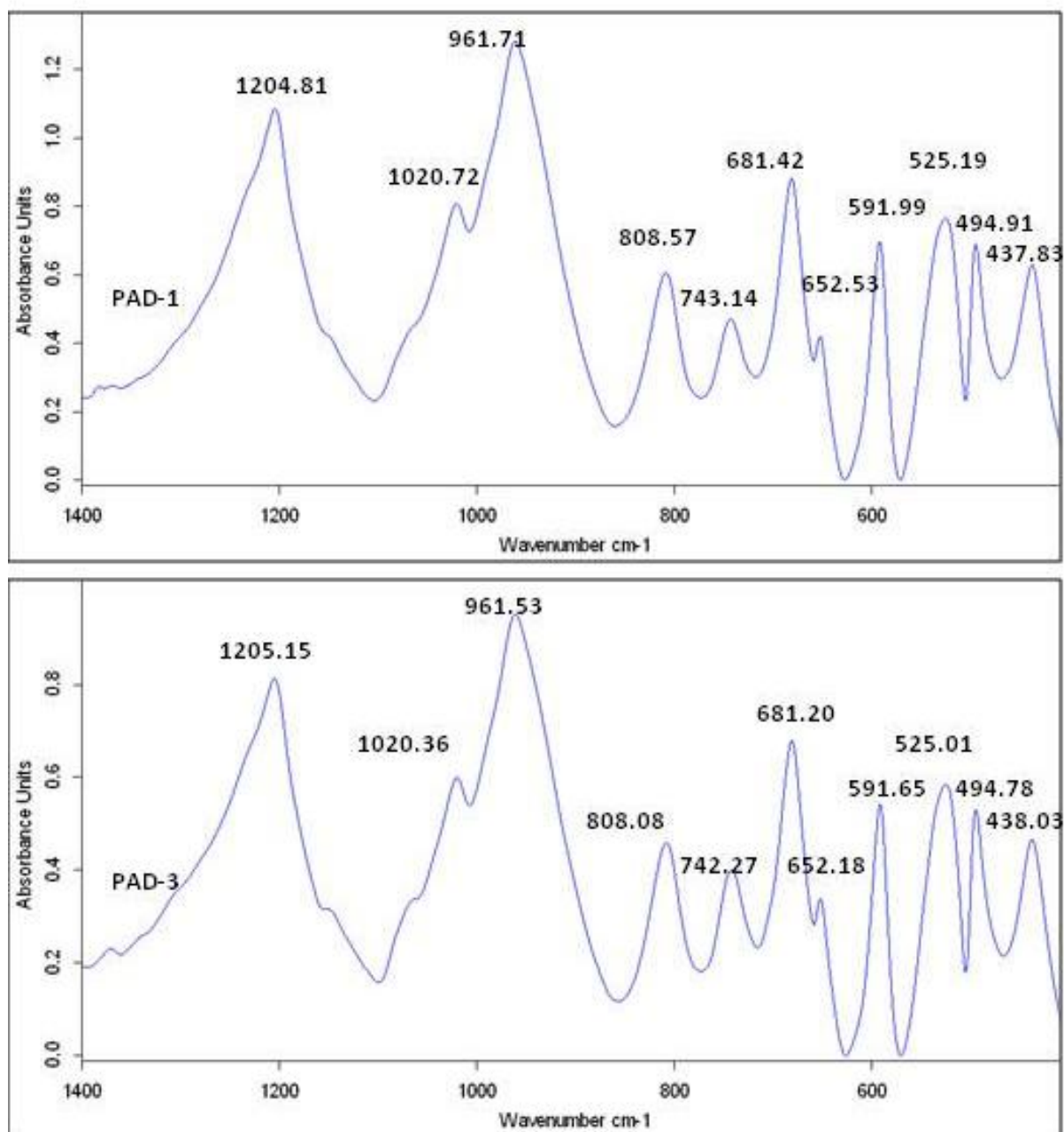


Fig.2 IR spectra of powdered samples PAD-1 and PAD-3 in the region from 400 cm<sup>-1</sup> to 1400 cm<sup>-1</sup>.

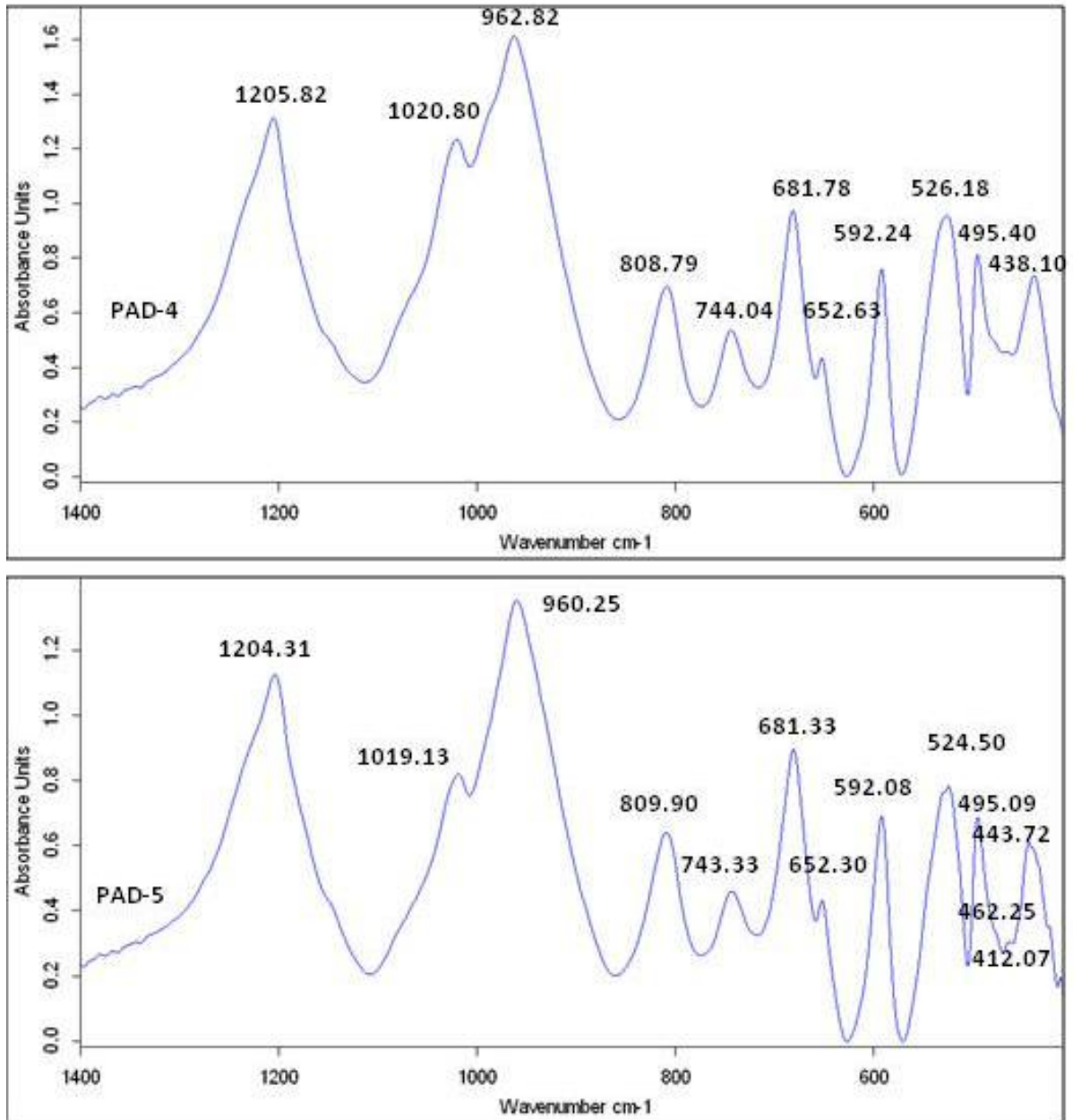


Fig.3 IR spectra of powdered samples PAD-4 and PAD-5 in the frequency region from 400  $\text{cm}^{-1}$  to 1400  $\text{cm}^{-1}$ .

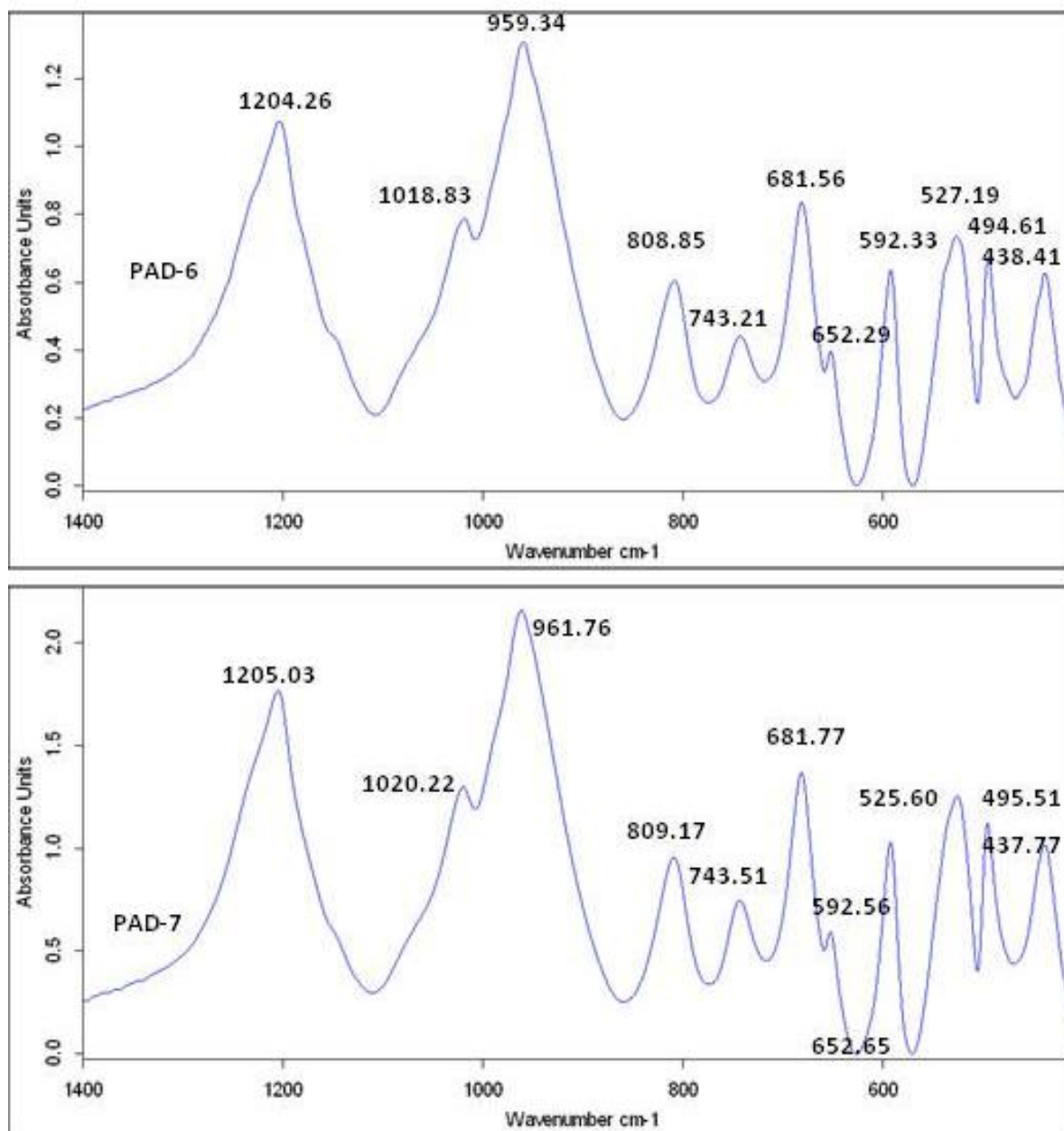


Fig. 4 IR spectra of powdered samples PAD-6 and PAD-7 in the finger print region from 400 cm<sup>-1</sup> to 1400 cm<sup>-1</sup>

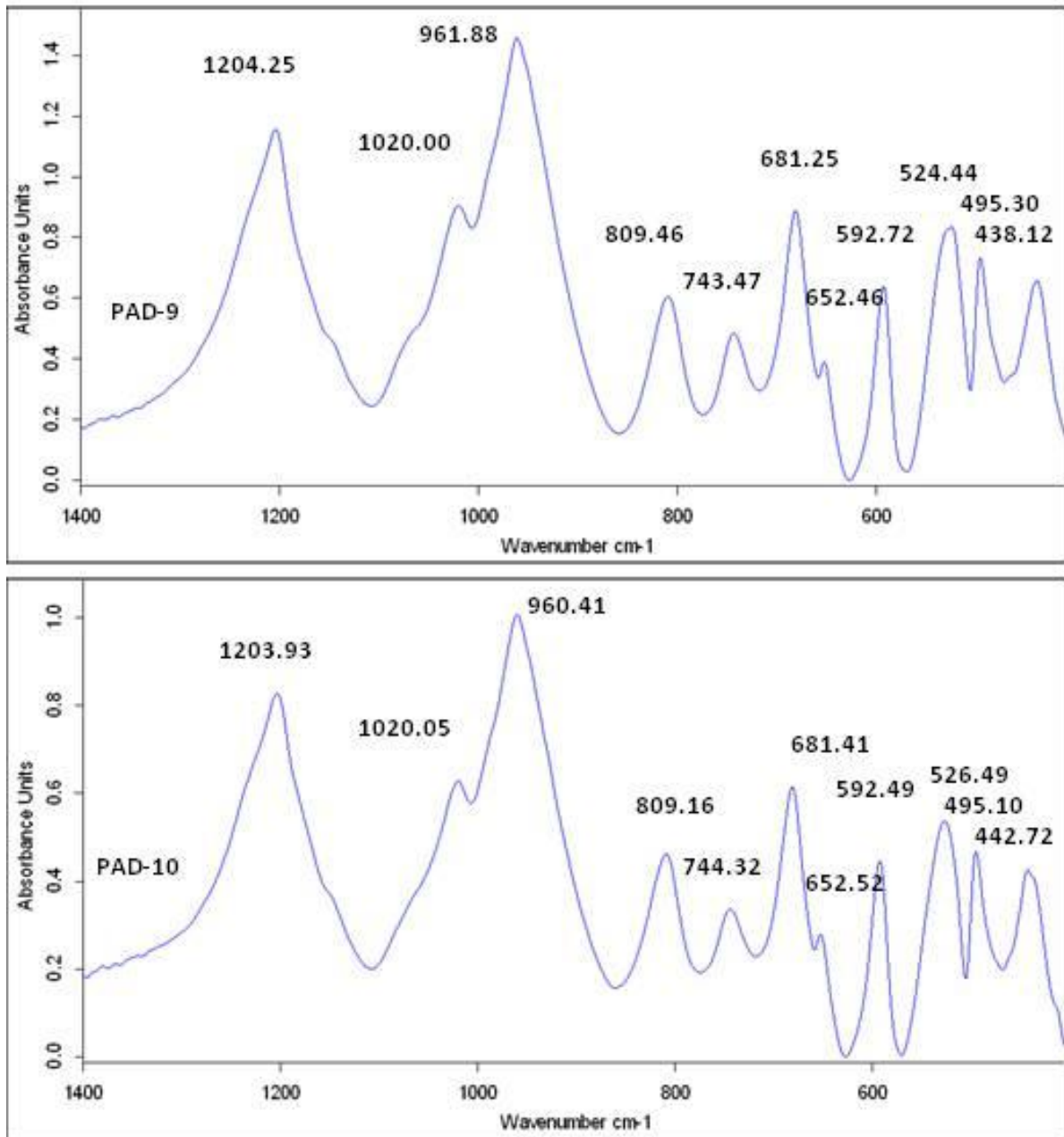


Fig. 5 IR spectra of powdered samples PAD-9 and PAD-10 from wave number 400 cm<sup>-1</sup> to 1400 cm<sup>-1</sup>

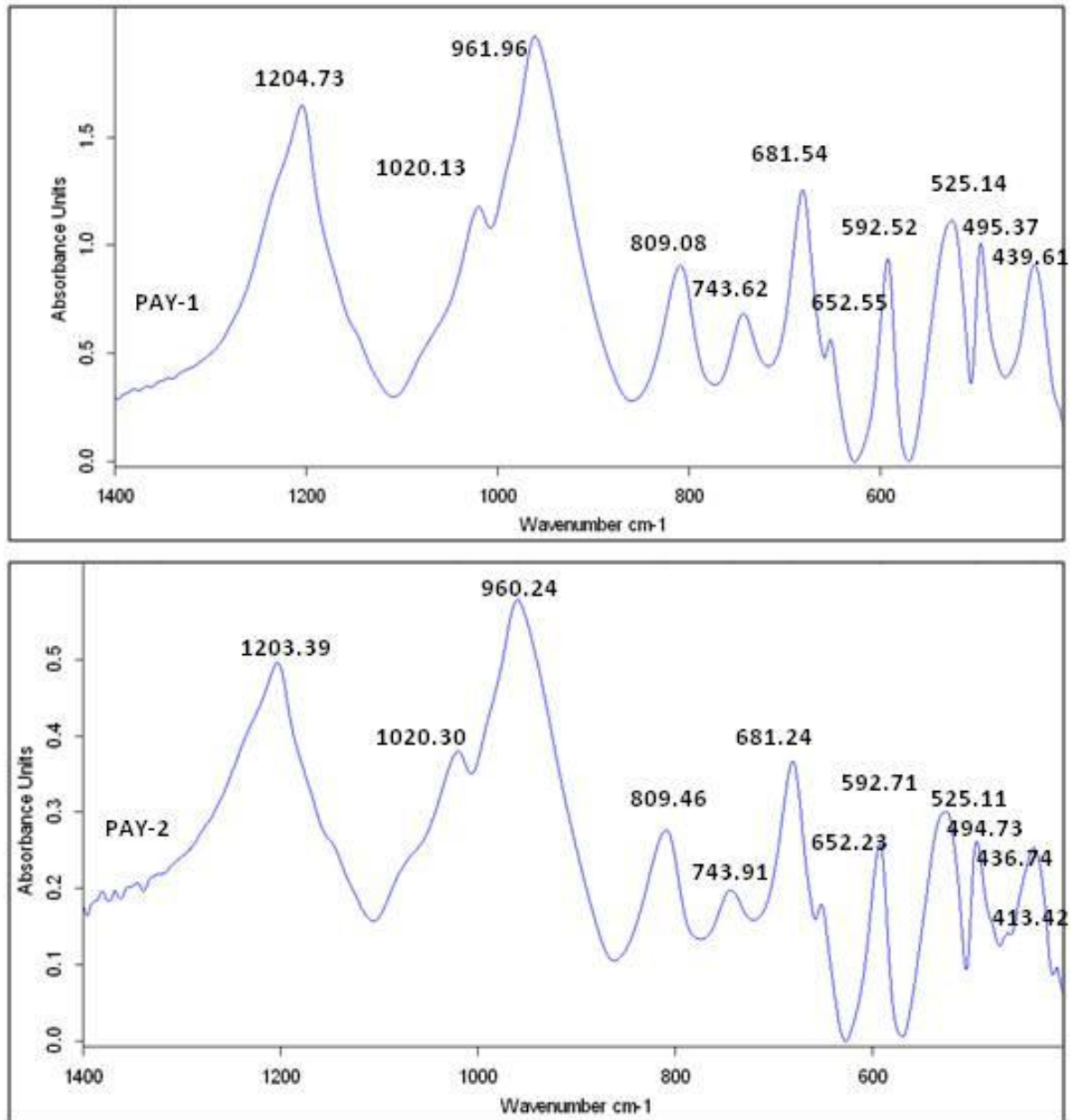


Fig. 6 IR spectra of powdered samples PAY-1 and PAY-2 in the finger print region from  $400 \text{ cm}^{-1}$  to  $1400 \text{ cm}^{-1}$ .

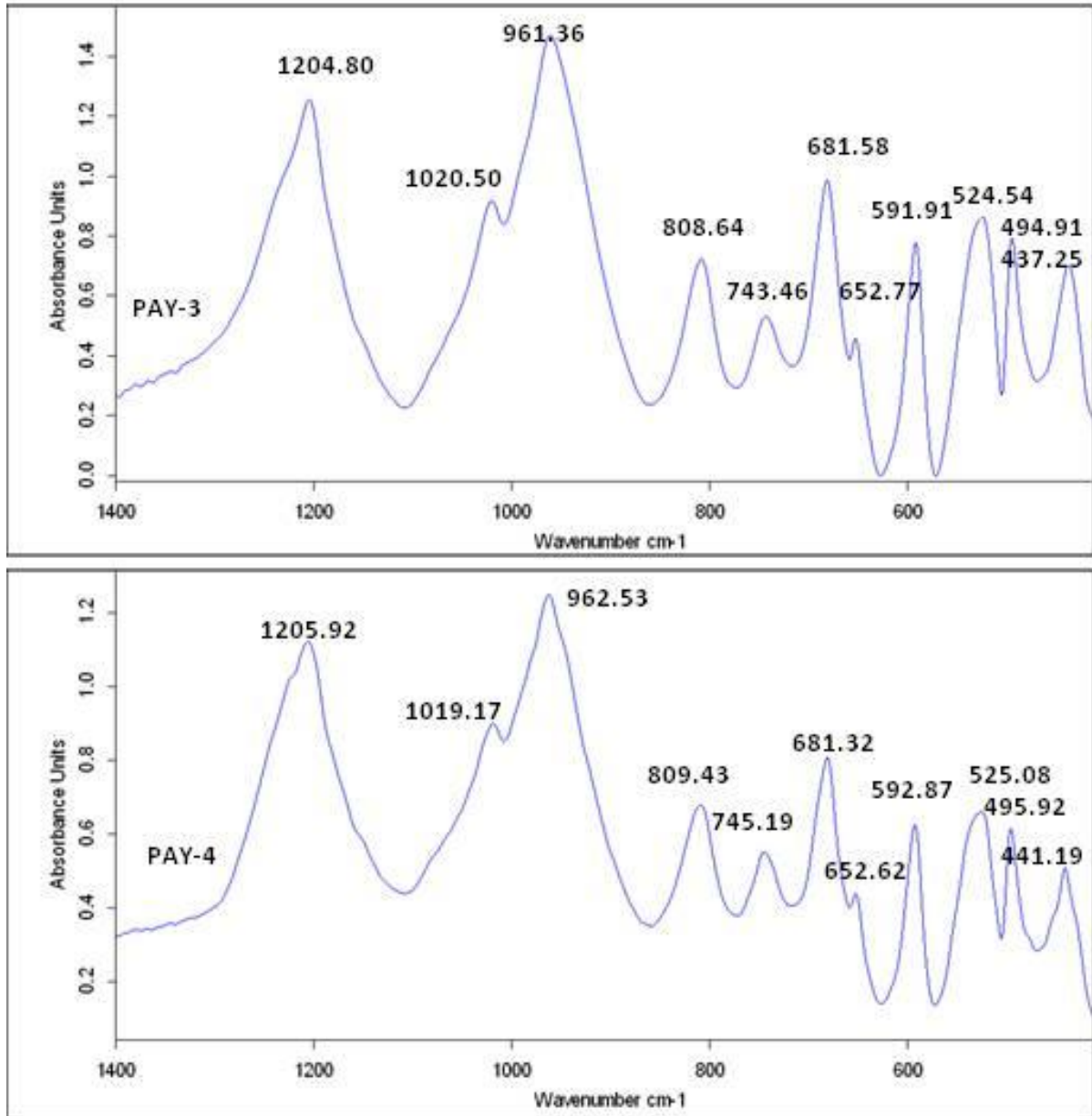


Fig. 7 IR spectra of powdered beryls PAY-3 & PAY-4 in the finger print region from 400  $\text{cm}^{-1}$  to 1400  $\text{cm}^{-1}$ .

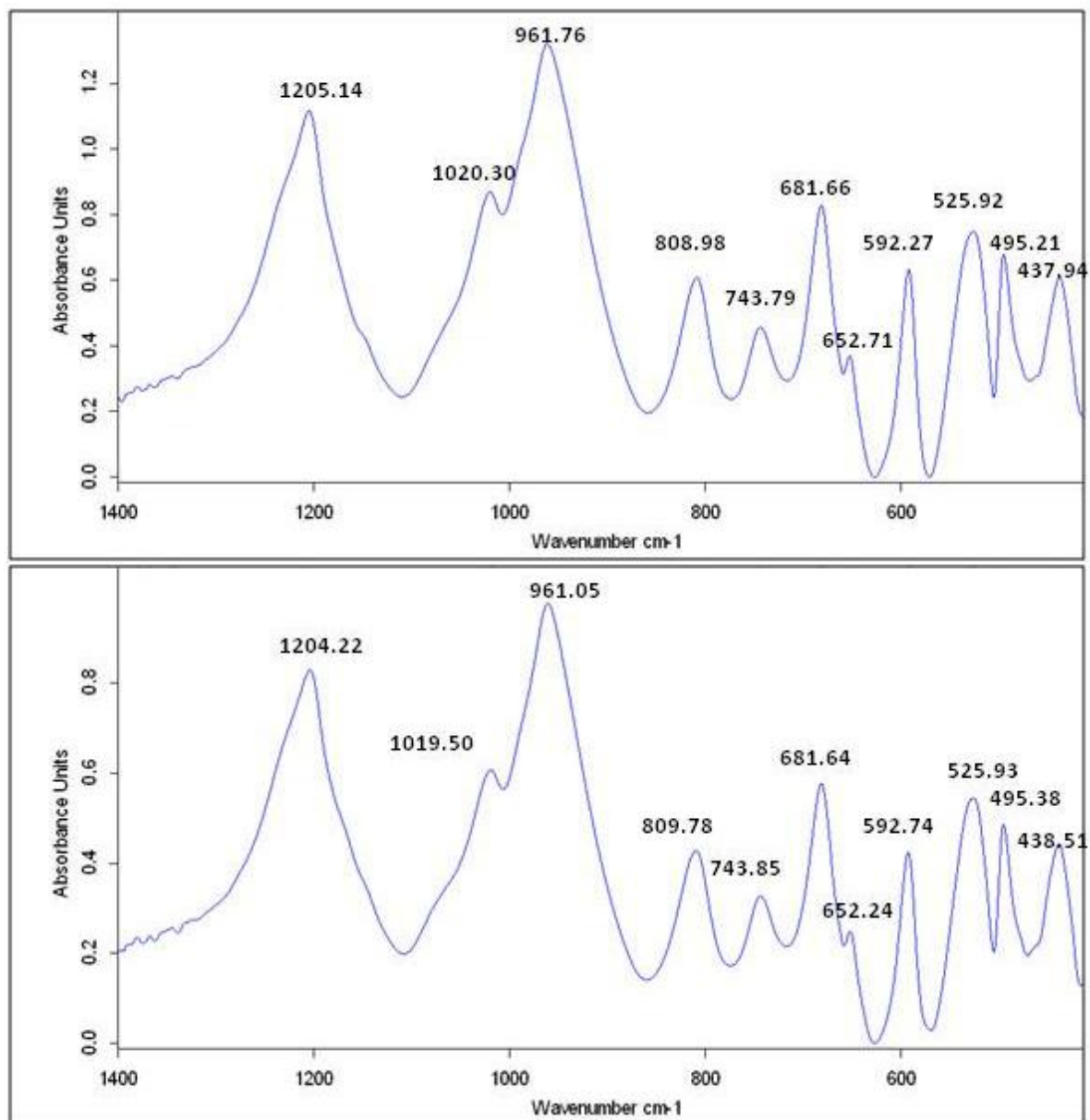


Fig. 8 IR spectra of powdered PAY-5 (above) and PAY-6 (below) in the frequency region from  $400 \text{ cm}^{-1}$  to  $1400 \text{ cm}^{-1}$ .

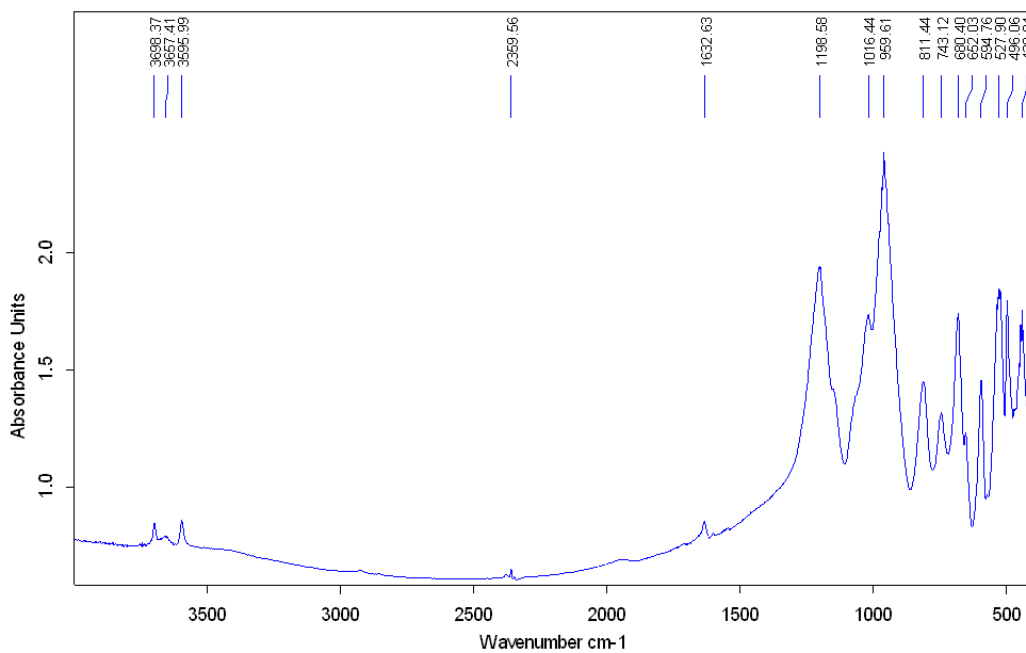


Fig. 9 IR spectrum of powdered sample PAD-8 with medium content alkali from  $400\text{ cm}^{-1}$  to  $4000\text{ cm}^{-1}$  under transmitted light

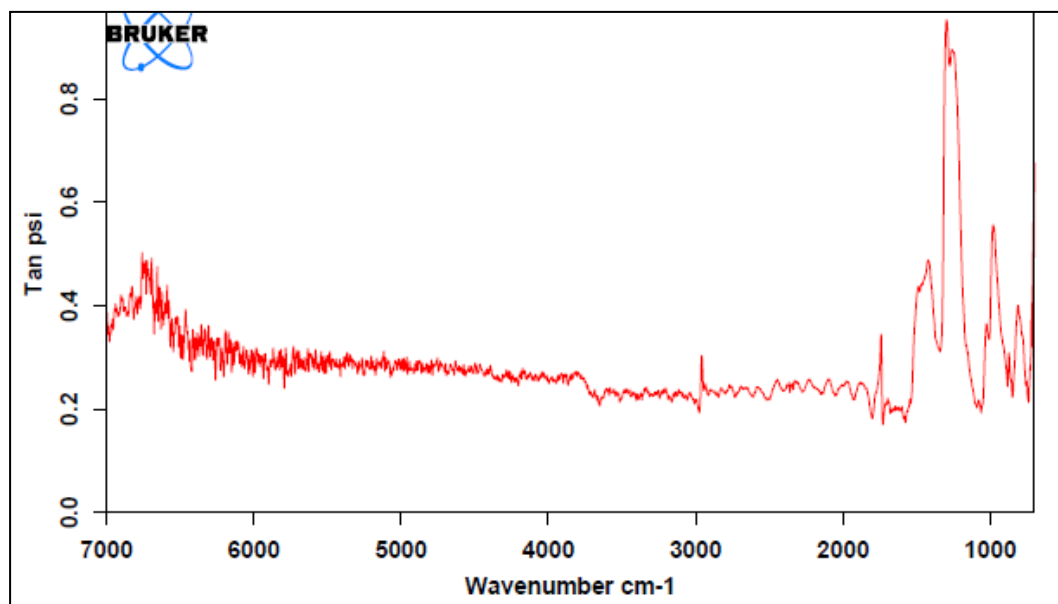


Fig. 10 IR spectrum of PAD-6 by reflection method from  $400\text{cm}^{-1}$  to  $7000\text{cm}^{-1}$ . 32 scans were obtained with a scanning velocity of  $40\text{ k Hz}$  with a resolution of 4 with Bruker, Vertex 70. Aperture was of  $1.5\text{mm}$  size.

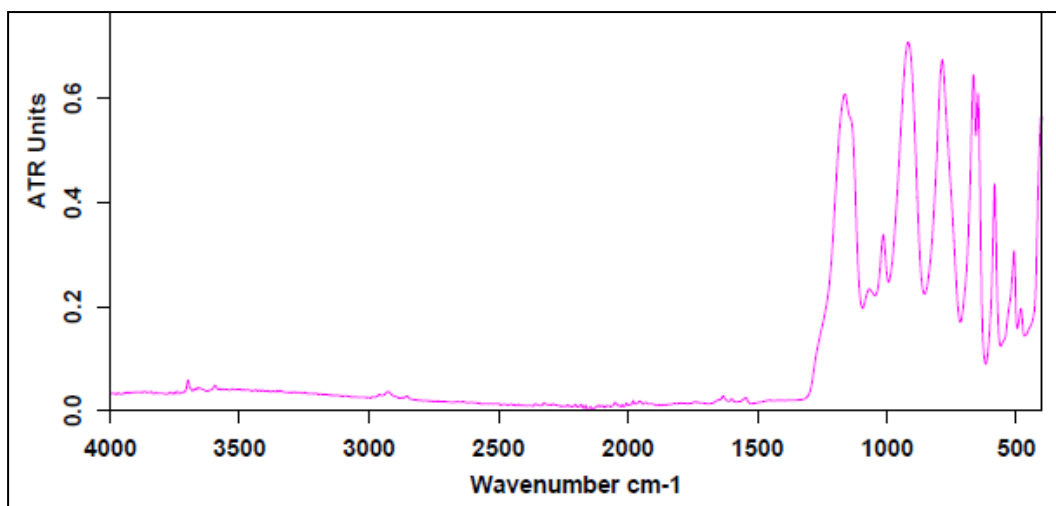


Fig. 11 Attenuated Total Reflection spectrum of PAD-6 sample from  $400\text{ cm}^{-1}$  to  $4000\text{ cm}^{-1}$ .  
32 scans at a resolution of 4 with scanning velocity of 7.5 with Bruker Alpha

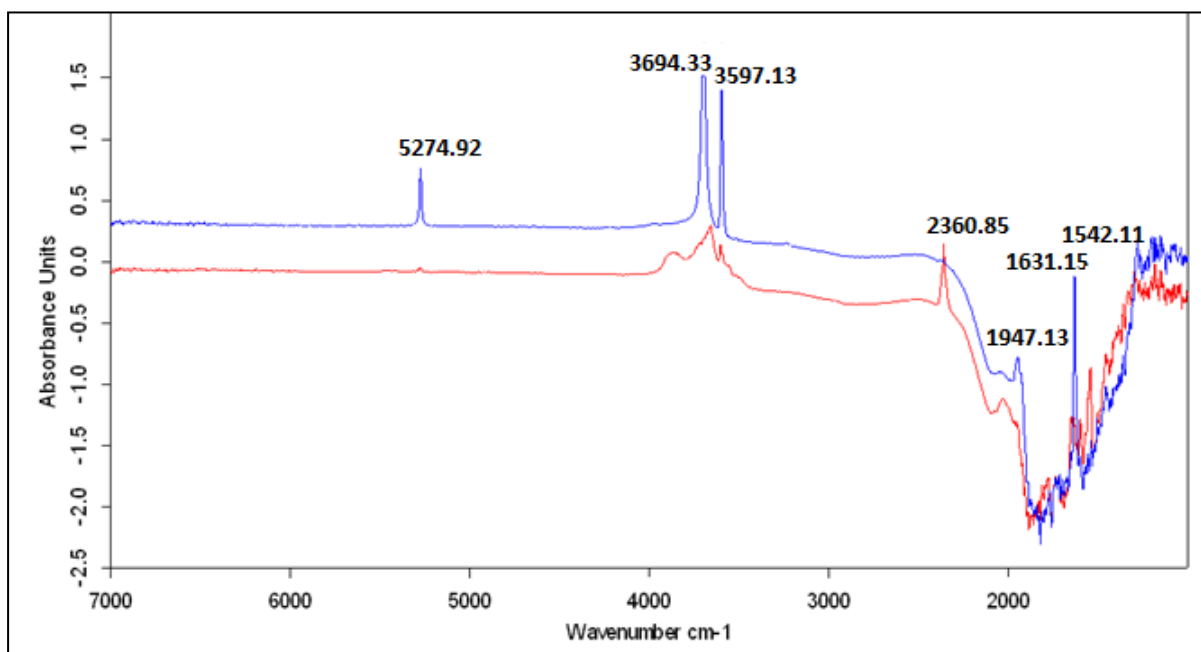


Fig. 12 IR spectra of PAD-5 single crystal under polarised light Blue line represents the spectrum when  $E \parallel c$  and red indicates when  $E \perp c$ .

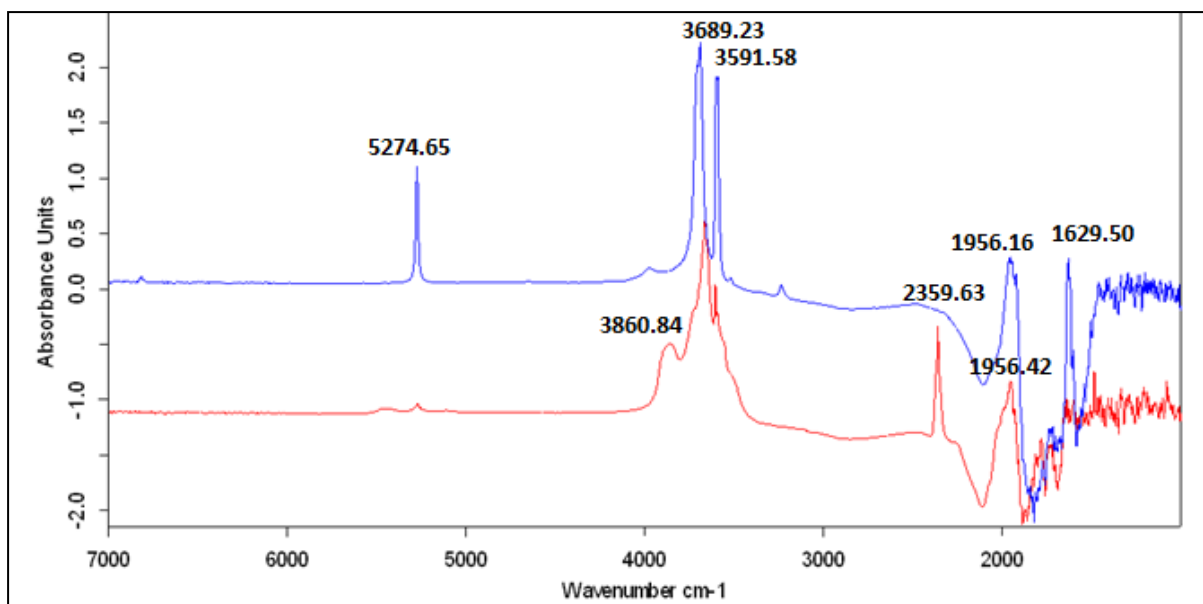


Fig. 13 IR spectra of PAY-2 single crystal under polarised light in the frequency region  $400\text{ cm}^{-1}$  to  $7000\text{ cm}^{-1}$

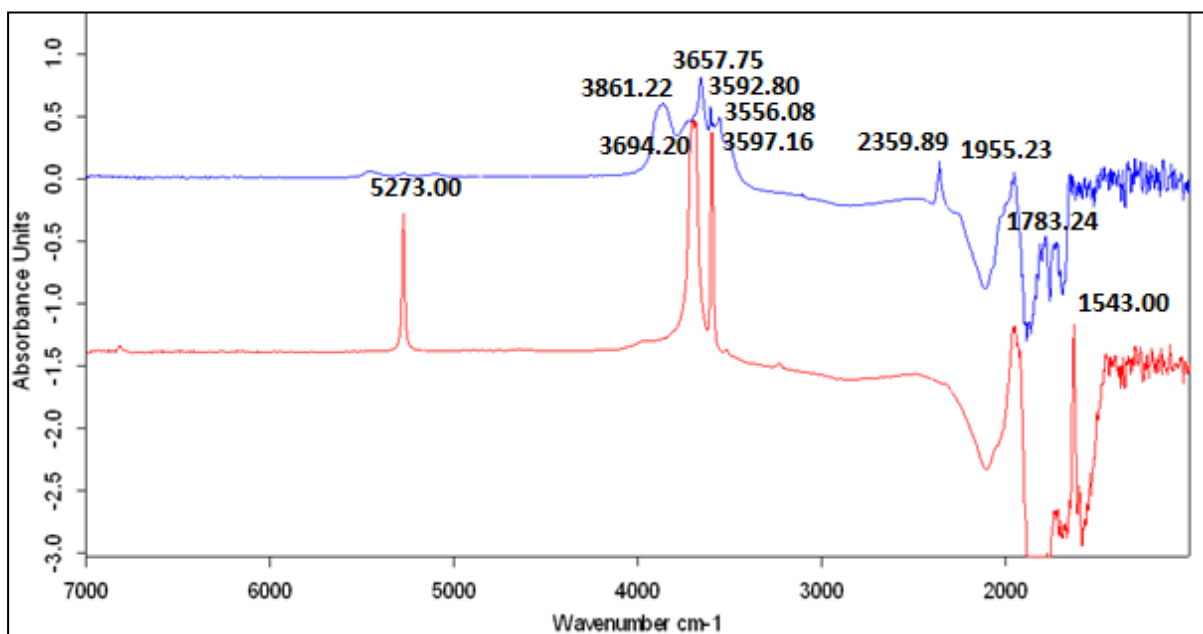


Fig. 14 IR spectrum of PAD-1 single crystal under polarised light from  $1400\text{ cm}^{-1}$  to  $7000\text{ cm}^{-1}$ .  
<sup>1</sup> Red line indicates spectrum under  $E||c$  orientation.

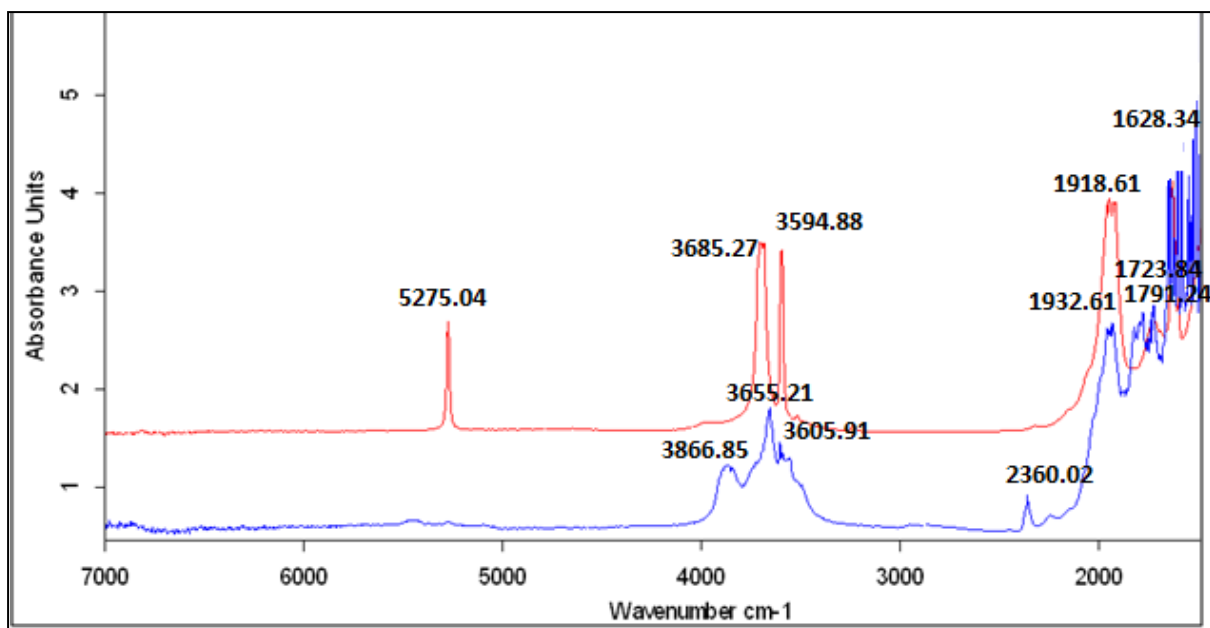


Fig. 15 IR spectra of PAY-5 single crystal under polarised light from 1400 cm<sup>-1</sup> to 7000 cm<sup>-1</sup>. Red line indicates the spectrum under E||c orientation. Blue line indicates the spectrum under E ⊥ c orientation.

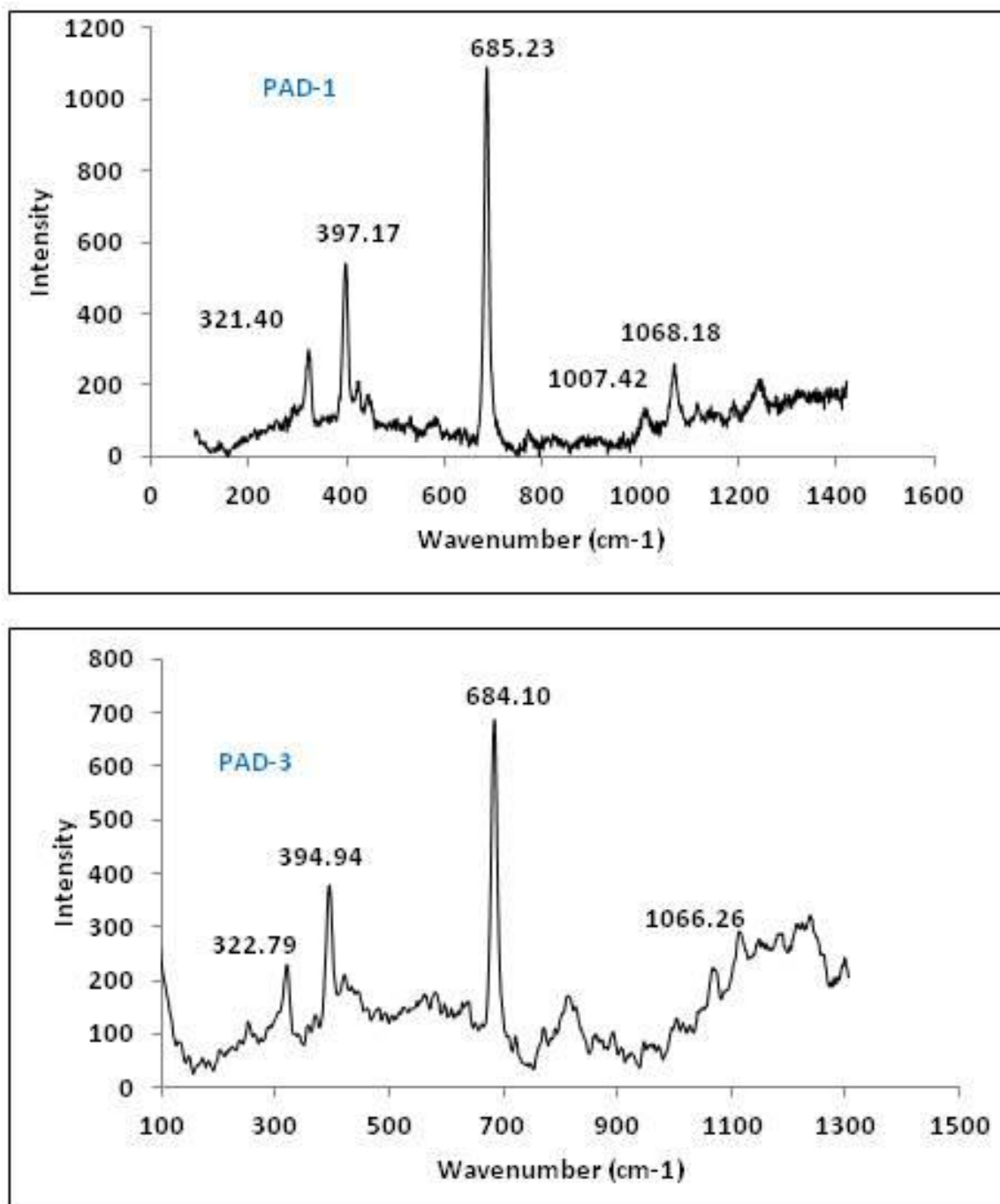


Fig. 16 Raman spectra of the samples PAD-1 & PAD-3 under polarised light under the orientation  $E \perp c$

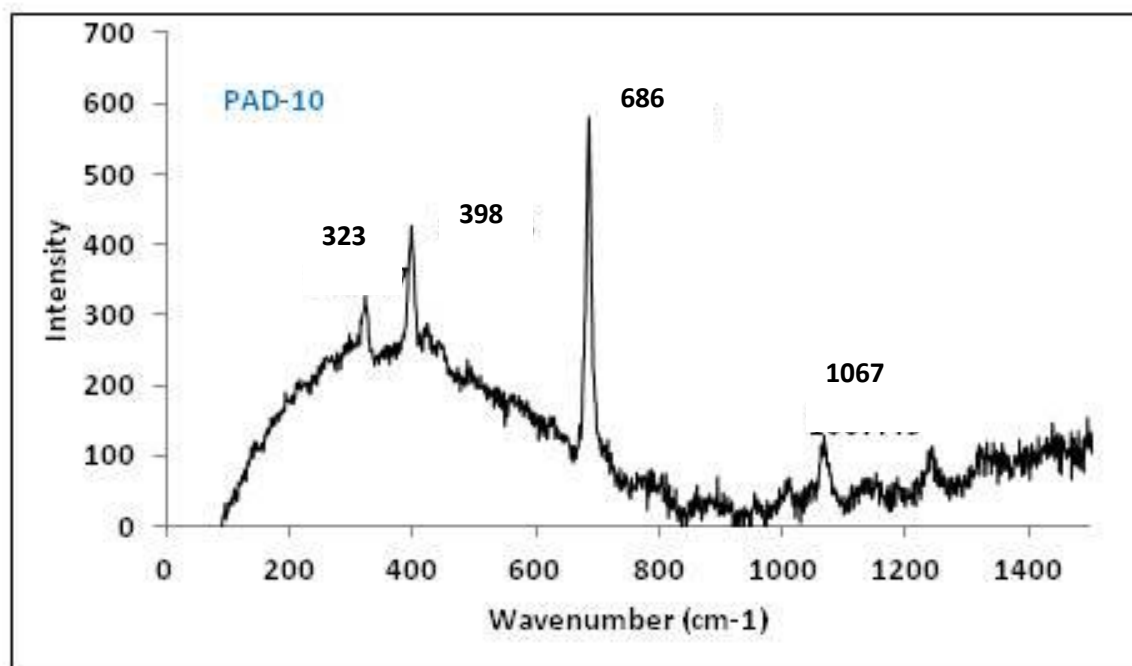


Fig. 17 Raman spectrum of PAD-10 when E $\perp$ c.

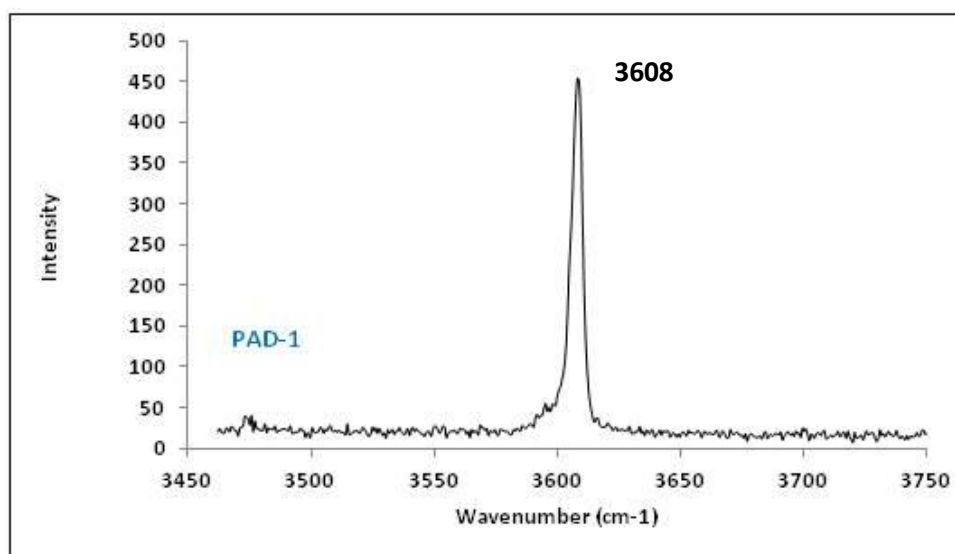


Fig. 18 Raman spectrum of PAD-1 in the water region

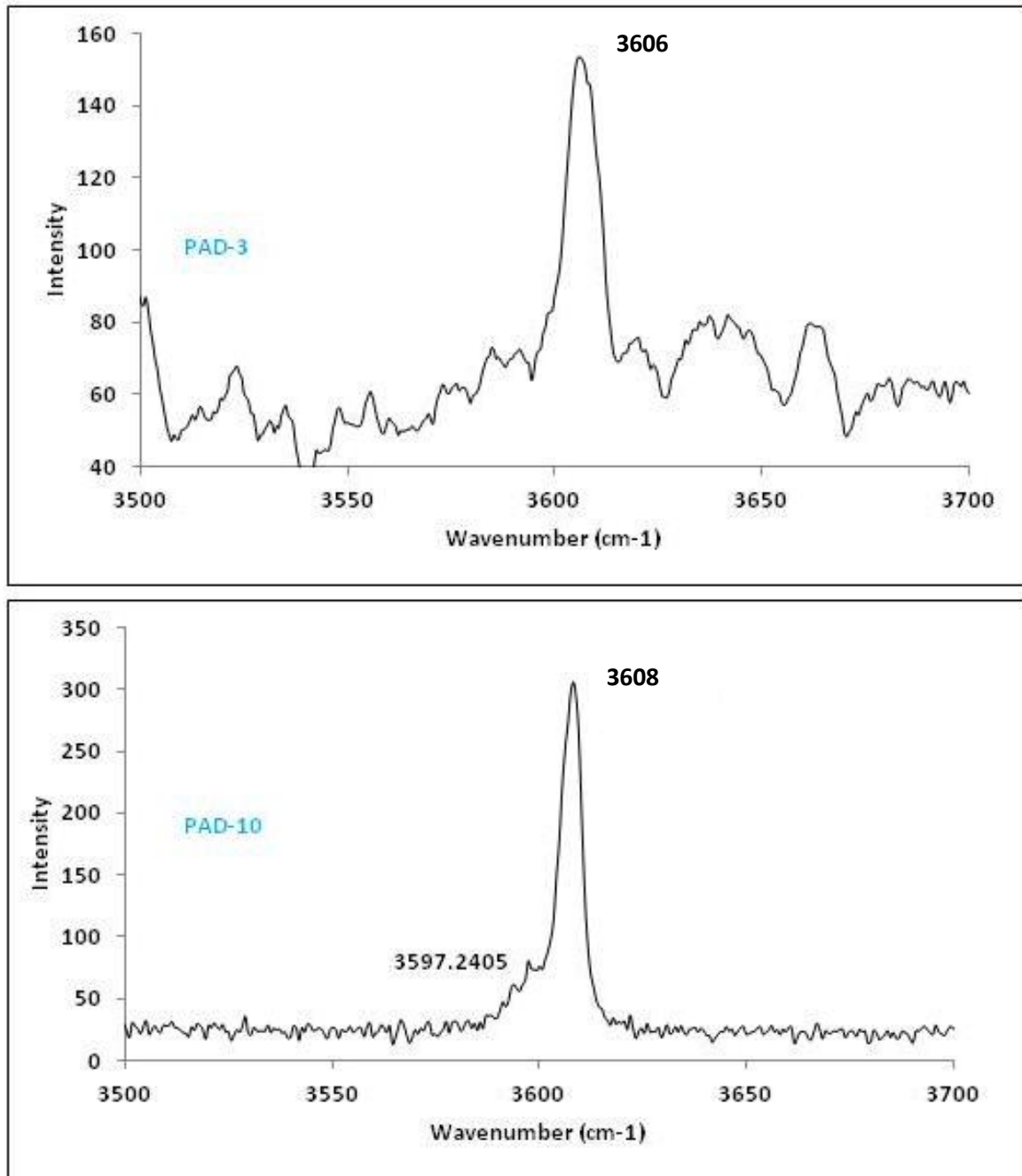


Fig. 19 Raman spectra of PAD-3 & PAD-10 in the water region

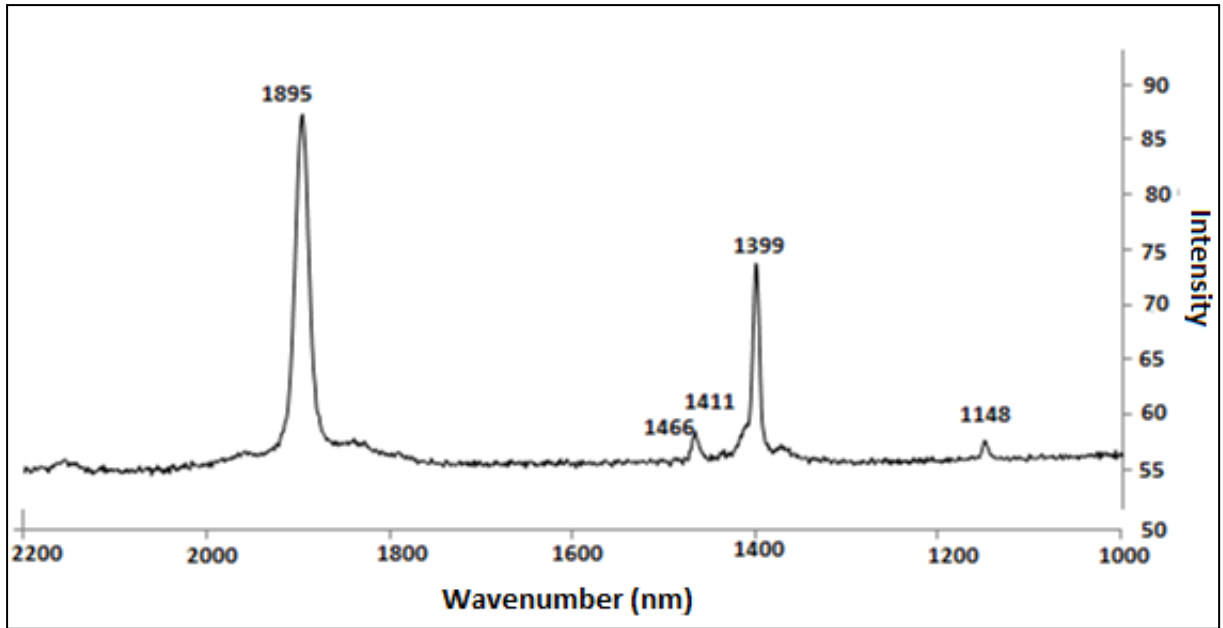


Fig.20 NIR spectrum of PAY-2 (Transmission method, E || c)

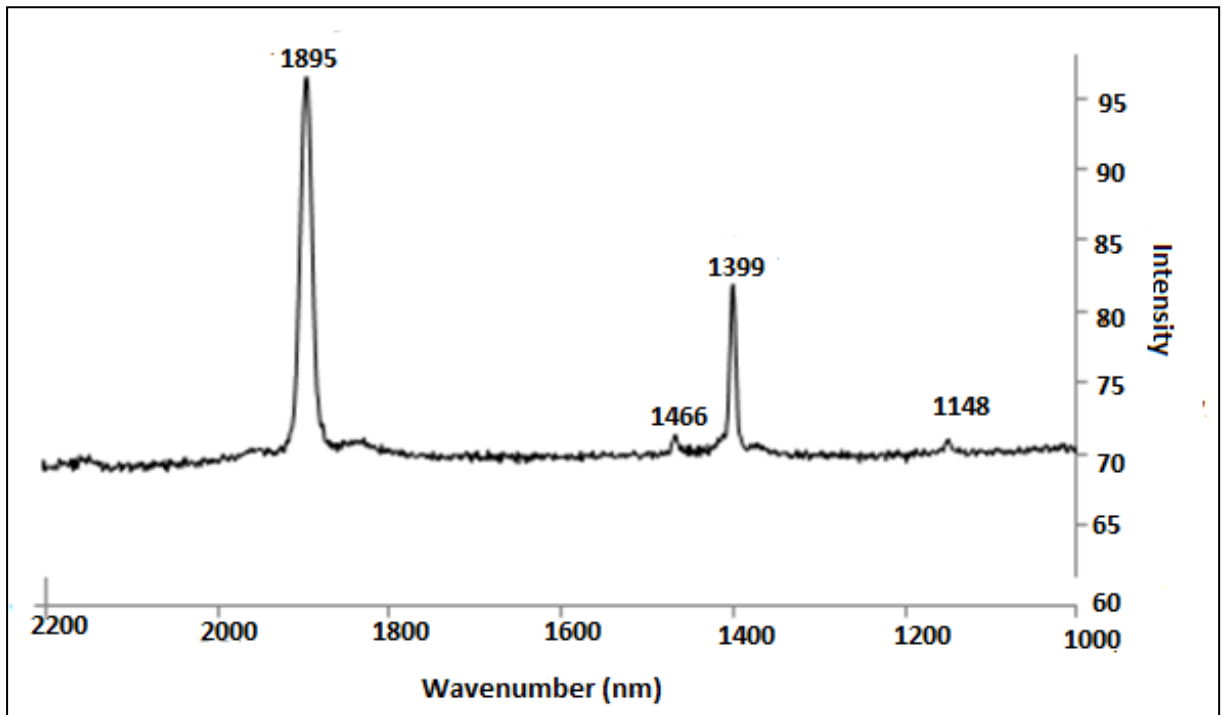


Fig. 21 NIR spectrum of PA-2 (E || c)

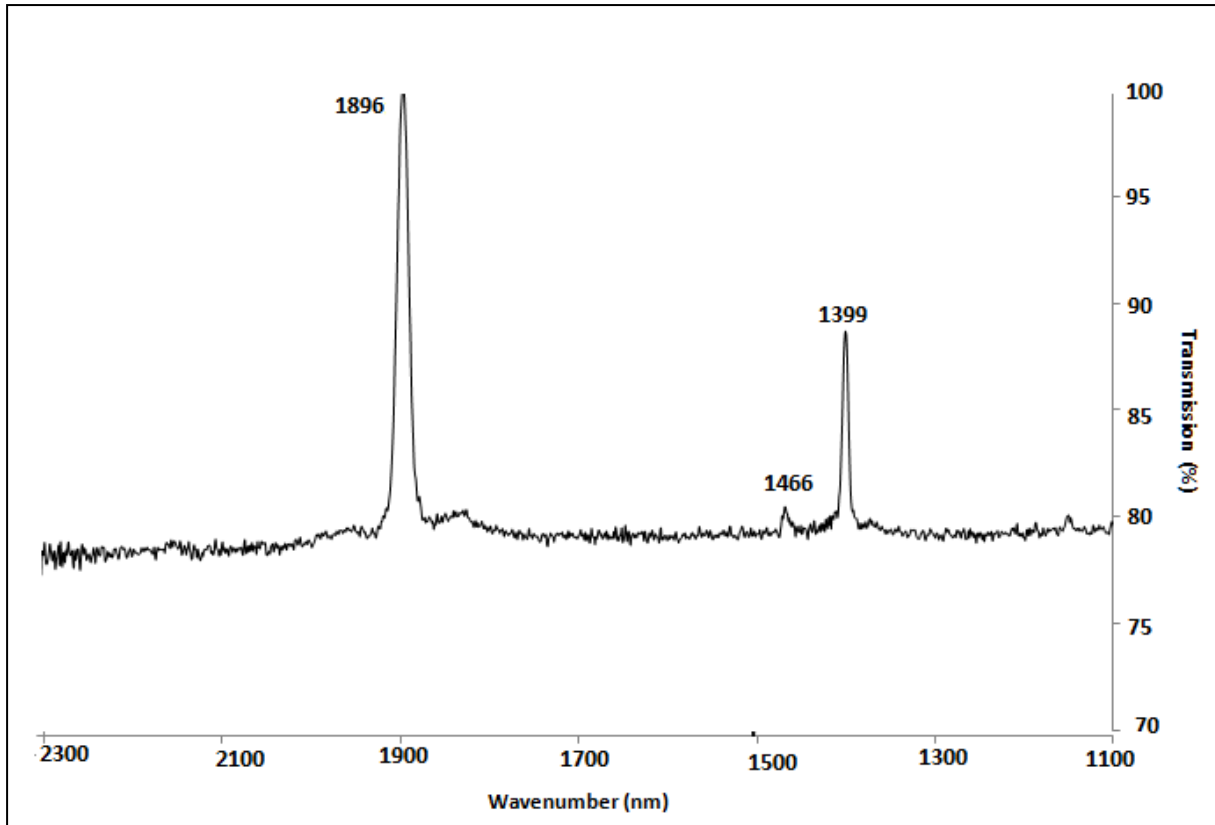


Fig. 22 NIR spectrum of PAD-5 (E||c)

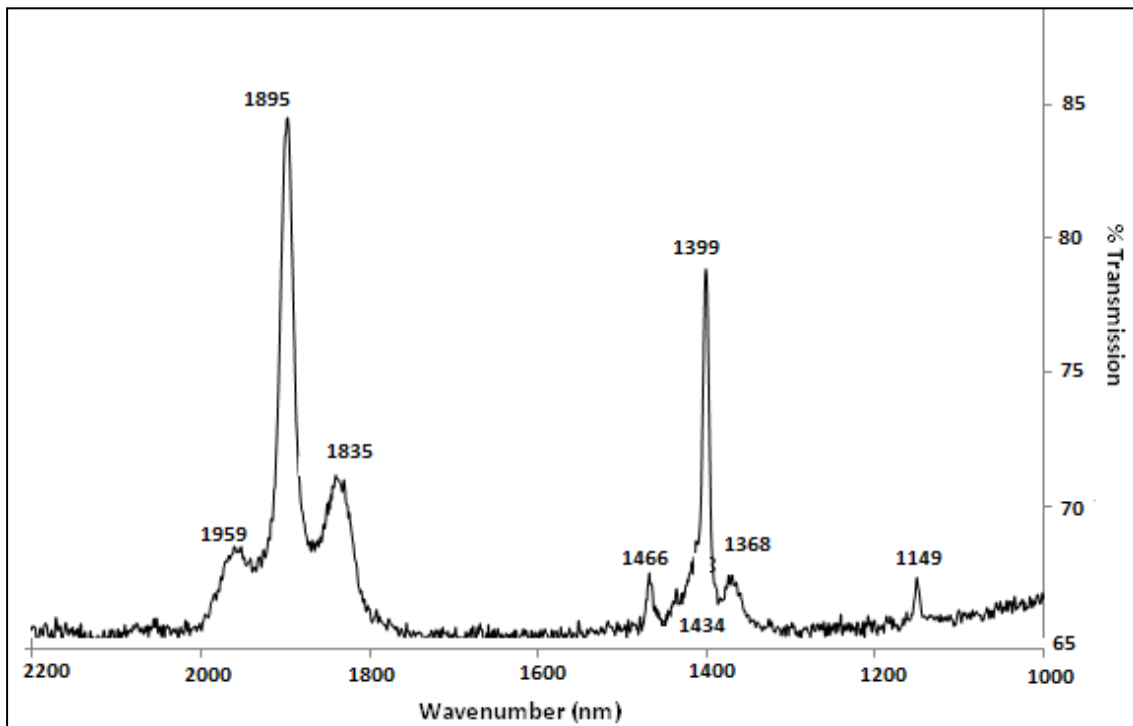


Fig. 23 NIR spectrum of PAY-1 (E⊥c)

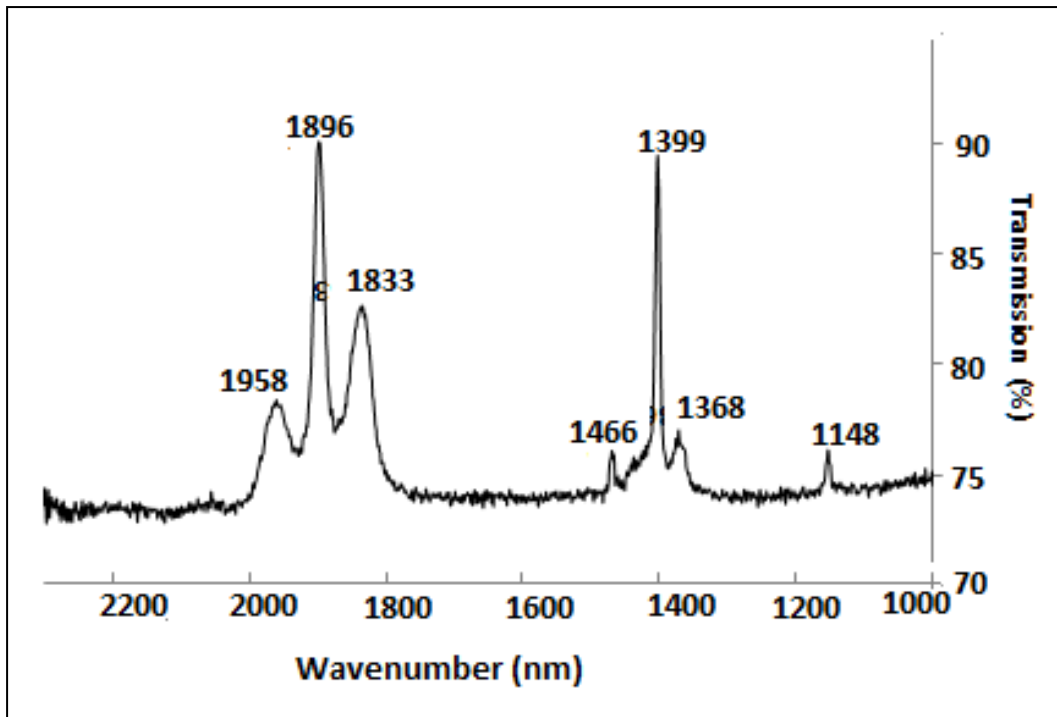


Fig. 24 NIR spectrum of PAY-4 (E.Lc)

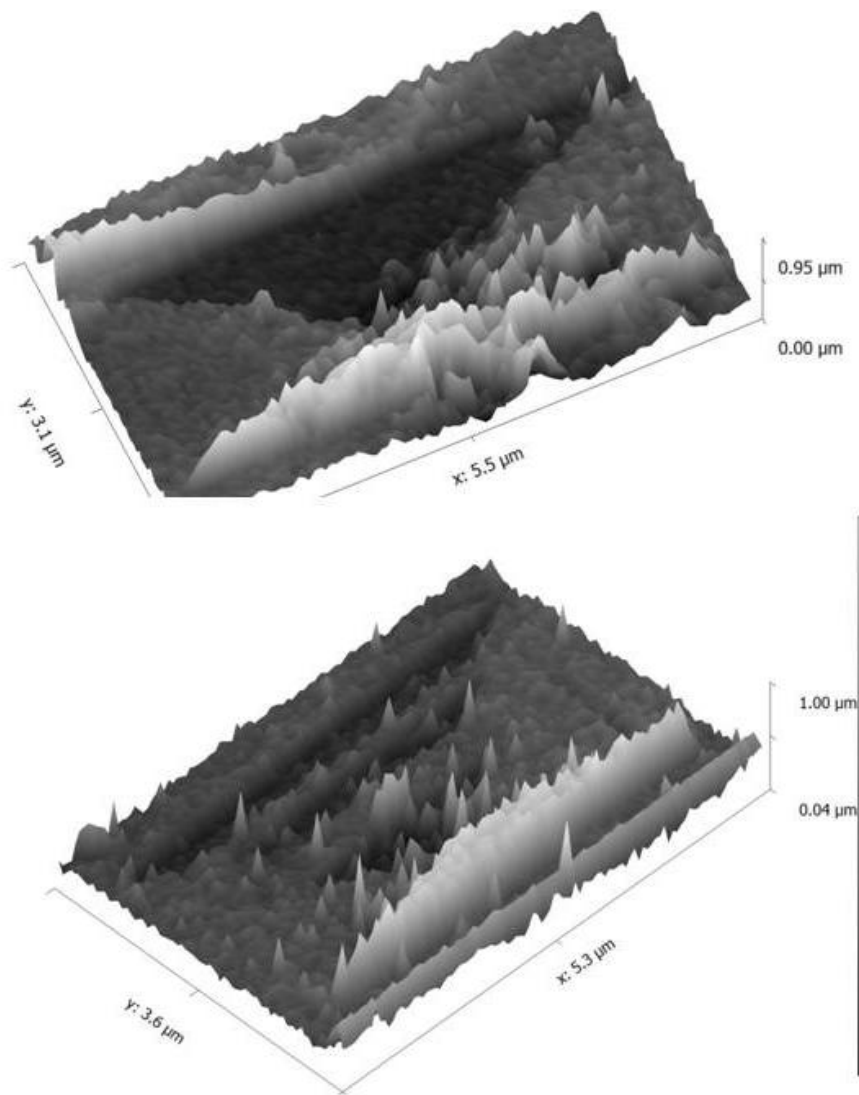


Fig. 25 Three dimensional reconstruction of P- type etch pit (above) and stepped etch pit (below)

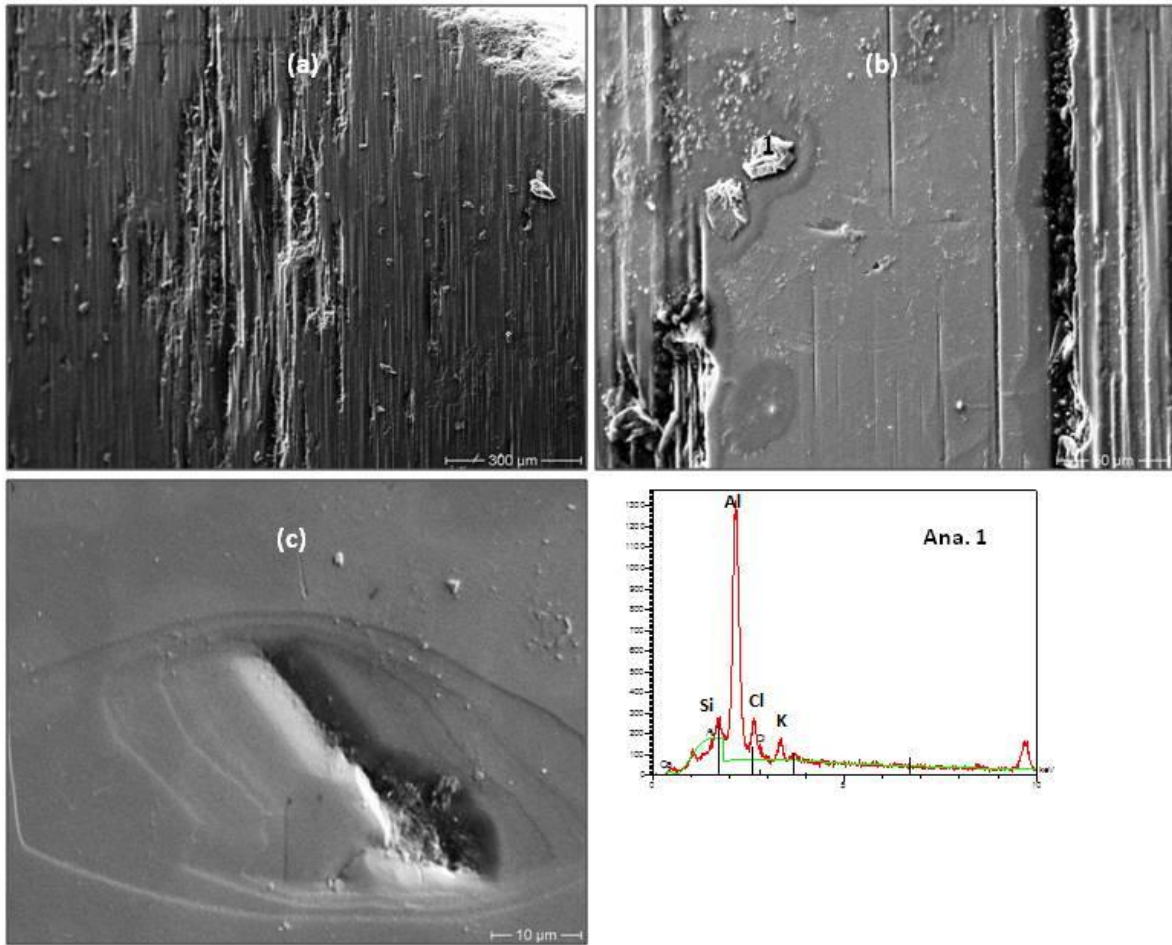


Fig. 26 (a) & (b) Irregular solution channels running parallel to c-axis on the prism face of PAD-7. The analysis shows the particle is rich in K and Cl. The amount of Si is very less. (c) Irregular to canoe shaped etch pit on the prism face of PAD-10 giving an appearance of steps.

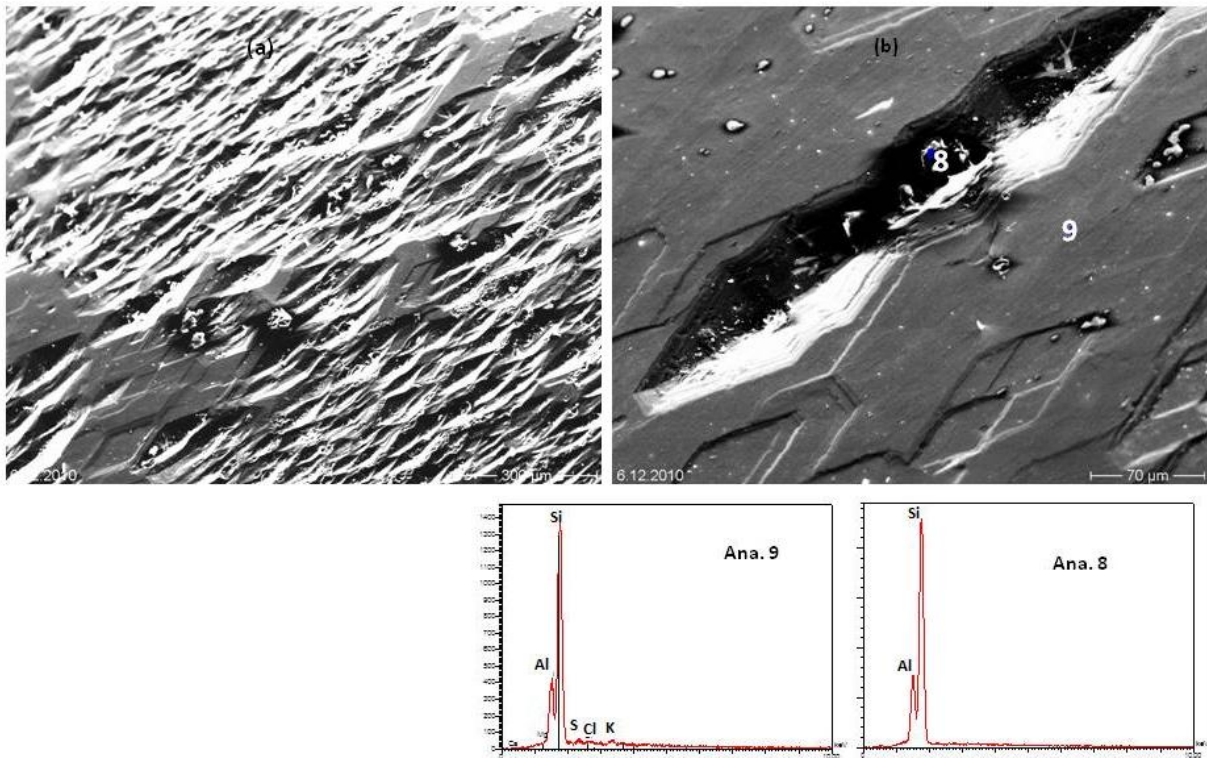


Fig. 27 (a) prism face of PAY-1 with very high etch pit density covered by diamond shaped, deep etch pits with pointed base and shallow etch pits with flat base. (b) Diamond shaped deep etch pits coalesce together. Analysis no. 9 indicates the presence of a very small amount of K and Cl.

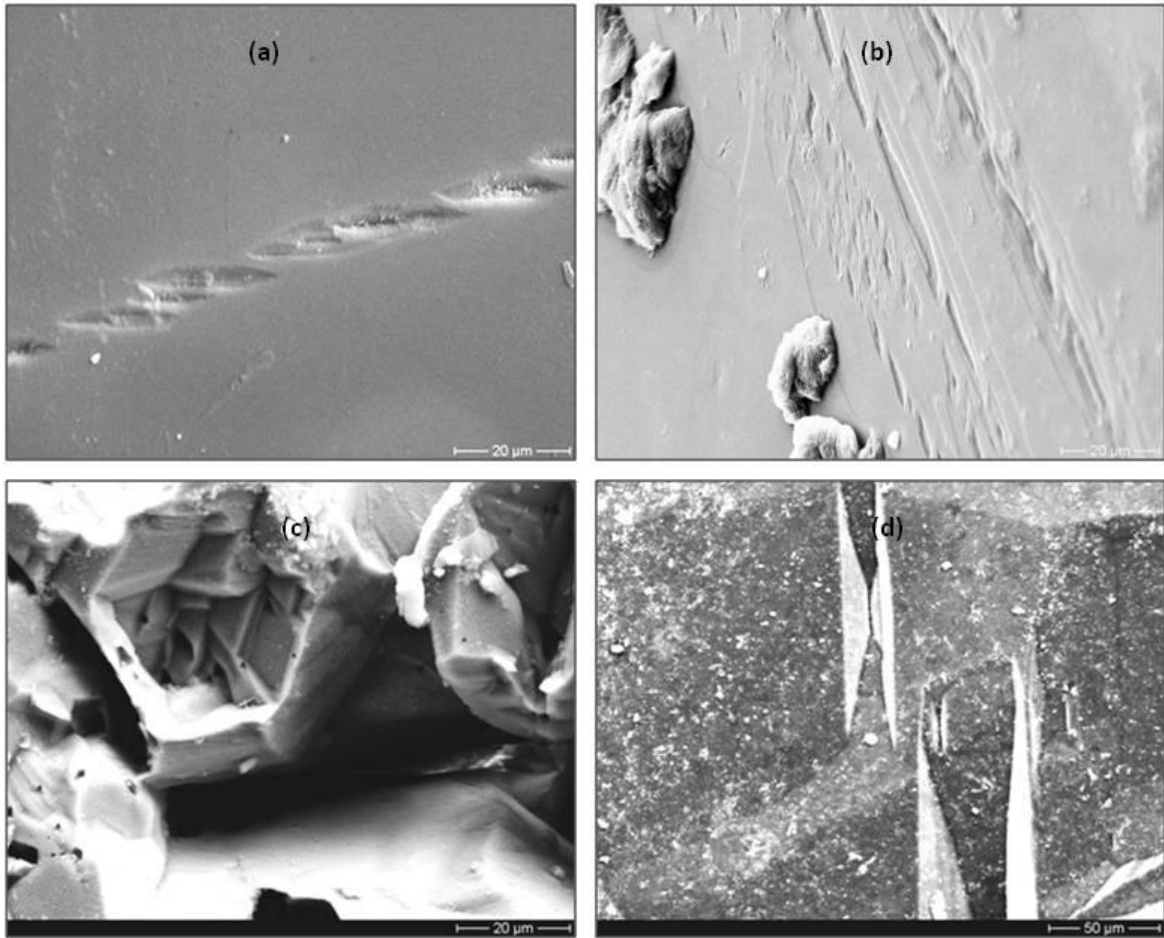


Fig. 28 (a) Canoe shaped etch pit aligned together on the prism face of PAY-3. The other parts are almost untouched by the solvent. (b) Etch pits almost rectangular shaped arranged in a line on PAY-3 prism face. (c) Hexagonal shaped etch pit on the base of BAA-2. Inside this etch pit, diamond shaped etch pits are discernable. (d) Elongated approximately rectangular shaped etch pits with their long axes perpendicular to c-axis on the prism face of BAA-2 sample. The walls are steep and the faces meet along a line at the base.

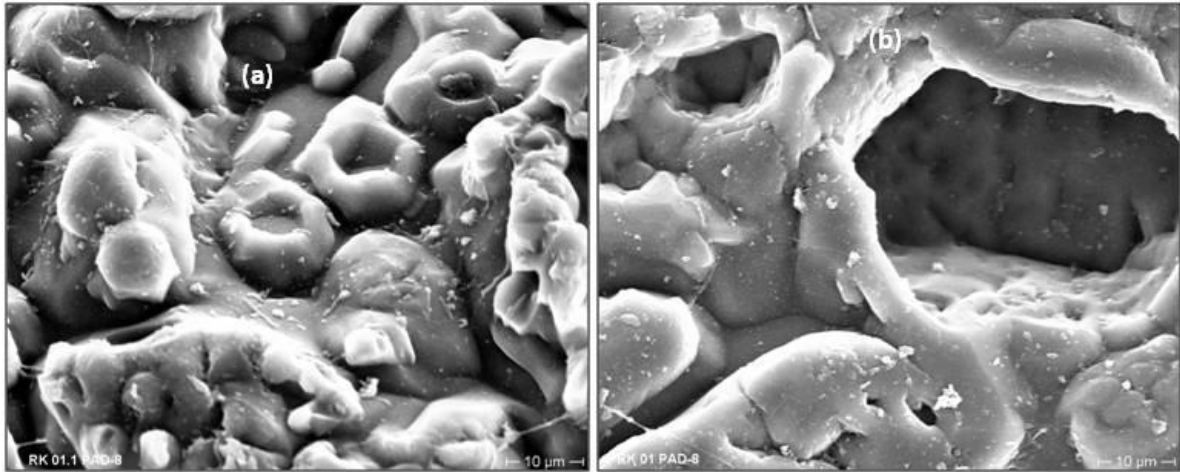


Fig. 29 Hexagonal shaped etch pit with flat base on the basal pinacoids of hydrothermally treated PAD-8 in NaCl solution. (b) Etch pit etch pit with steep walls. The bottom of the etch pit is flat.

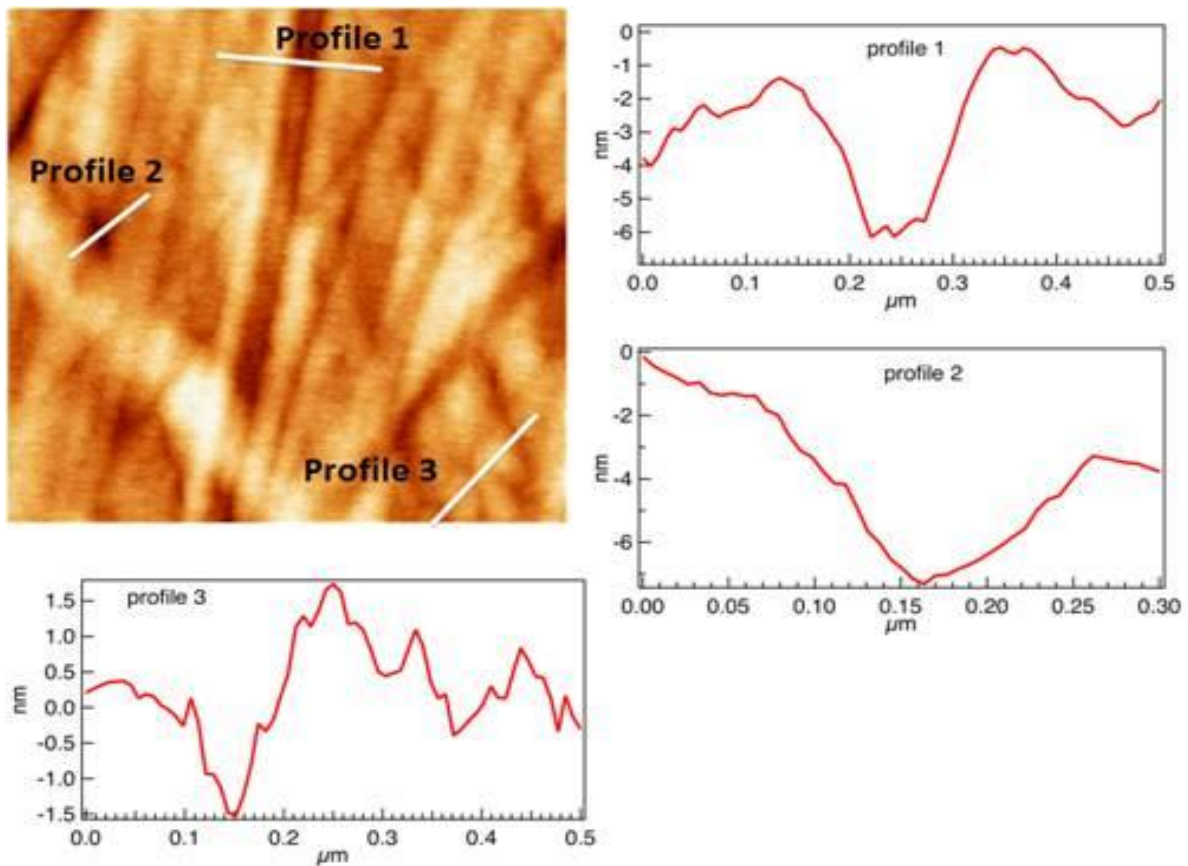


Fig. 30 Profiles along different directions on the polished surface of BA-1. Profiles. 1 & 2 show around 8 nm depth which could be due to polishing effects. Profile 3 shows depth of around 0.5 nm to 1.5 nm between sub atomic particles.

